Powerful far-infrared radiation of hot holes in a strained two-dimensional InGaAs/AlGaAs structure

Yu. L. Iványov, S. A. Morozov, V. M. Ustinov, and A. E. Zhukov

A. F. Ioffe Physicotechnical Institute, Russian Academy of Sciences, 194021 St. Petersburg, Russia
(Submitted April 27, 1998; accepted for publication April 27, 1998)
Fiz. Tekh. Poluprovodn. **32**, 1119–1121 (September 1998)

A sudden rise of far-infrared emission against the background saturation of the current–voltage characteristic of a strained InGaAs/AlGaAs structure in a strong electric field was observed in fields of about 1.5 kV/cm. As the electric field increases further, the intensity of the radiation changes nonmonotonically. It is suggested that the rise of emission is due to the formation of domains, which are responsible for the current saturation. © *1998 American Institute of Physics.* [S1063-7826(98)02109-7]

A considerable number of papers on far-infrared (IR) radiation of two-dimensional hot holes has recently been published (see, for example, Refs. 1–4). This topic is of interest because of the unusual nature of the energy spectrum of two-dimensional holes, because of the strong nonparabolicity of the dispersion curves of quantum-well subbands, and because of the existence of anticrossing points.[5] Under these conditions, it can be expected that as the holes are heated, an inverted distribution function is formed in a manner similar to that thought to occur in the case of uniaxially compressed germanium[6] (tunneling at the anticrossing point). However, in Ref. 7 it was shown that in uniaxially compressed germanium inversion does not arise in the split subbands. The reason is that in bulk germanium a close arrangement of split subbands at the anticrossing point exists only in the direction of compression (in the [111] crystallographic direction). Away from this direction the subbands ''move apart,'' tunneling does not arise, and inversion is impossible. At the same time, in two-dimensional structures a single direction of infinite motion is precluded and inversion in this scheme is more likely.

Far-IR radiation of two-dimensional hot holes was first observed from unstrained structures of the type GaAs/AlGaAs.[1–3] In those studies it was concluded that radiative transitions are of an intersubband character. In Ref. 2 it was shown that streaming of hot holes exists and streaming-associated evolution of the filling of the second quantum-well subband by hot holes in narrow (6.8 nm) quantum wells as a result of a change in the warming field was demonstrated, while in Ref. 3 the radiation spectrum from wide (20 nm) quantum wells was measured. No conclusions concerning the possibility of obtaining an inverted distribution were drawn. A strained structure based on InGaAs/GaAs was investigated in Ref. 4 . As a result of being heated in this system, holes are transferred from the well into the barriers, where they are effectively cooled because their effective mass is much larger than in the well. The possibilities of an inverted hole distribution are discussed on the basis of this effect.

In the present paper we report the results of a preliminary investigation of the far-IR radiation and transport of hot holes in a strained InGaAs/AlGaAs structure. The depth of hole quantum wells in this system exceeds 200 meV. Hole heating by an electric field applied along the quantum-well layers with such a well depth is unlikely to cause holes to be transferred from the well into the barriers, and all processes described below can be assumed to occur as a result of hole redistribution between quantum-well subbands.

The structure was grown by molecular-beam epitaxy in a standard RIBER-32P system with a solid-state arsenic source. A 0.2-μm-thick gallium arsenide buffer layer was grown on a semi-insulating GaAs (100) substrate. This was followed by an active region consisting of ten 15-nm-thick InGaAs quantum wells separated by 60 nm thick AlGaAs barriers. The thickness of the quantum wells did not exceed the critical thickness of pseudomorphous growth for the solid solution composition employed. The structure with quantum wells was bounded by 100-nm-thick AlGaAs barriers.

A two-dimensional hole gas was produced in the quantum wells by selective beryllium doping of narrow (2.5 nm) barrier layers, separated from the wells by 6.0-nm-thick spacers. The Be atom density in the layers was 1.2×10^{18} cm^{-3}. The entire structure was completed by a 200 Å thick GaAs layer. The growth temperature of the active region was equal to 510 °C, which made it possible to avoid reevaporation of In during the deposition process.

Samples with contacts, which were established by brazing in gold with zinc at a depth giving a reliable contact with the quantum-well layers, were made from the structures. The gap between the contacts in the experimental samples was equal to 2 mm. An electric field in the quantum-well layers was applied along the [110] crystallographic direction by means of 1-μs pulses with a repetition frequency of 10 Hz. All experiments were conducted at the liquid-helium temperature.

Modulated doping of the barriers in the structure gave good hole mobility. In our case the mobility in weak fields at liquid-helium temperature is on the order of 10^4 cm^2/(V·s). At this mobility streaming is observed in GaAs/AlGaAs-type structures; the streaming current depends

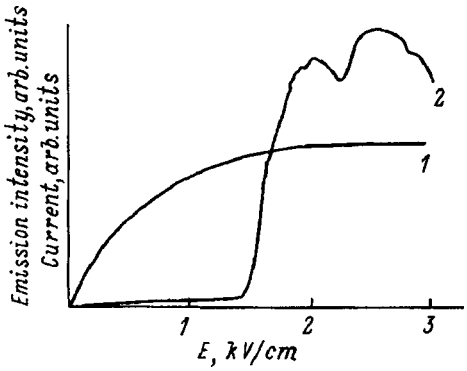

FIG. 1. Current (*1*) and far-IR radiation intensity (*2*) plotted as a function of the electric field E in the sample.

on the electric field, and the moment at which streaming is attained in an increasing electric field is characterized by a sharp kink in the current-voltage characteristic. Higher mobility causes streaming to occur in the weaker fields and causes the transition to be more abrupt (see Fig. 1 in Ref. 2). Nonetheless, total saturation of the current–voltage characteristic during streaming is not observed, since on reaching the energy of an optical phonon holes in ballistic flight have enough time to emit an optical phonon and penetrate into the active region to a depth which increases with increasing electric field, which accounts for the weak increase in the current.

A different picture is observed when a strong field is applied in the quantum-well layers of a strained InGaAs/AlGaAs structure. Despite good hole mobility in weak fields, in this case the current-voltage dependence does not have a characteristic kink, which should be observed when streaming commences, but rather it gradually passes into a region of actual current saturation (see Fig. 1, curve *1*). Such a behavior of the current-voltage characteristic for a strained structure can be explained by nucleation and growth of a domain — a region of high but fixed field — which controls the current that flows through the sample. As the potential difference on the contacts of the sample increases, the domain region grows, but the field in the domain and therefore the current remain constant.

Far-IR radiation was detected in the region of sensitivity of a boron-doped germanium photodetector (50–120 μm). Weak growth of the intensity, comparable in magnitude to that detected in Ref. 2 , is observed in weak fields. In a field of about 1.5 kV/cm the radiation intensity grows rapidly, increasing by several orders of magnitude (see Fig. 1, curve *2*). No sharp changes in the current are observed. As the field in the sample increases further, the radiation intensity varies nonmonotonically. The character of this variation with repeated passes remains the same, though the amplitude varies somewhat. In all cases, sharp growth of the radiation occurs in the same electric field.

The nonmonotonic character of the intensity of the powerful radiation as a function of the electric field indicates that the radiation is not associated with trivial processes in the sample (for example, electric breakdown). The rapid growth of the emission could be associated with domain formation, which in turn is associated with hole redistribution over quantum-well subbands, in which tunneling at anticrossing points does not play a crucial role. Unfortunately, we do not know the spectrum of the hole subbands of this structure. This spectrum can differ strongly from the corresponding spectrum of unstrained GaAs quantum wells, which is characterized by a large separation of the subbands at the anticrossing points.[5] At the same time, there are known cases of strained structures with dispersion curves which are close to one another at the anticrossing point, so that tunneling is entirely possible, and with a wide region with large effective mass in the Brillouin zone, which should allow the existence of a domain (see Fig. 1a in Ref. 8).

Under these conditions inversion and generation of stimulated radiation by the mechanism described above can appear. The threshold character of the powerful radiation supports this interpretation of the processes that have occurred.

This work was supported by the Russian Fund for Fundamental Research (Grant No. 98-02-18403) and the Interdisciplinary Science and Technology Program of Russia ''Physics of Solid-State Nanostructures'' (Grant No. 97-1044).

We wish to thank M. S. Kagan for long-standing discussions of the possibility of using strained quantum-well structures to obtain stimulated far-IR radiation. Those discussions had a positive influence on the organization of our experiments.

[1] L. E. Vorobjev, D. V. Donetsky, and A. Kastalsky, in *Nanostructures: Physics and Technology* (St. Petersburg, 1995), p. 221.
[2] Yu. L. Ivanov, G. V. Churakov, V. M. Ustinov, A. E. Zhukov, and D. V. Tarkhin, in *Nanostructures: Physics and Techology* (St. Petersburg, 1995), p. 225.
[3] L. E. Vorobjev, L. E. Golub, and D. V. Donetsky, in *Nanostructures: Physics and Technology* (St. Petersburg, 1996), p. 235.
[4] V. Ya. Aleshkin *et al.*, in *Nanostructures: Physics and Technology* (St. Petersburg, 1996), p. 443.
[5] L. G. Gerchikov and A. V. Subashiev, Phys. Status Solidi B **160**, 443 (1990).
[6] I. V. Altukhov, M. S. Kagan, K. A. Korolev, and V. P. Sinis, Zh. Éksp. Teor. Fiz. **103**, 1829 (1993) [J. Exp. Theor. Phys. **76**, 903 (1993)].
[7] E. V. Starikov and P. N. Shiktorov, Opt. Quantum Electron. **23**, S247 (1991).
[8] A. M. Cohen, S. R. Aladim, G. E. Margues, Surf. Sci. **267**, 464 (1992).

Translated by M. E. Alferieff

AMORPHOUS, GLASSY, AND POROUS SEMICONDUCTORS

Composition and porosity of multicomponent structures: porous silicon as a three-component system

L. V. Belyakov, T. L. Makarova, V. I. Sakharov, I. T. Serenkov, and O. M. Sreseli

A. F. Ioffe Physicotechnical Institute, Russian Academy of Sciences 194021 St. Petersburg, Russia
(Submitted April 22, 1998; accepted for publication April 27, 1998)
Fiz. Tekh. Poluprovodn. **32**, 1122–1124 (September 1998)

It is shown for the system porous silicon (*por*-Si)–silicon (Si) that effective nondestructive investigation of the interfacial morphology of layered semiconductor systems and of the composition of multicomponent layers by ellipsometry and Rutherford backscattering is possible. Both methods were used to determine the percentage composition of the main components of *por*-Si: crystal silicon, silicon oxide, and voids (porosity). It is shown that *por*-Si obtained by pulse-anodization contains a substantial quantity of silicon oxide. It is also shown that spectral ellipsometry can be used to determine the specific ratio of individual layers or components of multilayer and multicomponent systems (provided that the spectral dispersion of the optical constants of these components is known). © *1998 American Institute of Physics.* [S1063-7826(98)02209-1]

1. INTRODUCTION

Multicomponent systems containing quantum-well particles have recently been studied extensively. Such systems can be viewed as a new class of semiconductor materials with properties that differ substantially from those of the initial components. Examples of such materials are Ge and Si clusters in a SiO_2 matrix[1,2] and metal oxides[3] and superconducting ceramics[4] embedded in fullerenes.

A classical example of a multicomponent quantum-well system is porous silicon (*por*-Si). In the ideal case *por*-Si contains silicon microcrystallites and voids. Depending on the preparation method, it can also contain inclusions of amorphous silicon, silicon oxides, and even organosilicon compounds, which result from the treatment in organic mixtures.

Our objective in this study was to investigate the composition of the layers and the porosity of *por*-Si. This was done by using a combination of nondestructive methods — spectroscopic ellipsometry, Rutherford backscattering (RBS), and proton-induced x-ray emission (PIXE).

2. EXPERIMENT

Boron-doped, *p*-type Si with 2 $\Omega\cdot$ cm resistivity and $\langle 100\rangle$ orientation was used. Anodization was performed in a 1:1 ethanol solution of HF. Pulse-electrolysis with illumination ($\sim$40 mW/cm^2) was used. The duration of the square voltage pulses was $\tau=0.1-10$ ms and the pulse repetition frequency was $f=5-100$ Hz. The current density in a pulse was $j=10-50$ mA/cm^2 (charge $Q=1-10$ C/cm^2). The layers possessed a dense, shiny surface.

The measurements of the thickness and the optical constants *n* and *k* were performed on a LÉF-3M ellipsometer at angles of incidence in the range 50–70°. The use of He–Ne, He–Cd, and argon lasers as radiation sources made it possible to investigate the optical characteristics of *por*-Si in the photon energy interval $h\nu=1.96-2.801$ eV. Standard formulas were used to convert the measured values of the complex reflectance of the structure into the thicknesses and complex refractive indices of the material.[5] For a transparent film, the periodicity of the ellipsometric data as a function of the thickness made it necessary to make a preliminary estimate of the film thickness by means of interferometric measurements in a MII-4 microscope.

The composition and thickness of the layers were also investigated by RBS and PIXE.[6]

3. RESULTS AND DISCUSSION

The refractive index *n* and extinction coefficient *k* were determined by spectral ellipsometry. The values of the extinction coefficient *k* in the entire measured spectral range and at all thicknesses do not exceed 0.01. Since in the investigated layers $n\gg k$, the real part of the effective permittivity of these layers is determined only by the refractive index: $\varepsilon=n^2-k^2\simeq n^2$. The main and most important information about the layers can therefore be obtained by analyzing the measurements of the refractive index *n*.

Figure 1 shows the spectral dependence of the refractive index of one sample of porous silicon obtained by pulse-anodization ($j=40$ mA/cm^2, $\tau=5$ ms, $f=5$ Hz, $Q=2.3$ C). The Bruggemann effective-medium theory[7] was used to estimate the relative content of the components in a *por*-Si layer. The relationship between the experimentally determined effective permittivity ε_{eff} of a multicomponent system and the permittivities ε_i and relative content f_i of individual components is determined by the following equations extended to the case of *i* components:

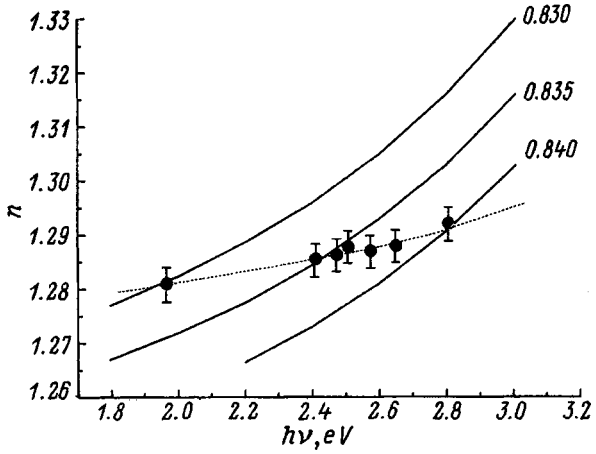

FIG. 1. Spectral dependences of the refractive index n of *por*-Si: Dots — experiment; solid lines — calculation in a two-component model silicon + void. The relative void fraction is indicated.

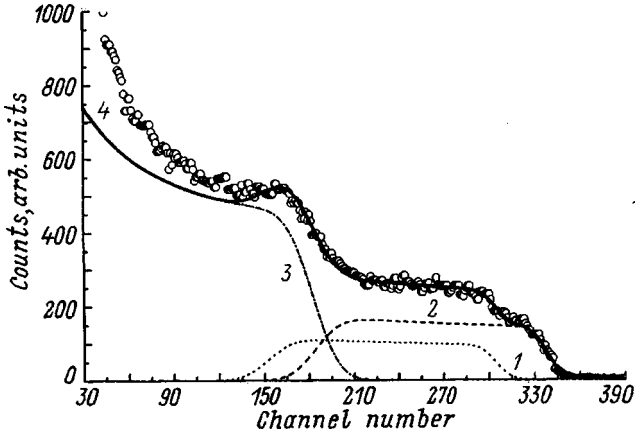

FIG. 2. RBS spectrum of a 8000 Å thick *por*-Si layer on a *c*-Si substrate. Dots — experiment, curves — model spectra: *1, 2* — oxygen and silicon partial spectra for a porous structure, *3* — silicon partial spectrum of the substrate, *4* — total model spectrum.

$$\sum_i f_i(\varepsilon_i-\varepsilon_{\text{eff}})/(\varepsilon_i+2\varepsilon_{\text{eff}})=0,$$

$$\sum_i =f_i=0.$$

The dielectric constant ε_1 of the silicon microcrystallites was assumed to be equal to bulk silicon. In the case of two components, silicon and voids, the spectral dependences of the refractive index are given in Fig. 1 (solid lines) for relative void concentrations of 0.830, 0.835, and 0.840. The deviation of the experimental points from the computed curves was attributed to the fact that the real structure deviates from the two-component model because of the presence of oxide. Since the dispersion of the oxide in the visible region of the spectrum is negligible, while a void has no dispersion at all, silicon is the only component that determines the slope of the experimental curve in Fig. 1.

In the three-component Bruggemann effective-medium model the concentration of each component of the system can be estimated from existing data on the optical constants of crystalline silicon *c*-Si (Ref. 8) and SiO_2. The following results are obtained assuming spherical components: porosity — 54.8%, *c*-Si — 6.4%, and SiO_2 — 38.8%.

A direct estimate of the atomic composition of a *por*-Si layer was made using the RBS data, which give the energy distribution of the protons reflected from the sample (Fig. 2). The thickness D of the films in units of the number of arbitrary atoms (arb. at.) Si_xO_{1-x} per cm^2 can be calculated from these data.[9] We obtained $D=2.750\times10^{18}$ arb. at./cm^2. The atomic ratio is Si : O = 0.37 : 0.63, which corresponds to the composition $SiO_{1.7}$. The PIXE measurements, which show the relative intensities of the O and Si lines, confirm these results. The PIXE measurements in random and channeling directions (Fig. 3) show that channeling is observed only for silicon, but not for oxygen, which decreases the signal by $\sim$12%. This indicates the presence of a crystalline phase (*c*-Si) in the porous layer. As is well known, in crystalline silicon the ratio of the PIXE signals in the random and channeling directions is 0.03–0.05. On this basis we estimate the *c*-Si content in the layer to be 14.2%.

The silicon/oxygen ratio which was obtained corresponds to the layer composition Si : O = 1 : 1.7. Since the *c*-Si concentration is 14.2%, the fraction of silicon bound with oxygen is 85.8%. It is obvious that the ratio 0.858 : 1.7 corresponds exactly to the composition of silicon dioxide. This makes it possible to interpret porous silicon as a system consisting of three components (silicon, silicon dioxide, and voids), if the other possible compounds of silicon with oxygen are disregarded.

Given the thickness D, the density of a film can be calculated from the equation

$$\rho=DA/d,$$

where A is the mass of an arbitrary atom in grams, and d is the thickness of the layer in cm. From the known layer thickness (8000 Å) we obtain a density of 1.167 g/cm^3. Since the density of *c*-Si is 2.33 g/cm^3 and that of SiO_2 is 2.3 g/cm^3, the porosity is 49.4% and the *c*-Si and SiO_2 fractions are 7.2% and 43.3%, respectively.

The good agreement between the results obtained by two fundamentally different methods thus indicates that spectral

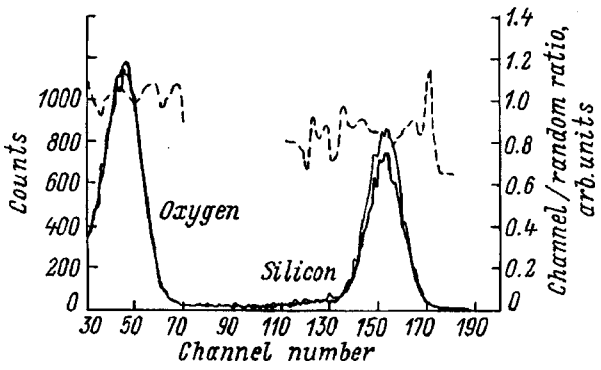

FIG. 3. PIXE spectra of a *por*-Si layer in the channeling direction (solid heavy line) and the random direction (fine line), and their ratio (dashed line).

ellipsometry can be used in a new way to study interfaces in layered semiconductor systems and to correctly choose a metod for analyzing a multicomponent medium.

Two features stand out in the ratio of components in *por*-Si: the relatively low porosity of the layer and its high oxide content. It should be noted that the second feature is to be expected. Our objects of investigation were *por*-Si layers obtained by pulse anodization.[10] This method yields layers with a smooth shiny surface, which is necessary for ellipsometric measurements. Moreover, the photoluminescence spectrum obtained by pulse-anodization of *por*-Si is characterized by an intense fast-luminescence band,[10] which is usually attributed to the presence of a substantial quantity of oxide in the layer.[11] In this study we have confirmed the relationship between features of the photoluminescence spectrum and the oxide content in the *por*-Si layer.

The low values of the porosity of the layer are explained mainly by the fact that the oxide in the layer was taken into account, since in the two-component system the porosities exceed 80% (see Fig. 1). At the same time, it should be noted that the weight method ordinarily used to determine the porosity of *por*-Si layers gives values that are too high because of errors in estimating the layer thickness, especially in the presence of a so-called crater — general settling of the porous layer relative to the initial silicon surface.[12]

4. CONCLUSIONS

1. It was shown that spectral ellipsometry can be used to determine the specific ratio of individual layers or components of multilayer and multicomponent systems (provided that the spectral dispersion of the optical constants of these components is known).

2. The relationship between the fast-luminescence band of *por*-Si and the presence of oxide in the layer was confirmed experimentally.

This work was supported by the Russian Fund for Fundamental Research (Grants N 96-02-17903 and N 96-02-17926), INTAS (N 93-3325), and the program ''Physics of Solid-State Nanostructures'' of the Ministry of Science.

[1] K. V. Shcheglov, C. M. Yang, K. J. Vahala, and H. A. Atwate, Appl. Phys. Lett. **66**, 745 (1995).
[2] P. Mutti, G. Ghislotti, S. Bertoni, L. Bonoldi, G. F. Cerofolini, L. Meda, E. Grilli, and M. Guzzi, Appl. Phys. Lett. **66**, 851 (1995).
[3] D. Wang, J. Zuo, O. Zhang, Y. Luo, Y. Ruan, and Z. Wang, J. Appl. Phys. **81**, 1413 (1997).
[4] S. Sathahiah, R. A. Zagraro, M. T. T. Pacheco, L. S. Grigorian, and K. Yakushi, J. Appl. Phys. **81**, 2400 (1997).
[5] R. Azzam and N. Bashara, *Ellipsometry and Polarized Light*, Elsevier, North-Holland, 1987 [Mir, Moscow, 1983].
[6] V. V. Afrosimov, G. O. Dzyuba, R. N. Il'in, M. P. Panov, V. I. Sakharov, I. T. Serenkov, and E. A. Ganza, Zh. Tekh. Fiz. **66**, 76 (1996) [Tech. Phys. **41**, 1240 (1996)].
[7] D. A. G. Bruggemann, Ann. der Phys. **24**, 636 (1935).
[8] D. E. Aspnes and A. A. Studna, Phys. Rev. B **29**, 985 (1983).
[9] W. K. Chu, J. Majer, and M.-A. Nickolet, *Backscattering Spectrometry* (Academic Press, N. Y., 1978).
[10] L. V. Belyakov, D. N. Goryachev, and O. M. Sreseli, Pis'ma Zh. Tekh. Fiz. **22**, 14 (1996) [Tech. Phys. Lett. **22**, 97 (1996)].
[11] D. I. Kovalev, I. D. Yaroshetzkii, T. Muschik, V. Petrova-Koch, and F. Koch, Appl. Phys. Lett. **64**, 214 (1994).
[12] C. H. Villeneuve, J. E. Peou, C. Levy-Clement, and P. Allongue, in *Abstracts 191 ECS Meeting*, (Montreal, Canada, 1997) **97-1**, p. 182.

Translated by M. E. Alferieff

PHYSICS OF SEMICONDUCTOR DEVICES

Charge limit effects in emission from GaAs photocathodes at high optical excitation intensities

B. I. Reznikov

A. F. Ioffe Physicotechnical Institute, Russian Academy of Sciences, 194021 St. Petersburg, Russia

A. V. Subashiev

St. Petersburg State Technical University, 195251 St. Petersburg, Russia

(Submitted April 21, 1998; accepted for publication April 22, 1998)
Fiz. Tekh. Poluprovodn. **32**, 1125–1134 (September 1998)

The stationary characteristics of a photocathode and the characteristic times of transient processes accompanying instantaneous switching of the illumination on and off under the conditions of high excitation intensity are examined in a nonlinear diffusion model, with allowance for the photovoltage dependence of the parameters of the skin layer. Analytical expressions for the quantum yield as a function of the photovoltage and radiation intensity are obtained for the stationary case. The critical value of the illumination intensity corresponding to a transition into the emission charge limit regime is found. It is shown that the time of emergence into a stationary state depends on the magnitude of the photovoltage established on the barrier and is determined mainly by the equilibration time between the electron and hole fluxes on surface recombination centers. At high illumination intensities the equilibration time is inversely proportional to the illumination intensity. At intensities corresponding to complete blocking of the cathode, this results in an emission charge limit. The photovoltage relaxation time can reach microseconds. The photovoltage dependence of the tunneling transmittance of the activation layer can be reconstructed by comparing with experiment the computational results obtained for the quantum yield as a function of the photovoltage.
 [S1063-7826(98)02309-6]

Semiconductor photocathodes employing electron emission from the surface of a GaAs epitaxial film activated to negative electron affinity have a broad range of important applications in infrared technology and modern physics: in high energy physics[1,2] and in investigations of crystal surfaces and the magnetic properties of thin films.[3] The possibilities of using photocathodes in electron microscopy and electronic lithography are being studied extensively[4]

Optical orientation of electrons in the process of absorption of circularly polarized light near the interband absorption edge is used to obtain beams of polarized electrons. Since the excitation of the semiconductor structure occurs in the low-absorption region, intense sources of excitation must be used to obtain beams of adequate intensity. In so doing, diverse nonlinear effects are observed experimentally, both in the stationary state[5] and during pulsed excitation.[5–7] These effects are associated with a limitation of the emision current and charge as a result of the photovoltaic effect, which decreases the band bending at the surface and increases the work function.[8] For applications of photocathodes as easily controlled sources of polarized electrons, the maximum current (in the continuous regime) and the maximum charge per pulse (in the pulsed regime) are important. The charge limit in emission is the main obstacle to increasing the electron-beam intensity required for a number of planned accelerator experiments.[6]

Although the qualitative picture[8] of the phenomenon is quite clear and largely explains the experiments,[5–7] the quantitative results in Ref. 8 were obtained as a result of a model numerical calculation. This makes it impossible to use the results of Ref. 8 to clarify the dependence of the observed quantities on the structural parameters of the photoemitter, to estimate the maximum achievable parameters and the possibility of optimizing the parameters of photoemitters, or to determine the structural parameters of photoemitters from the experimental data.

The phenomena occurring in the surface region of space charge and of the activating layer (AL) present the greatest difficulties for experimental and theoretical study. Experiments on low-energy electron diffraction from an activated surface attest to the degree of amorphization of the structure of the AL.[9] As a result, even for cathodes with high and similar values of the quantum yield there is a large variance in the observed characteristics, for example, in the energy distributions of the emitted electrons and in the degradation kinetics. The wide energy distribution of the emitted electrons and their weak depolarization under optical orientation conditions show that the fluctuation potential plays a large role in the space-charge region (SCR).[10] The diverse

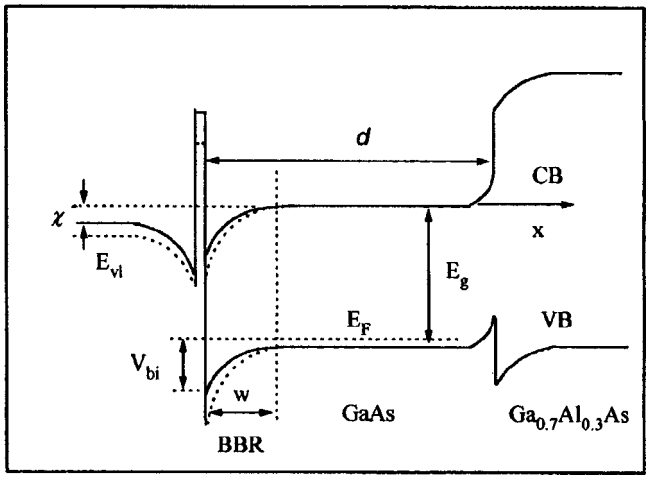

FIG. 1. Energy band diagram of a photocathode. The dotted line shows the position of the vacuum level and the band edges in the space-charge region before illumination.

properties of the AL are also manifested in the behavior of cathodes under intense excitation conditions.

In our study we used a three-step diffusion-drift model of photoemission[11] to investigate the mechanisms that impede the photovoltaic effect and to clarify the possibilities of characterizing photocathode structures according to the experimental data. Methods for optimizing the structure of photocathodes are discussed.

1. FORMULATION OF THE PROBLEM

1.1. During activation of an atomically clean surface of a heavily doped GaAs epitaxial film to a state of negative electron affinity, a layer (the activating layer), which is an energy barrier for photoelectrons and is no more than 3 nm thick, forms on the surface of the film. Pinning of the Fermi level at the surface on donor-type localized states in the band gap results in band bending at the surface and in the formation of a space-charge region (SCR), whose thickness w is determined by the magnitude of the band bending and the acceptor density N_a. The energy diagram of a photocathode structure with a working region of thickness d is shown in Fig. 1.

Photoelectron transport in the working layer $0 \leqslant x \leqslant d$ is described by the diffusion equation

$$\frac{\partial n}{\partial t} + \frac{\partial q_n}{\partial x} = \alpha I_i e^{-\alpha x} - \frac{n}{\tau}, \quad q_n = -D_n \frac{\partial n}{\partial x} - \mu_n E n. \quad (1)$$

Here n is the electron density, the coordinate x is measured in a direction rightward from the barrier, I_i is the near-surface light intensity in the photoconductor, and α is the absorption coefficient. For not too high doping levels and room temperatures the electron motion in the SCR can be described quasiclassically. Consequently, we shall examine separately the dynamics of electrons in the space charge layer $0 \leqslant x \leqslant w$ and in the quasineutral region $w \leqslant x \leqslant d$, matching the solutions at the boundary $x = w$.[12]

1.2. The boundary condition at $x = 0$ describes electron capture and recombination with positively charged centers on the surface and electron emission into the vacuum

$$q_n(0) = -q_{sn} - q_{emi}. \quad (2)$$

The recombination flux q_{sn} can be written in the form $q_{sn} = \alpha_n N_s^+ n_0$ or

$$q_{sn} = s_n n_0 (1 - f). \quad (3)$$

Here f is the fraction of the positive surface charge eN_s that is neutralized by recombination with electrons, $N_s^+ = N_s(1 - f)$ is the surface density of the positively charged centers in the presence of illumination, $s_n = \alpha_n N_s$ is the surface recombination rate, and α_n is the electron capture coefficient.

In the expression (3) the term describing the inverse process — electron transfer into the conduction band — is omitted. It is important if the surface levels on which trapping occurs lie quite close to the conduction band. For an activated GaAs surface, the terms associated with thermal generation are negligible both in the interior and at the surface.

Experiments studying the energy distribution of the emitted electrons in the presence of a weak excitation intensity[13,14] show that the energy of the emitted electrons and the width of the distribution correspond to a band $\Delta E = E_c - E_{vl}$ between the conduction band edge and the vacuum level. This band is close to the magnitude of the negative electron affinity $\Delta E \approx \chi$, attesting to rapid electron capture in the SCR well and low transmittance of the surface effective potential barrier (see Fig. 1). We can therefore write the electronic emission current q_{emi} in the form

$$q_{emi} = -V_n^T T_w (n_0 - n_0^*). \quad (4)$$

Here $V_n^T = v_n T_n$ is the rate of escape of electrons from the SCR, v_n is the average electron velocity, and T_n is the transmittance of the effective barrier in the region of the activating layer. The average depth V_{bi} of the SCR well is much greater than ΔE, so that at high excitation intensity the depth of the SCR well and the energy band ΔE accessible for electron emission decrease. This decreases the emission current. This circumstance is taken into account in Eq. (4) by the factor T_w, which is the effective ''transmittance of the quantum well'' of the SCR. The density n_0^* corresponds to equilibrium at $I_i = 0$. The boundary condition (2) is nonlinear because of the dependence of the recombination q_{sn} and emission q_{emi} currents on the degree of filling of the surface centers by electrons.

1.3. At the right-hand boundary of the working region $x = d$, we shall use the surface-recombination condition in the form

$$D_n \partial n / \partial x = -s_1 (n(d) - n_d^*), \quad (5)$$

where s_1 is the corresponding recombination rate, and n_d^* is the dark electron density, which in p-type samples is much lower than the characteristic densities in the working region in the presence of illumination and can be set equal to zero in the entire working region.

1.4. The boundary condition on the left-hand boundary of the working region $x = w$, which relates $n(0)$ and $n(w)$, can be easily obtained by assuming that the transit time through the space-charge region (but not the equilibration time between the SCR states and the surface states) is much

shorter than the carrier lifetime. Expressions for the distribution of the flux and densities inside the SCR $0 \leqslant x \leqslant w$ follow from Eq. (1):[12]

$$q_n = q_n(0) + I_i(1 - e^{-\alpha x}) \approx q_n(0) + I_i \alpha x, \tag{6}$$

$$n(x) = e^{U(x)-U_0}\left[n_0 - \frac{1}{D_n}\int_0^x q_n(x') e^{-[U(x')-U_0]}\, dx' \right], \tag{7}$$

where $U(x) = e\phi(x)/kT$, and $\phi(x)$ is the electric-field potential. Substituting expression (6) into (7), we obtain the following equations if the condition $\alpha x \ll 1$ is satisfied:

$$n(W) = e^{U(W)-U_0}\left\{ n_0 - \frac{L_d}{D_n}[q_n(0) J_1(W) + I_i \tilde{\alpha} J_2(W)] \right\}, \tag{8}$$

$$J_1(W) = \int_0^W \exp[-(U - U_0)]\, dX,$$

$$J_2(W) = \int_0^W X \exp[-(U - U_0)]\, dX. \tag{9}$$

Here X and W are, respectively, the coordinate and width of the space-charge layer normalized to the Debye radius $L_d = \sqrt{\varepsilon \varepsilon_0 kT/N_a e^2}$: $X = x/L_d$, $W = w/L_d = (2V_{bi}/kT)^{1/2}$, $\tilde{\alpha} = \alpha L_d$ [$V_{bi} = e\phi(0)$ — band bending]. In the depleted-layer approximation $U = (W - X)^2/2$, and the integrals $J_1(W)$ and $J_2(W)$, which appear in Eq. (8) when $W \gtrsim 2$, are

$$J_1(W) \approx \sqrt{\pi/2} \exp(W^2/2),$$

$$J_2(W) \approx (W\sqrt{\pi/2} - 1) \exp(W^2/2).$$

Moreover, in this approximation $L_d/D_n = W/(\mu_n E_0) = \overline{v}^{-1}$.

The final expression for $n(w)$ is

$$n(w) = \frac{-q_n(w)\sqrt{\pi/2}}{\overline{v}} + \frac{I_i \tilde{\alpha}}{\overline{v}} + n_0\, e^{-W^2/2}. \tag{10}$$

It follows from the expression (10) that the density at the SCR boundary and in the quasineutral region is a sum of three terms, which are connected with the diffusion flux from the region of maximum densities of the working layer by the photogeneration and by electrons that diffuse from the surface in a direction opposite to the field. The quantity $\overline{v}/\sqrt{\pi/2}$ plays the role of an effective recombination rate at the boundary of the working layer. Since in the working region $E = 0$ and $q_n(w) = -D_n dn/dx(w)$, Eq. (10) establishes a relation between the derivative and the density at the left-hand boundary of the quasineutral region. We note that the quantity $q_n(w)$ obtained by solving the diffusion equation fixes the value of $q_n(0)$ by the relation (6). Using this relation and Eqs. (2)–(4), we obtain

$$n_0 = \frac{-q_n(w) + I_i \alpha w}{S}, \quad S = V_n^T T_w + s_n(1 - f). \tag{11}$$

Eliminating $q_n(w)$ with the help of the relation (10) for $n(w)$, we obtain

$$n_0 = \frac{n(w)\overline{v}\sqrt{2/\pi} + I_i \alpha (w - \sqrt{2/\pi}\, L_d)}{S + \sqrt{2/\pi}\, \overline{v} e^{-W^2/2}}. \tag{12}$$

We note that the surface electron density n_0 depends, in terms of the thickness w of the SCR and the ''effective recombination rate'' S, on the degree of filling of the centers by electrons.

1.5. The change in the degree of filling of the surface states as a result of exposure to light is regulated by the difference in the fluxes of electrons and holes captured by surface centers,

$$N_s \frac{df}{dt} = q_{sn} - q_{sp} \tag{13}$$

with the initial value $f_0 = 0$ which corresponds to dark equilibrium.

The hole flux to the surface increases the number of positively charged surface states and the surface charge. A change in the degree of filling of these centers changes the surface charge density eN_s^+, the height V_{bi}, and the width W of the energy barrier for holes

$$V_{bi} = 2\pi \frac{e^2 N_s^{+2}}{\varepsilon_s N_a} = V_{bi}^0 (1 - f)^2, \quad W = \sqrt{\frac{2V_{bi}^0}{kT}}(1 - f), \tag{14}$$

and it leads to the photovoltaic effect — the appearance of a photovoltage δV, which changes the position of the conduction band edge relative to the vacuum level,

$$\delta V = V_{bi}^0 - V_{bi} = V_{bi}^0 f(2 - f), \quad E_{vl} = E_{vl}^0 + \delta V. \tag{15}$$

This decreases the fraction of electrons which overcome the barrier. The total charge of electrons emitted from a unit area of the photocathode is

$$Q = e\int_0^\infty v_n T_n T_w (n_0 - n_0^*)\, dt. \tag{16}$$

1.6. The hole flux $q_{sp} = \alpha_p N_s^0 p_0$, ignoring thermal generation, can be written in a form such as Eq. (3): $q_{sp} = s_p p_0 f$. It describes the capture of holes on neutral centers with density $N_s^0 = N_s f$ at the rate $s_p = \alpha_p N_s$, where α_p is the hole capture coefficient. The hole surface density p_0 is determined by the total flux of holes reaching the surface from the working region $p_0 = q_{p0}/V_p$, which consists of two parts — the thermal emission current and the tunneling current through the barrier of the space-charge layer:[15–17]

$$q_{sp} = [q_{sth}^0 (e^{U_0 y} - 1) + q_{st}^0 (e^{\lambda U_0 y} - 1)] f,$$

$$y = \frac{\delta V}{V_{bi}^0} = f(2 - f), \tag{17}$$

$$q_{sth}^0 = s_p N_v e^{-U_0}, \quad q_{st}^0 = s_p N_* e^{-\lambda U_0}, \tag{18}$$

$$\lambda = \frac{\sqrt{2} L_d}{l_t}, \quad N_* = \frac{1}{3\sqrt{2}\pi^{5/2}} \frac{D/kT}{L_d l_t^2},$$

$$l_t = \hbar/(2m_p^* kT)^{1/2}. \tag{19}$$

Here N_v ($\propto l_t^{-3}$) is the effective number of states in the valence band; the quantity D, which appears in the definition of N_*, has the dimension of energy (~ 0.02 eV) and is the so-called overlap integral (see Ref. 16, Vol. 2, p. 107). We note that the relative contribution of the tunneling current depends on the effective mass of the tunneling holes and on the particular features of the structure of the SCR. The choice of the numerical values for the parameters of the tunneling current therefore requires substantiation, which falls outside the scope of this paper.

It follows from Eq. (17) that the restoring hole current depends on the degree f of filling of the centers and on the photovoltage y. Using relation (17) and the dependence $\delta V(f)$ [(Eq. 15)], it is convenient to use the kinetic equation (13) for y

$$\frac{N_s}{2\sqrt{1-y}}\frac{dy}{dt}=q_{sn}-[q_{sth}^0(e^{U_0 y}-1)+q_{st}^0(e^{\lambda U_0 y}-1)]f,$$

$$f=1-\sqrt{1-y}. \tag{20}$$

2. QUASISTATIONARY EXCITATION

In the model described above, the steady-state value of the photoemission current under steady-state excitation conditions can be found analytically. The construction of the steady-state solution is based on obtaining a relation between n_w and q_w from the solution of the boundary-value problem (1). We thus obtain an additional relation between n_0 and n_w, which together with Eq. (12) can be used to obtain expressions for n_0 and q_{sn} and to determine, from the condition $q_{sn}=q_{sp}$, the stationary characteristics. The final result is

$$n_0=\frac{I_i\alpha}{v_{\text{eff}}}L_{\text{eff}}, \tag{21}$$

$$v_{\text{eff}}=V_n^T T_w+s_n(1-f)+v_{\text{dif}}\,\theta e^{-W^2/2},$$

$$L_{\text{eff}}=L_1+L_2, \quad L_1=L_d[W-(1-\theta)], \tag{22}$$

$$L_2=\frac{\gamma\theta L_{\text{dif}}}{1+\alpha L_{\text{dif}}}e^{-\alpha w},$$

$$\gamma=\left\{\delta-\frac{\kappa}{\Delta}[(\kappa+S_1)e^{\kappa}-(\kappa-S_1)e^{-\kappa}+2(\delta-S_1)e^{-\delta}]\right\}\Big/(\delta-\kappa), \tag{23}$$

$$\Delta=(\kappa+S_1)\,e^{\kappa}+(\kappa-S_1)\,e^{-\kappa}, \quad \kappa=d/L_{\text{dif}},$$

$$\delta=\alpha d, \quad S_1=s_1 d/D_n, \tag{24}$$

$$\theta=\left(1+\sqrt{\frac{\pi}{2}}\frac{v_{\text{dif}}}{\overline{v}}\right)^{-1}, \quad v_{\text{dif}}=\beta\frac{D_n}{L_{\text{dif}}}, \quad L_{\text{dif}}=\sqrt{D_n\tau},$$

$$\beta=\frac{(\kappa+S_1)e^{\kappa}-(\kappa-S_1)e^{-\kappa}}{\Delta}. \tag{25}$$

Expression (21) describes the relationship between the number of photoexcited electrons and the number of electrons that leave the working region. The parameter γ in the expression for L_2 depends on three parameters — the volume κ and surface S_1 recombination in the working region and the optical thickness δ of the working region. In the limiting case of a thick active layer $d \gg L_{\text{dif}}$, we have $\kappa \to \infty$, $\gamma \to 1$, and $\beta \to 1$. We note that the constants β and γ are close to 1 even for $\kappa \simeq 1$ and $\delta \simeq 1$. Specifically, for $d=1$ μm, $s_1=10^5$ cm/s, $\tau=10^{-9}$ s, $D_n=40$ cm^2/s, and $\alpha=10^4$ cm^{-1} we have $\kappa=1/2$, $S_1=1/4$, $\delta=1$, $\gamma=0.821$, $\beta=0.782$, and $\theta_0=0.881$. In the limit $\kappa \to 0$, the parameter $\gamma=1-e^{-\delta}$ and $\beta=\kappa$.

Using the definition (3), we write an expression for q_{sn} for $\omega \ll d$, L_{dif}, $1/\alpha$ in the form

$$q_{sn}=I_i\frac{\alpha L_{\text{dif}}}{1+\alpha L_{\text{dif}}}\gamma\theta \times\frac{s_n(1-f)}{s_n(1-f)+V_n^T T_w+v_{\text{dif}}\,\theta e^{-W^2/2}}. \tag{26}$$

It follows from Eq. (26) that for $s_n(1-f) \gg V_n^T T_w$ the stationary value of q_{sn} is virtually independent of f, which allows us to ignore the explicit dependence $q_{sn}(f)$ and to assume that q_{sn} is a given function of the intensity of the radiation, which enters the working layer, and of the quantities which characterize the collected charge (αL_{dif}, γ, etc.).

3. QUANTUM EFFICIENCY

3.1. An expression for the quantum yield $Y=q_{emi}/I_i$ can be obtained from Eq. (4) using Eq. (21). We give an explicit expression for Y in the case $w \ll d$, L_{dif}, $1/\alpha$, under the assumption that, in general, s_n and T_n depend on the excitation intensity:

$$Y=\gamma\theta\frac{\alpha L_{\text{dif}}}{1+\alpha L_{\text{dif}}} \times\frac{\eta T_w T_n}{\eta T_w T_n+s_n/s_{n0}(1-y)^{1/2}+v_{\text{dif}}/s_{n0}\,\theta e^{-W^2/2}}, \tag{27}$$

where $\eta=v_n/s_{n0}$. According to Eq. (27), the quantum efficiency is determined by the product of several cofactors which depend on the characteristics of the working region (γ), the incident radiation (αL_{dif}), and the conditions at the barrier [η, $T_w(y)$, $T_n(y)$]. The cofactor θ depends on the characteristics of the working region (v_{dif}), on the effective transport velocity $\overline{v}$ in the space-charge layer, and (in terms of the thickness W of the layer) on the photovoltage at the barrier. We emphasize that expression (27) is valid for an arbitrary dependence of the transmittances $T_n T_w(y)$.

The dependence of the transmittance T_w on the magnitude of the band bending is related to the relaxation kinetics and the electron energy distribution arising in the SCR well. In the uniform-distribution approximation

$$T_w=\frac{E_c-E_{vl}}{V_{bi}}=\frac{r-y}{1-y}=1-\frac{1-r}{(1-f)^2},$$

$$r=\frac{E_c-E_{vl}^0}{V_{bi}^0}=T_{w0}. \tag{28}$$

In the presence of intense excitation the increase in the photovoltage and degree of filling of the centers results in a decrease of the ''transmittance of the well.'' The maximum value of the dimensionless photovoltage, at which the surface barrier becomes nontransmitting for electrons and the quantum efficiency vanishes, depends on the initial values of the vacuum level and the band bending: $y_m=\delta V_m/V_{bi}^0=r$. The degree of filling of the centers is $f_{\max}=1-\sqrt{1-r}$. An expression for the radiation intensity corresponding to this condition follows from the equality $q_{sn}=q_{sp}$ at $y=r$. Ignoring electron diffusion in a direction opposite to the field, we obtain

$$I^{cr}=\frac{[1+(\alpha L_{\rm dif})^{-1}]}{\gamma\theta(r)}[q_{sth}^0(e^{U_0 r}-1)+q_{st}^0(e^{\lambda U_0 r}-1)]\times(1-\sqrt{1-r}\,). \tag{29}$$

Expression (29) is valid for an arbitrary dependence $T_w(y)$. Here it must be assumed that $T_w(r)=0$. It is significant that an increase in E_{vl}^0 (decrease of r) results in a strong decrease of I^{cr}. Conversely, a decrease of s_n and an increase of s_p shift the limit of opacity of the barrier to higher intensities.

It follows from Eq. (27) that the decrease in the quantum efficiency of the photocathode is due to three factors. The first one is the decrease in T_w as a result of a narrowing of the energy interval where electrons can still overcome the barrier. The second factor is the decrease in the probability T_n of tunneling through the barrier as a result of a shift of the electron distribution function in the well in a direction of high energies in the presence of a photovoltage at the barrier. It is manifested as a dependence of the barrier transmittance T_n on the photovoltage (field). The third factor is the loss of electron density as a result of surface recombination.

At low illumination intensities $f, y\ll 1$, the quantity Y is

$$Y_0=\gamma\theta_0\frac{\alpha L_{\rm dif}}{1+\alpha L_{\rm dif}}\,\frac{v_n T_{n0}T_{w0}}{s_{n0}+v_n T_{n0}T_{w0}}. \tag{30}$$

The relation (30) becomes the expression derived for the quantum efficiency for the special case of a thick active layer ($\gamma=1$) with a low optical excitation level.[18] It follows from Eq. (30) that for a high surface recombination rate or a low rate of tunneling through the barrier the quantum yield $Y_0\sim 1/s_{n0}$, while for a low surface recombination rate the quantum yield Y_0 does not depend on s_{n0} and tends toward the maximum possible value determined by volume generation and recombination in the working region of the photocathode.

According to Eq. (27), the normalized quantum yield Y/Y_0 as a function of y depends on three parameters: r, η, and the ratio $v_{\rm dif}/\overline{v}_0$, which appears in the definition of θ [Eq. (25)]. Additional factors influencing Y are contained in the function $T_n(y)$. We note that if $v_{\rm dif}\ll\overline{v}_0$, which corresponds to $\theta_0\approx 1$, then the velocity $\overline{v}$ characterizing carrier transport in the space-charge layer has essentially no effect on the quantum efficiency.

3.2. Let us examine the behavior of Y for $y\ll 1$ by expanding expression (27) in a series in powers of y. Qualitative results can be obtained by studying the case $s_n=s_{n0}$, $T_n=T_{n0}$. Ignoring the last term in the denominator in Eq. (27), we obtain

$$Y=Y_0\left[1+\left(\frac{3/2+\eta}{1+\eta r}+\frac{1-\theta_0}{2}-\frac{1}{r}\right)y\right]. \tag{31}$$

It follows from Eq. (31) that the quantum yield Y at first increases and reaches a maximum if $r>r_m$, where

$$r_m=\left[\sqrt{\left(1-\frac{\theta_0}{4}\right)^2+\eta\frac{(1-\theta_0)}{2}}+1-\frac{\theta_0}{4}\right]^{-1}\approx\frac{2/3}{1+(1/3+2/9\eta)(1-\theta_0)} \tag{32}$$

[the righ side of (32) holds for $1-\theta_0\ll 1$].

In the opposite case $r<r_m$ the quantity Y decreases immediately with increasing illumination intensity. The physical reason for the appearance of a maximum is competition between two effects — the decrease of the surface recombination rate and the decrease of the effective barrier transmittance. The term $1-\theta_0$ describes the change in the conditions at the left-hand boundary of the working region. It follows from Eq. (31) that a decrease of r or η (increase of the rate s_{n0}) leads to dependences $Y(I_i)$ with a negative derivative dY/dI_i.

Let us estimate the position of the maximum of the quantum efficiency, ignoring the last term in the denominator in Eq. (27) and making the assumption that $\theta/\theta_0\approx 1$ in the interval $[0, y_m]$. In this approximation Y has a maximum at $y_m=3r-2$

$$\frac{Y_m}{Y_0}\approx\frac{1+\eta r}{r}\,\frac{1}{\eta+3^{3/2}(1-r)^{1/2}/2}\approx\left(1-\frac{27}{8}\,\frac{(r-2/3)^2}{1+\eta r}\right)^{-1} \tag{33}$$

(the right-hand side is valid for $r-2/3\ll 1$).

The dependences $Q=Y/Y_0$, shown in Fig. 2, for different values of E_{vl}^0 (or r) confirm the qualitative character obtained analytically. The derivative $[d(Y/Y_0)/dy]_0$ decreases as E_{vl}^0 increases, changing sign. The main feature of the model investigated with $s_n/s_{n0}=1$ and $T_n/T_{n0}=1$ is the presence of a maximum of Y for values of the vacuum level E_{vl} substantially below the conduction band.

3.3. Let us now examine the behavior of $Y(y)$ for $y\ll 1$ when the capture coefficient α_n depends on the field. According to Ref. 19, in the case capture occurs in an attractive field $\alpha_n\sim E^{-3/2}$ and increases as the photovoltage at the barrier increases. In the depleted-layer approximation

$$E(0)=kT/(eL_d)W=E_0(1-f),$$

and

$$\alpha_n=\alpha_{n0}(1-f)^{-3/2},\quad s_n=s_{n0}(1-y)^{-3/4}.$$

In this case the analog of the expansion (31) has the form

$$\frac{Y}{Y_0}=1+\left(\frac{3/4+\eta}{1+\eta r}+\frac{1-\theta_0}{2}-\frac{1}{r}\right)y. \tag{34}$$

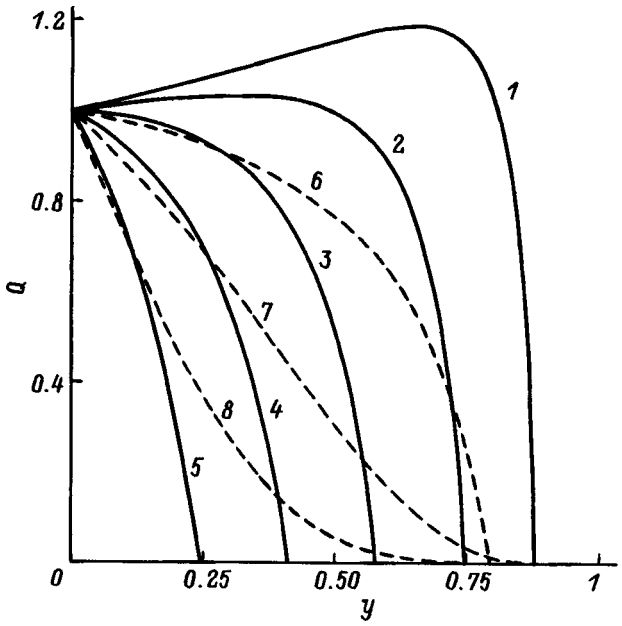

FIG. 2. Curves of the quantum yield $Q=Y/Y_0$ of a photocathode versus the photovoltage on the barrier $y=\delta V/V_{bi}^0$ for initial vacuum levels E_{vl}^0, eV: *1*, *6–8* — 1.16, *2* — 1.2, *3* — 1.25, *4* — 1.3, *5* — 1.35; values of the computed model parameters: solid lines — $s_n/s_{n0}=1$, $T_n/T_{n0}=1$; dashed lines — *6* — $\nu=3/2$, $T_n/T_{n0}=1$; *7* — $\nu=3/2$, $T_n(E)$; *8* — $\nu=10$, $T_n/T_{n0}=1$.

Y can increase if $r>r_m$, where

$$r_m=\frac{8/3}{1+2/3(1-\theta_0)+\sqrt{(1+2/3(1-\theta_0))^2+32/9\eta(1-\theta_0)}}\approx\frac{4/3}{1+(2/3+8/9\eta)(1-\theta_0)}. \quad (35)$$

The right-hand side of Eq. (35) corresponds to the case $1-\theta_0\ll 1$.

It follows from Eq. (35) that Y can increase, but only for small surface recombination ($\eta\gg 1$, $\theta_0\neq 1$), because the effective electron transport length increases with decreasing thickness of the space-charge layer ($\theta_0\neq 1$). For $\eta\simeq 1$ $Y(y)$ decreases; here the rate of decrease increases as r decreases.

The dependence $Q=Y/Y_0(y)$ for $E_{vl}^0=$ const when the capture coefficient α_n depends on the field as $\alpha_n\sim E^{-\nu}$ is shown in Fig. 2 — curves *1* ($\nu=0$), *6* ($\nu=3/2$), and *8* ($\nu=10$). We see that when α_n increases as the field decreases, the normalized quantum efficiency decreases more rapidly than in the case $s_n/s_{n0}=1$. For a more critical dependence $\alpha_n(E)$ ($\nu=10$, curve *8*) the quantum efficiency decreases almost to zero for values of y much smaller than r, which corresponds to the onset of opacity of the quantum well, and the function $Q(y)$ has a positive slope. The calculations show that negligible growth of $Q(y)$ is possible, but only for small initial values of the capture coefficients ($\alpha_n\leqslant 10^{-8}$ cm^3/s with $\nu=3/2$).

3.4. Let us now examine the combined effect of all three factors on Y and take into account the decrease in the probability of tunneling through the barrier because of the shift in the electron spectrum into the high-energy range. The the dependence of the transmittance of the activating layer on the electron energy has been discussed extensively. In some cases, including in Refs. 8 and 18, it was assumed that the height of the effective surface barrier is on the order of the atomic energy, and that the thickness of the barrier is small, which leads to the conclusion that the dependence of the transmittance of the activating layer on the electron energy and photovoltage is weak. Apparently, the model with an effective triangular barrier with a lower (on the order of V_{bi}^0) height and larger width,[9] chosen from to the observed value of the quantum yield, gives a better description of the energy distribution of the emitted electrons.

We reconstructed the function $T_n(y)$, using Eq. (27), from the experimental data presented in Ref. 5 on the illumination intensity dependence of the quantum yield and the photovoltage. The function $T_n(y)$ can be quite accurately approximated as

$$T_n=T_{n0}^{(1+y)^\omega}, \quad (36)$$

where the exponent $\omega=1/2-3/4$. This dependence supports the model of an effective triangular barrier of comparatively low height.

For small $y\ll 1$

$$T_n/T_{n0}=1+(\omega\ln T_{n0})y,$$

and the behavior of $Y(y)$ for an arbitrary power-law dependence $\alpha_n\sim E^{-\nu}$ is described by the expression

$$\frac{Y}{Y_0}=1+\left[\frac{(3-\nu)/2+\omega\ln T_{n0}+\eta}{1+\eta r}+\frac{1-\theta_0}{2}-\frac{1}{r}\right]y. \quad (37)$$

For $\nu=0, \omega=0$ the expression (37) is identical to Eq. (31), and for $\nu=3/2$ it is identical to Eq. (34). It follows from Eq. (37) that allowance for the dependence $T_n(E)$ decreases the derivative dY/dy. It also follows from Eq. (37) that

$$-\frac{dY/Y_0}{d\delta V}+\left(\frac{(3-\nu)/2+\omega\ln T_{n0}+\eta}{1+\eta r}+\frac{1-\theta_0}{2}\right)\times\frac{1}{V_{bi}^0}=\frac{1}{E_c-E_{vl}^0}. \quad (38)$$

Accordingly, if the derivative $(dY/Y_0)/d\delta V$, the rate s_{n0}, and the quantity T_{n0} are known, we can determine the value of E_{vl}^0 for small values of r.

Comparing the results obtained on the basis of different models of the transmittance and recombination reveals substantial quantitative and qualitative differences between the dependences $Y(y)$. The main differences are a more rapid decrease of $Y(y)$ in the region $y\ll 1$ and the appearance of a positive slope for high photovoltages. These differences are clearly seen in Fig. 2, where the computational results for Y for all models studied are presented for $E_{vl}^0=1.16$ eV (curves *1*, *6*, and *7*). The appreciable differences obtained for the computational results for $Y(y)$ in different models attest to the importance of taking into account all factors that describe the conditions at the surface.

3.5. Let us now examine the dependence of the quantum yield Y on the excitation intensity. A simple analytic expression can be obtained from Eqs. (26) and (17) in the special case $y\ll 1$, $f\ll 1$:

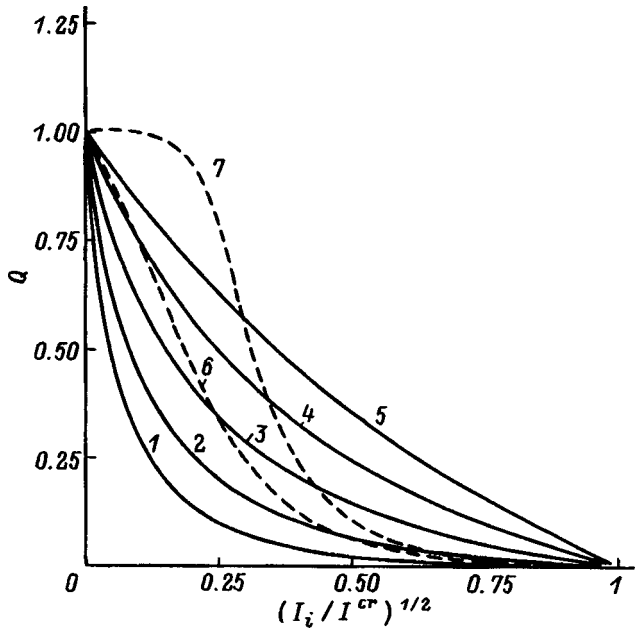

FIG. 3. Quantum yield $Q=Y/Y_0$ of a photocathode as a function of the illumination intensity $I=\sqrt{I/I^{cr}}$ with allowance for the dependence $T_n(E)$ for different initial values E_{vl}^0 of the vacuum level (curves 1–5) and the electron capture coefficient (curves 6 and 7). Solid lines for $\alpha_n=10^{-7}$ $\mathrm{cm}^3\cdot\mathrm{s}^{-1}$, E_{vl}^0, eV: *1* — 1.16, *2* — 1.2, *3* — 1.25, *4* — 1.3, *5* — 1.35; dashed lines — for $E_{vl}^0=1.16$ eV and α_n, $\mathrm{cm}^3\cdot\ \mathrm{s}^{-1}$: *6* — 10^{-8}, *7* — 10^{-9}.

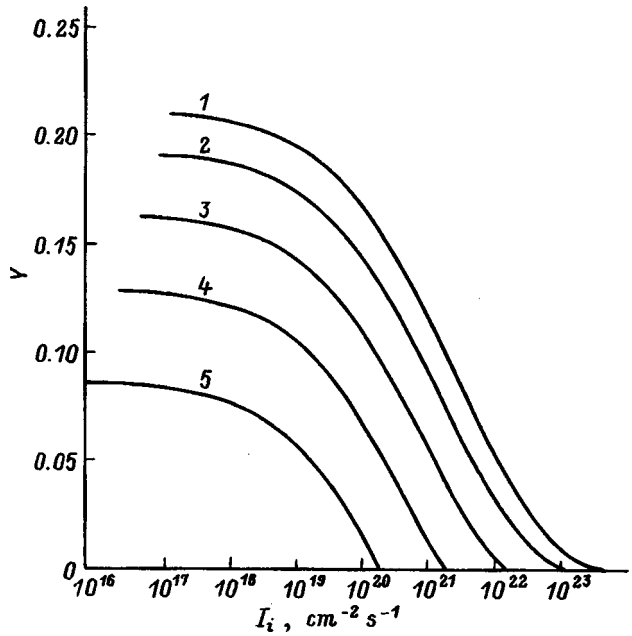

FIG. 4. Quantum yield Y of a photocathode versus illumination intensity I_i with allowance for the dependence $T_n(E)$ with $\alpha_n=10^{-7}$ $\mathrm{cm}^3\cdot\mathrm{s}^{-1}$ for different values of the vacuum level E_{vl}^0, eV: *1* — 1.16, *2* — 1.2, *3* — 1.25, *4* — 1.3, *5* — 1.35.

$$y=C\sqrt{I_i},$$

$$C=\left(2\frac{\alpha L_{\mathrm{dif}}}{1+\alpha L_{\mathrm{dif}}}\frac{\gamma\theta_0}{1+\eta r T_{n0}(q_{sth}^0+q_{st}^0\lambda)U_0}\frac{1}{U_0}\right)^{1/2}. \qquad (39)$$

For $y=r$ the intensity $I_i=I^{cr}$, and we obtain $y/r=\sqrt{I_i/I^{cr}}$. From Eq. (27) it follows that in the limits $y\to 0$, $r\to 0$

$$Y/Y_0=1-y/r=1-\sqrt{I_i/I^{cr}}.$$

The results for Y with arbitrary values of y and r were obtained by numerical computation.

3.6. We shall now present the results of numerical calculations of the quantum yield for a typical photocathode based on a GaAs epitaxial film on a wide-gap buffer for the parameters $d=1$ μm, $\alpha=10^4$ cm^{-1}, $s_1=10^5$ cm/s, $N_a=5\times10^{18}$ cm^{-3}, $V_{bi}^0=0.3$ eV, $T_n=0.04$, $D_n=40$ cm^2/s, and $\tau=10^{-9}$ s. The electron and hole capture coefficients at surface centers are $\alpha_n=\alpha_p=10^{-7}$ cm^3/s. The quantity y_{st} was found from the condition $q_{sn}=q_{sp}$, which, with allowance for the definitions (17) and (26), gave the intensity as an explicit function of the photovoltage at the barrier. The dependence $Y(y)$ was calculated from the relation (27), and the electron flux through the barrier was calculated as $j/e=I_iY(y)$.

The y-dependences of the normalized quantum efficiency for $V_{bi}^0=0.3$ eV and different values of the effective electron affinity ($1.16\leqslant E_{vl}^0\leqslant 1.35$ eV, $0.25\leqslant r\leqslant 0.88$) were discussed earlier (Fig. 2) and revealed a strong dependence of $Y(y)$ on the values of E_{vl}^0. Similar features also are observed for the function $Y/Y_0(\sqrt{I_i/I^{cr}})$, which depends strongly on r and s_n (Fig. 3). We see from Fig. 3 that the curves $Y/Y_0(\sqrt{I_i/I^{cr}})$ become nearly linear as r decreases.

The function $Y(I_i)$ (Fig. 4) shows that Y_0 decreases and the region $Y\leqslant 0$ becomes narrower as E_{vl}^0 increases. As the electron and hole capture coefficients increase, the situation does not change, but Y_0 decreases.

Curves of the electron current $j(I_i)$ for different values of E_{vl}^0 are presented in Fig. 5. We see that there exists a maximum current $j_{\max}$, which corresponds to the excitation intensity I_m above which j decreases rapidly. As E_{vl}^0 is increased, because the effective transmittance T_w decreases,

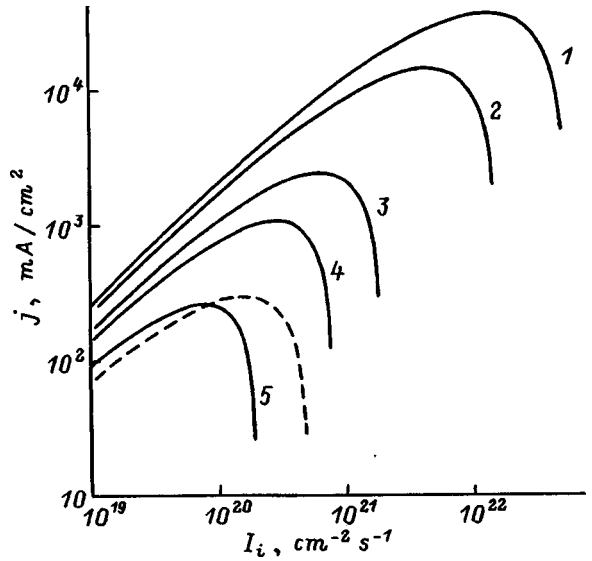

FIG. 5. Photoelectron current j versus the illumination intensity I_i ($\alpha_n=10^{-7}$ $\mathrm{cm}^3\cdot\mathrm{s}^{-1}$) for initial values of the vacuum level E_{vl}^0, eV: *1* — 1.22, *2* — 1.25, *3* — 1.3, *4* — 1.32, *5* — 1.35. The dashed line corresponds to the parameters for which the dependence (27) is close to the experimental dependence obtained in Ref. 5.

the value of $j_{\max}$ decreases strongly, while the position of the maximum (I_m) shifts in the direction of lower intensities.

4. CHARACTERISTIC TIMES OF TRANSIENT PROCESSES AND THE TOTAL CHARGE

4.1. We shall estimate the characteristic times of transient processes for the cases where the illumination is switched on and off instantaneously. For typical photocathode parameters the diffusion time $t_*=d_e^2/D_n$ $[d_e=\min(d,1/\alpha)]$ is short, and the characteristic time scale is the equilibration time τ_s between the electron and hole fluxes at the surface centers. From Eq. (20), which describes the kinetics of filling of the centers in the case of low intensities $U_0 y \ll 1$, $\lambda U_0 y \ll 1$, it follows that

$$y=y_s \tanh(t/\tau_s), \quad y_s=\sqrt{2q_{sn}/(q_{sth}^0+q_{st}^0\lambda)U_0},$$
$$\tau_s=N_s/\sqrt{2q_{sn}(q_{sth}^0+q_{st}^0\lambda)U_0}. \tag{40}$$

We see from Eq. (40) that as the intensity is increased, τ_s decreases as $\sim I_i^{-1/2}$, and that y_s increases as $\sim I_i^{1/2}$. Numerical estimates show that for $I_i \sim 1-5$ W/cm^2 the equilibration time is of the order of 1 μs. For low intensities, at which the parameters of the space-charge layer change very little, the restoration time with the illumination switched off, matches the time τ_s. For high values of I_i, at the stage of rapid growth of the surface electron density n_0, of the degree of filling f of the centers, and of the photovoltage y, there is not enough time for quasiequilibrium to be established between the fluxes q_{sn} and q_{sp}. The time $\tau_s \sim N_s/q_{sn}$ decreases [see Eq. (20)], and in the charge limit regime we have $\tau_s \sim I_i^{-1}$. This behavior of the current-saturation time was observed in Ref. 5.

4.2. The expressions obtained for the quantum yield and the equilibration times make it possible to estimate the maximum charge emitted from a unit area of the photocathode for the case of high excitation intensity

$$Q=eI_i\int_0^t Y\,dt=eI_i\overline{Y}\tau_s, \tag{41}$$

where the average quantum yield $\overline{Y} \sim Y_0\overline{(T_w/T_{w0})T_n/T_{n0}}$, and $\tau_s \sim I_i^{-1}$ is the equilibration time corresponding to the case of high intensities. The final result has the form

$$Q/e=B\frac{v_n T_{n0}T_{w0}}{(s_{n0}+v_n T_{n0}T_{w0})}N_s. \tag{42}$$

The coefficient B is essentially independent of the photocathode parameters, the intensity, and the models chosen for the transmittance of the quantum well and the surface barrier. For our range of the basic parameters and our model of an effective triangular barrier with transmittance (36), which decreases with increasing voltage, the coefficient varies in the range $B \simeq 0.1-1.5$. The lower limit refers to the parameter range corresponding to the charge limit regime. Comparison of expressions (42) and (30) shows that the maximum charge collected from unit area for cathodes with identical parameters of the working layer is proportional to the quantum yield at low excitation intensities and that it increases with the acceptor density and the overall transmittance $T_{n0}T_{w0}$. For photocathodes with high transmittance and low surface recombination $v_n T_{n0}T_{w0} \gg s_{n0}$ the total charge is $Q/e \approx N_s$. These results as well as the estimate of the charge agree with the experimental observations.[6]

5. DISCUSSION. POSSIBILITY OF DETERMINING THE EMITTER PARAMETERS BY COMPARING THEORY WITH EXPERIMENT

The results of our theoretical analysis agree qualitatively with the experimental data of Refs. 5–7, but the character of the observed functions $Y(I_i)$, the value of the maximum current, and the collected charge in these experiments were found to be substantially different, which suggests that the parameters of the activating layer are different. We used the most complete set of experimental data, presented for one of the photocathodes investigated in Ref. 5, to determine the range of the model parameters where $Y(\delta V)$ (27) is close to the experimentally measured dependence. The latter was found from the dependences $Y(I_i)$ and $\delta V(I_i)$ presented in Ref. 5. The following should be noted:

1) The observed behavior of $Y(\delta V)$ in Ref. 5 is qualitatively similar to the computed curve *8* in Fig. 2, while in Ref. 7 the behavior is similar to curve *3* in the same figure;

2) when comparing the dependences of Y on δV instead of the dependence on I_i, the question of restorating the hole current and of the corresponding parameters does not arise.

The procedure for determining the unknown parameters reduces to solving simultaneously Eqs. (30) and (38), with allowance for the definitions for η and θ_0. The parameters T_{n0} and α_n were assumed to be known, while the values of E_{vl}^0 and V_{bi}^0 were determined. After fixing α_{n0} and varying T_{n0}, we obtained a set of values of E_{vl}^0 and V_{bi}^0, which fit the given values of V_0 and $(dY/Y_0)/d\delta V$ in the limit $\delta V \to 0$. Comparing the theoretical dependences $Y(\delta V)$ with experiment showed that parameters such as $E_{vl}^0=1.31$ eV and $V_{bi}^0=0.33$ eV can be used to obtain a theoretical relation that describes the experiment qualitatively and quantitatively with barrier transmittance in the range 0.01–0.02 and electron capture coefficient $a_{n0}=10^{-7}$ cm^3/s, in agreement with the data presented in Ref. 5. The maximum current of the photocathode can serve as an additional condition influencing the choice of model parameters. For the variants investigated, $j_{\max}=300-400$ mA/cm^2 (Fig. 5).

6. CONCLUSIONS

The observed characteristics of photocathodes agree with the results obtained in a nonlinear diffusion-drift model of photoemission. To obtain a high quantum yield it is found that activation resulting in a negative electron affinity $\chi \gtrsim 0.2$ eV is optimal. Calculation of the emission with intense pumping shows that the maximum emitted charge increases rapidly with increasing χ, with decreasing electron capture at the centers, and with increasing transmittance of the surface barrier.

The model representation of the effective tunneling transmittance of an activating layer, the quantum well in the space-charge region used by us, and the corresponding parameters need to be refined on the basis of experiments.

Experiments performed with intense excitation by light and with energy resolution could yield substantial information.

This work was supported by a U.S. CRDF grant (Award No. RPI-351), Grant No. 95-1.23 from the Russian State Program ''Surface and Atomic Structures,'' and by the Russian Fund for Fundamental Research through Grant No. 96-02-19187a.

[1] D. T. Pierce, in *Experimental Methods in Atomic, Molecular and Optical Physics: Charged Particles*, Vol. 29A, series on *Experimental Methods in the Physical Sciences*, edited by F. B. Dunning and R. G. Hulet (Academic Press, 1995) p. 1.
[2] K. Abe *et al.*, Phys. Rev. Lett. **75**, 4173 (1995).
[3] H. C. Siegmann, J. Phys.: Condens. Matter **4**, 8395 (1992).
[4] J. E. Scneider, A. W. Baum, and G. I. Winograd *et al.*, J. Vac. Sci. Technol. B **14**, 3782 (1996).
[5] A. S. Jaroshevich, M. A. Kirillov, D. A. Orlow, A. G. Paulish, H. E. Sheibler, and A. S. Terechov, in *Proceedings of the 7th International Workshop on Polarized Gas Targets and Polarized Beams*, Urbana, 1997, p. 232.
[6] H. Tang, R. K. Alley, H. Aoyagy, and J. E. Clendenin *et al.*, SLAC-PUB-6515 (1994).
[7] Y. B. Bolkovityaninov, A. M. Gilinsky, and C. W. de Jager *et al.*, in *Proceedings of the 12th International Symposium on High-Energy Spin Physics*, edited by C. D. W. de Jager *et al.* (World Scientific, Singapore, 1997), p. 700.
[8] A. Herrera-Gómez, G. Vergara, and W. E. Spicer, J. Appl. Phys. **79**, 7318 (1996).
[9] É. L. Nolle, Fiz. Tverd. Tela (Leningrad) **31**(11), 225 (1989) [Sov. Phys. Solid State **31**, 1965 (1989)].
[10] L. G. Gerchikov, B. D. Oskotskii, and A. V. Subashiev, in *Proceedings of the 12th International Symposium High-Energy Spin Physics*, edited by C. W. de Jager, T. J. Ketel, P. J. Mulders *et al.*, (World Scientific, Singapore, 1997) p. 746.
[11] W. E. Spicer, Phys. Rev. **112**, 114 (1958).
[12] B. I. Reznikov and G. V. Tsarenkov, Fiz. Tekh. Poluprovodn. **25**, 1922 (1991) [Sov. Phys. Solid State **25**, 1158 (1991)].
[13] C. Herman, H.-J. Drouhin, G. Lampel, Y. Lassailly, D. Paget, J. Peretti, R. Houdré, F. Ciccacci, and H. Riehert, in *Spectroscopy of Nonequilibrium Electrons and Phonons*, edited by C. V. Shank and B. P. Zakharchenya (Elseiver Science, B. V., 1992) p. 135.
[14] A. S. Terekhov and D. A. Orlov, Proc. SPIE **2550**, 157 (1995).
[15] V. L. Bonch-Bruevich and S. G. Kalashnikov, *Semiconductor Physics* [in Russian] (Nauka, Moscow, 1977).
[16] S. Sze, *Physics of Semiconductor Devices*, Wiley, N. Y. [Mir, Moscow, 1984].
[17] C. Y. Chang and S. M. Sze, Solid-State Electron. **13**, 727 (1970).
[18] B. D. Oskotskij, A. V. Subashiev, and Yu. A. Mamaev, Phys. Low-Dimens. Semicond. Struct. **1/2**, 77 (1997).
[19] A. G. Milnes, *Deep Impurities in Semiconductors*, Wiley, N. Y., 1973 [Mir, Moscow, 1977].

Translated by M. E. Alferieff

Use of two low-temperature emitters to determine the cutoff wavelength of the photosensitivity of infrared photodetectors

V. V. Vasil'ev and Yu. P. Mashukov

Institute of Semiconductor Physics, Siberian Branch of the Russian Academy of Sciences, 630090 Novosibirsk, Russia

(Submitted December 24, 1997; accepted for publication February 10, 1998)
Fiz. Tekh. Poluprovodn. **32**, 1135–1138 (September 1998)

This paper is the continuation of the analysis of a method of determining the cutoff wavelength λ_c of infrared photodetectors by irradiating the sample with radiation from two blackbodies with different temperatures. The emitters can operate at lower temperatures as the cutoff wavelength λ_c is increased. The parameters of a system employing two blackbodies, which are placed inside a liquid-nitrogen cryostat and have temperatures of 260 and 320 K, respectively, are presented. It is shown that an error of 1 K in determining the lower or higher temperature produces an error of approximately 0.3 and 0.2 μm, respectively, in λ_c if $\lambda_c = 10$ μm. Measurements on photodiodes fabricated on the basis of $Cd_{0.24}Hg_{0.76}Te$ ($\lambda_c = 8.1$ μm) epitaxial layers showed that the difference in the values of λ_c obtained by this method and from spectral measurements is no more than several tenths of a micron. It is suggested that this method be used as a standard method. © *1998 American Institute of Physics.* [S1063-7826(98)02409-0]

Emitters of thermal radiation (model of a perfect blackbody) are widely used for testing infrared (IR) photodetectors, for example, for determining the integrated power versus current sensitivity.[1] As shown in Ref. 2, by using two perfect blackbodies with two different temperatures it is possible to determine a characteristic of the photosensitivity spectrum — the position of the long-wavelength limit (the cutoff wavelength) λ_c.

We have shown elsewhere[3] that as λ_c is increased, lower blackbody temperatures should be used in order to determine the cutoff wavelength by this method. For $\lambda_c \sim 10$ μm these temperatures lie in the room-temperature range. In Ref. 3 we employed a blackbody which was placed inside a nitrogen cryostat. The temperature of the blackbody was varied in the range 150–450 K.

In the present paper we report, first, the results of an analysis of the accuracy of this method which we began in an earlier study (see Ref. 3) —we calculated the error in determining λ_c due to the error in determining the blackbody temperatures. Second, we present the parameters of a system employing two blackbodies inside a cryostat.

1. ERROR ANALYSIS OF THE METHOD

This method of determining λ_c is based on the fact that we measure the ratio of the photosignals produced by blackbodies with temperatures T_1 and T_2, while λ_c is determined from theoretical relations calculated on the basis of Planck's formula. In contrast to Ref. 2, where Planck's distribution was used for the radiation energy, we employ Planck's distribution for the number of photons. In the case of photon photodetectors this approach is simpler and clearer.

Figure 1 shows the idealized spectral dependence of the quantum yield η for a photodetector with $\lambda_c = 10$ μm and Planck's distribution at the temperatures 260 and 320 K. These temperatures were subsequently chosen as the working temperatures on the basis of a number of considerations which were examined in Ref. 3. Specifically, we took into account the fact that the ratio of the photosignals from two blackbodies varies most rapidly in relation to a change in the λ_c if the maximum emissivity of the blackbodies lies at a wavelength greater than λ_c. On the other hand, the temperatures must not be too low since then the photodetector signal becomes too weak.

One of the most important factors influencing the accuracy with which λ_c is determined by the method under consideration is the accuracy with which the temperatures T_1 and T_2 are determined. To estimate this factor we write the expression for the ratio of the photosignals as

$$F(\lambda_c, T_1, T_2) = \frac{\sigma' T_2^3 f(\lambda_c T_2)}{\sigma' T_1^3 f(\lambda_c T_1)}. \tag{1}$$

Here $\sigma' T^3$ is the expression from the Stefan–Boltzmann law for the number of photons,[1] and $f(\lambda_c T)$ is the fraction of photons having wavelengths in the range from 0 to λ_c.[4] Taking the logarithm of Eq. (1) and then differentiating it, we find an expression for the relative differential

$$\frac{dF}{F} = \left[T_2 \frac{f'(x_2)}{f(x_2)} - T_1 \frac{f'(x_1)}{f(x_1)} \right] d\lambda_c - \left[\frac{3}{T_1} + \frac{f'(x_1)}{f(x_1)} \lambda_c \right] dT_1 + \left[\frac{3}{T_2} + \frac{f'(x_2)}{f(x_2)} \lambda_c \right] dT_2, \tag{2}$$

where $x_{1,2} = \lambda_c T_{1,2}$. The function $f(x)$ and its derivative in the range of x of interest to us are shown in Fig. 2. Substituting in Eq. (2) the parameter values presented in Fig. 1, we obtain the expression

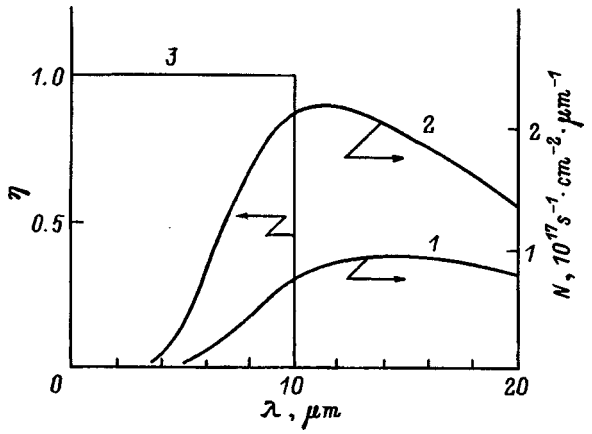

FIG. 1. Emission spectrum of an ideal thermal emitter (N — number of photons) at temperatures 260 K (*1*) and 320 K (*2*) and the quantum yield η for an ideal photon photodetector (*3*). *1* and *2* — Right-hand scale, *3* — left-hand scale.

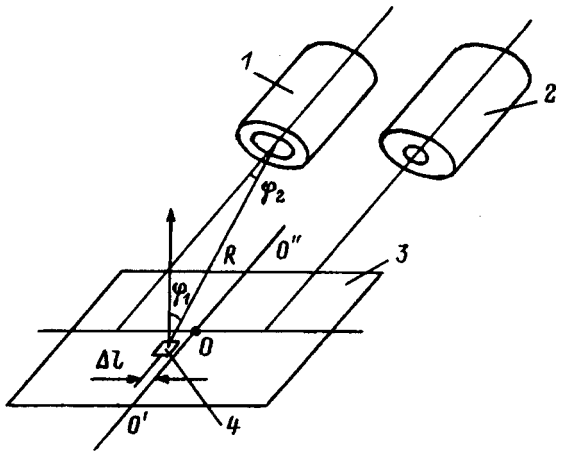

FIG. 3. Arrangement of the blackbodies. *1*, *2* — Blackbodies with temperatures of 260 and 320 K, respectively; *3* — plane of the photodiode matrix, *4* — measured photodiode.

$$\frac{dF}{F} = -0.0964 d\lambda_c - 0.0265 dT_1 + 0.0186 dT_2 \qquad (3)$$

(λ_c is expressed in μm and T in K). We thus see that an error of 1 K in one of the temperatures results in an error of 0.2 or 0.3 μm in λ_c.

The next source of possible error in this method is the error in the determination of the signal ratio, i.e., the function F. To decrease this error, specifically, to eliminate the influence of the nonlinearity of the power–current characteristic of the photodetector, the signals must be balanced by placing the blackbodies at different distances (as in Ref. 2) or by making blackbodies with different surface areas, as we have done. We assumed the ratio of the areas to be 4 : 1. For the indicated temperatures the signals will then be equal to one another when $\lambda_c = 9.5$ μm.

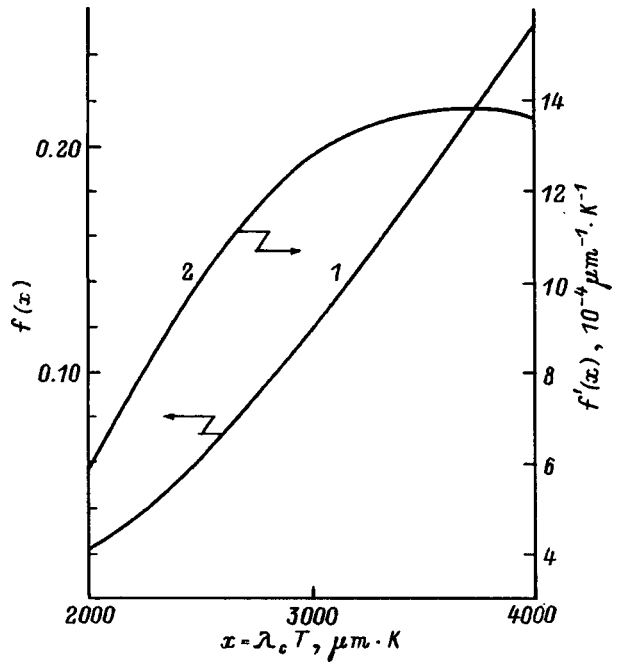

FIG. 2. The function $f(x)$ — the fraction of photons emitted by an ideal thermal emitter in the wavelength interval from 0 to λ_c (*1*, left-hand scale) and the derivative $f'(x)$ (*2*, right-hand scale).

2. APPARATUS DESIGN AND MEASUREMENT PROCEDURE

Let us consider the design features of our model apparatus, which was placed in the same cryostat as previously (see Ref. 3). The blackbodies consisted of 18-mm-diam and 18-mm-high copper cylinders, in which, respectively, 10.5 and 5.5 mm in diameter cylindrical depressions were made. The cylindrical cavities served as a source of radiation; their surface was coated with BF-2 glue with graphite powder. Copper wire wound on top of the cylinders and glued to the cylinders with the same glue served as heaters. The blackbodies were surrounded by a solid metal screen, which contained, respectively, 10- and 5-mm-diam collimating holes opposite the emitting holes. The screen was connected to two cold ducts, which passed into liquid nitrogen. A mobile shutter with a 11-mm hole was located outside the screen in front of the collimating holes. The shutter could either cover both bodies or expose one of them. The screen, cold duct, and shutter were made of aluminum, which has good thermal conductivity and low emissivity. As a result, the photodetector tested was not exposed to any radiation other than the testing radiation. It is very difficult to produce such conditions when blackbodies are located outside the cryostat.

The blackbodies were located next to one another (Fig. 3), and their emitting holes lay in the same plane. The sample was located on the horizontal surface of a cooled table. The arrangement of the blackbodies and the screen made it possible (just as in Ref. 3) to observe the sample from above in a binocular microscope, which was necessary in order to aim the controlled probe at the contact area of a selected element. The plane passing through the axes of the emitters thus made a 58° angle, rather than a 90° angle, with the horizontal plane. The elements investigated were located near the point O on the straight line formed by the intersection of the two indicated planes and at the same distance

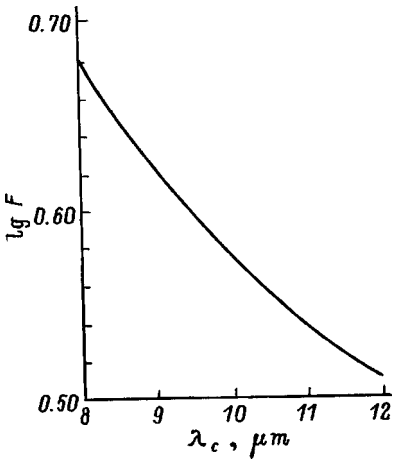

FIG. 4. Logarithm of the ratio of the photosignals produced in an ideal photon photodetector by two thermal emitters with temperatures of 320 and 260 K, respectively, versus the cutoff wavelength of the photodetector.

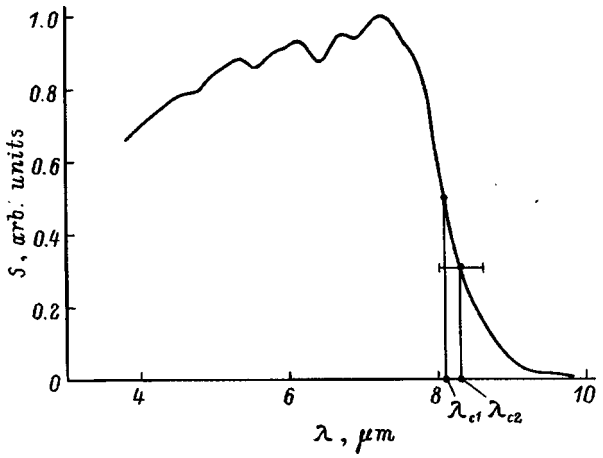

FIG. 5. Power–current sensitivity spectrum S of one of the photodiodes. λ_{c1} — cutoff wavelength, determined according to half-maximum of the photosensitivity; λ_{c2} — analogous quantity determined by the method considered by us.

from the centers of the emitting holes of the blackbodies (we call this point the central point).

A total power of 8 W was required to maintain the working temperatures of 260 and 320 K. The temperature was measured with copper-constantan thermocouples soldered to the blackbodies; the other ends of the thermocouples were located on the outside, and their temperature was monitored with a mercury thermometer. The nonuniformity of the temperature in the copper base of the blackbodies and the temperature of their inner coating apparently differed by no more than 1 K from the measured temperature. This can be inferred from the power dissipated by the bodies, from the thermal conductivity of the copper base and the coating, and from the direction of the heat fluxes. The error introduced in λ_c by this factor should not exceed 0.1–0.2 μm. The temperature of the copper bases of the blackbodies was determined to within a fraction of a degree. This procedure did not allow setting precisely the above-indicated temperatures T_1 and T_2, which could differ from the base temperatures by several degrees.

The computed working realtion between $\log F$ and λ_c for the base temperatures and equal emitter areas is constructed in Fig. 4. To make use of this dependence we must introduce corrections which allow for the inequality of the areas, for the deviation of the temperatures from the base values, and for the deviation of this photodetector from the central point:

$$\log F = \log \frac{4I_0(T_2)}{I_0(T_1)} - 0.434 \frac{\partial \ln F}{\partial T_1} dT_1 - 0.434 \frac{\partial \ln F}{\partial T_2} dT_2 - 0.045 \Delta l, \quad (4)$$

where $I_0(T_2)$ and $I_0(T_1)$ are the photosignals obtained from the two blackbodies, the number 4 represents the ratio of the emitter areas, the constant 0.434 converts the natural logarithm to a base-10 logarithm, the derivatives $\partial \ln F/\partial T_1$ and $\partial \ln F/\partial T_2$ are determined from Eq. (2), dT_1 and dT_2 are the deviations of the emitter temperatures from the base temperatures, and Δl is the distance (in mm) between the element under study and a line which lies in the sample plane and whose points are located at equal distances from the centers of the emitting holes (the line $O'O''$); $\Delta l > 0$ if the element is displaced in the direction of the emitter with the higher temperature T_2.

The latter correction was calculated using an expression for the irradiance of the photodetector element made from either blackbody, which is proportional to the expression $\cos\varphi_1 \cos\varphi_2 / R^2$, where R is the radius vector that connects the center of an emitter and the photodetector, and φ_1 and φ_2 are the angles between R and the normals to the photodetector and emitter planes, respectively. We note that for the central point $\cos\varphi_1 = 0.79$, $\cos\varphi_2 = 0.93$, and $R = 28$ mm.

The corrections seemingly reduce the real situation to the one for which the working dependence is constructed. Since the temperature corrections depend on λ_c, which is not known in advance, the method of successive approximations must be used, i.e., one must first use the corrections for the proposed value of λ_c and then, after λ_c is determined, refine them and determine λ_c again.

The process of measuring one element thus consisted of measuring 1) the dark current of the photodiode, 2, 3) the currents under irradiation by the first and then the second blackbody, and 4, 5) the indications of the first and second thermocouples. All this can be easily done within no more than 1 min. In that time the temperature of the blackbodies changed by no more than 0.1 K.

3. EXPERIMENTAL RESULTS

The testing was done on photodiodes based on an epitaxial layer of $Cd_xHg_{1-x}Te$ ($x = 0.24$) grown by molecular-beam epitaxy on a GaAs substrate. The photosensitivity spectrum for one of the photodiodes is shown in Fig. 5. The value $\lambda_c = 8.1$ μm was determined as the wavelength at which the power–current sensitivity S equals half its maximum value. When a matrix was tested by the procedure under study, the measured element was located at the central point. To obtain experimental confirmation of the proposed

ratio of the emissivities of two blackbodies, the ratio of the photosignals with equal blackbody temperatures was measured beforehand and was found to be 4.1 ± 0.1. This ratio was then taken as the working value. Determination of λ_c for the element shown in Fig. 5 gave the result 8.3 ± 0.3 μm; i.e., good agreement with the data from spectral measurements was observed.

4. CONCLUSIONS

In summary, it was shown that the idea of using low-temperature emitters placed in a cryostat can be implemented very successfully in the method considered for determining the wavelength of the photosensitivity edge of IR photodetectors with $\lambda_c \sim 10$ μm to within several tenths of a micron. The required accuracy (0.2 K) in determining the blackbody temperatures was easily attained. A cold screen around the blackbodies prevented background radiation from entering the cryostat. The method can also be proposed as a standard method for determining λ_c. The only requirement is that a decision must be made as to the pair of emitter temperatures to be used.

We wish to thank V. N. Ovsyuk for interest in this work and for helpful suggestions. We also thank A. O. Suslyakov for performing the spectral measurements and for useful discussions.

[1] R. D. Hudson, Jr., *Infrared System Engineering*, Wiley, N. Y., 1969 [Mir, Moscow, 1972].
[2] R. M. Liberati, N. Sparvieri, and M. Marini, Infrared Phys. **31**, 361 (1991).
[3] V. V. Vasil'ev, Yu. P. Mashukov, and V. N. Ovsyuk, Fiz. Tekh. Poluprovodn. **31**, 749 (1997) [Semiconductors **31**, 642 (1997)].
[4] I. K. Kikoin [Ed.], *Tables of Physical Quantities* [in Russian], Atomizdat, Moscow (1976).

Translated by M. E. Alferieff

Spectral and mode characteristics of InAsSbP/InAsSb/InAsSbP lasers in the spectral region near 3.3 μm

A. A. Popov, V. V. Sherstnev, and Yu. P. Yakovlev

A. F. Ioffe Physicotechnical Institute, Russian Academy of Sciences,[a] *194021 St. Petersburg, Russia*
(Submitted January 28, 1998; accepted for publication February 10, 1998)
Fiz. Tekh. Poluprovodn. **39**, 1139–1144 (September 1998)

The characteristic features of the continuous-wave lasing spectra near 3.3 μm of multimode InAsSbP/InAsSb/InAsSbP double-heterostructure diode lasers are shown. The observation of mode switching to longer and shorter wavelengths at cryogenic temperatures is reported. It is shown that suppression of the longitudinal side modes closest to the main mode results in large mode jumps in energy during mode tuning by current. The characteristics which were observed are explained by gain spectrum inhomogeneity due to spectral hole burning in narrow-gap semiconductors. The intraband charge-carrier relaxation times in the active region are estimated. © *1998 American Institute of Physics.* [S1063-7826(98)02509-5]

1. INTRODUCTION

Tunable diode lasers for the wavelength range 3–4 μm are a key component of instrumentation for monitoring atmospheric pollutants and for molecular spectroscopy.[1,2] To date, such lasers have been produced on the basis of the narrow-gap semiconductor compounds GaSb and InAs. Most groups are studying ways to obtain high-temperature lasing and to increase the optical power [see the review article (Ref. 3)]. However, of special importance are the laser characteristics that are vital for spectral applications of the lasers. The basic requirements for middle-infrared range lasers for spectral applications were formulated in detail in Ref. 4. One requirement is the possibility of broad-band, current-controlled tuning of the main mode in the continuous-wave (CW) lasing regime in the absence of mode switchings. There are a number of studies of the current-controlled tuning of InAsSb lasers in the continuous-wave regime[4–6] and in the long-pulse regime,[7–9] whereas no special attention has been given to the mode composition in a wide interval of currents and temperatures. At the same time, the lasing spectra of III–V narrow-gap semiconductor lasers have certain peculiarities.[10–12] Investigation of the optical power distribution over the generated modes in InAsSb/InAsSbP lasers for the spectral region near 3.6 μm has shown that the mode power increases with temperature.[11] Side-mode suppression has been observed at temperature $T=95$ K.[11,12] For GaInAsSb/GaSb (Ref. 9) and InAsSbP/InAsSb (Refs. 5 and 12) antimonide heterostructure lasers with a Fabry–Perot cavity, a single-frequency lasing regime with side-mode suppression to 29 dB has been demonstrated. Moreover, the observation of tuning of the lasing wavelength of InAs(Sb) lasers to longer wavelengths by current, even with a suprathreshold injection current, has been reported.[6] The tuning rates observed to date (0.035 cm^{-1}/mA and 0.3 cm^{-1}/K) are much lower than the corresponding characteristics of GaAs and InP near-IR lasers and lower than expected on the basis of the temperature-dependence of the band gap (1.4 cm^{-1}/K).[13] The tuning mechanism of long-wavelength pulsed InAsSb lasers has been investigated in a number of studies.[8,14] Wavelength tuning in the case of pulsed lasers has been attributed to an increase in the charge carrier density[8,15] and the influence of self-focusing of the radiation,[14] whereas in the continuous-wave regime the spectral and mode characteristics of InAsSb lasers have not been studied and their dynamics has not been explained in a wide interval of currents and temperatures.

Our goal in the present paper is to analyze in detail the dynamics of the variation of the spectral characteristics of long-wavelength InAsSb lasers in the continuous-wave regime in a wide current and temperature intervals. The investigation was performed by analyzing the weak minor modes for the example of multimode diodes emitting in the spectral region near 3.2 μm at cryogenic temperatures. This method showed that intraband relaxation is slower in InAsSb lasers, and that it has an effect on the direction of mode tuning.

2. EXPERIMENT

InAsSbP/InAsSb/InAsSbP double-heterostructure lasers with a *p*-InAsSb active region were investigated (Fig. 1). The InAsSbP emitter layers symmetrically bordered the active region on both sides. The deep mesa stripe construction with 12 to 14-μm-wide stripes, created by photolithography, produced lateral confinement. A *p*-InAs layer was used as the contact layer. The InAsSb active layer was not deliberately doped. The natural impurity density there was equal to $(1-2)\times10^{16}$ cm^{-3}. Wide-gap *N*- and *P*-type InAsSbP layers bordering the active region were grown with a phosphorus concentration of 0.28 (the computed band gap $E_g=480$ meV) and doped with Sn and Zn to $(2-5)\times10^{18}$ and $(0.8-1.2)\times10^{18}\,\mathrm{cm}^{-3}$, respectively. The active layer was 0.6 μm thick, each InAsSbP layers was 2.5 μm thick, and the contact layer was 0.8 μm thick. Laser diodes with a 250 to 300-μm-long Fabry–Perot cavity were produced by cleaving and they were soldered with the substrate to a special copper block. The top contact was created with a 30-μm-diam gold wire soldered to a mesa stripe.

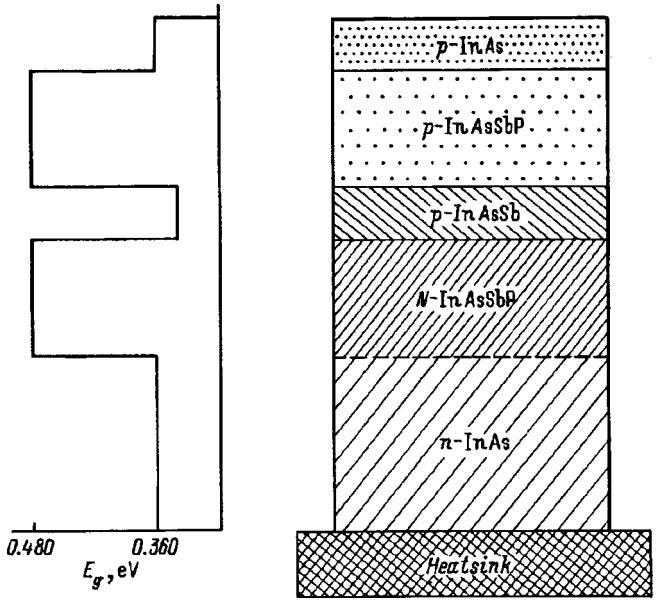

FIG. 1. Diagram of the experimental InAsSb/InAsSbP double laser heterostructure. The energy diagram of the heterostructure is shown on the left-hand side of the figure.

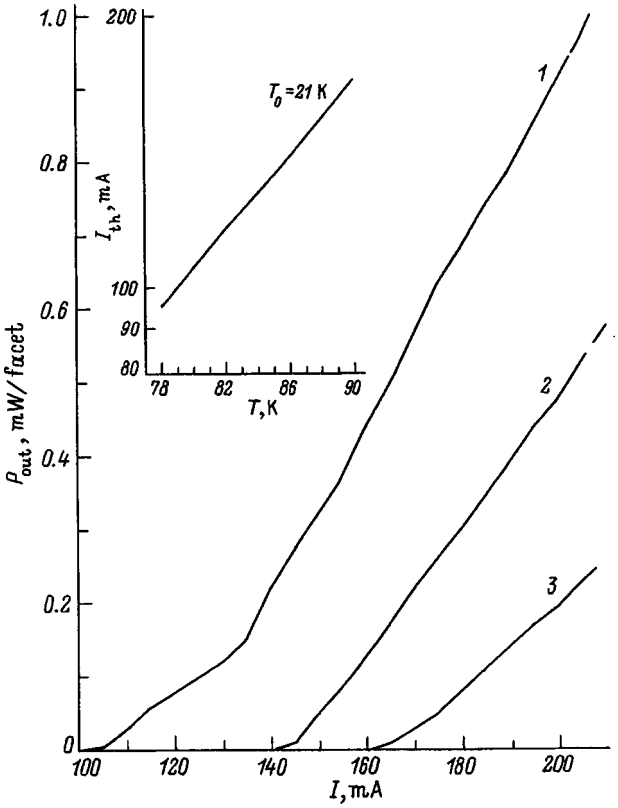

FIG. 2. Current dependences of the optical output power of a V1126-39 diode laser. The curves were obtained in the cw lasing mode at $T=80$ (*1*), 85 (*2*), and 90 K (*3*). Inset: Temperature-dependence of the threshold current I_{th}.

The laser was mounted in the evacuated part of a standard LA-5736 optical Dewar vessel. This made it possible to stabilize the temperature in the range 80–100 K to within 0.1 K. An ILX Lightwave LDC 3742 low-noise laser controller was used as a stabilized dc current source. The power measurements were performed using a Laser Precision RS5900 pyroelectric radiometer. The radiometer self-calibrated electronically with accuracy reaching 1%. The far radiation field of the laser was visualized with an infrared video camera. The radiation spectrum was monitored with a Digikrom 480 monochromator with better than 0.5 nm resolution. The optical signal was detected with a HgCdTe photodetector (Polytec HCT70) and amplified with a Stanford Research SR530 synchronous detector. Storage and analysis of the spectra and automatic control of the apparatus were performed via an IEEE-488 interface using standard computer software and hardware. A distinguishing feature of the experimental setup was the high dynamical range ($\sim$50 db) of the analog-to-digital converter, making it possible to resolve weak side modes.

3. RESULTS

The lasers were investigated in the continuous-wave lasing regime in the temperature range $T=78-90$ K. The threshold lasing current I_{th} was equal to 65–90 mA at temperature $T=78$ K. The temperature increase of the threshold current of the laser was described by an exponential law with characteristic temperature $T_0=21$ K (see the inset in Fig. 2).

Detailed investigations of the spectra were performed right up to pump currents I exceeding the lasing threshold by a factor of 1.8–2.2. The dependences obtained for the output optical power P_{out} for three temperatures are displayed in Fig. 2. The optical power increased in the entire experimental range of currents and temperatures. Power saturation was not observed. If at $T=80$ K the dependence consisted of two sections, then as temperature was raised, the first section, which corresponds to a lower quantum efficiency, vanished. The maximum optical output power at $T=80$ K reached 1 mW on the face and decreased as temperature was raised. However, in the entire experimental current range the power increased, while the power–current characteristic had no significant discontinuities. This attests to the absence of hard mode switching.

For the samples selected for subsequent investigations, the spatial field of the laser in the far field was checked. The results of the measurements attested to lasing on the main longitudinal mode (Fig. 3). This corresponds to the results of an earlier investigation of the structure of the spatial modes,[14] where it was shown that lasing in InAsSb mesa stripe lasers with a Fabry–Perot cavity with stripe width less than 14 μm is excited only on the main longitudinal mode. This conclusion corresponded to the geometry of the diodes chosen for the present investigation.

The lasing spectra at temperatures 80, 85, and 90 K are shown in Figs. 4a, 4b, and 4c. Each figure represents a section view of three-dimensional lasing spectra with respect to the optical power. Figure 4a shows the results of measurements performed near liquid-nitrogen temperature ($T=80$ K). The spectrum can be conventionally divided into two sections. The first one corresponds to currents up to

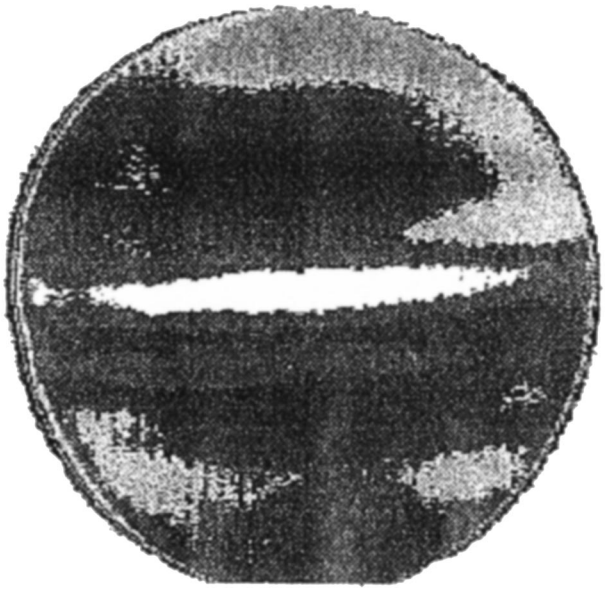

FIG. 3. View of the far-field radiation of a V1126-39 laser diode at $T=80$ K and pump current 140 mA. The field is visualized with an infrared video camera, whose output window was located 30 mm from the laser crystal.

$I=1.4I_{th}$; in this interval the spectrum remains unimodal. The intermode spacing was of the order of 4.3 cm^{-1} and corresponded to a refractive index of 3.58, close to that of InAs.[13] However, a characteristic feature of this region is mode tuning in the short-wavelength direction. The radiative recombination efficiency grows negligibly with current (the flat section in the power–current characteristic — Fig. 2). On the second section, where $I>1.4I_{th}$, multimode lasing is detected. The first mode described above stabilizes in wavelength. Lasing on this mode is observed with no further mode switchings in a wide range of pump currents, right up to twice the lasing threshold. However, the lasing spectrum becomes nonuniform. A characteristic feature of this region is that as the current increases, lasing is observed in the long-wavelength region, displaced by 5 intermode spacings. As current increases ($I>170$ mA), the energy width of the region where lasing is suppressed increases up to 8 intermode spacings. For this region, in contrast to the first one, the mode switches into the long-wavelength region. Mode switchings into a neighboring mode, separated by an interval $\sim 4.2-4.9$ cm^{-1}, are observed. The mode stabilizes. Side-mode excitation starts in the spectral region where lasing has thus far been suppressed. A further increase of the pump current to $I=2I_{th}$ results in excitation of all side modes closest to the main mode. The lasing spectrum broadens uniformly and acquires the typical form for multimode diode lasers.

The mode pattern obtained at 85 K is shown in Fig. 4b. It is distinguished by the fact that the region of single-frequency lasing, stable with respect to mode switchings, disappears. If one mode again shifts in the short-wavelength direction, then on the long-wavelength side the mode shifts into the long-wavelength region. From the moment lasing appears the switchings correspond to 1 intermode spacing.

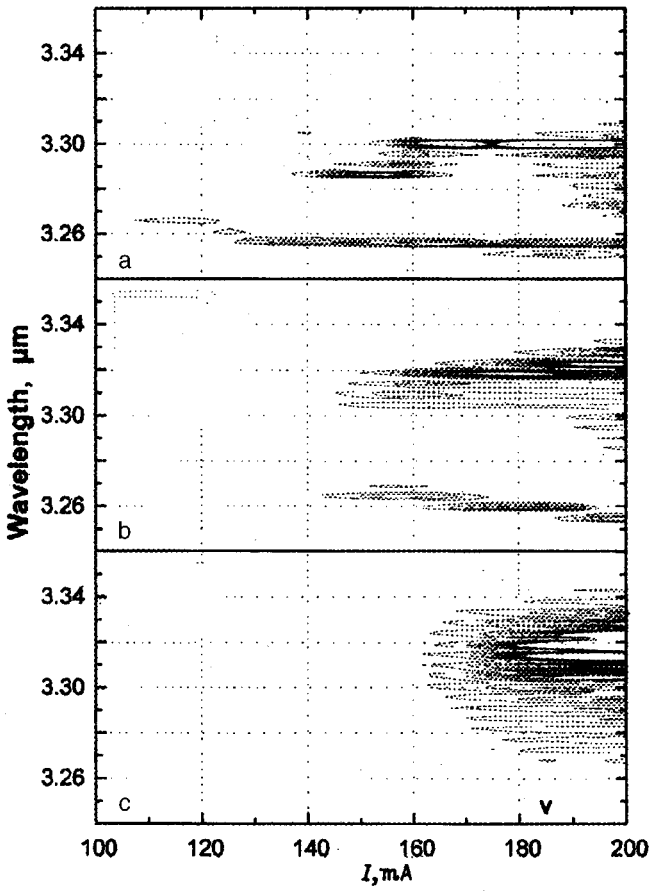

FIG. 4. Mode compositions obtained for a diode laser in the cw lasing mode at $T=80$ (a), 85 (b), 90 K (c). A sectional view of the three-dimensional lasing spectra with respect to power is shown.

The spectral region of suppression of lasing and the nonuniformities observed at $T=80$ K remain. The difference is that the energy gap reaches 8–10 intermode spacings even at the lasing threshold. At high current levels ($I\sim 180$ mA) the lasing spectrum again tends to homogeneous broadening. Increasing the temperature to 90 K (Fig. 4c) results in uniform broadening even at the lasing threshold. Although the main mode is slightly displaced into the long-wavelength region of the spectrum, the standard multimode lasing, whose spectrum corresponds to lasing of a multimode semiconductor laser, is observed. The regions of unimodal lasing and nonuniformity were not observed.

4. DISCUSSION

Summarizing the lasing features that were observed, we note that their main characteristic feature is the nonuniformity of the mode spectrum. This nonuniformity is attributable to the presence of a large gap observed in the spectrum of longitudinal modes at cryogenic temperatures. These nonuniformities could be the result of the characteristic features of the gain spectrum in narrow-gap InAsSb semiconductor laser diodes. Near liquid-nitrogen temperature and with a small gain excess above threshold ($I<1.4I_{th}$, $T=80$ K), lasing is observed at a single frequency. For this region the temperature broadening of the spectral gain contour is small and homogeneous. This corresponds to an increase in power

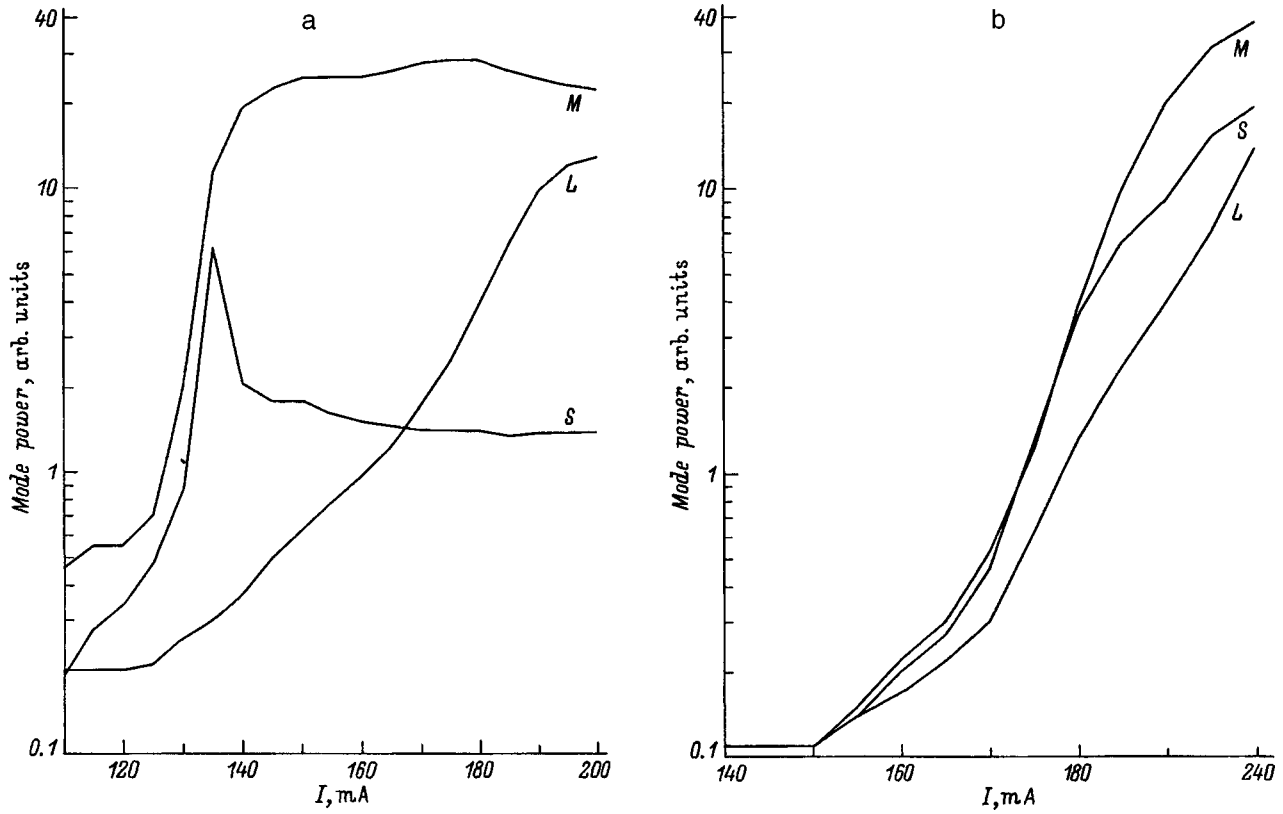

FIG. 5. Curves of the output power of a V1126-39 diode laser versus current for the main (*M*) mode and the nearest short-wavelength (*S*) and long-wavelength (*L*) side modes at temperatures 80 (a) and 90 K (b).

in the main and the nearest short- and long-wavelength modes as the pump current increases to 135–140 mA (Fig. 5a). As the current increases, a shift of the lasing to shorter wavelengths is observed. It could be due to an increase in radiation absorption by free carriers and changes in the effective refractive index that accompanies an increase in the charge-carrier density. Such behavior has been observed earlier for the pulsed lasing regime.[7] It should also be noted that there is a substantial absorption in the valence band, which is very intense in GaSb and InAs compounds, where resonance of the band-gap energies and the spin-orbit splitting off is observed.[16] As a result of the spectral limitation of the mode gain, the maximum of the mode gain can shift in the direction of shorter wavelengths. For this reason, in InAs-based lasers, in contrast to wider-gap analogs based on III–V InP and GaAs, the short-wavelength shift is also observed above the lasing threshold.

As the current and carrier density increase further, the spectral gain contour deforms. As a result, lasing appears on longitudinal modes 5–10 interband spacings away. This corresponds to suppression of the nearest long-wavelength mode with intensification of the main and short-wavelength modes in the current range $I>140$ mA (Fig. 5a). As a result, a dip near the generated mode forms in the gain spectrum. Gain is suppressed on the short-wavelength side and intensifies on the long-wavelength side. The region of mode-gain suppression (Fig. 4a) corresponds to an energy dip of 2–7 meV in the gain contour. The magnitude of the dip makes it possible to estimate roughly, from the uncertainty relation $\tau\sim 2\pi h/\Delta E$, the interband relaxation time, which is found to be 0.1–0.6 ps. This is several times greater than the corresponding times for InP and GaAs lasers.[13] Calibrated power measurements make it possible to estimate the internal noise level α_{int} in terms of the relation[13]

$$P_{\text{out}}=\frac{h\nu}{2q}\,\frac{\alpha_m}{\alpha_m+\alpha_{\text{int}}}(I-I_{\text{th}}), \tag{1}$$

where P_{out} is the optical power, $h\nu$ is the photon energy, q is the electron charge, and α_m are the exit losses (39 cm^{-1}). Calculations with Eq. (1) give $\alpha_{\text{int}}=80-130$ cm^{-1}, attesting to high losses in the active region. The calculations performed in Ref. 17 also confirm the high level of internal losses in InAsSb/InAsSbP lasers. Physically, the high losses could be due to strong nonradiative Auger recombination processes at the characteristic temperature $T_0=21$ K. The slowing down of intraband relaxation and the small heterobarrier heights, compared with the band gap, in narrow-gap III–V semiconductors give rise to leakage of injected hot carriers out of the active region. The photon lifetime τ_p in the cavity can be easily estimated using the relation[13]

$$\tau_p=1/\{v_g[\alpha_{\text{int}}+1/L\,\ln(1/R)]\}, \tag{2}$$

where v_g is the group velocity, α_{int} are the internal losses, L is the cavity length, and R is the reflectance of the mirrors, which determines the exit losses. The photon lifetime estimated from the relations (1) and (2) is 1.0–0.7 ps. For this reason, the carrier thermalization time in the mode suppres-

sion region approaches the photon lifetime in the cavity. This corresponds to the fact that a ''hole'' in the gain spectrum serves as a reason for the decrease in the lasing power near the main generated mode. The slowing down of the relaxation is observed at low temperatures. A result of the heating (by a continuous current with the pump level raised to $I \sim 170-180$ mA, just as by an increase in temperature to $T=90$ K) is uniform thermal broadening of the gain contour. This leads to the observed excitation of multimode lasing in all neighboring modes and corresponds to simultaneous homogeneous gain of the short- and long-wavelength modes (Fig. 5b). For this reason, at high currents and high temperatures switching occurs to a neighboring mode, while large mode switchings do not occur. The shifting of the modes to longer wavelengths under these conditions confirms the increase in temperature in the active region and the thermal mechanism of the displacement of the characteristic modes of the laser cavity at high pump levels and temperatures. To explain the observed current-controlled tuning to shorter and longer wavelengths in narrow-gap semiconductor lasers, it is important that at $T=80$ K gain increases with increasing current more rapidly for the short-wavelength mode, whereas even at a current $I=140$ mA tuning to shorter wavelengths saturates because of gain exhaustion on the short-wavelength side. At high pump levels and high temperatures the gain increases for the short- and long-wavelength modes at approximately the same rate. Saturation of mode tuning in this case is not observed.

In summary, the long intraband relaxation times produce characteristic features in the gain spectrum of InAsSbP/InAs/InAsSbP double-heterostructure diode lasers. The chief feature is the nonuniformity of the gain spectra at low temperatures. At cryogenic temperatures this results in mode switching to longer and shorter wavelengths. Suppression of the longitudinal modes closest to the main mode as a result of spectral hole burning in the gain contour results in large mode switchings (over 5–10 modes) during current-controlled tuning of continuous-wave lasing of a laser diode, noted earlier[10–12] but not explained. Although the slowing down of intraband relaxation increases the likelihood of nonradiative leakage of injected hot carriers in the emitter regions, under conditions when gain exceeds losses by a small amount, this can result in side-mode suppression and single-frequency lasing, which is observed in narrow-gap laser diodes, based on lightly doped semiconductor compounds InAsSb, with a Fabry–Perot cavity.

We thank A. M. Monakhov and T. N. Danilova for helpful discussions and for a discussion of the results of this work.

This work was supported in part by a grant in laser optics from the Ministry of the Russian Federation, by an INCO-COPERNICUS grant from the European Society, and by the Competitive Center of Fundamental Natural Science of the St. Peterburg Science Center and the government of St. Petersburg.

[a)]Tel.: (812) 247-9956; Fax: (812) 247-0006;
E-Mail: AP@iropto.ioffe.rssi.ru

[1] R. U. Martinelli, Laser Focus World **3**, 77 (1996).
[2] P. Werle, Spectrochimica Acta A **54** (1998) in press.
[3] H. K. Choi, Current Opinion in Sol. St. & Mater. Sci. **1**, 212 (1996).
[4] A. Popov, V. Sherstnev, Yu. Yakovlev, R. Muecke, and P. Werle, Proc. SPIE **2834**, 46 (1996).
[5] A. Popov, V. Sherstnev, Yu. Yakovlev, R. Muecke, and P. Werle, Spectrochim. Acta A **52**, 863 (1996).
[6] A. N. Baranov, A. N. Imenkov, V. V. Sherstnev, and Yu. P. Yakovlev, Appl. Phys. Lett. **64**, 2480 (1994).
[7] T. N. Danilova, A. P. Danilova, O. G. Ershov, A. N. Imenkov, M. V. Stepanov, V. V. Sherstnev, and Yu. P. Yakovlev, Fiz. Tekh. Poluprovodn. **31**, 1392 (1997) [Semiconductors **31**, 1200 (1997)].
[8] T. N. Danilova, O. I. Evseenko, A. N. Imenkov, N. M. Kolchanova, M. V. Stepanov, V. V. Sherstnev, and Yu. P. Yakovlev, Fiz. Tekh. Poluprovodn. **22**, 7 (1996) [Semiconductors **22**, 645 (1996)].
[9] N. V. Zotova, S. A. Karandashev, B. A. Matveev, M. A. Remenniĭ, N. M. Stus', and G. N. Talalakin, Pis'ma Zh. Tekh. Fiz. **23**, 72 (1997) [Tech. Phys. Lett. **23**, 41 (1997)].
[10] H. K. Choi, S. J. Eglash, and M. K. Connors, Appl. Phys. Lett. **63**, 3271 (1994).
[11] A. Popov, V. Sherstnev, Yu. Yakovlev, R. Muecke, and P. Werle, Appl. Phys. Lett. **68**, 2790 (1996).
[12] A. Popov, V. Sherstnev, Yu. Yakovlev, R. Muecke, and P. Werle, Proc. SPIE **3001**, 52 (1997).
[13] K. Petermann, *Laser Diode Modulation and Noise* (Kluwer Academic Publishers, Dordrecht, 1988).
[14] A. N. Baranov, T. N. Danilova, O. G. Ershov, A. N. Imenkov, V. V. Sherstnev, and Yu. P. Yakovlev, Pis'ma Zh. Tekh. Fiz. **19**, 30 (1993) [Tech. Phys. Lett. **19**, 543 (1993)].
[15] T. N. Danilova, A. P. Danilova, O. G. Ershov, A. N. Imenkov, V. V. Sherstnev, and Yu. P. Yakovlev, Fiz. Tekh. Poluprovodn. **31**, 1200 (1997) [Semiconductors **31**, 1392 (1997)].
[16] M. P. Mikhaĭlova, A. A. Rogachev, and I. N. Yassievich, Fiz. Tekh. Poluprovodn. **10**, 1460 (1976) [Sov. Phys. Semicond. **10**, 866 (1976)].
[17] T. N. Danilova, A. N. Imenkov, N. M. Kolchanova, A. A. Popov, and Yu. P. Yakovlev, Fiz. Tekh. Poluprovodn. **30**, 1265 (1996) [Semiconductors **30**, 667 (1996)].

Translated by M. E. Alferieff

Photocurrent amplification in $Au/SiO_2/n$-6H-SiC MOS structures with a tunnel-thin insulator

I. V. Grekhov, M. I. Veksler, P. A. Ivanov, T. P. Samsonova, and A. F. Shulekin

A. F. Ioffe Physicotechnical Institute, Russian Academy of Sciences, 194021 St. Petersburg, Russia
(Submitted February 13, 1998; accepted for publication February 17, 1998)
Fiz. Tekh. Poluprovodn. **32**, 1145–1148 (September 1998)

The first observation of amplification of the photogeneration current in $Au/SiO_2/n$-6H-SiC structures with a tunnel-thin insulator is reported. This effect can be used to increase the efficiency of existing UV-range 6H-SiC-based photodiodes. It also shows that bipolar SiC transistors with a MOS tunnel emitter can be produced. © *1998 American Institute of Physics.* [S1063-7826(98)02609-X]

1. INTRODUCTION

Silicon carbide, just like silicon, oxidizes with the formation of a homogeneous silicon dioxide (SiO_2) film on the surface. Thermal oxide on *n*-6H-SiC exhibits a high electric strength; the interfacial density of states can be lowered to values of the order of 10^{11} cm^{-2}, and classic MOS transistors of different types have already been developed on the basis of SiC.[1]

Besides classic devices, SiC-based devices with a tunnel-thin oxide could be of interest (to date, investigations in this direction have not been performed). If transistor action could be obtained in SiC structures with a tunnel-thin oxide, just as in silicon-based tunnel structures, then it would be possible to improve the parameters of UV-range SiC photodiodes and to produce bipolar transistors with a MOS tunnel emitter.

Transistor action in silicon MIS structures with a tunnel-thin insulator was discovered in the 1970s (Ref. 2) and has been studied in detail in $Al/SiO_2/n$-Si structures. The effect is explained by the large difference in the values of the electron and hole tunneling currents: Under the conditions of strong band inversion at the semiconductor surface, the current of electrons injected from the metal into the semiconductor can exceed the current of holes reaching the surface to compensate for their leakage from the inversion layer into the metal, which actually signifies amplification of the hole current flowing into the inversion layer.[3,4] Despite the fact that the theory of tunneling in MIS structures is quite well developed,[5,6] it is difficult to predict even roughly the current gain in the case of SiC structures, because there is no information on the values of the energy barriers at a tunnel-thin SiO_2-SiC interface.

In the present paper we report the results of investigations of SiC structures with tunnel-thin oxide. These are the first such structures prepared and studied for the purpose of observing possible transistor action.

2. EXPERIMENTAL OBJECTS AND PROCEDURE

To estimate the current amplification we compared the photoresponse in $Au/SiO_2/n$-6H-SiC MOS and Au/*n*-6H-SiC MS structures, which were fabricated on the same substrate and which differed structurally from one another only by the presence or absence of a thin intermediate SiO_2 layer (Fig. 1). Homoepitaxial *n*-6H-SiC films, grown by sublimation and chemical deposition from the gas phase on a (0001) Si face of *n*-type Leli substrates, were used. The uncompensated donor density in the films was 10^{17} cm^{-3} and 3×10^{15} cm^{-3}, respectively, and the thickness of the films was in the range 3–10 μm.

The experimental procedure consisted of the following. First, Schottky diodes were formed on each wafer by evaporating gold through a mask and their current–voltage characteristics under illumination with a mercury lamp were measured. Special reticular filters were used to vary the intensity of the illumination. Each filter made it possible to decrease the illumination intensity sixfold with no change in the spectral composition. Next, the gold contacts were etched off, and to prepare the SiC surface for ''thin'' oxidation prolonged high-temperature oxidation was conducted, and the thick oxide was then removed. A thin oxide was formed by dry oxidation at variable temperature and duration of the process (850–900°C and 15–60 min, respectively) so as to find the required regimes for oxidation and investigation of the influence of the insulator thickness on the characteristics of MOS photodetectors. In all other respects, the work with MOS structures (we have in mind deposition of the gold contacts and the procedure for measuring the photoresponse) was identical to that performed with MS structures. At the last stage of the investigations, to check the reproducibility of the results obtained, Schottky diodes were again formed on the same wafers and the characteristics of the diodes were measured.

3. RESULTS AND DISCUSSION

Phototransistor action in a MIS tunnel structure consists in the following. When a bias voltage needed for the inversion regime is applied to a MIS structure, this voltage is divided between the depleted region of the semiconductor and the insulator layer. The voltage drop across the insulator layer, which determines the useful electronic tunnel current, is set (under the conditions of moderate doping of the semi-

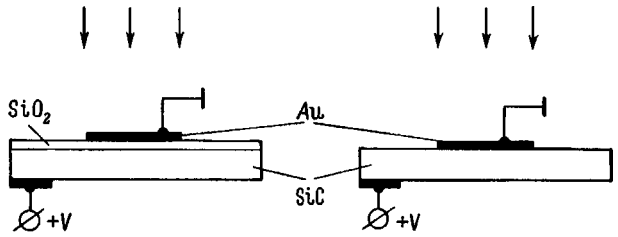

FIG. 1. Schematic diagram of the photoresponse measurements in $Au/SiO_2/n$-6H-SiC (left-hand side) and Au/n-6H-SiC (right-hand side) structures. The arrows indicate the direction of the flux of ultraviolet radiation.

conductor) by the surface density of minority carriers in the inversion layer (holes — in the case of a *n*-type semiconductor). In turn, the stationary surface density of holes is set at a value such that there would be a balance between their generation channels (in the case of SiC this is essentially only photogeneration in the depleted layer of the semiconductor) and their loss channels (tunneling leakage through the insulator, diffusion in the interior of the semiconductor out of the inversion layer at low voltage on the structure and recombination with electrons tunneling through the insulator). By varying the intensity of illumination of the MIS structure we vary the photogeneration current J_{ph}. This changes the stationary hole density in the inversion layer, the voltage drop across the insulator, and correspondingly the electron tunneling current J_e.

Thus, if for a certain voltage across the insulator the electron tunneling current is much higher than the hole current, then small changes in the current J_{ph} can in principle result in large changes in the current J_e, indicating amplification. In transistor terminology, the gate of the MIS structure plays the role of an electron emitter and the inversion layer plays the role of a light-induced *p*-type base, while the depleted region of the semiconductor plays the role of a collector of electrons ''injected'' from the emitter. Since recombination in the thin induced base can be ignored because of the very short transit time through it, the amplification in such a transistor can be very large if the emitter is sufficiently efficient.

The typical current-voltage characteristics of our experimental MOS structures under illumination with ultraviolet light of different intensity are shown in Figs. 2a and 2c. As one can see, for them the voltage dependence of the current is more complicated than in the case of the characteristics of the MS structures (Figs. 2a and 2d). The characteristic features of the MOS structures are as follows:

First — very low short-circuit photocurrent;

second — rapid (almost exponential) current growth above a certain threshold voltage;

third — current saturation, the saturation current is proportional to the illumination

intensity.

We note that the current–voltage characteristics of the MS structures are sublinear in the entire voltage range, while at zero bias the short-circuit photocurrent is quite high. It is important that the saturation current in the MOS structures is 3–7 times higher than the corresponding currents in MS structures. This can be interpreted as an amplification of the photogeneration current.

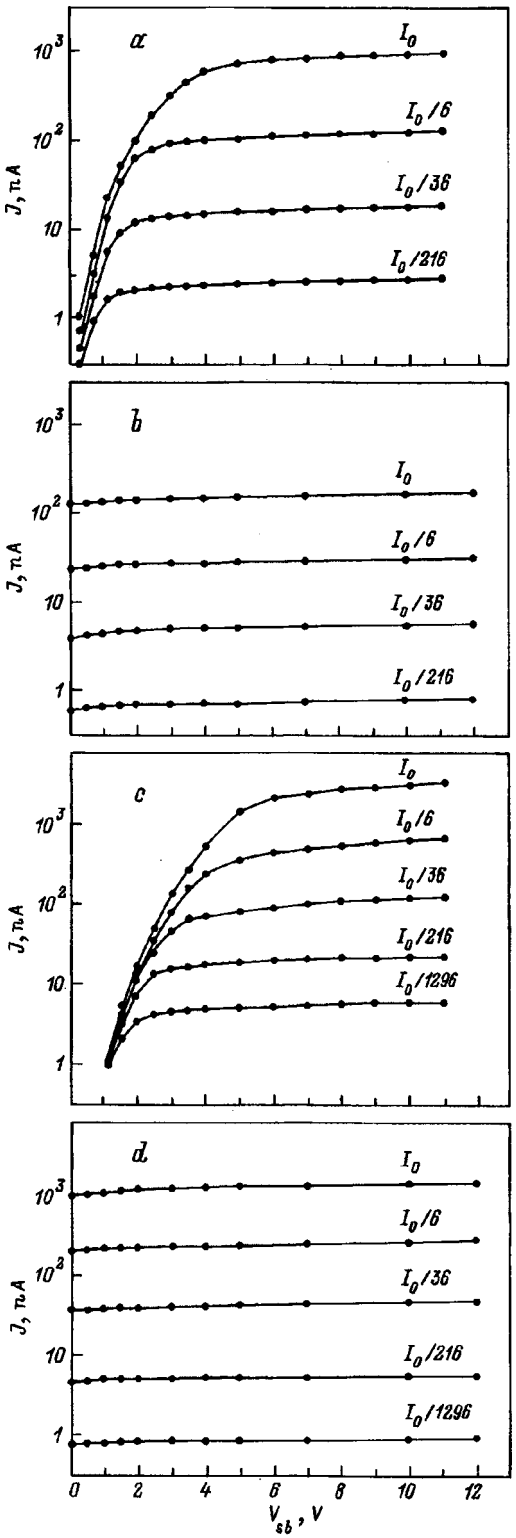

FIG. 2. Current-voltage characteristics of $Au/SiO_2/n$-6H-SiC MOS structures (a, c) and Au/n-6H-SiC MS structures (b, d) with different illumination intensities (neighboring curves correspond to a sixfold change in the illumination intensity). Epitaxy methods and the uncompensated donor density in the film $N_D - N_A$, cm^{-3}: a, b — Sublimation, 10^{17}; c, d — vapor-phase, 3×10^{15}. Conditions for the formation of a thin oxide layer: Oxidation temperature 950 °C; oxidation time t, min: a — 15, c — 60.

The current–voltage characteristics shown in Figs. 2a and 2c correspond to the above-described principle of operation of a tunnel phototransistor. Indeed, for subthreshold voltages on the structure (in this case there is still no strong inversion) the voltage drop across the insulator is small, the current through the structure is low (there is no electron injection from the semiconductor into the metal), and the applied voltage falls across the space-charge region. When a suprathreshold voltage, corresponding to strong inversion (the photogeneration current must be sufficiently high), is applied, there appears an electron tunneling current, which grows rapidly with increasing bias voltage, because a substantial portion of the increment to the bias voltage falls across the insulator. At the same time, the hole portion of the increment to the bias voltage falls across the insulator. At the same time, the hole diffusion fluxfrom the surface into the interior of the semiconductor decreases.

The current through the structure continues to grow until the hole diffusion current drops to zero and a balance is established between the hole leakage, which increases with voltage, through the insulator and the rate of photogeneration of holes in the depleted region. Next, the surface density of holes in the inversion layer ceases to depend on the bias voltage, whose increment falls almost entirely in the semiconductor; under these conditions, the current through the structure stabilizes (its magnitude is proportional to the photogeneration current).

Additional evidence supporting the current flow mechanism considered above is the character of the influence of the SiO_2 thickness on the device characteristics. As one can see by comparing Figs. 2a and 2c, the threshold voltage increases with the oxide thickness. This effect is explained mainly by the fact that the thicker the oxide, the larger the voltage drop across the insulator that is required to attain a tunneling current with the prescribed value (the section of exponential current growth is essentially the current–voltage characteristic of the oxide). Thus, all characteristic features of our structures are qualitatively similar to those of $Al/SiO_2/n$-Si structures.[4]

The characteristics of structures fabricated on the same substrate showed good reproducibility and remained quite stable during repeated measurements. The absolute values of the currents were higher in MOS and MS structures fabricated on the basis of epitaxial films with a lower uncompensated donor density. This is explained by the large thickness of the depleted region, where carrier photogeneration occurs, and correspondingly by the higher hole current flowing to the surface.

4. CONCLUSIONS

The characteristics of MOS structures based on thermally oxidized 6H-SiC with a tunnel-thin insulator were studied. It was shown that in such structures the hole component of the tunneling current is at least 3–7 times smaller than the electronic component. In practice, this can give a considerable increase in the efficiency of existing 6H-SiC photodiodes (in the UV region of the spectrum) because of the phototransistor action.

The values obtained by us for the injection coefficient of a SiC-based MOS emitter are far from maximal. Apparently, much higher values can be obtained by optimizing the system. In view of this circumstance, it is of interest to produce and investigate three-electrode devices based on ballistic SiC induced-base transistors and a tunneling MOS emitter.[4] Such transistors could be competitive with respect to classical bipolar SiC transistors. The current gain for the latter does not exceed 10–15 (Ref. 1) because of the small diffusion length of the minority carriers in the base region and because of their high recombination rate in the space-charge region of the injecting p–n junction. In contrast, in transistors with a MOS tunnel emitter there is virtually no recombination in the base, since the thickness of the induced base is very small (less 5 nm) and the electrons pass through it ballistically in a time of the order of 10^{-14} s.[7] The photocurrent gain of such a transistor can apparently be quite large, since it is determined solely by the injection coefficient of the emitter, and under high voltages on the emitter (greater than E_g/q) it increases even more as a result of impact ionization in the collector.[7]

[1] P. A. Ivanov and V. E. Chelnokov, Fiz. Tekh. Poluprovodn. **29**, 1921 (1995) [Semiconductors **29**, 1003 (1995)].
[2] M. A. Green and F. D. King, Solid-State Electron. **7**, 551 (1974).
[3] J. G. Simmons and G. W. Taylor, Solid-State Electron. **29**, 287 (1986).
[4] I. V. Grekhov, A. F. Shulekin, and M. I. Vexler, Solid-State Electron. **38**, 1533 (1995).
[5] K. M. Chu and D. L. Pulfrey, IEEE Trans. **ED-35**, 188 (1988).
[6] M. I. Veksler, Fiz. Tekh. Poluprovodn. **30**, 1718 (1996) [Semiconductors **30**, 899 (1996)].
[7] I. V. Grekhov, E. V. Ostroumova, A. A. Rogachev, and A. F. Shulekin, Pis'ma Zh. Tekh. Fiz. **17**, 44 (1991) [Tech. Phys. Lett. **17**, 476 (1991)].

Translated by M. E. Alferieff

PERSONALIA

Vladimir Idelevich Perel' (On His 70th Birthday)

Fiz. Tekh. Poluprovodn. **32**, 1151–1152 (September 1998)

[S1063-7826(98)02709-4]

Vladimir Idelevich Perel', a prominent theoretical physicist, Chief Editor of the journal ''Fizika i tekhnika poluprovodnikov,'' and Corresponding Member of the Russian Academy of Sciences, celebrated his 70th birthday on August 24, 1998. V. I. Perel' was born in Sverdlovsk (Ekaterinburg) into the family of a teacher. In 1950, after graduating from the Department of Physics at Leningrad State University, he was assigned a job as teacher at the Petrozavodsk Railroad School. At that time, Yuriĭ Maksimovich Kagan worked at Petrozavodsk University. Scientific contacts with him determined the field of the young theoretician's first research work — the candidate's dissertation ''On the motion of positive ions in their proper gas,'' defended in 1956, summed up Vladimir Idelevich's scientific work at Petrozavodsk University and the Pedagogical Institute. One of his teachers was L. É. Gurevich, to whose section at the Physicotechnical Institute V. I. Perel' transferred for work in 1958. The association with Lev Émanuilovich over many years, the creative atmosphere fostered by him, and the constant contacts with younger coworkers in the section undoubtedly contributed to the development of the V. I. Perel's scientific, pedagogical, and organizational talents.

His 40 years of work at the Physicotechnical Institute are marked by outstanding results in diverse fields of physics — the diagrammatic technique for calculating kinetic coefficients, theoretical investigations of optical orientation in gases and semiconductors, the prediction of the existence of electromagnetic waves in metals (helicons), the discovery of recombination waves in semiconductors, the discovery (together with experimentors) of optical momentum alignment of electrons, and the development of the theory of hot photoluminescence in semiconductors, nonradiative recombination of electrons and holes, phenomena accompanying interband absorption of intense picosecond light pulses, and many other interesting physical effects. The results obtained are reflected in many original articles, review articles and monographs. His services have been acknowledged by the State Prize of the USSR and the I. F. Ioffe Prize of the Russian Academy of Sciences. V. I. Perel' likes and knows how to work in close contact with experimentors. He possesses a remarkable gift of being able to identify among many details of a complicated experimental picture the key effects whose theoretical description gives an orderly, mathematically rigorous model of the phenomenon under study. Every formula, assumption, and word in his published theoretical papers have been checked repeatedly. ''Theoretical jargon'' and ''vulgar simplifications'' are equally foreign to these works.

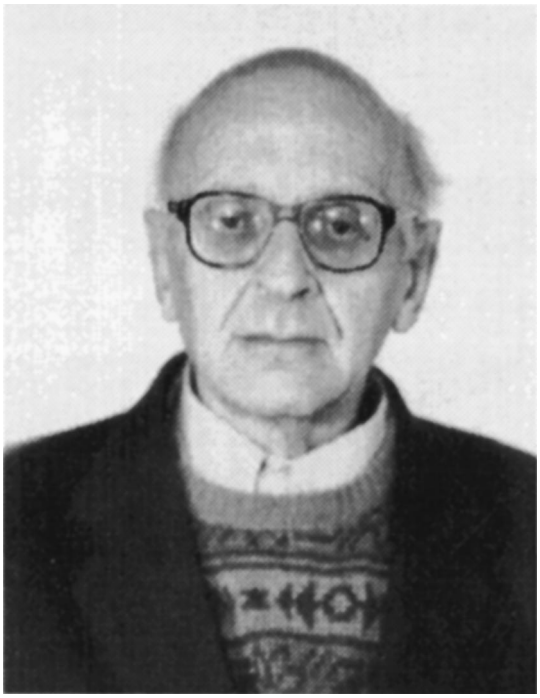

The surprising cordiality of the scientist and the man are strikingly manifested in V. I. Perel's pedagogical work. The fatherly concern, the ability to formulate a problem in a simple, clear and absolutely strict form, the ability to hear out ''murky'' arguments and to extract from them the sensible kernel, and the many hours of discussions about the physics of the phenomena under study and ways to describe them mathematically determined the future fate of his research and graduate students and many theoreticians beginning their career at the Physicotechnical Institute, who still consider themselves with pride as members of Vladimir Idelevich's school. Graduates of the main Department of Optoelectronics at the St. Petersburg Electrotechnical University, where V. I. Perel' has given for the past 25 years a course in solid-state physics, and young colleagues in the section ''Physics and Technology of Semiconductors,'' which V. I. Perel' has headed since 1983, can rightfully consider themselves to be V. I. Perel's students.

Administrative duties also befell V. I. Perel' when this section was formed. From 1988 to 1994 he also served as Deputy Director of the Division of Solid-State Electronics at the Physicotechnical Institute, and since 1991 he has been the Chief Editor of the journal ''Fizika i Tekhnika Polupro-

vodnikov.'' To work with such a leader is at once surprisingly pleasant, interesting, and very difficult. Under today's difficult working conditions, gentleness and kindness, careful thinking before making decisions, combined with demanding much of himself, stimulate better than any sharp rebukes good work from his groups. It is not surprising that Vladimir Idelevich enjoys great authority and love at the Physicotechnical Institute and well beyond its walls.

On the day of his seventieth birthday we sincerely wish him good health, happiness, and success in his new scientific endeavors.

Zh. I. Alferov, B. P. Zakharchenya, V. E. Golant, I. P. Ipatova, I. N. Yassievich, D. N. Mirlin, I. A. Merkulov, and M. I. D'yakonov

Editorial Board of the journal ''Fizika i Tekhnika Poluprovodnikov''

Translated by M. E. Alferieff

ATOMIC STRUCTURE AND NON-ELECTRONIC PROPERTIES OF SEMICONDUCTORS

Correlation between the temperature dependence of the band gap and the temperature dependence of the enthalpy of semiconductor crystals

A. F. Revinskiĭ*)

Brest State University, 224665 Brest, Belarus
(Submitted August 4, 1997; accepted for publication February 2, 1998)
Fiz. Tekh. Poluprovodn. **32**, 1025–1028 (September 1998)

The first-principles pseudopotential method of density-functional theory is used to study electron-phonon interactions in silicon. The temperature shift of the indirect band gap, the phonon spectrum, and the enthalpy are calculated consistently within the density-functional theory. The relationship between the temperature dependence of the energy gap $\Delta E_g(T)$ and the temperature dependence of the enthalpy $\Delta H(T)$ is $\Delta H(T)=K|\Delta E_g(T)|$. The physical origin of this correlation is discussed. © *1998 American Institute of Physics.* [S1063-7826(98)00109-4]

As was noted earlier,[1] a correlation is observed between the exponential temperature dependence of the band gap $\Delta E_g(T)$ and the enthalpy increment $\Delta H(T)$ in semiconductor crystals, which is expressed in the form of a linear dependence

$$\Delta H(T)=K|\Delta E_g(T)|. \tag{1}$$

Proceeding from the thermodynamic premise that the band gap should be equal to the free energy of the electronic subsystem of the semiconductor per electron–hole pair, several studies, a review of which is given in Ref. 2, have theoretically obtained in the most general case the linear dependence

$$\left(\frac{\partial E_g}{\partial T}\right)_p \sim C_v, \tag{2}$$

from which Eq. (1) follows for temperatures below the Debye temperature, where the specific heats C_p and C_v differ only slightly.

Relations (1) and (2) are important for studies of the mechanisms for semiconductor–metal phase transformations.[3] In this regard, it is of interest to ground the correlation (1) in the framework of quantum-mechanical approach since it makes it possible to take the most complete account, in particular, of the effect of the electron–phonon interaction (EPI) on the temperature dependence of the band gap and of the various thermodynamic functions.

It is well known[4] that the exact solution of the total system of self-consistent equations for the electrons and phonons using the many-particle Fröhlich Hamiltonian is fraught with certain difficulties. They are due, first of all, to calculating the vertex function in the self-energy part of the electron Green's function. At the same time, using the adiabatic approximation, which reduces to separating the coordinates of the electron and phonon subsystems, the phonon spectrum of metals and semiconductors can be reconstructed with quite high accuracy $\sim(m/M)^{1/2}$ (Ref. 5), where m and M are the masses of the electron and ion, respectively. However, taking the electron–phonon interaction into account leads to a substantial renormalization of the electron energy spectrum. In Refs. 6–8 in the adiabatic approximation with the help of Rayleigh–Schrödinger perturbation theory the following formula was obtained for the shifts of the energies $\varepsilon_{k,n}$ of the single-electron states $|\mathbf{k},n\rangle$ ($\mathbf{k}$ is a vector in the Brillouin zone, and n is the index of the zone in the electron spectrum) without allowance for anharmonicity effects:

$$\Delta E_{\mathbf{k},n}[\mathbf{u}(\xi,\kappa)]=\langle \mathbf{k},n|\hat{H}_{\text{int}}|\mathbf{k},n\rangle + \sum_{\mathbf{k},n\neq\mathbf{k}',n'} \frac{\langle \mathbf{k}',n'|\hat{H}_{\text{int}}|\mathbf{k},n\rangle|^2}{\varepsilon_{\mathbf{k},n}-\varepsilon_{\mathbf{k}',n'}+i\eta}, \tag{3}$$

where the electron–phonon interaction Hamiltonian $\hat{H}_{\text{int}}$ was used in the form of a power-series expansion of the electron–ion interaction potential $V_\kappa[\mathbf{r}-\mathbf{R}(\xi,\kappa)-\mathbf{u}(\xi,\kappa)]$ in the Cartesian coordinates $u_\alpha(\xi,\kappa)$ of the displacements of the ion from its equilibrium position. Here $\mathbf{R}(\xi,\kappa)$ is the position vector of the ion in the lattice, ξ is the index of the unit cell, and κ is the index of the ion in the unit cell. The temperature dependence of the real part of the energy (3) can be obtained[7] by using the variational derivative $\delta(\Delta E_{\mathbf{k},n})/\delta N_{\mathbf{q},j}$ with respect to the Bose–Einstein phonon distribution function $N_{\mathbf{q},j}$:

$$\Delta E_{\mathbf{k},n}(T)=\sum_{\mathbf{q},j}\frac{\delta(\Delta E_{\mathbf{k},n})}{\delta N_{\mathbf{q},j}}\left[N_{\mathbf{q},j}+\frac{1}{2}\right], \tag{4}$$

where $\mathbf{q}$ is the phonon wave vector, and j is the index of the phonon branch. At present, quantum-mechanical calculations[7–9] of the temperature dependence of the band-structure parameters of group-IV and III–V semiconductors have been performed in the framework of the proposed model. A distinguishing feature of these studies is the fact that the phonon spectrum was not calculated from first principles. In these calculations the band structure was calculated[7,8] with the help of local ion pseudopotentials. Such an approach is motivated by the fact that the shifts of

the single-electron energies (4) are much smaller than the energy gaps in the band structure. For this reason, according to Refs. 7 and 8, there is no compelling need to carry out laborious self-consistent band calculations from first principles using nonlocal ion pseudopotentials. However, as was shown earlier,[10] allowance for the nonlocal component of the norm-preserving ion pseudopotentials when calculating the electron–phonon interaction parameters is very important and gives a contribution of $\sim 20\%$. In this light, it can be seen that in order to gain an understanding of the physical reasons for the existing interrelationship between the electronic structure of the crystal and its thermodynamic functions it is necessary to calculate the band structure, binding energy, phonon spectrum, and thermodynamic characteristics of the investigated materials in the framework of a unified approach. In view of this circumstance, with the goal of elucidating the physical mechanisms of the observed correlation (1) with the help of the density functional in the case of silicon with diamond structure, we present here a consistent calculation of the phonon contribution as a function of $\Delta E_g(T)$ and $\Delta H(T)$ using electron and phonon spectra obtained earlier from first principles.[11,12]

To understand the algorithm for calculating the energy shifts (4) it is necessary to use intermediate formulas. The single-electron energies were calculated by self-consistent solution of the Kohn–Sham equation

$$\left[\frac{\hbar^2}{2m}(\mathbf{k}+\mathbf{G})^2-\varepsilon_{\mathbf{k},n}\right]C_{n,\mathbf{k}}(\mathbf{G}) + \sum_{\mathbf{G}'} V(\mathbf{k}+\mathbf{G},\mathbf{k}+\mathbf{G}')C_{n,\mathbf{k}}(\mathbf{G}')=0, \tag{5}$$

where $V(\mathbf{k}+\mathbf{G},\mathbf{k}+\mathbf{G}')$ are the Fourier components of the effective single-electron pseudopotential, $\mathbf{G}$ is the inverse lattice vector, and $C_{n,\mathbf{k}}(\mathbf{G})$ are the coefficients of the plane-wave expansion of the pseudowave function

$$|\mathbf{k},n\rangle=\sum_{\mathbf{G}} C_{n,\mathbf{k}}(\mathbf{G})\exp[i(\mathbf{k}+\mathbf{G})\mathbf{r}]. \tag{6}$$

The screened effective pseudopotential $V(\mathbf{k}+\mathbf{G},\mathbf{k}+\mathbf{G}')$ is a sum of the ion potential, the Coulomb potential, and the exchange–correlation potential

$$V(\mathbf{k}+\mathbf{G},\mathbf{k}+\mathbf{G}')=V_{\text{ion}}(\mathbf{k}+\mathbf{G},\mathbf{k}+\mathbf{G}') + V_H(\mathbf{G}-\mathbf{G}')+V_{XC}(\mathbf{G}-\mathbf{G}'), \tag{7}$$

where the ion potential $V_{\text{ion}}(\mathbf{k}+\mathbf{G},\mathbf{k}+\mathbf{G}')$ was constructed as a superposition of shape-preserving nonlocal ion pseudopotentials.[13]

In Eq. (3) the first term (the Debye–Waller contribution) is due to smoothing of the crystal potential as a result of ion vibrations. The second term (the self-energy contribution) is the increase in the electron–phonon coupling in the second-order perturbation theory. The imaginary component of this term is the lifetime of the polaron (an electron accompanied by lattice deformations). The variational derivative $\delta(\Delta E_{\mathbf{k},n})/\delta N_{\mathbf{q},j}$ for the Debye–Waller contribution (with superscript DW) and the real part of the self-energy contribution (with superscript SE) were calculated according to the formulas[8]

$$\left|\frac{\delta(\Delta E_{\mathbf{k},n})}{\delta N_{\mathbf{q},j}}\right|^{\text{DW}}=-\frac{1}{2}\sum_{n',\kappa,\kappa'}\frac{B^*_\alpha(\mathbf{k},n,n',0,\kappa)B_\beta(\mathbf{k},n,n',0,\kappa')}{\varepsilon_{\mathbf{k},n}-\varepsilon_{\mathbf{k},n'}} \times\left[\frac{1}{M_\kappa}\mathcal{E}_\alpha(-\mathbf{q}|j\kappa)\mathcal{E}_\beta(\mathbf{q}|j\kappa) + \frac{1}{M_{\kappa'}}\mathcal{E}_\alpha(-\mathbf{q}|j\kappa')\mathcal{E}_\beta(\mathbf{q}|j\kappa')\right], \tag{8}$$

$$\left|\frac{\delta(\Delta E_{\mathbf{k},n})}{\delta N_{\mathbf{q},j}}\right|^{\text{SE}}=\sum_{n',\kappa}\frac{1}{M_{\kappa'}}\frac{|\mathbf{B}(\mathbf{k},n,n',\mathbf{q},\kappa)\mathcal{E}(\mathbf{q}|j\kappa)|^2}{\varepsilon_{\mathbf{k},n}-\varepsilon_{\mathbf{k}+\mathbf{q},n'}}, \tag{9}$$

where $\mathcal{E}_\alpha(\mathbf{q}|j\kappa)$ are the Cartesian components of the phonon polarization vectors.

The matrix element of the electron–ion interaction B_α was calculated in the approximation of the rigid unit-cell potential, which assumes that the displacement of the ion with index κ from its equilibrium position, $\mathbf{u}(\xi,\kappa)$, takes place without deformation of the potential due to that ion, V_κ. Mathematically, this reduces to the case in which the quantity B in expression (9) is determined only by the gradient of the ion pseudopotential in Eq. (7) without regard for the Coulomb and exchange–correlation potentials. Thus, the element B_α is equal to

$$B_\alpha(\mathbf{k},n,n',\mathbf{q},\kappa)=\sum_{\mathbf{G},\mathbf{G}'}\left[\frac{\hbar}{\omega(\mathbf{q},j)}\right]^{1/2}C_{\mathbf{k}+\mathbf{q},n}(\mathbf{G})C_{\mathbf{k},n}(\mathbf{G}') \times\exp[-i(\mathbf{k}'+\mathbf{G}'-\mathbf{k}-\mathbf{G})\boldsymbol{\tau}_\kappa] \times(\mathbf{k}'+\mathbf{G}'-\mathbf{k}-\mathbf{G})_\alpha V_\kappa(\mathbf{k}'+\mathbf{G}',\mathbf{k}+\mathbf{G}), \tag{10}$$

where $\omega(\mathbf{q},j)$ is the frequency of the normal vibrations, $\boldsymbol{\tau}_\kappa$ is the basis vector associated with the ion with index κ, and $V_\kappa(\mathbf{k}'+\mathbf{G}',\mathbf{k}+\mathbf{G})$ is the form factor of the screened nonlocal pseudopotential of the Si^{4+} ion.

In silicon, as is well known, the band gap is determined by the direct transition $(\Gamma'_{25,v}-\Delta^{\min}_{1,c})$. According to my earlier calculations,[11] $E_g=1.05$ eV, where the experimental value is $E_g^{\text{exp}}=1.17$ eV (Ref. 14). This discrepancy stems from the fact that the density functional method is intended to describe the properties of many-particle systems in the ground state. For this reason, the energies of the excited states in the conduction band are not accurately reproduced in the given approach. At the same time, this is not reflected in the calculated value of the phonon contribution to the temperature dependence of the band gap $\Delta E_g(T)$ since it is equal only to the sum of temperature shifts $\Delta E_{\mathbf{k},n}(T)$ of individual single-electron states, i.e., in our case

$$\Delta E_g(T)=\Delta E(\Gamma'_{25,v}|T)+\Delta E(\Delta^{\min}_{1,c}|T). \tag{11}$$

In the calculation of the dependence $\Delta E_{\mathbf{k},n}(T)$ according to Eq. (4) a difficulty of a calculational nature arises in the integration over the Brillouin zone. Specifically, to obtain

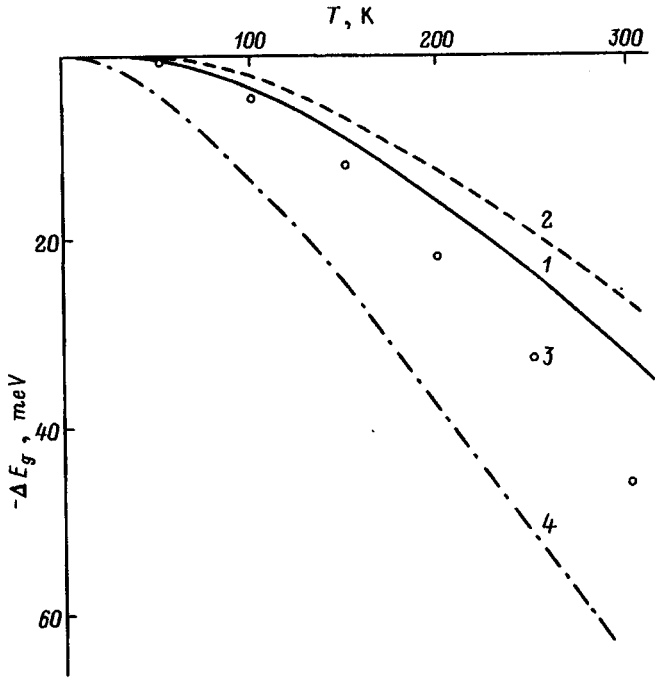

FIG. 1. Temperature dependence of the band gap of silicon. *1* — this work, *2* — calculation (Ref. 8), *3* — experiment (Ref. 17), *4* — calculation (Ref. 9).

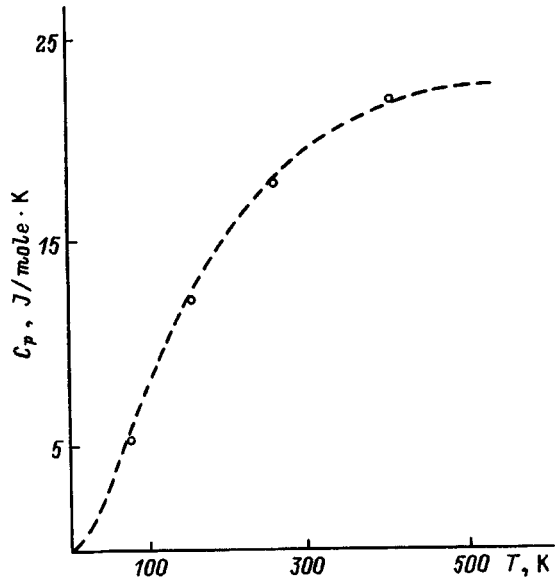

FIG. 2. Temperature dependence of the lattice specific heat of silicon. Points — this work, dashed line — experiment (Ref. 21).

numerical values of the quantities $\Delta E^{\mathrm{SE}}_{\mathbf{k},n}(T)$ for each vector $\mathbf{q}$ of the Brillouin zone it is necessary to obtain additional self-consistent solutions of the Kohn–Sham equation with the goal of calculating the energies $\varepsilon_{\mathbf{k}+\mathbf{q},n}$ and wave functions $|\mathbf{k}+\mathbf{q},n\rangle$. In order not to use up unjustifiably large amounts of computer time, we have first calculated the derivatives (9) for specially chosen symmetric points of the Brillouin zone (using the five-point Chadi–Cohen scheme[15]), after which the points in 1/48 of the Brillouin zone were chosen by the Monte Carlo method and the derivatives (9) were calculated with the help of an interpolation procedure.[16] The phonon polarization vectors $\mathcal{E}(\mathbf{q}|j\kappa)$ were calculated as eigenvectors of the dynamical matrix of silicon, obtained earlier in Ref. 12.

The phonon contribution to the decrease in the band gap of silicon $\Delta E_g(T)$ is plotted in Fig. 1 in comparison with the available experimental and theoretical data. An account of the nonlocality of the pseudopotential of the Si^{4+} ion gives somewhat better agreement with experiment in comparison with the calculations of Ref. 8, which were made with the help of local pseudopotentials. The large scatter of the theoretical results relative to the experimental data necessitates an analysis of the accuracy of the calculated dependence $\Delta E_g(T)$. We used two fundamental characteristics of silicon to calculate $\Delta E_g(T)$: its band structure, calculated with an accuracy of 0.01 eV (Ref. 11) [200 plane waves in expansion (6)], and the frequencies of the normal vibrations of the ions, calculated with an accuracy of 0.2 THz (Ref. 12). Varying the single-electron energies $\varepsilon_{k,n}$ and frequencies $\omega(\mathbf{q},j)$ within the indicated limits gives an absolute error for $\Delta E_g(T)$ of 2.5 meV. The accuracy of the experimental data[17] is 1 meV.

The calculation in Ref. 18 of the contribution $\Delta E^{\mathrm{TE}}_g(T)$ due to thermal expansion of the silicon crystal showed that anharmonicity effects are insignificant in the temperature interval plotted in Fig. 1. Specifically, for $T \leqslant 300$ K $\Delta E^{\mathrm{TE}}_g(T)$ is less than 2 meV.

The specific heats C_p and C_v of the crystal are interrelated by the standard thermodynamic relation

$$C_p(T) = C_v(T) + 9T\alpha^2(T)B_0\Omega, \tag{12}$$

where Ω is the volume of the crystal, $\alpha(T)$ is the temperature coefficient of linear expansion of silicon,[19] and B_0 is the bulk modulus, calculated at the minimum of the total energy of the silicon crystal at $T=0$ (Ref. 20). The lattice specific heat $C_v(T)$ was calculated with the help of the silicon phonon spectrum.[12] The theoretical dependence $C_p(T)$ obtained using Eq. (12) is plotted in Fig. 2. The phonon contribution to the temperature dependence of the enthalpy is

$$\Delta H_{\mathrm{ph}}(T) = \int_0^T C_p(T')dT'. \tag{13}$$

The change in the enthalpy due to formation of electron–hole pairs can be calculated using the formula[22]

$$\Delta H_{e-h}(T) = n_{e-h}E_g(T) + T\Delta S_{e-h}(T), \tag{14}$$

where n_{e-h} is the concentration of electron–hole pairs, and $\Delta S_{e-h}(T)$ is the change in the entropy. Calculations show that the contribution $\Delta H_{e-h}(T)$ is negligible in comparison with the phonon contribution $\Delta H_{\mathrm{ph}}(T)$.

Figure 3 plots the dependence $\Delta H_{\mathrm{ph}}(T) = K'|\Delta E_g(T)|$ calculated by us in comparison with the experimentally obtained dependence (1). It can be seen that a linear relationship is observed between $\Delta H_{\mathrm{ph}}(T)$ and $\Delta E_g(T)$ in the proposed calculational scheme. The electron–phonon interaction probably plays an important role in the appearance of this correlation. At the same time, the theoretical value of the coefficient K' is much greater than its experimental value. This discrepancy is due to the disagreement between the

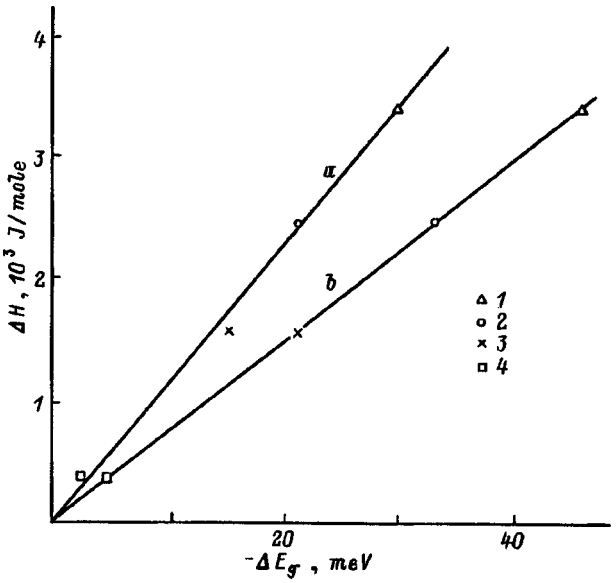

FIG. 3. The dependence $\Delta H(T)=K|\Delta E_g(T)|$ for silicon. a — this work, b — experiment (Refs. 17 and 21). T, K: *1* — 300, *2* — 250, *3* — 200, *4* — 100.

calculated dependence $\Delta E_g(T)$ and the corresponding experimental dependence (Fig. 1) since the calculated lattice specific heat $C_p(T)$ (Fig. 2) and consequently $\Delta H_{\rm ph}(T)$ are in good agreement with the measurements of Refs. 14 and 21.

The main reason why the calculated phonon contribution to the decrease in the silicon band gap with increase of the temperature does not reproduce the experimental dependence $\Delta E_g(T)$ can be attributed to the fact that the phonon contribution is not the only one. A consistent account of the other elementary excitations and interactions is needed, in particular the exciton–phonon interaction. The rigid potential approximation used to obtain in Eq. (10) also introduces a certain error. However, an account of additional terms in the variation of the single-electron effective potential (7) due to the Coulomb and exchange–correlation interactions of the electrons would substantially complicate an already cumbersome calculational procedure. In view of the discussion above, the proposed calculational scheme in any case should be considered as an initial approximation aimed at better understanding the physical reasons for the observed interrelationship between the structure of the electron energy spectrum and the thermodynamic functions of semiconductor crystals.

*)Fax: (162)230996; E-mail: Rev@univer.belpak.brest.by

[1] N. N. Sirota, in *Semiconductors and Semimetals*, edited by P. K. Willardson and A. C. Beer (Academic Press, New York, 1968), Vol. 4, p. 35.
[2] V. M. Fridkin, in *Photoferroelectrics* (Springer-Verlag, Berlin, 1979; Nauka, Moscow, 1976), p. 31.
[3] N. F. Mott, in *Metal–Insulator Transitions* [in Russian] (Nauka, Moscow, 1979), p. 35.
[4] E. G. Maksimov, D. Yu. Savrasov, and S. Yu. Savrasov, Usp. Fiz. Nauk **167**, 353 (1997) [Phys. Usp. **40**, 295 (1997)].
[5] E. G. Brovman and Yu. M. Kagan, Usp. Fiz. Nauk **112**, 369 (1974) [Sov. Phys. Usp. **17**, 125 (1974)].
[6] P. B. Allen and V. Heine, J. Phys. C: Solid State Phys. **9**, 2305 (1976).
[7] S. Zollner, M. Cardona, and S. Gopalan, Phys. Rev. B **45**, 3376 (1992).
[8] P. Lautenschlager, P. B. Allen, and M. Cardona, Phys. Rev. B **31**, 2163 (1985).
[9] M. Klenner, C. Falter, and W. Ludwig, Ann. Phys. (Leipzig) **1**, 34 (1992).
[10] A. F. Revinskiĭ, Fiz. Tverd. Tela (St. Petersburg) **37**, 2841 (1995) [Phys. Solid State **37**, 1567 (1995)].
[11] A. F. Revinskiĭ, Vestsi ANB. Ser. Fiz.-Met. Navuk **2**, 47 (1992).
[12] A. F. Revinskiĭ, Vestn. BGU. Ser. 1, 2, 33 (1994).
[13] G. B. Bachelet, D. R. Hamman, and M. Schlüter, Phys. Rev. B **26**, 4199 (1982).
[14] *Physical-Chemical Properties of Semiconductor Materials: Handbook* [in Russian] (Nauka, Moscow, 1978), p. 14.
[15] D. J. Chadi and M. L. Cohen, Phys. Rev. B **8**, 5747 (1973).
[16] M. A. Zolotarev and A. S. Poplavnoĭ, Izv. Vuzov. Fizika **5**, 78 (1983).
[17] W. Bludau and A. Onton, J. Appl. Phys. **45**, 1846 (1974).
[18] A. F. Revinskiĭ, Izv. Vuzov. Fizika **8**, 3 (1996).
[19] S. I. Novikova, in *Thermal Expansion of Solids* (Nauka, Moscow, 1974), p. 290.
[20] A. F. Revinskiĭ, Izv. Vuzov. Fizika **1**, 123 (1994).
[21] *Properties of the Elements, Part I: Physical Properties*, edited by G. V. Samsonov (Metallurgiya, Moscow, 1976), p. 150.
[22] K. P. O'Donnell and X. Chen, Appl. Phys. Lett. **58**, 2924 (1991).

Translated by Paul F. Schippnick

Formation of donor centers upon annealing of dysprosium- and holmium-implanted silicon

O. V. Aleksandrov and A. O. Zakhar'in

St. Petersburg State Electrical Engineering University, 197376 St. Petersburg, Russia

N. A. Sobolev[a)] and E. I. Shek

A. F. Ioffe Physicotechnical Institute, Russian Academy of Sciences, 194021 St. Petersburg, Russia

M. I. Makoviĭchuk and E. O. Parshin

Institute of Micro-Electronics, Russian Academy of Sciences, 150007 Yaroslavl', Russia
(Submitted February 9, 1998; accepted for publication February 10, 1998)
Fiz. Tekh. Poluprovodn. **32**, 1029–1032 (September 1998)

The implantation of a $10^{13}\,\mathrm{cm}^{-2}$ dose of 1-MeV dysprosium and holmium ions with subsequent annealing at temperatures in the range 600–900 °C leads to donor center formation. The donor center concentration increases with increasing oxygen concentration in the starting materials as well as upon additional oxygen implantation. Such behavior of the activation and the donor center concentration profiles as a function of the annealing temperature and oxygen concentration is observed in Si:Dy and Si:Ho. The results show that the formation of at least two types of donor centers containing rare-earth elements and/or oxygen atoms takes place.
 [S1063-7826(98)00209-9]

INTRODUCTION

Studies of the properties of erbium-doped silicon (Si:Er) have recently increased considerably.[1] These studies have been motivated by its potential for applications in silicon optoelectronics as a light source at 1.54 μm. The efficiency of erbium luminescence depends on the spectrum of optically and electrically active centers containing rare-earth elements (REE). There is so far, however, a lack of understanding of the processes by which electrically active erbium centers from in silicon. From this point of view, a study of the electrical properties of silicon doped with other rare-earth elements is of current interest for establishing the general trends of the processes of formation of electrically active centers in such systems. In addition, structures based on silicon doped with rare-earth elements can serve as sources of infrared radiation. In particular, silicon doped with dysprosium (Si:Dy) and holmium (Si:Ho) may be promising. Data on the formation of electrically active centers for these impurities are, to the best of our knowledge, lacking. In our study we have investigated the electrical properties of Si layers implanted with Dy and Ho.

EXPERIMENTAL CONDITIONS

As substrates we used polished silicon wafers of *n*-type conductivity, grown by the float-zone method (*n*-FZ), with resistivity in the range 80–140 $\Omega\cdot$cm, and of *n*-type and *p*-type conductivity, grown by the Czochralski method, with resistivities of 5 and 20 $\Omega\cdot$cm, respectively. The oxygen concentration in the starting material was: $<2\times10^{16}$ (*n*-FZ), 8.6×10^{17} (*n*-Cz), and $1.1\times10^{18}\,\mathrm{cm}^{-3}$ (*p*-Cz). A $Q_{\mathrm{tot}}=1\times10^{13}\,\mathrm{cm}^{-2}$ dose of 1-Mev dysprosium and holmium ions was implanted on a setup built by High Voltage Engineering Europe B2K. In addition, some of the wafers were implanted with oxygen ions: specifically, a 1×10^{14}-cm^{-2} dose of 145-keV ions into Si:Dy, and the same dose of 140-keV ions into Si:Ho, which corresponds to a maximum concentration of $\sim5\times10^{18}\,\mathrm{cm}^{-3}$. Their energy was chosen such that the projected mean free paths of the rare-earth ions and the oxygen ions coincided. Implantation was not accompanied by amorphization and was effected at a 7° angle so as to prevent ion channeling.

Isochronous (over the course of 30 min) anneals were performed in the temperature range 600–900 °C in a chlorine-containing atmosphere. The latter consisted of an oxygen flux containing 1 mol% carbon tetrachloride.

The type of conductivity of the surface layer was monitored with the help of a thermal probe. The sheet resistance R_s was measured by the four-probe method. The rare-earth distribution with depth was measured by secondary-ion mass spectroscopy (SIMS) on a Cameca IMS 4f setup. Concentration profiles of the charge carriers were determined by capacitance–voltage profiling with a mercury probe. The activation coefficient of the electrically active centers associated with rare-earth element implantation was calculated from the relation $k=(e\mu R_s)^{-1}/Q_{\mathrm{tot}}$, where Q_{tot} is the dose, e is the charge of an electron, and $\mu=1350\,\mathrm{cm}^2/\mathrm{V}\cdot\mathrm{s}$ is the electron mobility (it is assumed that it does not depend on the electron concentration).

RESULTS AND DISCUSSION

First let us consider the behavior of the holmium impurity. Curve *1* in Fig. 1 shows SIMS-profiles of the total holmium concentration after implantation. Subsequent isochronous anneals do not lead to any changes in the holmium

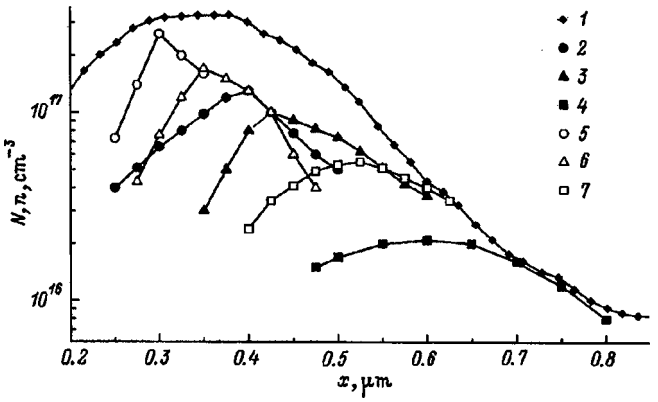

FIG. 1. Concentration profiles of holmium atoms $N(x)$ after implantation (*1*) and electrons $n(x)$ (*2–7*) in *p*-Cz-Si:Ho (*2–4*) and *p*-Cz-Si:Ho:O (*5–7*) after implantation and annealing for 0.5 h. Annealing temperature *T*, °C: *2*, *5* — 700; *3*, *6* — 800; *4*, *7* — 900.

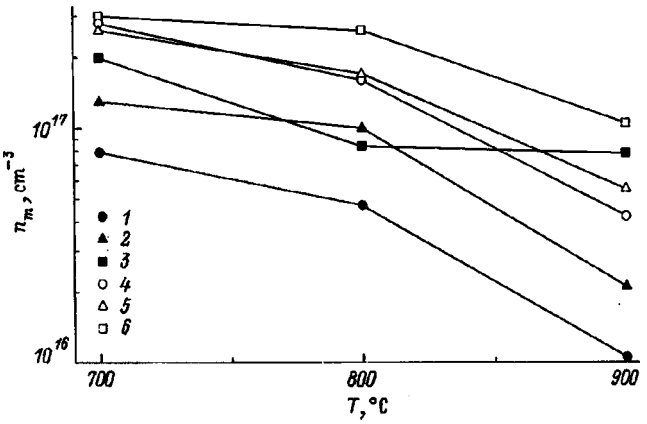

FIG. 3. Dependence of the maximum concentration of donor centers n_m on the annealing temperature *T* in *n*-FZ-Si:Ho (*1*), *p*-Cz-Si:Ho (*2*), *n*-Cz-Si:Ho (*3*), *n*-FZ-Si:Ho:O (*4*), *p*-Cz-Si:Ho:O (*5*), and *n*-Cz-Si:Ho:O (*6*).

distribution. No changes in the SIMS-profiles were observed in silicon implanted with erbium and annealed in the same temperature range. The absence of changes in this case was explained by the low values of the erbium diffusion coefficient.[2–4]

A postimplantation anneal at the above temperatures leads to the formation of donor centers. In this case, $p-n$-conversion of the type of conductivity of the implanted layer is observed in *p*-Cz-Si. The dependence of the activation coefficient on the temperature of the isochronous anneal is shown in Fig. 2 (curves *1* and *2*). The maximum values of the coefficient are observed at 700 °C and are equal to 18% for Si:Ho and 26% for Si:Ho:O, of the total dose of implanted holmium.

The concentration profiles of the electrons in the implanted layer $n(x)$ have the form of curves with a maximum. The nature of the variation of the distribution $n(x)$ as a function of annealing temperature for the *p*-Cz-Si:Ho and *p*-Cz-Si:Ho:O samples is shown in Fig. 1 (curves *2–7*). The maximum electron concentration was observed after annealing at 700 °C. Increasing the annealing temperature decreases the maximum electron concentration n_m and shifts the position of the maximum x_m deeper into the sample. In this case, the value of n_m in the sample with additionally implanted oxygen is higher, and x_m is situated closer to the surface than in Si:Ho.

Similar behavior of $n(x)$ as a function of the annealing temperature was observed in *p*-FZ-Si and *n*-Cz-Si doped with holmium. The dependence of n_m and x_m on the annealing temperature for the different grades of investigated silicon are plotted in Figs. 3 and 4.

Let us consider in more detail the data for *n*-FZ-Si:Ho. After the anneals at 700 and 800 °C the concentration of donor centers exceeded by not less than twofold the oxygen concentration in the starting material (Fig. 3, curve *1*). This gives us reason to believe that the dominant donor centers do not contain oxygen atoms. On the other hand, increasing the annealing temperature not only lowers the concentration of donor centers, but also shifts their maxima deeper into the sample (Fig. 4, curve *1*). Since diffusion of holmium atoms is not observed at these temperatures, it is reasonable to assume that in addition to the immobile rare-earth atoms, the more mobile intrinsic point defects (vacancies or interstitial

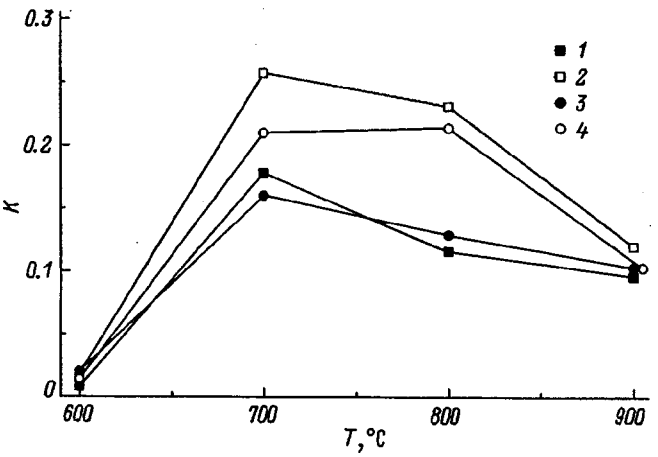

FIG. 2. Dependence of the activation coefficient *K* on the annealing temperature *T* in *p*-Cz-Si for implantation of *1* — holmium, *2* — holmium and oxygen, *3* — dysprosium, *4* — dysprosium and oxygen.

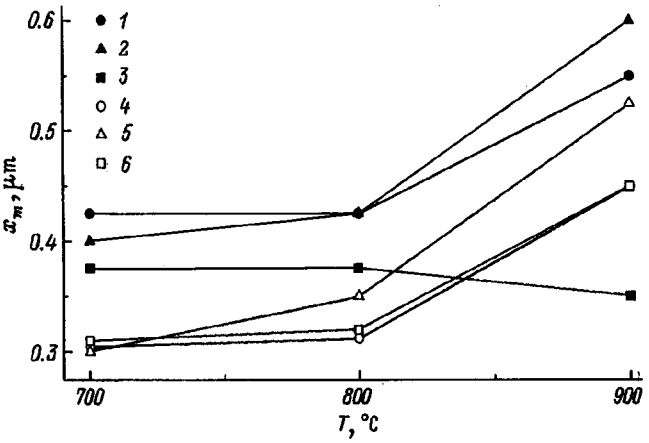

FIG. 4. Dependence of the position of the maximum concentration of donor centers x_m on the annealing temperature *T* in *n*-FZ-Si:Ho (*1*), *p*-Cz-Si:Ho (*2*), *n*-Cz-Si:Ho (*3*), *n*-FZ-Si:Ho: O (*4*), *p*-Cz-Si:Ho: O (*5*), and *n*-Cz-Si:Ho: O (*6*).

silicon atoms), which are formed during the annealing of the implantation defects, also participate in the formation of donor centers. The surface of the sample functions as a sink for the intrinsic defects. With an increase in the temperature, an increasing number of the intrinsic defects escape to the surface. As a result, the concentration of donor centers was found to decrease, and the maximum was found to shift deeper into the sample. The qualitative model for Si:Er described above was first proposed in Ref. 4. Later a quantitative model was developed, which assumed that erbium atoms and intrinsic interstitial atoms participate in the formation of donor centers.[5]

The increase in the concentration of donor centers in Cz-Si:Ho in comparison with FZ-Si:Ho (Fig. 3, curves *1–3*) is connected with the formation of new donor centers that contain oxygen atoms. Are two different donor centers with comparable concentrations formed in Cz-Si:Ho or does one center dominate? Our data do not allow us to answer this question It is important to note that after annealing at 700 °C the concentration of donor centers is higher in *n*-type Cz-Si than in the *p*-type material, although the ratio of oxygen concentrations in the starting samples is the reverse.

Additional coimplantation of oxygen also increases the concentration of donor centers. The largest (and almost the same) concentration of donor centers is reached after annealing at 700 °C in all grades of the investigated silicon (Fig. 3, curves *4–6*). Here the positions of the maxima also coincide (Fig. 4, curves *4–6*). The experimental data give us reason to believe that formation of oxygen-containing donor centers takes place. Their rate of formation at 700 °C is several orders of magnitude greater than the rate of formation of classical thermal donors formed in silicon that does not contain rare-earth elements.[6] With an increase in the annealing temperature, their concentration decreases, as in the case of classical thermal donors.

After dysprosium implantation and subsequent annealing at 600–900 °C the same regularities are observed as in the case of holmium implantation: the holmium distribution does not change during isochronous anneals, the maximum electron concentration in the implanted layer is observed after annealing at 700 °C, raising the annealing temperature lowers the electron concentration, and additional implantation of oxygen raises the electron concentration. The dependence of the activation coefficient of the donor centers associated with dysprosium implantation on the annealing temperature is plotted in Fig. 2 (curves *3* and *4*) and is identical to the corresponding dependence for holmium implantation.

Comparison of our results for Si:Ho and Si:Dy with the available data for Si:Er (Refs. 4, 7, and 8) reveals hardly any features associated with specific rare-earth elements. This is probably explained by their atomic structure. Differences between the elements are connected with changes in the degree of filling of the inner $4f$ shell. The outer electron shell, which determines their interaction with other atoms, is the same. As a result, the rare-earth elements are similar in their chemical properties.

In summary, we have examined the influence of annealing temperature and oxygen impurity on the electrical properties of silicon layers implanted with dysprosium and holmium. We found that implantation of rare-earth elements is accompanied by formation of donor centers whose concentration increases with increasing oxygen concentration. In addition to the rare-earth atoms, oxygen also participates in the formation of the donor centers.

We wish to thank Yu. A. Kudryavtsev for carrying out the secondary-ion mass-spectroscopy measurements of the the concentration profiles. We also thank B. A. Andreev for measuring the oxygen concentration.

This work was carried out with the partial financial support of CRDF (Grant No. 235), a joint arrangement of INTAS and the Russian Fund for Fundamental Research (Grant No. 95-0531), and a separate grant from the Russian Fund for Fundamental Research (Grant No. 96-02-17901).

[a)]Fax: (812) 2471017; E-mail: nick@sobolev.ioffe.rssi.ru

[1] *Rare Earth Doped Semiconductors II*. MRS Symp. Proc., Vol. 422 (1996).
[2] D. Moutonnet, H. L. Haridon, P. N. Favennec, M. Salvi, M. Gauneau, F. Arnaud, D. Avitaya, and J. Chroboczek, Mater. Sci. Eng. **4**, 75 (1989).
[3] F. Y. G. Ren, J. Michel, Q. Sun-Paduano, B. Zheng, H. Kitagawa, D. S. Jacobson, J. M. Poate, and L. C. Kimerling, MRS Symp. Proc., Vol. 301, 87 (1993).
[4] O. V. Aleksandrov, N. A. Sobolev, E. I. Shek, and A. V. Merkulov, Fiz. Tekh. Poluprovodn. **30**, 876 (1996) [Semiconductors **30**, 468 (1996)].
[5] N. A. Sobolev, O. V. Alexandrov, and E. I. Shek, MRS Symp. Proc., Vol. 442, 237 (1997).
[6] V. V. Emtsev, G. A. Oganesyan, and K. Schmalz, Solid State Phenom. **47–48**, 259 (1996).
[7] J. L. Benton, J. Michel, L. C. Kimerling, D. S. Jacobson, Y.-H. Xie, D. J. Eaglesham, E. A. Fitzgerald, and J. M. Poate, J. Appl. Phys. **70**, 2667 (1991).
[8] F. Priolo, S. Coffa, G. Franzò, C. Spinella, A. Carnera, and V. Bellani, J. Appl. Phys. **74**, 4936 (1993).

Translated by Paul F. Schippnick

Normal lattice vibrations and the crystal structure of anisotropic modifications of boron nitride

S. V. Ordin, B. N. Sharupin, and M. I. Fedorov

A. F. Ioffe Physicotechnical Institute, Russian Academy of Sciences, 194021 St. Petersburg, Russia
(Submitted April 15, 1998; accepted for publication April 20, 1998)
Fiz. Tekh. Poluprovodn. **32**, 1033–1042 (September 1998)

A multicomponent infrared study of boron nitride (BN) pyrocrystals was performed in polarized light. A series of textured polycrystals, which included samples with different dergees of ordering, with various ratios of the concentrations of the hexagonal and rhombohedral phase, was prepared by chemical vapor deposition. This study revealed the essential influence of the microstructure of the pyrocrystal on the reflection and transmission spectra. It is shown that to identify the normal oscillations of the hexagonal phase, crystal-optical effects and effects associated with phonon scattering must be taken into account. The normal oscillations of the rhombohedral phase of BN were identified directly from experimental spectra of pyrocrystals which are similar in their properties to a single crystal. On the basis of the results obtained by us it is shown that ionic–covalent bonds exist between some of the atoms of neighboring layers in anisotropic modifications of BN. A refined model of the lattice structure eliminates an entire host of contradictions between the experimental data and shows that in addition to sp^2 hybridized electrons, sp hybridized electrons participate in the formation of interatomic bonds in anisotropic BN. © *1998 American Institute of Physics.* [S1063-7826(98)00309-3]

Boron nitride (BN), almost from the very moment of its synthesis by chemical vapor deposition by one of the authors of this paper,[1] has found wide technological applications. Pyrocrystals of BN obtained by the given technique are textured, layered polycrystals, possess mechanical hardness, thermal stability, are chemically inert up to 2000 °C, and possess small dielectric losses in a wide frequency range. The unique thermal-physical and chemical properties of BN pyrocrystals are determined by a feature of the crystal structure of its anisotropic (hexagonal and rhombohedral) modifications: strong bonds of the B and N ions in hexagonal arrays that form monatomic layers, and a weak bond between the layers (which was previously assumed to be purely van der Waals). This configures the high degree of anisotropy of a number of physical properties of BN pyrocrystals: mechanical, thermal, chemical, and what is especially important for semiconductor technology, diffusion properties. Production equipment fabricated from BN pyrocrystals is ideally clean, i.e., it does not introduce impurities into any semiconductor material being grown in them.

In view of the properties of the crystal structure of BN, it is also a unique object for physical study. Theoretical calculations[2] have used BN as a model material for constructing electron bands of a two-dimensional and a quasi-two-dimensional insulator. However, the models of the crystal structure of BN used in these calculations were based on x-ray diffraction data obtained on polycrystals with weakly pronounced texture. Data available for a number of III–V semiconductor compounds,[3] to which class BN belongs, allow us to make some grounded assumptions about the properties of only the cubic modification of BN. Due to the absence of single crystals of anisotropic modifications of BN, there are no reliable data on the dispersion laws in such crystals of the electrons and phonons, which would make it possible to validate the calculational and theoretical model assumptions. Thus, as will be shown below, the band calculations of Ref. 2 and the group-theoretical analysis of the lattice reflection spectra of BN pyrocrystals carried out in Ref. 4 disregarded an important feature of the structure of the crystalline lattice of anisotropic modifications of BN.

The technique of chemical vapor deposition modified by the author of BN technology[1] has made it possible to obtain large, highly ordered pyrocrystals of the rhombohedral modification, from which by cubic compression perfect samples of the cubic modification have been obtained. A complex of infrared (IR) spectral studies of samples of BN of rhombohedral and cubic modification has shown that their properties are similar to those of single crystals. This has made it possible to uniquely identify the normal lattice vibrations not only in the isotropic cubic structure, but also in the anisotropic rhombohedral structure of BN. It was found that the high frequencies of the modes polarized parallel to the **C** axis in the anisotropic modifications are attributable to the existence in those modifications of ionic–covalent bonds between some of the atoms of neighboring layers. Allowance for interlayer bonds leads to a substantial correction in the model of the crystal structure of the anisotropic modifications of BN, thereby eliminating contradictions between a number of experimental data. The ideas developed by us pertain to an entire class of layered crystals, including the promising and actively investigated nitrides having a hexagonal modification.

1. MAIN CHARACTERISTICS OF THE INVESTIGATED BN PYROCRYSTALS

Anisotropic boron nitride is produced as the product of a pyrolytic reaction at the boundary of the gas phase and, at the initial moment, at the surface of the graphite substrate. As a result of pyrolysis, usually a white layered ceramic grows on the graphite substrate, consisting of small crystallites—scales of the hexagonal and rhombohedral phases of BN. The crystallites form growth cones, whose vertices are located on the graphite substrate, and correspond to nuclei of the anisotropic phase of BN. The dimensions of the crystallites and the deviation of their symmetry axes from the preferred orientation—the normal to the substrate surface—strongly depend on the conditions of growth–deposition. BN pyrocrystals with average misorientation angle of the crystallite axes $\alpha \approx 30°$ are characterized by a maximum concentration of the hexagonal phase with linear dimension of the crystallites along the symmetry axis $L_c \simeq 100$ Å and roughly an order of magnitude greater linear dimension in the transverse direction. When the misorientation angle of the crystallites is decreased to 10°, their dimensions were found to increase monotonically ($L_c \simeq 160$ Å), accompanied by the appearance of an asymmetry in their physical properties, in particular, their thermal conductivity.[1] Further increase of the degree of mutual orientation of the crystallites ($\alpha \approx 1°$) corresponds to an abrupt increase in the dimensions of the crystallites ($L_c \simeq 1000$ Å) and in the concentration of the rhombohedral phase. Optimization of the conditions of growth allowed us to obtain yellow, translucent pyrocrystals with an area of a few cm^2 and thickness ~ 5 mm in the form of a sheaf of rhombohedral crystallites—monolayers with mean thickness of the monolayer ~ 0.2 μm. In this case the anisotropy of some of the physical parameters of the rhombohedral pyrocrystals turned out to be lower than those of the ordered hexagonal crystals. In particular, the thermal conductivity along the **C** axis, which decreases monotonically as the misorientation of the crystallites decrease to 10°, increases monotonically as the degree of ordering of the crystallites is increased.

2. INFRARED SPECTRAL STUDIES OF BN PYROCRYSTALS

In this section we present the results of experimental studies of normal reflection R and transmission T spectra of BN pyrocrystals in polarized infrared light and a theoretical treatment of these results. The series of pyrocrystals for study included samples with varying degree of order of the crystallites and, correspondingly, with different ratios of the concentrations of the hexagonal and rhombohedral phases. In this case, the preferred orientation of the crystallographic axes of the crystallites coincided with the normal to the deposition–growth surface of the pyrocrystals and in what follows will be referred to as the **C** axis of the pyrocrystals. Studies of the reflection spectra were carried out on mechanically polished crystal planes, oriented at different angles to the **C** axis, and for different orientations of the **E** vector of the electromagnetic wave relative to the **C** axis. As these studies showed, the optical anisotropy of the BN pyrocrystals, like the anisotropy of the other properties, depends on their **C** axis. However, in contrast to uniaxial single crystals, in the case of pyrocrystals greater changes were observed in the reflection spectra corresponding to the ordinary wave $\mathbf{E} \perp \mathbf{C}$ when the mutual orientation of the **C** axis and direction of propagation of the light wave was varied. Therefore, to completely characterize the optical anisotropy of the BN pyrocrystals we examined the dependence of the reflection spectra on the orientation of the propagation vector of the radiation **k** relative to the **C** axis. We found that in this case the optical properties of the pyrocrystals varies monotonically. A monotonic transformation of the reflection spectra of the BN pyrocrystals was also observed when the concentration of the rhombohedral phase was increased at the expense of the hexagonal. The monotonic nature of these dependences makes it possible to carry out a qualitative analysis of the crystal-optical properties of the pyrocrystals and of the crystal structure of anisotropic BN using the reflection spectra of pyrocrystals of the extreme compositions, i.e., purely rhombohedral and purely hexagonal, with three mutually orthogonal orientations of the **k**, **E**, and **C** vectors: 1) $\mathbf{E} \perp \mathbf{C}$, $\mathbf{k} \parallel \mathbf{C}$, 2) $\mathbf{E} \perp \mathbf{C}$, $\mathbf{k} \perp \mathbf{C}$, 3) $\mathbf{E} \parallel \mathbf{C}$, $\mathbf{k} \perp \mathbf{C}$ (Fig. 1). The reflection spectra $R(\nu)$ shown in Fig. 1 reveal two characteristic lattice reflection bands: a high-frequency one at frequencies about 1500 cm^{-1}, and a low-frequency one at frequencies about 800 cm^{-1}. An intense high-frequency reflection band is observed at the polarization $\mathbf{E} \perp \mathbf{C}$ (Figs. 1a and 1b) both in the rhombohedral phase and in somewhat weakened form in the hexagonal phase, and is due to the strong bonds of the B and N ions in the hexagons. However, in the hexagonal phase for the given polarization a small reflection peak also shows up in the above-mentioned low-frequency region. The character of the spectra remains mostly unchanged as the orientation of the **k** vector is varied relative to the **C** axis, but the shape and amplitude of the observed oscillators undergo some changes. For the polarization $\mathbf{E} \parallel \mathbf{C}$, complete extinction of the high-frequency band, accompanied by a flare-up of an intense low-frequency band, is observed in the reflection spectrum of the rhombohedral phase (Fig. 1c). A qualitatively similar transformation is observed in the reflection spectrum of the hexagonal phase when the polarization is changed to $\mathbf{E} \parallel \mathbf{C}$, but the extinction of the high-frequency band and flare-up of the low-frequency band are incomplete. In addition, in the hexagonal phase the high-frequency band is described well by the two-oscillator model. In this case, the reflection peak corresponding to one of the oscillators (Fig. 1b) remains nearly constant when the polarization of the light is varied, both in intensity and in frequency (Fig. 1c). This peak is described well by the single-phonon dispersion relations; therefore, its identification by the authors of Ref. 4 as a two-phonon peak is in error.

The transmission spectra were investigated only for layers perpendicular to the **C** axis. Since the cleavages of the pyrocrystals had noticeable surface relief, in our studies of the transmission spectra we also used mechanically polished surfaces. To determine the absorption spectra in this case, we measured transmission spectra $T_{i,j}(\nu)$ of the sample as we successively shaved down its thickness $d_{i,j}$ from 150 to 5 μm, where the indices i and j are the steps of this process.

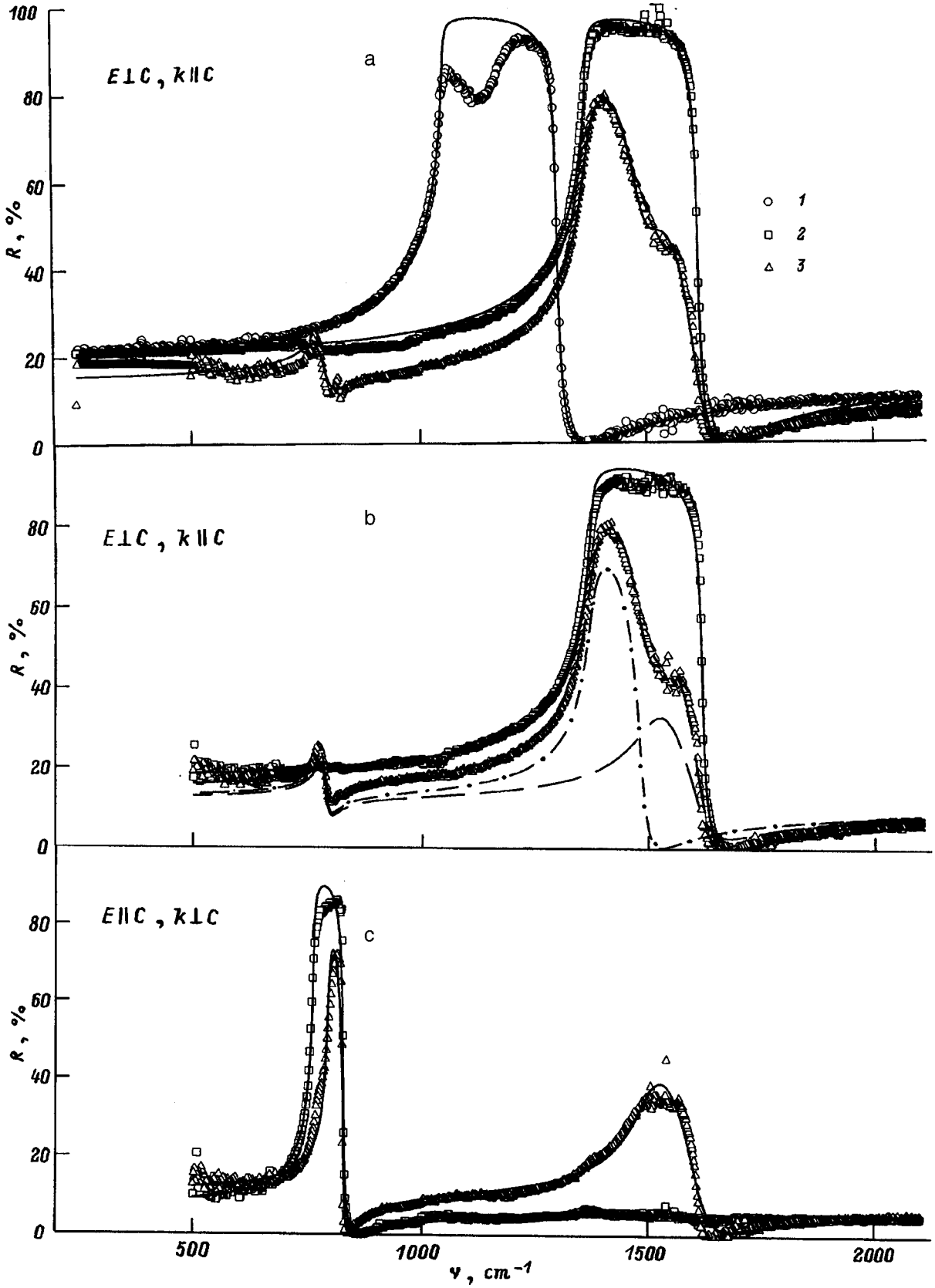

FIG. 1. Reflection spectra of the cubic (*1*), rhombohedral (*2*), and hexagonal (*3*) modifications of boron nitride for different polarizations and directions of propagation of the light. Points — experiment, solid lines — calculated spectra with all possible oscillators taken into account. b: dashed line — calculation of the reflection spectrum of a hexagonal crystal without allowance for the transverse oscillator; dot–dashed line — with allowance for the oscillator appearing in all polarizations.

The resulting absorption spectrum α was found from the simplified formula

$$\alpha(\nu)=\frac{1}{d_i-d_j}\log\frac{T_i(\nu)}{T_j(\nu)}, \tag{1}$$

which, for equivalent processing of the sample surfaces, is insensitive to the surface state of the sample but it strictly holds in the region of the absorption bands.

The absorption spectra recorded for the orientation $\mathbf{k}\|\mathbf{C}$, $\mathbf{E}\perp\mathbf{C}$ reveal a finer structure (Fig. 2). Upon going from the rhombohedral to the hexagonal pyrocrystal, the main absorption bands undergo a transformation in frequency and intensity similar to the transformation of the reflection spectra. The frequencies of the longitudinal and transverse phonons obtained by fitting the spectra calculated according to the dispersion relations are very close to the frequencies obtained from the reflection spectra. A number of absorption bands observed in the rhombohedral phase went beyond the framework of the phenomenological calculations. The weak absorption peaks at the frequencies $\nu_1=827\,\mathrm{cm}^{-1}$ and $\nu_2=753\,\mathrm{cm}^{-1}$, as can be seen from the reflection spectrum for orthogonal polarization, are due to parametric excitation of the longitudinal and transverse phonons polarized parallel to the **C** axis. In addition to the fundamental absorption bands, there are bands characteristic of multiphonon processe in the absorption spectra of the rhombohedral and hexagonal phases. The high-frequency doublet band in the frequency range 2800–2200 cm^{-1} probably corresponds to multiphonon sum processes, and the low-frequency band around 920 cm^{-1}, to multiphonon difference processes.

3. ANALYSIS OF THE INFRARED SPECTRAL FEATURES OF BN PYROCRYSTALS

The reflection spectra of BN pyrocrystals obtained and analyzed earlier in Ref. 4 are similar to the spectra we observed for purely hexagonal pyrocrystals (Fig. 1). The authors of Ref. 4 linked the spectral features of the weakly ordered hexagonal polycrystal with the normal modes of the BN crystalline lattice and, using a formal Kramers–Kronig procedure and a group-theoretic analysis, they attempted to determine to which lattice model of the hexagonal phase do the modes they introduced belong. Our infrared spectral studies show that the hexagonal pyrocrystals are characterized by a strong dependence of the shape of the lattice reflection and absorption bands on the microstructure formed by the crystallites—in first place, on the mutual misorientation angle of their hexagonal axes, which for purely hexagonal pyrocrystals is roughly 30°. It is therefore erroneous to assume that the lattice oscillators observed in pyrocrystals of the hexagonal phase for the orientations $\mathbf{E}\|\mathbf{C}$ and $\mathbf{E}\perp\mathbf{C}$ correspond uniquely to the normal vibrations of the crystalline lattice. To find the modes of the hexagonal phase from the given oscillators, a preliminary theoretical treatment, based on the models which account for crystal-optical effects in misoriented crystallites and phonon scattering at their boundaries, is needed. In particular, the polarization-independent, high-frequency reflection peak can be explained by reflection from crystallites whose hexagonal axis lies in the reflection plane, but forms an angle of roughly 30° with the normal to the reflection surface.[5] Such an analysis would, of course, contain many more uncertainties than an analysis of the lattice reflection of a single crystal. The production of large, highly ordered rhombohedral pyrocrystals of BN with deviation of the crystallographic axes of the crystallites from the **C** axis not greater than 1° and with linear dimensions of the crystallites more than two orders of magnitude greater than those of the hexagonal crystals enabled us to determine the normal modes of the rhombohedral phase directly from the experimentally observed lattice oscillators for polarization of the incident radiation parallel to the principal crystallographic axes (Fig. 1). The highly ordered texture of the rhombohedral pyrocrystal leads to hardly any loss of energy of the polarized radiation upon excitation of a selected mode, and this is manifested in the observation of only those oscillators that correspond to the modes with the prescribed polarization. Therefore, the high-frequency, weakly damped oscillator observed for $\mathbf{E}\perp\mathbf{C}$ corresponds to the longitudinal ($L_\perp$) and transverse ($T_\perp$) optical phonons polarized perpendicular to the **C** axis. Analogously, the lower-frequency oscillator observed for $\mathbf{E}\|\mathbf{C}$ corresponds to longitudinal ($L_\|$) and transverse ($T_\|$) optical phonons polarized parallel to the **C** axis. Since the oscillators are weakly damped, it is possible to first order to estimate the frequencies of the corresponding optical phonons from the real part of the dielectric constant $\varepsilon_1(\nu)$ (Ref. 6). Finding the extrema of the derivative of $R(\nu)$ in the region of the lattice oscillators, we obtain the desired frequencies for the rhombohedral phase (see Table I). A more rigorous method of determining the frequencies of the optical phonons involves a theoretical treatment of the experimental reflection spectra in the framework of the single-oscillator or many-oscillator model of the band of residual rays.

To determine the frequencies of the longitudinal and transverse phonons, we used the technique described in Ref. 7 for fitting the spectra calculated from the dispersion relations for the many-oscillator model of the band of residual rays to the experimentally measured spectra. Expressions for the dielectric constant and reflection and absorption coefficients were obtained from the zero-pole representation of the complex dielectric constant:

$$\varepsilon(\nu)=\varepsilon_1+i\varepsilon_2=\varepsilon_\infty+\sum_{j=1}^{N}\frac{f_j\nu_{Tj}^2}{\nu_{Tj}^2-\nu^2+i\nu\gamma_j\nu_{Tj}}, \tag{2}$$

$$f_j=\frac{\nu_{Lj}^2-\nu_{Tj}^2}{\nu_{Tj}^2}\prod_{j\neq k}^{N}\frac{\nu_{Lk}^2-\nu_{Tj}^2}{\nu_{Tk}^2-\nu_{Tj}^2}, \tag{3}$$

$$R=\left|\frac{\sqrt{\varepsilon}-1}{\sqrt{\varepsilon}+1}\right|^2, \tag{4}$$

$$\alpha=4\pi\nu\,\mathrm{Im}(\sqrt{\varepsilon}), \tag{5}$$

where $\varepsilon(\nu)$ is the complex dielectric constant, ε_∞ is the high-frequency dielectric constant, f_j is the jth oscillator, ν_{Tj} is its transverse frequency, ν_{Lj} is its longitudinal frequency, γ_j is its damping factor, and N is the number of oscillators in the band of residual rays.

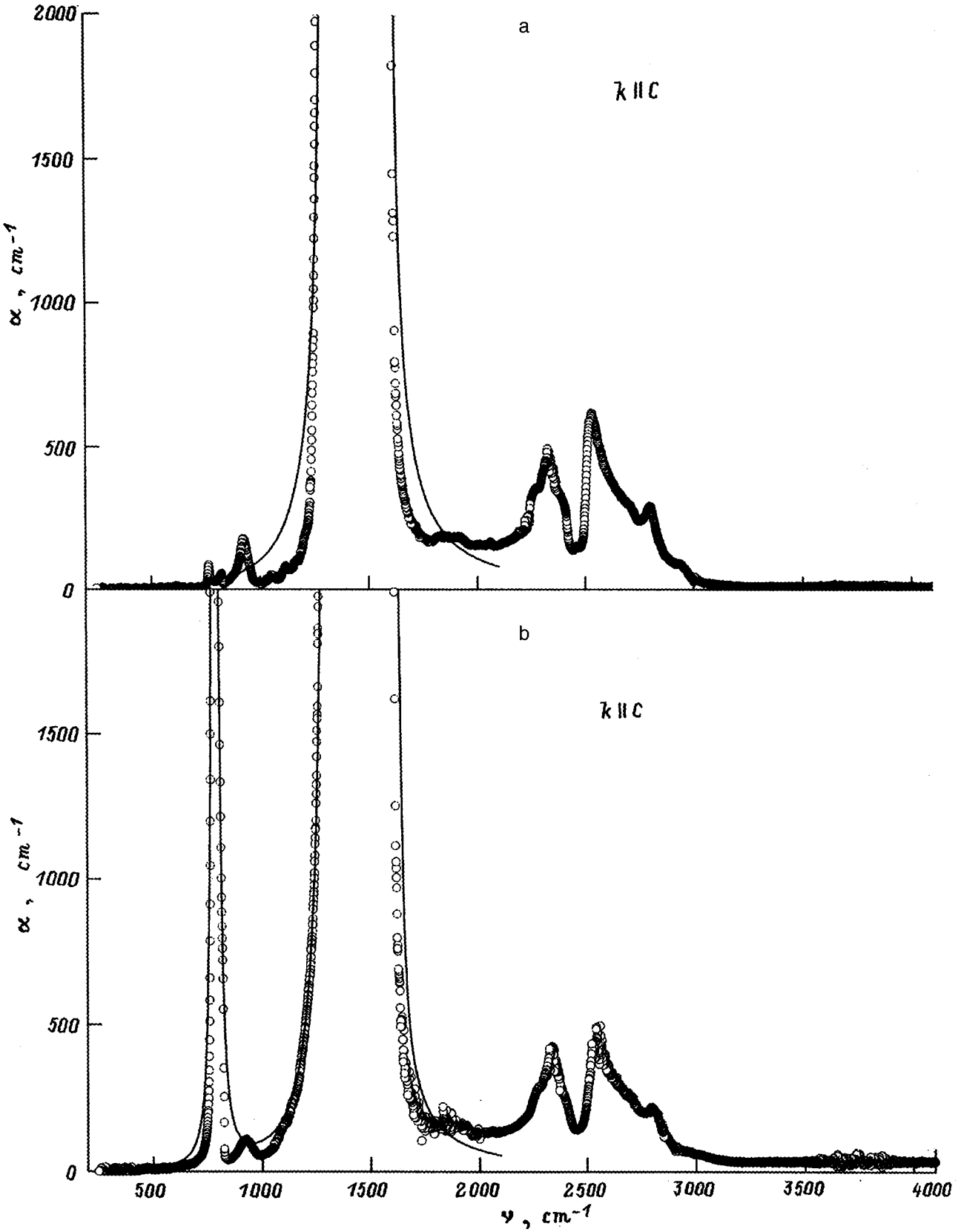

FIG. 2. Absorption spectra of rhombohedral (a) and hexagonal (b) boron nitride. Points — experiment, dashed lines — calculation.

TABLE I. Parameters of oscillators of boron nitride.

Structure	Orientation	Method of determination	ε_∞	$\nu_{T\perp}$, cm^{-1}	$\nu_{L\perp}$, cm^{-1}	$\gamma_\perp$	$\nu_{T\parallel}$, cm^{-1}	$\nu_{L\parallel}$, cm^{-1}	$\gamma_\parallel$	ν_{T3}, cm^{-1}	ν_{L3}, cm^{-1}	γ_3
cubic		$dR/d\nu$		1047	1306							
cubic		d/a R	4.6	1057	1306	0.0051						
rhomb		$dR/d\nu$		1365	1616		756	826				
rhomb	$\mathbf{k}\parallel\mathbf{C}$	$\alpha(\nu)$					753	827				
rhomb	$\mathbf{k}\parallel\mathbf{C}$	d/a R	5.2	1374	1617	0.0050						
rhomb	$\mathbf{k}\parallel\mathbf{C}$	d/a α	1.6	1355	1617	0.012						
rhomb	$\mathbf{E}\perp\mathbf{C}$	d/a R	4.3	1372	1617	0.0068						
rhomb	$\mathbf{E}\parallel\mathbf{C}$	d/a R	2.7				762	827	0.0057			
hex	$\mathbf{k}\parallel\mathbf{C}$	d/a R	3.8	779	794	0.063	1373	1487	0.023	1508	1615	0.068
hex	$\mathbf{k}\parallel\mathbf{C}$	d/a α	0.21	781	803	0.031	1321	1328	0.046	1338	1644	0.0030
hex	$\mathbf{E}\perp\mathbf{C}$	d/a R	3.7	780	790	0.033	1372	1487	0.021	1510	1616	0.067
hex	$\mathbf{E}\perp\mathbf{C}$	d/a R	3.2	795	829	0.0094				1498	1616	0.054

Note: d/a R — dispersion analysis of the reflection spectrum; d/a α — dispersion analysis of the absoprtion spectrum; cubic — cubic, rhomb —rhombohedral, hex — hexagonal.

The experimental spectra for the rhombohedral and cubic phases agree with the calculation for the single-oscillator model (see Figs. 1 and 2). The corresponding values of the frequencies and damping factors are listed in Table I. For the hexagonal phase it was possible to achieve better agreement between the theoretical and experimental spectra using the two- and three-oscillator models (Figs. 1 and 2). The com putation parameters for these models are also given in the table.

The high-frequency optical phonons polarized in the plane of the layer, $\nu_{L\perp}$ and $\nu_{T\perp}$, as has already been mentioned, can be uniquely associated with the vibrations of the ions at the intralayer bonds. The strength of the ionic–covalent bonds in the hexagons, ξ_h, determines the bond strength $\xi_\perp = 2\xi_h$ of the effective dipole which lies in the layer plane. It in turn determines the frequency of the transverse phonon polarized in the layer plane $\nu_{T\perp} = (2\xi_h/m^*)^{1/2}$, where $m^* = m_1 m_2/(m_1+m_2)$ is the reduced mass of the dipole, and m_1 and m_2 are the masses of the ions.[8] The ion charge q, the volume concentration of the dipoles lying in the layers, $n_\perp$, and the reduced mass m^* determine the oscillator strength and are thereby related to the frequency of the longitudinal optical phonon $\nu_{L\perp}$: $q^2(n_\perp)/\pi c^2 m^* = (\nu_{L\perp})^2 - (\nu_{T\perp})^2$. Calculations show that the values of the frequencies $\nu_{L\perp}$ and $\nu_{T\perp}$ obtained are not only in qualitative agreement with the BN lattice parameters, but can also be used to obtain quantitative estimates of some of them. No other reflection bands or intense absorption peaks for $\mathbf{E}\perp\mathbf{C}$ in the rhombohedral phase, except for those described, are observed down to 250 cm^{-1} (Figs. 1 and 2). Consequently, the frequency of the transverse mode, $\nu_{T\perp}$, is governed by short-range forces, and for quantitative calculations the implemented single-oscillator model is applicable. In particular, using the expression $q^2(n_\perp)/\pi c^2 m^*$, which determines the Coulomb splitting of the optical phonon frequencies and which is the square of the plasma frequency of the ions bound in the layer, $\nu^*_{p\perp}$, it is possible to determine the main parameters of the ion plasma in the layer.

The low-frequency optical phonons $\nu_{L\parallel}$ and $\nu_{T\parallel}$ are manifested in the rhombohedral phase in the reflection spectrum for the polarization $\mathbf{E}\parallel\mathbf{C}$ at the frequencies 826 and 756 cm^{-1} and in the absorption spectrum in the form of parametrically excited peaks for the orthogonal polarization $\mathbf{E}\perp\mathbf{C}$ at the frequencies 827 and 753 cm^{-1}, respectively. The disordered textures and growth of defects in the pyrocrystal as a result of the increase of the concentration of the hexagonal phase or as a result of introducing artificial defects into the crystal surface leads to a partial suppression of the reflection band in the frequency region under consideration for $\mathbf{E}\parallel\mathbf{C}$ and to a flare-up of the reflection band (Fig. 1) and the absorption band (Fig. 2) for $\mathbf{E}\perp\mathbf{C}$. Therefore, there is no basis for linking the oscillator observed in the given frequency region for $\mathbf{E}\parallel\mathbf{C}$ with lattice defects of the rhombohedral phase. The optical phonons observed for $\mathbf{E}\parallel\mathbf{C}$ are uniquely determined by normal lattice vibrations polarized along the **C** axis. Defects of the investigated rhombohedral pyrocrystals are manifested for $\mathbf{E}\parallel\mathbf{C}$ only in the large damping of the corresponding lattice oscillator and in the small divergence of the frequencies $\nu_{T\parallel}$ determined from an analysis of the reflection and absorption spectra, apparently due to the order-of-magnitude smaller linear dimension of the crystallites along the **C** axis. However, the high frequency of the observed transverse mode polarized along the **C** axis contradicts the previously held idea of a purely van der Waals interaction between the layers of hexagons. To elucidate the reasons for this contradiction requires an additional analysis of the lattice model of the rhombohedral phase, whose results are presented in the following section.

The positions of the principal reflection and absorption bands of the hexagonal phase correspond primarily to the frequencies of the normal vibrations in the rhombohedral phase (Figs. 1 and 2). However, the principal band corresponding to the polarization-selected crystallographic direction is somewhat suppressed. Here excitation of the orthogonal mode is observed for $\mathbf{E}\perp\mathbf{C}$ to a lesser degree, and for $\mathbf{E}\parallel\mathbf{C}$ to a greater degree. Noting that a substantial misorientation of the hexagonal axes of the crystallites of roughly 30° is observed in the hexagonal phase, the damping of the fundamental mode and excitation of the orthogonal mode can be linked with the crystal-optical effect defined by projections of the **E** vector onto the crystallographic directions of the

crystals.[5] Here mode mixing due to intercrystallite and intracrystallite phonon scattering cannot be ruled out.

4. ANALYSIS OF THE CRYSTAL STRUCTURE OF ANISOTROPIC BN

The model of the crystal structure of anisotropic BN contains as its main element flat layers formed by boron–nitrogen hexagons. Here the B and N atoms alternate in such a way that each B atom is surrounded in the layer by three N atoms, and vice versa. The side of the hexagon corresponding to the minimum interatomic distance has length 1.445 Å, which is roughly equal to the sum of the covalent radii of B and N (Ref. 9). It is thought that the symmetry of the atomic environment in the layer and the strength of the intralayer bonds are uniquely determined by sp^2 hybridized electrons on both the B atom and the N atom.

In the hexagonal modification of BN, the interplanar distance d_n is equal to 3.335 Å. In their model of the structure a number of authors place the atoms of neighboring layers exactly one on top of the other (Fig. 3a). The other view is that the hexagons of neighboring layers are shifted, one relative to the other, in such a way that three atoms of the shifted hexagon are located above the atoms of the underlying layer while three are located above the centers of the hexagons (Fig. 3b).[3,4,9] The third layer, for an analogous shift relative to the second layer, is located such that its atoms are found exactly above the atoms of the first layer. Since in the direction perpendicular to the layer, atoms of different elements are located on neighboring lattice sites, both lattice models of the hexagonal phase give the same period of translation along the **C** axis, equal to twice the interplanar distance, $2d_h$ (Figs. 3a and 3b).

For the above-described layer shift, three atoms of the second layer can be located above the six atoms of the hexagon in two different ways. If we alternate the shift rule, then we obtain a model of the crystal structure of the rhombohedral phase of BN with periodic translation equal to triple the interplanar distance $3d_r$ (Fig. 3c). The interplanar distance for the rhombohedral phase is 3.337 Å.

The large interplanar distances in the anisotropic modifications of BN, which exceed the interatomic distances in the layer by more than a factor of 2, were taken as an unambiguous indication of a purely van der Waals interaction of the dipoles of neighboring layers, although the lattice models themselves assign a specific arrangement to the atoms of neighboring layers.

As was already mentioned, the modes polarized along the **C** axis do not have high frequencies corresponding to weak van der Waals interactions.[10] Moreover, the frequency of the transverse mode $\nu_{T\parallel}$, polarized parallel to the **C** axis, is equal to 757 cm^{-1} for the rhombohedral phase and exceeds by almost a factor of 3 the frequency of the transverse vibrations in the purely ionic compound LiF $\nu_T = 285$ cm^{-1} (Ref. 11). This ionic compound is found in the same series as BN and its reduced ion mass m^* is 15% lower than that of BN. Thus, the bond strength of the dipoles parallel to the **C** axis in the rhombohedral phase of BN, $\zeta_\parallel = \nu_{T\parallel}^2 m^*$, exceeds even the strength of the bond created by the Coulomb interaction $\zeta_\parallel \simeq 8.5\zeta_{\mathrm{LiF}}$. Using the frequency of the transverse mode in the cubic modification of BN obtained from the reflection spectra, $\nu_{\perp \mathbf{C}} = 1047\,cm^{-1}$ $(dR/d\nu)$ or 1057 cm^{-1} (dispersion analysis) and noting the change in the atomic

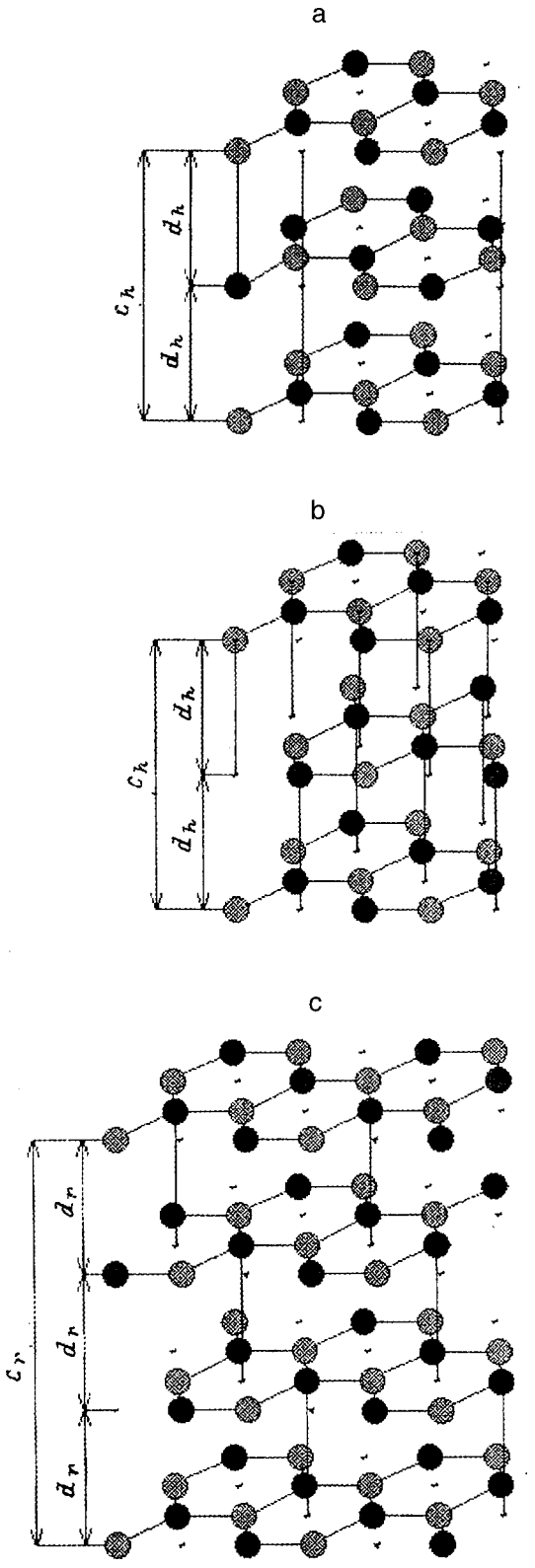

FIG. 3. Crystalline structure of boron nitride: a — hexagonal boron nitride, the variant without displacement of the centers of the hexagons; b — the same, but with displacement of the centers of the hexagons; c — rhombohedral boron nitride.

environment, we find that the decrease in the bond strength by about 10%, which occurs upon going from the anisotropic modification to the cubic, corresponds to an increase in the interatomic distance from 1.445 to 1.545 Å. Comparing in a similar way the strength of the intralayer and interlayer bonds in rhombohedral BN, we find that an increase in the interatomic distance by a factor of 2.3 corresponds to a decrease in the strength of the B–N bond by a factor of 1.6. Making even the mild assumption that this weakening of the bond depends only on the Coulomb interaction, we find that the given increase in the interatomic distance should correspond to a decrease in the bond strength by a factor of 12. Proceeding from the above-enumerated contradictions and an entire host of other contradictions arising in the model constructed from the x-ray diffraction data, we can assume that this model reflects only the main feature of the crystalline lattice of the rhombohedral phase, and takes only partial account of the effects of the interaction of the atoms of neighboring layers, but only indirectly, in terms of the mutual arrangement of the layers. If the given model lattice is sectioned by a plane that passes through the sides of the hexagons and the **C** axis (Fig. 4), then it can be seen that the arrangement of some of the atoms above the centers of the hexagons corresponds to two nonequivalent interatomic distances along the **C** axis. In this case, the B–N pairs formed from atoms of neighboring layers are staggered at a distance equal to triple the interplanar distance. Clearly, these pairs of neighboring atoms form dipoles which interact with the radiation that is polarized along the **C** axis. It is also clear that the Coulomb interaction of the ions of such an ion pair substantially exceeds their interaction with the ions of distant pairs. An account of the immediate intralayer environment of the ions of a given pair (Fig. 4) shows that the Coulomb interaction in a dipole is partly screened. As a result, the force of their mutual attraction is weakened by a factor of 4.4. Nevertheless, taking into account the high degree of ionicity of this compound,[12] it follows directly from the x-ray diffraction data that a Coulomb component is necessarily present in the interlayer interaction. However, as can be seen from the above estimates, the screened Coulomb interaction of such distant ions cannot be explained by the observed high frequencies of the vibrations and, consequently, the high strength of the interlayer dipole bonds $\zeta_{\parallel}$. On the other hand, the relatively high value of $\zeta_{\parallel}$ does not contradict the high anisotropy of the mechanical properties of the pyrocrystals since, first of all, $\zeta_{\parallel} \simeq \zeta_{\perp}/1.6$ and, secondly, the volume concentration of the interplanar bonds $n_{\parallel}$ is three times smaller than the concentration of the intralayer bounds $n_{\perp}$. In contrast, the existence of strong interlayer bonds explains the decrease in the anisotropy of the mechanical properties and the thermal conductivity of the pyrocrystals with increasing concentration of the highly ordered rhombohedral phase[1] and the fact of the existence of this highly ordered phase. However, these arguments and estimates fly in the face of the large values of Coulomb splitting of the frequencies of the optical phonons polarized along the **C** axis. It follows from the experiments that the ratio of squares of effective plasma frequencies for the dipoles lying in the layer $(\nu^*_{p\perp})^2$ and the interlayer dipoles $(\nu^*_{p\parallel})^2$ is ~ 6.85. At the same time, the above estimates, together with the fact that the same ion charge enters into the effective plasma frequencies, yield the value ~ 12. The contradiction in the rhombohedral model between the experimentally observed high frequency of the transverse interlayer vibrations and the model-derived high plasma frequency for the interlayer dipoles is removed if we assume that the ions in the interlayer dipoles are displaced from the layers toward each other. This assumption completely explains the increase in the Coulomb contribution to the interlayer interaction due to a decrease in the screening of the ions of the interlayer dipoles and provides the conditions necessary for the appearance between the displaced ions of a covalent bond, which can only correspond to the observed high strength of the interlayer bonds. The existence of interlayer ionic–covalent bonds also explains the high electron density in the interlayer space revealed by the x-ray diffraction data. The suggested displacement of the ions from the layers in the framework of the implemented model alternates in direction within the layer (Fig. 4); therefore, x-ray structural analysis methods are insensitive to the resulting nonplanarity of the hexagons and splitting of the monatomic planes. To directly observe the displacements of the atoms, high-resolution transillumination electron microscopy is needed.

The proposed refinement of the lattice model naturally raises the following question: What kind of orbitals give rise to ionic–covalent bonds between the atoms in the lattice? A comparative analysis of the frequencies of the normal vibrations in the rhombohedral and cubic modifications leads us to the qualitative conclusion that the interlayer covalent bonds arise becaause of sp hybridized electrons. Since the strength of the interlayer bonds is roughly 1.5 times lower than the strength of the bonds in the cubic phase, the interlayer bonds do not correspond to sp^3 hybridized orbitals. This is also indicated by the higher strength of the intralayer bonds (in comparison with the cubic phase), which in the framework of the refined model corresponds to sp^2 hybridized orbitals. The absence in the rhombohedral lattice of sp^3 hybridization indicates that the displacement of the ions from the layers is by less than 1/3 of a bond length, i.e., by less than 0.5 Å. Thus, the intralayer bond arises from somewhat distorted sp^2 hybridized orbitals. The assumed distance between the atoms in the interlayer dipole 2.8–2.9 Å is somewhat large for a covalent bond between B and N (we do not have any literature data on such a bond). However, since sp^2 hybridization is linked with excitation of atoms and since in boron nitride s^0 and p^0 states in the B atom remain unactivated while in the N atom in the analogous orbitals s^1 and p^1 electrons remain unactivated, and also noting the symmetry of the interlayer bond, it can be asserted that the strong dipole bond is created from unactivated electrons in linear asymmetric sp hybridized orbitals. Thus, analogous to the intralayer sp^2-sp^2 bonds, in the interlayer dipole an $sp-sp$ bond arises.

The interplanar ionic–covalent bonds detected in rhombohedral BN also substantially alter the picture of the hexagonal modification of BN. To analyze the hexagonal lattice, especially to obtain quantitative estimates, it is necessary, as was shown above, to take account of the influence of the

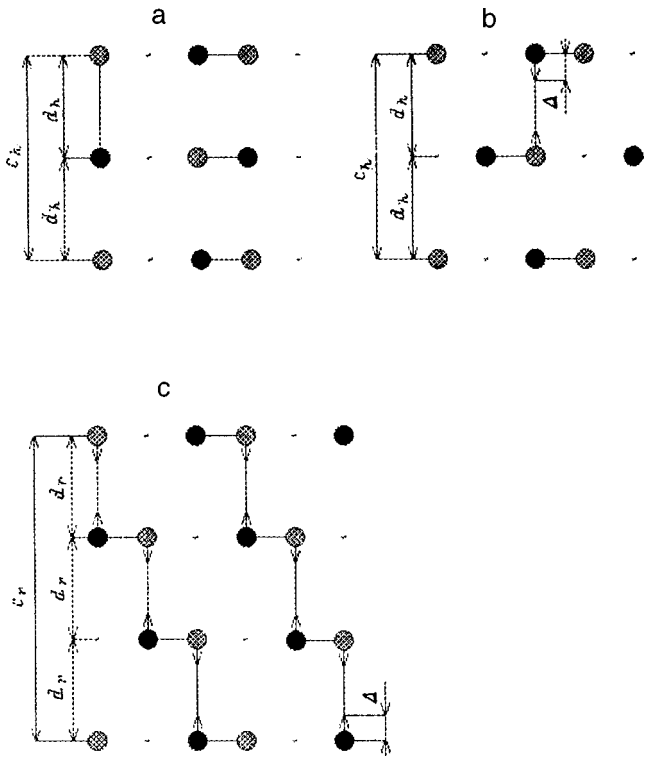

FIG. 4. Cross section of the crystal structure of hexagonal and rhombohedral boron nitride along the sides of the hexagons and along the **C** axis. The notation is the same as in Fig. 3. Δ — displacement of the ion.

microstructure. However, since in the case of the hexagonal lattice the dominant motif can be assumed to have been reliably established by x-ray diffraction studies while the interlayer bonds show up in the same frequency region as in the rhombohedral phase, distortions corresponding to interlayer bonds are probably present (Fig. 4b). From the section of the hexagonal lattice shown in Fig. 4 it can be seen that for displacements in the given lattice, in contrast to the rhombohedral lattice, there is no preferred direction. The direction of the displacements depends on the displacement of the neighboring atom, and not on the arrangement of the atoms. Therefore, during synthesis, as the temperature is lowered, formation of the first interlayer dipole is equally likely at any site; i.e., the probability for the appearance of a large concentration of nuclei of the hexagonal phase is high. This is probably also the reason for the large inhomogeneity, the small size of the crystallites, and the lower degree of ordering of the texture in the hexagonal phase. Thus, the disordering of the texture of the hexagonal pyrocrystals reflects the instability and imperfection of the crystalline lattice of the crystallites themselves.

[1] B. N. Sharupin, in *Chemical Gas-Phase Deposition of Refractory Inorganic Materials*, edited by V. S. Shpak and R. G. Avarbé (Leningrad, 1976).
[2] F. Bassani and G. P. Parravicini, *Electron States and Optical Transitions in Solids* (Nauka, Moscow, 1982).
[3] O. Madelung, *Physics of III–V Compounds* (Wiley, New York, 1964).
[4] R. Geick, C. H. Perry, and G. Rupprecht, Phys. Rev. **146**, 543 (1966).
[5] H. Poulet and J. P. Mathieu, *Vibrational Spectra and Symmetry of Crystals* (Gordon and Breach, Paris, 1970).
[6] G. N. Zhizhin, G. N. Mavrin, and V. F. Shabanov, *Vibrational Spectra of Crystals* (Nauka, Moscow, 1984).
[7] V. K. Zaĭtsev, S. V. Ordin, V. I. Tarasov, and M. I. Fedorov, Fiz. Tverd. Tela **21**, 2517 (1979) [Sov. Phys. Solid State **21**, 1454 (1979)].
[8] *Optical Properties of III–V Semiconductors* (Mir, Moscow, 1970).
[9] G. B. Bokiĭ, *Crystal Chemistry* (Nauka, Moscow, 1971).
[10] Yu. S. Barash, *van der Waals Forces* (Nauka, Moscow, 1988).
[11] *Handbook of Optics*, edited by W. G. Driscoll (McGraw-Hill Book Company, N.Y., 1974), p. 7–40, 41, 65, 9–100.
[12] J. P. Suchet, *Chemical Physics of Semiconductors* (Van Nostrand, New York, 1965).

Translated by Paul F. Schippnick

ELECTRONIC AND OPTICAL PROPERTIES OF SEMICONDUCTORS

Physical properties of $Cu_xAg_{1-x}In_5S_8$ single crystals and related surface-barrier structures

I. V. Bodnar' and E. A. Kudritskaya

Belorussian State University of Information Science and Radio Electronics, 220069 Minsk, Belarus

I. K. Polushina, V. Yu. Rud', and Yu. V. Rud'

A. F. Ioffe Physicotechnical Institute, Russian Academy of Sciences, 194021 St. Petersburg, Russia
(Submitted November 27, 1997; accepted for publication December 30, 1997)
Fiz. Tekh. Poluprovodn. **32**, 1043–1046 (September 1998)

The electrical properties and photoluminescence spectra of single crystals of the ternary compounds $CuIn_5S_8$, $AgIn_5S_8$ and their solid solutions have been investigated. We have determined the type of conductivity, the mobility, charge carrier concentrations and energies of the radiative transitions in these materials. We have fabricated surface-barrier structures from these single crystals and measured the voltaic photosensitivity.[S1063-7826(98)00409-8]

INTRODUCTION

The ternary semiconductor compounds $CuInS_2$ and $AgInS_2$ have been confirmed as materials suitable for use in high-efficiency thin-film converters and photodiodes of linearly polarized radiation.[1,2] The development of the fabrication technology of these compounds identified various phases in the systems $Cu_2S–In_2S_3$ and $Ag_2S–In_2S_3$, which can arise under certain fabrication conditions and whose formation and suppression must be controlled in order to obtain high-efficiency converters. In this regard, the need arises to study the fundamental properties of compounds such as $CuIn_5S_8$ and $AgIn_5S_8$ (Refs. 3–5). In the present paper we report the results of a study of some physical properties of the compounds $CuIn_5S_8$ and $AgIn_5S_8$, the solid solutions $Cu_xAg_{1-x}In_5S_8$, and surface-barrier structures based on these materials.

GROWTH OF SINGLE CRYSTALS

The indicated compounds and their solid solutions were synthesized by the two-temperature method. The bars obtained after synthesis were loaded into double quartz cells with a conical bottom. The evacuated cells was placed in a vertical two-zone furnace in which the single crystals were grown. The temperature in the melting zone was held at 1390–1420 K, and in the annealing zone, at 1100–1120 K. The cell with the melt was dragged through the crystallization front at a speed of 0.26–0.52 mm/h with a temperature gradient in the crystallization zone of 30–40 deg/cm. The single crystals grown in this way had diameter 12–14 mm and length ~ 50 mm.

X-RAY STUDIES

The composition and homogeneity of the crystals were determined with the help of microprobe x-ray spectral analysis. It was found that the composition of the $CuIn_5S_8$ and $AgIn_5S_8$ crystals and their solid solutions corresponds to the calculated composition within the limits of error of the method.

The structure and parameters of the crystal lattices of the indicated materials were determined by x-ray diffraction. The diffraction patterns were recorded with the help of a DRON-3M setup with Cu$K\alpha$ radiation and a nickel filter. These studies showed that both the ternary compounds $CuIn_5S_8$ and $AgIn_5S_8$ and their solid solutions $Cu_xAg_{1-x}In_5S_8$ crystallize in the spinel-type cubic structure. The resolution of the high-angle lines in the diffraction patterns indicates equilibration of the ternary compounds and homogeneity of the solid solutions. The unit cell parameters calculated using the least-squares method from the lines for which $2\theta > 60°$ are $a = 10.769$ Å for $CuIn_5S_8$ and $a = 10.825$ Å for $AgIn_5S_8$. The parameter a varies linearly as a function of the composition (x), in accordance with Végard's rule.

ELECTRICAL PROPERTIES OF THE SINGLE CRYSTALS

The electrical properties of the crystals were investigated in weak, constant electric and magnetic fields. The sample crystals had the shape of rectangular parallepipeds with dimensions $1 \times 2 \times 8$ mm^3. An ohmic contact was prepared using pure indium solder ($\sim 200\,°$C, time ~ 3 min). As the measurements showed (see Table I), all crystals of the solid solutions and the starting compounds $CuIn_5S_8$ and $AgIn_5S_8$ had n-type conductivity. The free electron concentrations n in these crystals encompass a wide range from 10^{14} to 10^{19} cm^{-3}. The measurements show that the value of n has no definite correlation with the composition of the solid solution, i.e., with x, and is more likely determined, according to Ref. 5, by the concentration of the dominant donor defects V_S. The Hall mobilities u are worthy of note, and are quite

TABLE I. Electrical and luminescence properties of $Cu_xAg_{1-x}In_5S_8$ single crystals.

	$T=300$ K		$T=77$ K		E_g, eV
x	n, cm^{-3}	u, $cm^2/(V\cdot s)$	$\hbar\omega_m$, eV	$\delta_{1/2}$, meV	Ref. 5
1.0	2×10^{16}	240	1.22 (inflection 1.35)	270	1.30
0.8	7×10^{14}	75	1.09	160	—
0.6	1×10^{18}	5	1.26 (inflection 1.35)	280	—
0.2	2×10^{17}	150	1.26 (inflection 1.35)	230	—
0.0	3×10^{19}	120	1.63	260	1.80

typical for diamond-like semiconductors (see Table I). Therefore, we may assume that in the spinel-type crystal structure conditions are also present for efficient charge-carrier transport. This conclusion is very important since it was previously assumed that a diamond-like structure is needed to realize semiconductor properties.[6,7] For the investigated crystals, as for ordinary III–V semiconductors and their analogs, we have found that growth of n is accompanied by a decrease in the Hall mobility of the electrons. This latter fact may be due to an increase in scattering by static lattice defects, whose role in samples of the given system is filled by vacancies in the sulfur sublattice V_S.

LUMINESCENCE MEASUREMENTS

Photoluminescence (PL), whose intensity fell rapidly with temperature, was observed in samples of the ternary compounds $CuIn_5S_8$ and $AgIn_5S_8$ and the solid solutions $Cu_xAg_{1-x}In_5S_8$ when excited by an argon laser (with power density $P\simeq0.8$ W/cm^2) at 77 K. Photoluminescence was recorded from freshly cleaved surfaces, from the illuminated side. The spectral dependence of the photoluminescence was closely reproduced when scanning different segments of the sample surfaces (diameter of the laser spot ~0.2 mm), which indicates good homogeneity in their radiative properties. The fact should also be emphasized that the photoluminescence intensity for continuous excitation did not reveal any degradation. Typical spectral curves of the photoluminescence are shown in Fig. 1, and quantitative parameters, position of the band maximum $\hbar\omega_m$, and full width at half-maximum (FWHM) $\delta_{1/2}$ are given in the table. It can be seen that the photoluminescence spectra, both for the starting compounds and for the solid solutions, are characterized by rather wide bands. Their FWHM values, $\delta_{1/2}$, suggest that the radiative transitions responsible for the photoluminescence band are non-elementary. Evidence for this conclusion is also provided by the circumstance that for some samples in the short-wavelength falloff another inflection, which is associated with changes in the recombination channels, is clearly resolved. The energy of the photoluminescence band maximum, as can be seen from the table, turned out to be less than the band gap E_g in all the samples for the starting compounds.[5] Therefore, there is reason to believe that photoluminescence in the investigated materials is associated with radiative transitions of nonequilibrium carriers to lattice

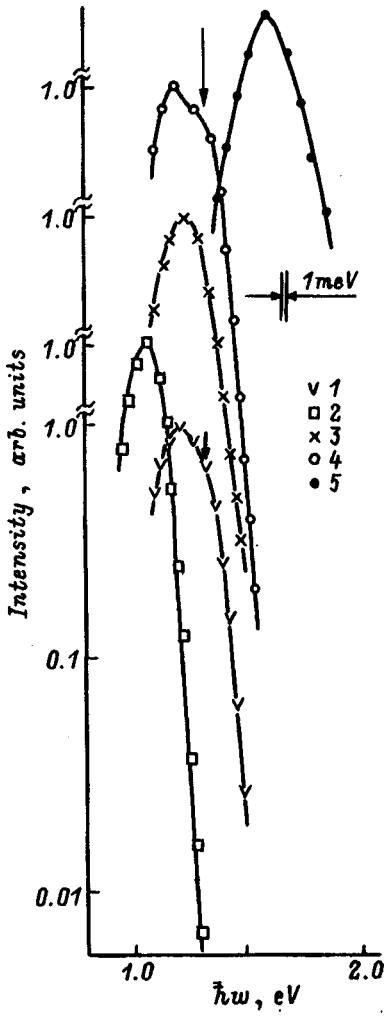

FIG. 1. Spectral dependence of the stationary photoluminescence of n-$Cu_xAg_{1-x}In_5S_8$ single crystals at $T=77$ K. x: *1* — 1.0, *2* — 0.8, *3* — 0.6, *4* — 0.2, *5* — 0.0. Arrows show inflection at 1.35 eV.

defect levels offset from one of the free bands by 0.08–0.17 eV. The results also show that $\hbar\omega_m$, like the electrical characteristics of the crystals, does not exhibit a smooth dependence on x. This most likely reflects the fact that for compositions $x<0.2$, recombination is due to one type of lattice defect, for which the energy level is insensitive to the ratio of copper and silver atoms in the solid phase, and these are most likely defects in the sulfur sublattice.

SURFACE-BARRIER STRUCTURES

We tried to create the first photosensitive structures based on crystals of this system. As our studies showed, photosensitive structures can be created by vacuum thermal deposition of pure indium onto a cleavage surface of the crystal without heating it during or after deposition. Such a contact is characterized by a rectification factor up to 10^2 for bias voltages up to 5 V. When illuminated it generates a photovoltage corresponding to positive polarity in the n-$Cu_xAg_{1-x}In_5S_8$ crystal.

In samples with $x=1$ and $x=0.8$ we prepared structures with maximum voltaic photosensitivity $S_u\simeq10^2$ V/W at 300 K. The sign of the photovoltage did not depend on either the

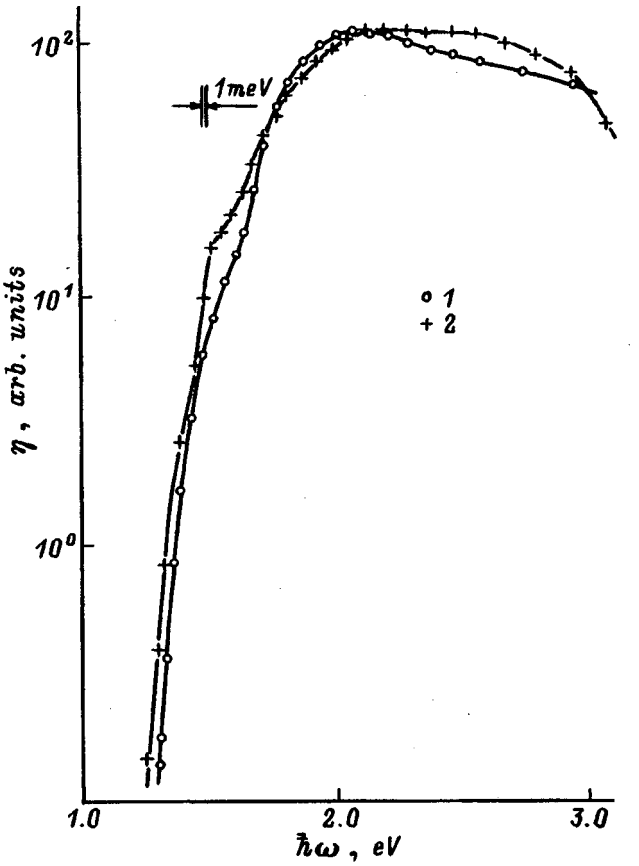

FIG. 2. Spectral dependence of the relative quantum efficiency of photoconversion of In/n-$Cu_xAg_{1-x}In_5S_8$ surface-barrier structures at $T=300$ K. The structures were irradiated by natural radiation along the normal to the surface from the side of the barrier contact. x: *1* — 1.0, *2* — 0.8. $\hbar\omega_m$, eV: *1* — 2.02: *2* — 2.15.

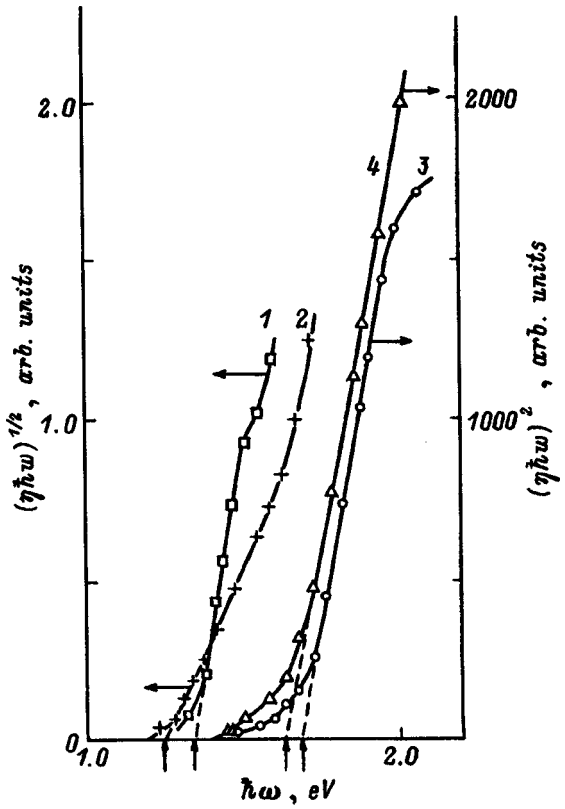

FIG. 3. Spectral dependence of the long-wavelength edge of the relative quantum efficiency of photoconversion of In/n-$Cu_xAg_{1-x}In_5S_8$ surface-barrier structures at $T=300$ K. x: *1, 3* — 1.0; *2, 4* — 0.8. The extrapolated intercepts of the energy axis (dashed lines, indicated by arrows) are 1.28, 1.34, 1.62, 1.68 eV.

position of the light probe or the energy of the incident photons, which indicates the absence, apart from the surface barrier, of other ''parasitic'' barrier structures. In this case the greatest photosensitivity is realized when the structures are illuminated from the side of the metal barrier layer. Typical examples of the spectral dependence of the relative quantum efficiency of photoconversion η under conditions generated by a weak signal, when the photoresponse is proportional to the incident light flux density, are shown in Fig. 2. In a structure based on the ternary compound (curve *1*), and a structure based on the solid solution (curve *2*) the photosensitivity spectrum, normalized to the number of incident photons, has a wideband character. The rapid growth of the photosensitivity in both structures begins at a photon energy $\hbar\omega>1.2$ eV. The spectral contours of the photosensitivity for barriers created on crystals of different compositions turned out to be similar. Maximum photosensitivity in them is attained at energies $\hbar\omega\simeq 2.0$ eV, which turns out to be higher than the band gap E_g of the starting compounds (see table). The high quantum efficiency of photoconversion deep in the fundamental absorption region indicates that the created energy barriers quite efficiently suppress the influence of surface recombination, which was manifested in the abrupt short-wavelength falloffs of the photoconductivity.[5] This circumstance indicates that such barriers on $Cu_xAg_{1-x}In_5S_8$ crystals can be used as wideband photoconverters of natural radiation in the energy range $\hbar\omega=1.8-2.7$ eV.

A plot of the long-wavelength photosensitivity edge of typical structures in the coordinates $(\eta\hbar\omega)^{1/2}$ — $\hbar\omega$ and $(\eta\hbar\omega)^2$ — $\hbar\omega$ is shown in Fig. 3. The results of this analysis are similar to those obtained for the optical absorption coefficients of the starting compounds $CuIn_5S_8$ and $AgIn_5S_8$ in Ref. 5. As can be seen from Fig. 3 (curves *1* and *2*), the experimental spectra $\eta(\hbar\omega)$ are straightened out in the coordinates $(\eta\hbar\omega)^{1/2}$ — $\hbar\omega$. This allows us to conclude that interband transitions in the ternary compound $CuIn_5S_8$ and in the solid solution (for the composition with $x=0.8$) are indirect, and the extrapolation $(\eta\hbar\omega)^{1/2}\rightarrow 0$ can be used to obtain the energies for the indirect optical transitions: 1.28 eV for $CuIn_5S_8$ and 1.34 eV for $Cu_{0.8}Ag_{0.2}In_5S_8$ at 300 K. The high-energy segment of the spectral dependence $\eta(\hbar\omega)$ is straightened out in the coordinates $(\eta\hbar\omega)^2$ — $\hbar\omega$, and an analogous extrapolation (curves *3* and *4*, Fig. 3) allows us to estimate the energies of the direct optical transitions for $CuIn_5S_8$ — 1.62 eV and $Cu_{0.8}Ag_{0.2}In_5S_8$ — 1.68 eV. The estimate of the energy of the interband transitions for the ternary compound $CuIn_5S_8$, which we obtained from photoelectric measurements, is in satisfactory agreement with the results of conventional analysis of the optical absorption coefficient,[5] but the observed discrepancy of these estimates

may be a consequence of deviations from stoichiometry. This latter point requires further study.

It is important to note that upon formation of the solid solutions the nature of the interband absorption remains the same as in the starting compounds.

[1] K. L. Chopra and S. R. Das, *Thin Film Solar Cells* (Plenum Press, New York, 1983).
[2] Yu. V. Rud' and Z. A. Parimbekov, Zh. Tekh. Fiz. **54**, 2253 (1984) [Sov. Phys. Tech. Phys. **29**, 1320 (1984)].
[3] M. Robbins and M. A. Miksovsky, Mater. Res. Bull. **6**, 359 (1971).
[4] C. Paorici, L. Zanotti, N. Romeo, G. Sberveglieri, and L. Tarricone, Mater. Res. Bull. **12**, 1207 (1977).
[5] A. Usujima, S. Takeuchi, S. Endo, and T. Trie, Jpn. J. Appl. Phys. **20**, 505 (1981).
[6] N. A. Goryunova, *Chemistry of Diamond-like Semiconductors* (Leningrad State Univ. Press, Leningrad, 1963).
[7] F. P. Kesamanly and Yu. V. Rud', Fiz. Tekh. Poluprovodn. **27**, 1761 (1993) [Semiconductors **27**, 969 (1993)].

Translated by Paul F. Schippnick

Optical reflection in $Pb_{0.78}Sn_{0.22}Te$ doped to 3 at.% with indium

A. N. Veĭs and S. A. Nemov

St. Petersburg State Technical University, 195251 St. Petersburg, Russia
(Submitted January 19, 1998; accepted for publication January 20, 1998)
Fiz. Tekh. Poluprovodn. **32**, 1047–1048 (September 1998)

The spectral dependence of the optical reflection of n-$(Pb_{0.78}Sn_{0.22})_{1-x}In_xTe$ ($x=0.02$ and 0.03) and p-$Pb_{0.78}Sn_{0.22}Te$ doped with 3 at.% In and 1.5 at.% Tl has been investigated at $T=300$ K. Minima associated with plasma vibrations of the free carriers were observed in all the experimental spectra. The electron density n and the hole density p were estimated by the Kukharskiĭ–Subashiev method. It is shown that the value of n so obtained is much smaller than its value obtained from the Hall effect only in n-$(Pb_{0.78}Sn_{0.22})_{0.97}In_{0.03}Te$ in which, as had been assumed previously, hopping conductivity dominates. This result may be viewed as an independent experimental confirmation of the unusual character of conduction in n-$(Pb_{0.78}Sn_{0.22})_{1-x}In_xTe$ solid solutions with high indium content. © *1998 American Institute of Physics.* [S1063-7826(98)00509-2]

As is well known,[1] the electrical and optical properties of PbTe and its solid solutions $Pb_{1-x}Sn_xTe$, doped with small amounts of indium at concentration levels $N_{im} \leqslant 1$ at. %, can be explained on the basis of the model of a quasilocal impurity level E_0 located near the bottom of the conduction band at 4.2 K. As the dopant concentration N_{im} is increased, the nature of the temperature dependence of the kinetic coefficients in PbTe:In and $Pb_{0.78}Sn_{0.22}Te$:In becomes markedly more complex.[2,3] To interpret the entire set of experimental data on transport phenomena obtained in PbTe and $Pb_{1-x}Sn_xTe$ with high indium content, we used the concept of hopping conductivity over the indium impurity states.

Despite the qualitative similarity of the properties of PbTe and $Pb_{1-x}Sn_xTe$ with high indium content, quantitatively they differ significantly. This difference shows up most clearly in the temperature dependence of the Hall coefficients R_H. A comparison of the data in Refs. 2 and 3 shows that in heavily doped samples, at the same indium concentrations and temperatures, the Hall electron concentrations n_H [$n_H=(eR_H)^{-1}$] in $(Pb_{0.78}Sn_{0.22})_{1-x}In_xTe$ turn out to be substantially higher than in $Pb_{1-x}In_xTe$. Moreover, in $(Pb_{0.78}Sn_{0.22})_{1-x}In_xTe$ for $x \geqslant 0.1$ the values of n_H turn out to be comparable to the indium concentration and even exceed it. This indicates that the Hall coefficient and its temperature dependence in $(Pb_{0.78}Sn_{0.22})_{1-x}In_xTe$ for high impurity content does not reflect the value of the electron concentration in the conduction band. Such a situation is possible under conditions of hopping conductivity.[4]

We therefore thought it worthwhile to carry out an independent experiment that would enable us to obtain additional information about the nature of the conductivity in such materials. The need to set up such an experiment stemmed from the fact that peculiarities of the temperature dependence of each of the kinetic coefficients examined in Refs. 2 and 3 can be explained in another, alternative way. It is possible to verify the assumption of a hopping conductivity mechanism enunciated in Refs. 2 and 3 if we determine the free current carrier concentration in some independent way.

In samples with a known dispersion law the indicated problem can be solved by examining the optical reflection spectra R in the region of the plasma minimum.[5] Therefore, in our study we examined the spectral dependence $R(\lambda)$ in $(Pb_{0.78}Sn_{0.22})_{1-x}In_xTe$ with n- and p-type conductivity. The experiments were performed at $T=300$ K. The indium concentration in the investigated samples did not exceed 3 at. %. For such low impurity concentrations, on the one hand, it is possible not to suspect the considerable influence the indium impurity has on the magnitudes of the principal parameters of the energy spectrum of $Pb_{1-x}Sn_xTe$. On the other, for $N_{im}=3$ at. % in $(Pb_{0.78}Sn_{0.22})_{1-x}In_xTe$ all of the peculiarities in the kinetic coefficients, which were thought to be linked with a manifestation of hopping conductivity, have already been observed.[3]

The samples investigated by us were prepared, as in Refs. 2 and 3, by the metalloceramic method and were subjected to a homogenizing anneal for 100 h at $T=650\,^{\circ}C$. As in Refs. 2 and 3, the indium concentration was determined from the amount of the stock material. In one of the investigated samples the donor action of indium was compensated for by introducing an acceptor impurity (thallium, 1.5 at. %).

The results of these experiments are plotted in Fig. 1. It is clear from the figure that plasma minima are observed in the optical reflection spectra $R(\lambda)$ of all the investigated samples, which shift toward shorter wavelengths with increasing Hall electron (n_H) and hole (p_H) concentrations. However, in the samples with electronic conductivity the shift of the plasma minimum with increasing n_H is small, despite the fact that the values of n_H in them differ by more than an order of magnitude ($1.27\times10^{18}cm^{-3}$ for $x=0.02$ and $1.7\times10^{19}\,cm^{-3}$ for $x=0.03$). This indicates that the free electron concentrations n in these samples are similar.

To estimate the free current carrier concentrations in the investigated samples, we calculated the optical reflection spectra $R(\lambda)$. We were thus able to determine the values of

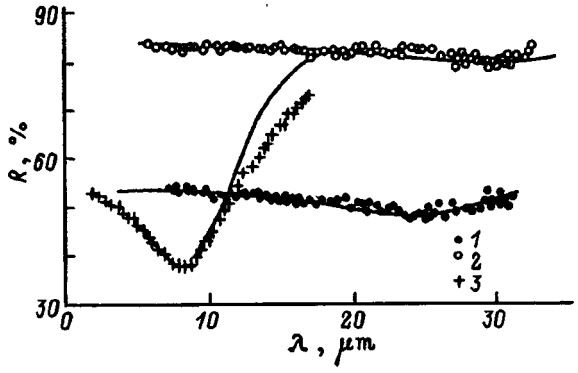

FIG. 1. Spectral dependence of the reflection coefficient R in n-$(Pb_{0.78}Sn_{0.22})_{1-x}In_xTe$ with n-type (*1,2*) and p-type conductivity (*3*) at $T=300$ K. x: *1, 3* — 0.03, *2* — 0.02. Hall concentrations of the electrons (holes) $n_H(p_H)\times10^{18}$, cm^{-3}: *1* — 17.0, *2* — 2.27, *3* — 102. Points — experiment; lines — calculation according to the method in Ref. 6. For sample 2 the R values are increased by 30%.

the high-frequency dielectric constant ε_∞ and the plasma frequency $\omega_p=(4\pi ne^2m_R^{-1}\varepsilon_\infty^{-1})^{1/2}$. The dependences $R(\lambda)$ were calculated using the method developed in Ref. 6. We also used a method proposed by the authors of Ref. 5 to estimate ε_∞ and ω_p. Note that the two methods for determining ε_∞ and ω_p yielded similar results. In particular, in the investigated samples ε_∞ turned out to be equal to 41.5 ±2.5, which corresponds to the available experimental data[7] for solid solutions with the composition $Pb_{0.8}Sn_{0.2}Te$.

For the conductivity effective mass m_R we adopted the value $m_R=0.05m_0$ (m_0 is the mass of the free electron). This value, which is the average for samples having free electron concentrations $n=(1-5)\times10^{18}$ cm^{-3}, was obtained in the framework of the Kane model from Eqs. (6.43) and (A.3) in Ref. 8. Here we used the effective mass at the bottom of the PbTe conduction band $m_{d0}^*=0.17m_0$ ($T=300$ K), which was determined in Ref. 9, and the extrapolation formula, from Ref. 10, for the band gap in $Pb_{1-x}Sn_xTe$

$$E_g(x,T)=171.5-535x+[12.8^2+0.19(T+20)^2]^{1/2}\ \text{meV}.$$

The calculated dependences $R(\lambda)$ are plotted in Fig. 1 by solid lines. It can be seen that we have a reasonably good agreement in a wide spectral interval between the experimental data and the calculated curves. We were thus able to determined ω_p and estimate n. It turns out that the free electron concentrations in n-$Pb_{0.78}Sn_{0.22}Te$:In are indeed close and are equal to $(1.3\pm0.2)\times10^{18}$ cm^{-3} for $x=0.02$ and $(2.4\pm0.3)\times10^{19}$ cm^{-3} for $x=0.03$. Note that the first of the above values of n agrees with n_H, whereas the second (for $x=0.03$) deviates sharply from the Hall data.

In material with p-type conductivity, a direct estimate of the free hole concentration is hindered since the parameters of n-$Pb_{0.78}Sn_{0.22}Te$ are not known with sufficient accuracy. Therefore, on the basis of the data obtained in n-$Pb_{0.78}Sn_{0.22}Te$:In we determined the value of m_R corresponding to the Hall hole concentration. It turns out that in the investigated sample the conductivity effective mass is equal to $(0.19\pm0.02)m_0$ and is found to be in reasonable agreement with the results of Refs. 7 and 11.

We note in conclusion that a noticeable discrepancy between the Hall electron concentration n_H and the free carrier concentration found from the optical reflection spectra $R(\lambda)$ is observed only in the sample in which the hopping conductivity mechanism was suspected to play a dominant role. This conclusion is consistent with Ref. 4. Therefore, the results obtained here constitute an independent confirmation of the ideas developed in Refs. 2 and 3 about the nature of the conductivity in PbTe and $Pb_{0.78}Sn_{0.22}Te$ with large indium content.

[1] V. I. Kaĭdanov and Yu. I. Ravich, Usp. Fiz. Nauk **145**, 51 (1985) [Sov. Phys. Usp. **28**, 31 (1985)].
[2] S. N. Lykov, Yu. I. Ravich, and I. A. Chernik, Fiz. Tekh. Poluprovodn. **11**, 1731 (1977) [Sov. Phys. Semicond. **11**, 1016 (1977)].
[3] S. A. Nemov, Yu. I. Ravich, A. V. Berezin, V. É. Gasumyants, M. K. Zhitinskaya, and V. I. Proshin, Fiz. Tekh. Poluprovodn. **27**, 303 (1993) [Semiconductors **27**, 19 (1993)].
[4] N. F. Mott and E. A. Davis, *Electronic Processes in Non-Crystalline Materials* (Clarendon Press, Oxford, 1971).
[5] T. S. Moss, T. D. F. Hawkins, and G. J. Burrell, J. Phys. C **1**, 1435 (1968).
[6] A. A. Kukharskiĭ and V. K. Subashiev, Fiz. Tverd. Tela (Leningrad) **8**, 753 (1966) [Sov. Phys. Solid State **8**, 603 (1966)].
[7] G. Dionne and J. C. Woolley, Phys. Rev. B **6**, 3898 (1972).
[8] Yu. I. Ravich, B. A. Efimova, and I. A. Smirnov, *Methods of Study of Semiconductors Applied to Lead Chalcogenides*: PbTe, PbSe, PbS (Nauka, Moscow, 1968).
[9] M. K. Zhitinskaya, V. I. Kaĭdanov, and I. A. Chernik, Fiz. Tverd. Tela (Leningrad) **8**, 296 (1966) [Sov. Phys. Solid State **8**, 195 (1966)].
[10] G. Nimtz and B. Schlicht, *Narrow Gap Lead Salts*, *Springer Tracts in Modern Physics* (Springer, 1983), Vol. 98.
[11] I. M. Nesmelova, N. S. Baryshev, Yu. S. Kharionovskiĭ, Zh. I. Akhmedova, and V. I. Kosheleva, Fiz. Tekh. Poluprovodn. **9**, 991 (1975) [Sov. Phys. Semicond. **9**, 650 (1975)].

Translated by Paul F. Schippnick

Electrical properties of silicon, heat-treated at 530 °C with subsequent electron bombardment

V. B. Neĭmash,[a] V. M. Siratskiĭ, A. N. Kraĭchinskiĭ, and E. A. Puzenko

Institute of Physics, Ukrainian Academy of Sciences, 252650 Kiev, Ukraine
(Submitted December 16, 1997; accepted February 17, 1998)
Fiz. Tekh. Poluprovodn. **32**, 1049–1053 (September 1998)

The effect of heat treatment at 530 °C and electron bombardment on the electrical parameters of silicon single crystals has been investigated by DLTS and by the Hall effect. The temperature 530 °C was found to correspond to the minimum efficiency of generation of oxygen-related thermal donors (OTD) in the temperature interval 500–600 °C. It is shown that thermal defects created at 530 °C (OTD-530) do not influence the formation of the main types of secondary radiation defects upon subsequent electron bombardment. It is found that the spectrum of OTD-530 levels is complex and that it depends on the duration of the heat treatment. The main characteristics of these levels were determined. An abnormally small cross section for capture of the electrons by the OTD-530 donors and the absence of any interaction between the OTD's and the primary radiation defects are explained in terms of screening of their interaction with the mobile charges as a result of the nonuniform spatial distribution of the OTD's. The local OTD concentration in the microinhomogeneities is estimated to lie in the range $10^{17}-10^{19}\,\mathrm{cm}^{-3}$. © *1998 American Institute of Physics.* [S1063-7826(98)00609-7]

INTRODUCTION

The effect of heat treatment on the properties of silicon has been studied extensively. The main results of these studies were reported in sufficient detail in two review articles (see Refs. 1 and 2). It was found, for instance, that the main reason for changes in most of the properties of crucible silicon for non-quenching forms of heat treatment is decomposition of supersaturated solid solutions of oxygen impurity (O_i) in silicon. As a result, a series of oxygen-containing defects which differ greatly in size, concentration, structure, and other properties, has been obtained. Special attention has been focused on the electrically active forms of the oxygen-containing defects, the so-called oxygen-containing thermal donors (OTD), which are most efficiently formed in the temperature intervals 350–500 and 600–800 °C. It most cases the OTD's are the cause of the inhomogeneity and thermal instability of the electrical parameters of silicon crystals. From the point of view of application, it is important to study OTD's in order to improve the fabrication technology of silicon-based devices.

Until now, there has been no unanimity of opinion about the structure and specific mechanism of formation of OTD's. One aspect of this problem is the question of similarities and differences between OTD's formed in the two temperature intervals indicated above (OTD-1 and OTD-2, respectively). In this context, a study of the properties of defects arising in silicon during heat treatment in the intermediate temperature interval 500–600 °C is of interest, as well as transitional forms of the thermal defects between OTD-1 and OTD-2. For heat treatments in this temperature range, intense formation of OTD's has not been noted, even though oxygen actively escapes from the dissolved state. For heat treatments at these temperatures many O_i defects formed during the decay process are electrically neutral, which substantially hinders their study. However, it is possible to obtain information about their properties by using electrical methods which examine the effect of the given defects on the accumulation of electrically active secondary radiation defects (RD).

OBJECTS AND METHODS OF STUDY

We used commercial silicon of grade KÉF-45 with the following initial parameters:[1)] the free electron concentration at 300 K $n_e=(7-8)\times10^{13}\,\mathrm{cm}^{-3}$, the concentration of the oxygen impurity in the interstitial state $N_O=(8-9)\times10^{17}\,\mathrm{cm}^{-3}$, the concentration of carbon in the implanted state $N_C<5\times10^{16}\,\mathrm{cm}^{-3}$. All samples were cut from a single crystal.

To generate thermal defects we performed a heat treatment in air with temperature stabilization to within 2 °C. Radiation defects were generated by bombardment with 3.5-MeV electrons at a current density of 0.2 μA/cm^2 in the flux range $10^{15}-10^{16}\,\mathrm{cm}^{-2}$ at room temperature. The accumulation of electrically active thermal and radiation defects was monitored by tracking the temperature dependence of the Hall effect and by deep-level transient spectroscopy (DLTS).

RESULTS AND DISCUSSION

In any study of transitional states of oxygen precipitates between the defect states OTD-1 and OTD-2, of particular interest are defects arising at temperatures at which OTD-1 defects are essentially no longer generated but OTD-2 defects are still formed only in small amounts. To determine such temperatures, we investigated the dependence on the heat-treatment temperature of the free-electron concentration increment at $T=300$ K, $\Delta n_{300}=n_i-n_0$ (n_0 is the electron concentration in the untreated silicon, and n_i is the electron

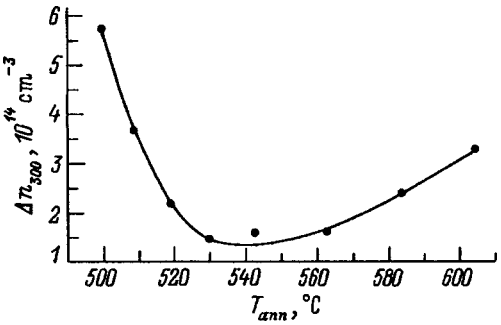

FIG. 1. Dependence of the concentration increment of the free electrons at $T=300$ K Δn_{300} on the isochronous heat-treatment temperature T_{ann}.

concentration in the heat-treated silicon) after a 5-hour heat treatment in the temperature interval 500–600 °C. The results shown in Fig. 1, are plots of the dependence of Δn_{300} on the isochronous heat-treatment temperature. It can be seen that the minimum of Δn_{300}, which corresponds to the minimum of the production rate of both types of OTD's, lies at $T=530$ °C. Next we studied samples heat-treated at this temperature.

Figure 2 plots the dependence of Δn on the duration of the heat treatment at 530 and at 450 °C. It can be seen that over the entire investigated time interval the generation rate at 530 °C of the OTD's responsible for Δn is almost an order of magnitude lower than the generation rate of OTD-1 defects at 530 °C in this same material.

The temperature dependence of the free electron concentration in the samples that had undergone heat treatment at 530 °C has a complex character and cannot be described by either a one- or two-level defect model. This may indicate the presence of several close-lying defect levels in the band gap. Hall-effect data enabled us to determine the effective ionization energy of the OTD's formed at 530 °C (E_i) from an analysis of the low-temperature part of the dependence $n(1/T)$. Results of this analysis are presented in Table I. It can be seen from the table that the ionization energy E_i decreases monotonically with increasing duration of heat treatment at 530 °C, which agrees with the results of Refs. 3 and 4.

TABLE I.

t_{ann}, h	E_i, meV
5	39
25	26
150	23
300	22

Much greater possibilities for monitoring the electrical characteristics of OTD's are presented by the method of deep-level transient spectroscopy (DLTS). Figures 3 and 4 show characteristic DLTS spectra for the same samples as were used in the measurement of the Hall effect. Three peaks can be distinguished in the DLTS spectrum of the samples heat-treated for 5 h at 530 °C (Fig. 3a). All three peaks correspond to exponential relaxation of the DLTS signal, including the low-temperature peak *1*, which is found in the temperature interval corresponding to recharging of phosphorus. The amplitude of peak *3* varies substantially from sample to sample in the same heat-treatment regime. In the samples heat-treated for 25 h (Fig. 3b) the peaks which were present in the preceding spectrum are preserved. At the same time, two new peaks (*4* and *5*) appear in the low-temperature

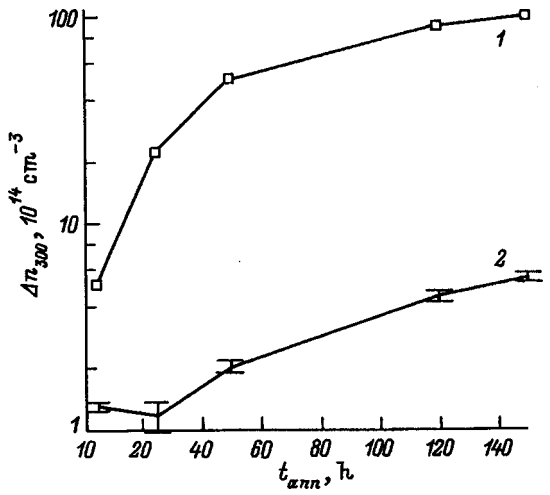

FIG. 2. Dependence of the concentration increment of the free electrons on the heat-treatment time, t_{ann}, for T_{ann}, °C: *1* — 450, *2* — 530.

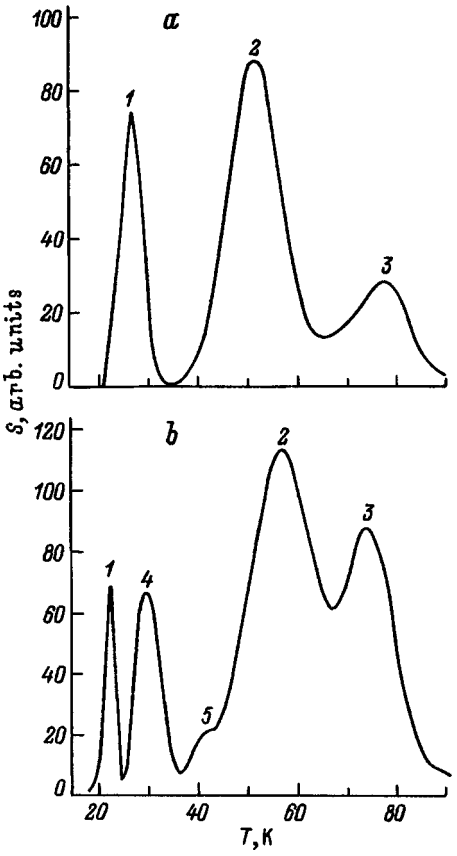

FIG. 3. Temperature dependence of the amplitude of the DLTS signal of a sample heat treated at 530 °C for t_{ann}, h: a — 5, b — 25.

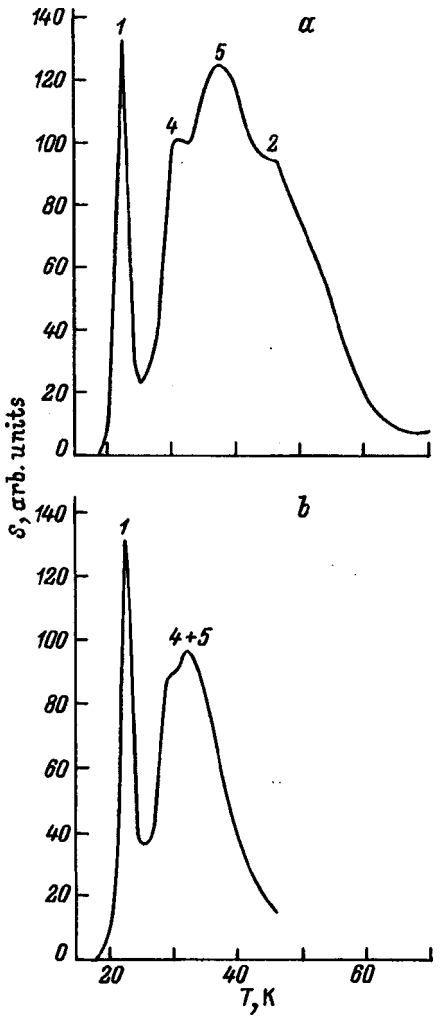

FIG. 4. Temperature dependence of the amplitude of the DLTS signal for a sample heat treated at 530 °C for t_{ann}, h: a — 150, b — 300.

part of the spectrum. Peak *1* acquires the pronounced triangular shape characteristic of a phosphorus peak. The amplitude of peak *3* again depends strongly on the choice of sample. Significant changes in the DLTS spectrum are observed after 150 h of heat treatment (Fig. 4a). Instead of separate peaks we see a new wide peak which is formed by the superposition of at least three separate peaks. Here the amplitude of peak *2* has decreased considerably with simultaneous increase of the amplitudes of peaks *4* and *5*. In comparison with the spectrum in Fig. 3b, this combined peak is shifted slightly toward the low-temperature region. Further transformation of the spectrum after 300 h of heat treatment is shown in Fig. 4b. This spectrum contains the phosphorus peak and the broadened peak, still further shifted toward the low-temperature region in comparison with Fig. 4a. The shift of the DLTS peak toward lower temperatures is evidence of a lower ionization energy of the center responsible for the appearance of this peak. From the shape of the peak in Fig. 4b it is difficult to determine the number of initial DLTS peaks from which it is formed. We can say that only the component corresponding to peak *2* in Fig. 3a has completely disappeared. As will be shown below, computer analysis can be used to describe the given spectrum by the superposition of two peaks. It should be noted that the significant fluctuation of the amplitude of peak *3* from sample to sample, and also the absence of any obvious correlation between its amplitude and the duration of the heat treatment do not allow us to identify this peak as corresponding to any OTD.

To determine the ionization energy and the cross section for capture of current carriers (σ) by centers corresponding to each specific peak of the DLTS, we used a special computer program for isolating overlapping peaks. Table II presents the results of this analysis of the above-mentioned experimental data using this program.

The results of these calculations may be considered as approximate for the ionization energies E_i and as merely rough estimates for the cross sections σ_i for the following reasons:

First, the relaxation of the DLTS signal corresponding to some of the peaks is nonexponential. Thus, in the case of phosphorus the nonexponential character is due to a significant relaxation of the conductivity. In the samples heat treated for 150 and 300 h, this renders any calculations of parameters of the given peak impossible since the OTD concentration is close to the concentration of the small impurity.

Second, the results of the analysis are possibly influenced by the Poole–Frenkel' effect since we are dealing here with shallow donor centers. However, comparison of Tables I and II reveals satisfactory agreement between the values of E_i determined by two different methods. This may be an indication of insignificant influence of the above-mentioned factors. Peak *1* in the DLTS spectra has the characteristic triangular shape and corresponds to the phosphorus impurity. Since we used capacitance instead of current spectroscopy, this peak is shown schematically. However, the possibility of observing it is a qualitative confirmation of the existence of levels with ionization energies $E_i < 0.044$ eV. It is characteristic that peaks *4* and *5*, and also peak *2* in Fig. 4a, which have ionization energies less than that of phosphorus, are observed at higher temperatures than the phosphorus peak. This is possible because the cross section σ for the capture of electrons by the centers corresponding to these peaks is several orders of magnitude smaller than the cross section for

TABLE II.

t_{ann}, h	E_1, eV	σ_1, cm^{-2}	E_2, eV	σ_2, cm^{-2}	E_3, eV	σ_3, cm^{-2}	E_4, eV	σ_4, cm^{-2}	E_5, eV	σ_5, cm^{-2}
5	0.042	3.3×10^{-12}	0.05	1.4×10^{-18}	0.083	8.9×10^{-18}	—	—	—	—
25	0.047	4.7×10^{-12}	0.058	6.2×10^{-18}	0.087	2.3×10^{-17}	0.033	8.9×10^{-17}	0.039	9.7×10^{-19}
150	—	—	0.03	3.7×10^{-20}	—	—	0.019	3.3×10^{-19}	0.022	5×10^{-20}
300	—	—	—	—	—	—	0.018	1.7×10^{-19}	0.019	3.5×10^{-20}

TABLE III.

N^*, cm^{-3}	σ, cm^{-2}
10^{17}	5×10^{-18}
10^{18}	6×10^{-19}
10^{19}	4×10^{-20}
10^{20}	3×10^{-21}

capture by phosphorus atoms.[5,6] Such values of σ are more characteristic of repulsive centers. One possible explanation for this result may be the strongly nonuniform spatial distribution of these centers. According to Ref. 7, the cross section for capture of electrons at a positively charged center can be represented in the form

$$\sigma = 4\pi r^3/3L, \tag{1}$$

where $r = e^2Z/4\pi\varepsilon\varepsilon_0 kT$ is the capture radius, eZ is the charge of the center, and L is a temperature-independent parameter. If the OTD's are found in clusters in which their local concentration is significantly higher than its volume average, then this can lead to screening of the charge of the defects, which affects their interaction with the mobile charges. Taking such screening into account (for $Z=1$), we can find r from the equation

$$e^2 \exp(-r/r_D)/4\pi\varepsilon\varepsilon_0 r = kT, \tag{2}$$

where r_D is the Debye screening length. We determined the capture radius r from relation (2) for temperatures corresponding to the peaks in the DLTS spectra and substituted them into expression (1). We obtained the following values of the capture cross section σ as a function of the local OTD concentration in the cluster (N^*); see Table III. From a comparison of the calculated (Table III) and experimental (Table II) data it can be seen that there is agreement for the local OTD concentration $N^* = 10^{17}-10^{19}\,cm^{-3}$, in agreement with the data obtained in Refs. 8 and 9.

Thus, heat treatment at 530 °C leads to the appearance in the silicon band gap of at least four new levels. Their number and concentration vary with duration of the heat treatment. Specifically, as the heat-treatment time is increased, the concentration of the deeper levels formed at the outset decreases all the way to complete disappearance with the simultaneous formation of shallower levels and growth of their concentration. This probably corresponds to a restructuring of the OTD's similar to that observed at 450 °C.[1,2] However, at 530 °C this restructuring is of a more pronounced nature.

To bring to light any possible bistability properties of the investigated defects (OTD-530), we investigated the dependence of the shape and amplitude of the DLTS spectra on the duration of the filling pulse and the conditions of cooling. However, over the entire range of durations of the heat treatments at 530 °C we did not detect any such influence.

To examine the effect of heat treatment on the generation of radiation defects in silicon, we subjected the same samples (after a preliminary heat treatment at 530 °C) to electron bombardment. We then again recorded DLTS spectra and the temperature dependence of the free electron concentration. After bombardment we recorded the levels of the two main secondary radiation defects (RD): the A center (E_c equal to 0.17 eV) and the E center (E_c equal to 0.44 eV). Analysis of the DLTS spectra showed that bombardment has no effect on the OTD parameters for any of the preliminary heat treatment times at 530 °C. In turn, the parameters of the radiation defects and their generation rate are independent of the duration of the preliminary heat treatment and coincide with the values in the control (untreated) samples. We obtained the following values of the generation rates of the A and E centers: $dN_A/d\Phi = (0.20\pm0.05)\ cm^{-1}$ and correspondingly $dN_E/d\Phi = (0.05\pm0.01)\ cm^{-1}$. The rates of removal of the current carriers, determined from Hall measurements at 300 and 100 K, also depend on the duration of the preliminary heat treatment times.

This result is analogous to the results of Ref. 10, which showed that defects of the types OTD-1 and OTD-2 are significantly less sensitive to the action of ionizing radiation than are chemical donors and have no effect on the accumulation of the main secondary radiation defects. These are not trivial results since they imply the absence of any interaction or an unusually weak interaction between a negatively charged (under typical experimental conditions) primary radiation vacancy and a positively charged OTD. Such an interaction in the case of chemical donors leads to the formation of an E center (a ''vacancy–donor'' complex). A possible explanation for this absence may be the situation in which most of the OTD-530 defects are concentrated in small, but very dense clusters.[3] Thus, if the condition $R \ll d \ll L$ is satisfied (R is the mean diameter of the clusters, L is the mean distance between them, and d is the mean free path of the vacancies), then the indicated effect can be attributed to the low probability of encountering vacancies (V) and OTD's in comparison with the probability for the capture of a vacancy at other sinks. An alternative explanation would be screening of the OTD's in microclusters, which would be capable of substantially weakening the Coulomb interaction of the OTD's with the vacancies, by analogy with the explanation suggested above in the interpretation of the cross sections for capture of electrons by the OTD-530 defects. However, in our case it is legitimate to speak of the role of screening only in a qualitative sense since the correlated distribution of the O_i atoms in the OTD microclusters and around them remains unaccounted for. The OTD microclusters are apparently always immersed in an ''atmosphere'' of O_i atoms, because they are the product of precipitation of O_i atoms in the initial microfluctuations of the O_i concentration — ''oxygen clouds'' (Ref. 11). This atmosphere may serve as an additional obstacle to penetration of the vacancies into the OTD microclusters and, consequently, to their interaction.

CONCLUSIONS

The results obtained by us lead us to the following conclusions.

1. The minimum of the efficiency of generation of oxygen-containing thermal donors with respect to variation of the heat-treatment temperature T_{ann} was found to lie in the region $T_{ann} \simeq 530$ °C, which corresponds to the transition

from dominance of defects of the type OTD-1 (formed in the interval of heat-treatment temperatures $T_{ann}=350-500\,^{\circ}C$) to dominance of defects of the type OTD-2 ($T_{ann}=600-800\,^{\circ}C$). However, at the heat-treatment temperature $T_{ann}=530\,^{\circ}C$ generation of oxygen-containing thermal defects takes place at an initial rate of $\sim 2\times 10^{9}\ cm^{-3}\cdot s^{-1}$.

2. At $T_{ann}=530\,^{\circ}C$ at least four donor levels of the OTD-530 defects are formed in silicon, whose concentrations and ionization energies depend on the the heat treatment time. For heat-treatment times from 5 to 300 h the ionization energy of these OTD's varies from 0.05 to 0.018 eV. The concentration of OTD-530 for $t_{ann}=300$ h reaches $10^{15}\,cm^{-3}$; however, this is not its limiting value.

3. The cross section for cappture of electrons by OTD-530 defects is several orders of magnitude smaller than by a chemical donor (phosphorus). OTD-530 defects, in contrast to the phosphorus donor, do not lose their electrical activity when subjected to electron bombardment and do not influence the generation of secondary radiation defects. Both these factors may be an indication of a strongly nonuniform spatial distribution of the OTD-530 defects (i.e., of the existence of microfluctuations of the concentration of OTD's with local density on the order of $10^{17}-10^{19}\,cm^{-3}$), which leads to a significant weakening of the interaction of the OTD's with the mobile charges as a result of screening.

4. The electrically neutral forms of the second phase of oxygen, which occurs at 530 °C, do not have a strong effect on the kinetics of accumulation of the main vacancy-type secondary radiation defects.

We thank A. N. Kabaldin for helpful discussions of the results of this work.

[a)]Fax: 38-044-2651589; E-mail: neimash@elvisti.kiev.ua

[1)]The grade KÉF-45 is *n*-type silicon doped with phosphorus, having a resistivity of 45 Ω·cm.

[1] A. Bourett, in *Proceedings of the Thirteenth International Conference on Defects in Semiconductors*, 1985, edited by L. C. Kimerling and J. M. Parsey, Jr. Warendale (1985); Warendale Metallurgical Society AIME (1985), p. 192.
[2] P. Wagner and J. Hage, Appl. Phys. A **49**, 123 (1989).
[3] V. M. Babich, N. P. Baran, Yu. P. Dotsenko, L. T. Zotov, and V. B. Koval'chuk, Fiz. Tekh. Poluprovodn. **26**, 447 (1992) [Sov. Phys. Semicond. **26**, 436 (1992)].
[4] K. Schmalz and P. Gaworzewski, Phys. Status Solidi A **64**, 151 (1981).
[5] L. S. Berman and A. A. Lebedev, *Deep Levels Transient Spectroscopy in Semiconductors* [in Russian] (Nauka, Moscow, 1991).
[6] J. Bourgoin and M. Lanoo, *Point Defects in Semiconductors* (Springer-Verlag, New York, 1983).
[7] V. I. Abakumov, V. I. Perel', and I. N. Yasievich, Fiz. Tekh. Poluprovodn. **12**, 3 (1978) [Sov. Phys. Semicond. **12**, 1 (1978)].
[8] V. B. Neĭmash, T. R. Sagan, V. M. Tsmots', V. I. Shakhovtsov, V. L. Shindich, and V. S. Shtym, Ukr. Fiz. Zh. **37**, 437 (1992).
[9] A. N. Kabaldin, V. B. Neĭmash, V. M. Tsmots', A. V. Batunina, V. V. Voronkov, G. I. Voronkova, and V. P. Kalinushkin, Ukr. Fiz. Zh. **38**, 34 (1993).
[10] V. B. Neĭmash, T. R. Sagan, V. M. Tsmots', V. I. Shakhovtsov, and V. L. Shindich, Fiz. Tekh. Poluprovodn. **25**, 1857 (1991) [Sov. Phys. Semicond. **25**, 1117 (1991)].
[11] A. N. Kabaldin, V. B. Neĭmash, V. M. Tsmots', V. I. Shakhovtsov, and V. S. Shtym, Ukr. Fiz. Zh. **40**, 218 (1995).

Translated by Paul F. Schippnick

The effect of antisite defects on the band structure and dielectric function of $In_{1-x}Ga_xSb$ solid solutions

V. G. Deĭbuk and V. I. Studenets

Chernovytsy State University, 274012 Chernovytsy, Ukraine
(Submitted June 31, 1997; accepted for publication February 26, 1998)
Fiz. Tekh. Poluprovodn. **32**, 1054–1056 (September 1998)

A nonlocal empirical pseudopotential scheme that includes the spin-orbit interaction is used to calculate the electronic structure of $In_{1-x}Ga_xSb$ solid solutions. A modified virtual-crystal approximation is used to explain the nonlinear experimental dependence of the width of the band gap on composition. The computed band structure is then used to calculate the dispersion of the dielectric constant and compare it with experimental results. © *1998 American Institute of Physics.* [S1063-7826(98)00709-1]

Semiconductor $In_{1-x}Ga_xSb$ alloys are promising materials for optoelectronic devices in the near- infrared spectral region. In the design and analysis of such devices, optical properties are particularly important. Although thorough studies of the dielectric functions of GaSb and InSb have recently been published,[1–3] information about these same properties for their alloys is quite sketchy. Therefore, in this paper we propose to determine the dielectric function of these alloys, which is directly related to their fundamental optical characteristics, by starting from a correct calculation of the band structure.[1]

Let us write the single-electron pseudopotential Hamiltonian in the following form [using the Rydberg (Ry) as the unit of energy]:

$$H=-\nabla^2+V_p(\mathbf{r}), \tag{1}$$

where

$$V_p(\mathbf{r})=V(\mathbf{r})+\sum_t (E-E_t)|b_t\rangle\langle b_t|, \tag{2}$$

where $V(r)$ is the true crystal potential, and $|b_t\rangle$ is the wave function of the ground state with energy E_t. If we ignore the nonlocal behavior in the pseudopotential, we can write the Fourier transform of $V_p(\mathbf{r})$ as follows:

$$V_p(\mathbf{r})=\sum_{\mathbf{G}} V_L(\mathbf{G})e^{i\mathbf{G}\mathbf{r}}, \tag{3}$$

where

$$V_L(\mathbf{G})=\sum_{\alpha} S_\alpha(\mathbf{G})v_\alpha(\mathbf{G}), \tag{4}$$

and

$$S_\alpha(\mathbf{G})=\frac{1}{N_\alpha}\sum_j e^{-i\mathbf{G}\mathbf{R}_j^\alpha}, \tag{5}$$

where $\mathbf{G}$ is a vector of the reciprocal lattice, $v_\alpha(\mathbf{G})$ are atomic form factors; N_α is the number of atoms of type α, and $\mathbf{R}_j^\alpha$ determines the position of the jth atom of type α. For A^NB^{6-N} compounds with zincblende structure, these equations can be written in the form

$$V_L(\mathbf{G})=v^S(\mathbf{G})\cos\mathbf{G}\boldsymbol{\tau}+iv^A(\mathbf{G})\sin\mathbf{G}\boldsymbol{\tau}, \tag{6}$$

where

$$V^S(\mathbf{G})=[v_A(\mathbf{G})+v_B(\mathbf{G})]/2,$$
$$V^A(\mathbf{G})=[v_A(\mathbf{G})-v_B(\mathbf{G})]/2, \tag{7}$$

and $\boldsymbol{\tau}=(a/8)(1,1,1)$, where a is the lattice constant.

In the method of empirical pseudopotentials we consider only the first four values of v^S and v^A. Following Refs. 4 and 5, we write the nonlocal atomic correction in terms of the nonlocal ionic correction in the form

$$V_{NL}=(\mathbf{K},\mathbf{K}',E)=\frac{V_{NL}^{\text{ion}}(\mathbf{K},\mathbf{K}')}{\varepsilon(\mathbf{q})}, \tag{8}$$

where $q=|\mathbf{K}-\mathbf{K}'|$, $\varepsilon(\mathbf{q})$ is the local linear screening factor, and

$$V_{NL}^{\text{ion}}(\mathbf{K},\mathbf{K}')=-\sum_{l=0,2} A_l(E)f(\mathbf{r})\,\hat{P}_l\,. \tag{9}$$

Here $A_l(E)$ is a fitting parameter with dimensions of energy that depends on the depth of the potential well, $\hat{P}_l$ is a projection operator for the lth component of angular momentum, and

$$f(\mathbf{r})=\begin{cases}1, & \mathbf{r}>\mathbf{R}_l\,,\\ 0, & \mathbf{r}\geqslant\mathbf{R}_l\,.\end{cases} \tag{10}$$

We can find the band structure by solving the secular equation

$$\det(\{\mathbf{k}^2-E_n(\mathbf{k})\}\delta_{\mathbf{G}\mathbf{G}'}\delta_{ss'}+\{V_L(\mathbf{G}-\mathbf{G}')+V_{NL}(\mathbf{K},\mathbf{K}',E)\}\delta_{ss'}+V_{so}^{ss'}(\mathbf{K},\mathbf{K}'))=0. \tag{11}$$

The spin-orbit term is

$$V_{so}^{ss'}(\mathbf{K},\mathbf{K}')=\mathbf{K}\times\mathbf{K}'\sigma_{ss'}\{-i\lambda^S\cos(\mathbf{K}-\mathbf{K}')\boldsymbol{\tau}+\lambda^A\sin(\mathbf{K}-\mathbf{K}')\boldsymbol{\tau}\}. \tag{12}$$

Here s and s' are spin states, σ_{ik} are Pauli matrices, and λ^A and λ^S are treated as fitting parameters.

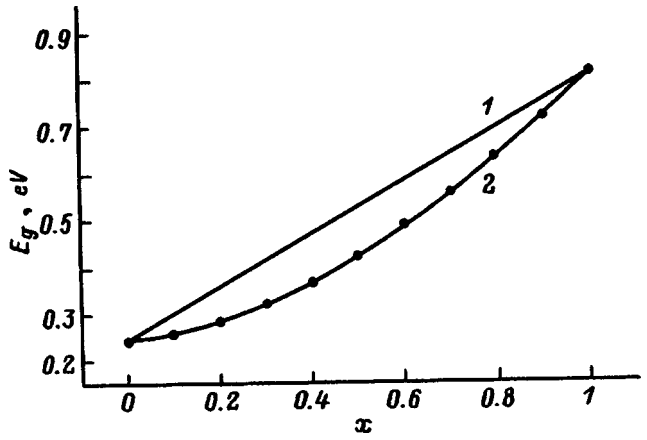

FIG. 1. Dependence of the width of the band gap on composition x for the solid solution $In_{1-x}Ga_xSb$. The solid curves are calculations: *1* — in the virtual-crystal approximation; *2* — in our modified model of the virtual crystal. The points are the experimental data of Ref. 7.

In the usual virtual-crystal approximation (VCA), the lattice constant and pseudopotential form factors of the solid solution $In_{1-x}Ga_xSb$ are defined by the following linear combinations:

$$a_{ss}=a_{\mathrm{GaSb}}x+a_{\mathrm{InSb}}(1-x),$$
$$V_{ss}=V_{\mathrm{GaSb}}x+V_{\mathrm{InSb}}(1-x), \tag{13}$$

where a_{ss} and V_{ss} are the lattice constant and form factors of the substitutional solid solution.

Equation (13) will hold if Ga atoms are substituted for In atoms or conversely. However, since the synthesis of the solid solution takes place under conditions far from thermodynamic equilibrium, these cation atoms can also occupy the positions of anion atoms in the lattice as well. Let us investigate how these antisite defects in the lattice affect the band structure of $In_{1-x}Ga_xSb$ in the modified virtual-crystal approximation.[6] In this approximation the form factor of atoms of the solid solution should depend on the probability for each type of atom to occupy some particular position. Then the symmetric form factors do not change, while the antisymmetric form factors have the form

$$V^a_{ss}=[1-8\alpha x(1-x)][V^a_{\mathrm{GaSb}}x+V^a_{\mathrm{InSb}}(1-x)]. \tag{14}$$

In deriving Eq. (14) we used the fact that the probability of an antisite defect depends quadratically on composition:

$$1-W_{\mathrm{In}}=1-W_{\mathrm{Ga}}=1-W_{\mathrm{As}}=4\alpha(1-x)x, \tag{15}$$

where α is a coefficient equal to the probability of forming an antisite defect when $x=0.5$. Because the degree of disorder in the solid solution at this composition is saturated, α corresponds to the maximum value of this probability.

The band structure was calculated numerically in high-symmetry directions of the Brillouin zone using a basis of 137 plane waves. For the limiting cases $x=1$ (GaSb) and $x=0$ (InSb), the calculated values of the energy at high-symmetry points was found to be in good agreement with known experimental data. Figure 1 shows that the dependence of the width of the band gap on the composition of the solid solution calculated in the VCA model and in the modified VCA model for $\alpha\approx 0.05$. The experimental data were taken from Ref. 7. Comparing these results, we see that these lattice defects lead to a considerable departure from linearity in the composition dependence of the band gap width for $In_{1-x}Ga_xSb$ alloys.

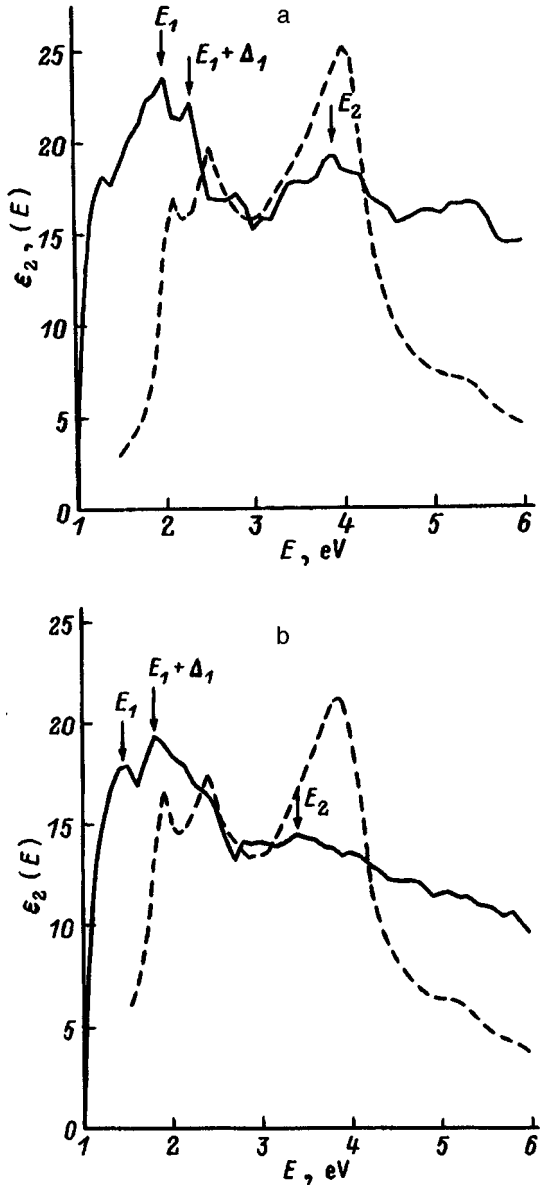

FIG. 2. Theoretical (solid curve) and experimental (dashed curve) spectra (see Ref. 2) of the dielectric function $\varepsilon_2(E)$ for GaSb (a) and InSb (b).

If we know the energy structure, we can investigate the frequency dependence of the dielectric function. The imaginary part of the dielectric function is calculated from the expression[5]

$$\varepsilon_2(\omega)=\frac{e^2\hbar}{\pi m}\sum_{n_cn_v}\int\frac{f_{n_cn_v}(\mathbf{k})dS}{E_{n_cn_v}(\mathbf{k})|\nabla_{\mathbf{k}}E_{n_cn_v}(\mathbf{k})|}, \tag{16}$$

where

$$E_{n_cn_v}(\mathbf{k})=E_{n_c}(\mathbf{k})-E_{n_v}(\mathbf{k}), \tag{17}$$

and

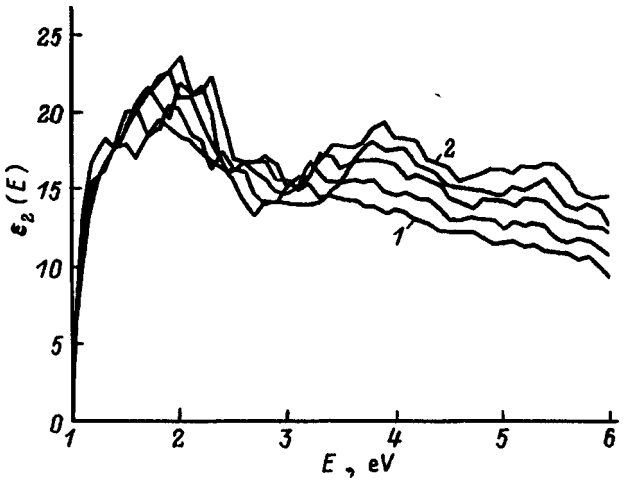

FIG. 3. Calculated spectra $\varepsilon_2(E)$ for $In_{1-x}Ga_xSb$ alloys: *1*—$x=0$, *2*—$x=1$. The quantity x changes in steps of $\Delta x=0.25$ between curves *1* and *2*.

$$f_{n_c n_v}(\mathbf{k})=\frac{\hbar^2}{m}\frac{|\langle n_c,\mathbf{k}|\nabla|n_v,\mathbf{k}\rangle|^2}{E_{n_c n_v}(\mathbf{k})} \tag{18}$$

is the interband oscillator strength. The sum runs over initial states in the valence band n_v and final states in the conduction band n_c, and S is a constant energy surface in k-space.

Figure 2 shows the calculated energy spectrum $\varepsilon_2(E)$, along with the corresponding experimental curves. The agreement between them is good for the most part. The most important discrepancy between the calculated and experimental data is the fact that the amplitude of the peak E_2 compared with peaks E_1 and $E_1+\Delta_1$ is too small. Because integration with a decreased energy step size from 0.05 to 0.02 eV does not change the fine structure in the curves shown in Figs. 2a and 2b, we can assume that the fine structure in these curves is determined primarily by the band structure and not the integration technique. The fact that the experimental peaks E_1, $E_1+\Delta_1$, and E_2 in the spectrum $\varepsilon_2(E)$ are somewhat smaller than the calculated ones is worth discussing. To explain it, we note that the pseudodielectric function would exactly equal the bulk dielectric function of the sample if the surface were infinitely sharp and free. However, it is well know[8] that high-quality surfaces are harder to prepare on semiconductor alloys than on binaries like GaSb and InSb. It is also known that microscopic roughness of the surface affects the dielectric function of semiconductors. In Fig. 3 we show calculated spectra $\varepsilon_2(E)$ for $In_{1-x}Ga_xSb$ alloys with a step $x=0.25$. The calculated $In_{1-x}Ga_xSb$ spectrum shifts toward higher energies with increasing x, in agreement with Ref. 8. The results of these calculations are in good agreement with the experimental data over the entire energy range.

[1] S. Zollner, M. Garriga, J. Humlicek, S. Gopalan, and M. Cardona, Phys. Rev. B **43**, 4349 (1991).
[2] D. E. Aspnes and A. A. Studna, Phys. Rev. B **27**, 985 (1983).
[3] J. R. Chelikowsky and M. L. Cohen, Phys. Rev. B **14**, 556 (1976).
[4] T. P. Humphreys and G. P. Srivastava, Phys. Status Solidi B **112**, 581 (1982).
[5] M. L. Cohen and V. Heine, Solid State Phys. **24**, 37 (1970).
[6] A. P. Dmitriev, N. V. Evlakhov, and A. S. Furman, Fiz. Tekh. Poluprovodn. **30**, 106 (1996) [Semiconductors **30**, 60 (1996)].
[7] D. Auvergne, J. Camassel, H. Mathieu, and A. Joullie, J. Phys. Chem. Solids **35**, 133 (1974).
[8] S. Imai and S. Adachi, Jpn. J. Appl. Phys. **32**, 3860 (1993).

Translated by Frank J. Crowne

Pressure dependence of the dielectric and optical properties of wide-gap semiconductors

S. Yu. Davydov and S. K. Tikhonov

A. I. Ioffe Physicotechnical Institute, Russian Academy of Sciences, 194021 St. Petersburg, Russia
(Submitted November 22, 1996; accepted for publication March 4, 1998)
Fiz. Tekh. Poluprovodn. **32**, 1057–1059 (September 1998)

The Harrison bond-orbital model is used to derive expressions for the pressure dependence of the static dielectric constant ε_0 and rf dielectric constant ε_∞, and also the longitudinal $\omega_{\mathrm{LO}}(0)$ and transverse $\omega_{\mathrm{TO}}(0)$ optical frequencies of the wide-gap semiconductors 3C-SiC, BN, AlN, and GaN. © *1998 American Institute of Physics.* [S1063-7826(98)00809-6]

The dielectric and optical properties of silicon carbide and boron, aluminum, and gallium nitrides are of great interest for microelectronics applications.[1] In two recent papers (Refs. 2 and 3), we discussed the cubic modifications of these compounds in the framework of the Harrison bond-orbital model.[4] Because it is important to understand how these properties change under pressure, both from an applications and from a theoretical point of view, in this paper we investigate the dependence of the static (ε_0) and high-frequency (ε_∞) dielectric constants and optical frequencies $\omega_{\mathrm{TO}}(0)$ and $\omega_{\mathrm{LO}}(0)$ on pressure P.

We begin our discussion with the function $\partial\varepsilon_\infty/\partial P$, using the expression for ε_∞ we derived in Ref. 2. Using the definition of the bulk modulus B (Ref. 5), we can show that

$$\frac{\partial\varepsilon_\infty}{\partial P}=-\eta\frac{\varepsilon_\infty-1}{3B}, \tag{1}$$

where $\eta=2(1-3\alpha_p^2)$. Here α_p measures the degree of polar character of the compound.[2–4] Expressions for B were given in Refs. 3, 4, and 6.

The following relation holds between the static (ε_0) and rf (ε_∞) dielectric constants within the Harrison model:[2]

$$\frac{\varepsilon_0-1}{\varepsilon_\infty-1}=1+\vartheta, \tag{2}$$

where $\vartheta=\alpha_p^2(1+2\alpha_c^2)/2\alpha_c^4$, α_c is the covalency of the compound, and $\alpha_c^2+\alpha_p^2=1$. It follows from Eq. (2) that

$$\frac{\partial\varepsilon_0}{\partial P}=(\varepsilon_\infty-1)\frac{\partial\vartheta}{\partial P}+(1+\vartheta)\frac{\partial\varepsilon_\infty}{\partial P} \tag{3}$$

and

$$\frac{\partial\vartheta}{\partial P}=-\frac{2}{3B}\frac{\alpha_p^2}{\alpha_c^2}\left(3+2\frac{\alpha_p^2}{\alpha_c^2}\right). \tag{4}$$

Table I lists our calculated results for $\partial\varepsilon_\infty/\partial P$ and $\partial\varepsilon_0/\partial P$. The matrix elements were calculated using the correlated scheme of Harrison and tables of Fisher atomic terms.[7,8]

Unfortunately, we know of no experimental data on the pressure dependence of the dielectric characteristics of these materials. However, the first-principles calculation of the quantity $\partial\varepsilon_\infty/\partial P$ for 3C-SiC described in Ref. 9, which is based on the density functional formalism, gives (at low pressures) nearly the same result as our calculation. Table I indicates that the quantity $\partial\varepsilon_\infty/\partial P$ changes sign as the compounds become more ionic. This is connected with the sign change of the parameter η, which goes from positive to negative for $\alpha_p>1/\sqrt{3}\simeq0.58$. Now, the scale of the Phillips ionicity f_i (see Ref. 10) is related to the Harrison parameters by the relation[3]

$$f_i=1-\alpha_c^3, \tag{5}$$

where f_i^* is the boundary value of ionicity that separates $\partial\varepsilon_\infty/\partial P<0$ from $\partial\varepsilon_\infty/\partial P>0$. Using this fact, we find that $f_i^*=1-(2/3)^{3/2}\simeq0.46$, which corresponds exactly to compounds such as AlN and AlSb.

We now derive the pressure dependence of the phonon frequencies. Let us assume that the Lyddane–Sachs–Teller relation holds:[11]

$$\frac{\omega_{\mathrm{TO}}^2(0)}{\omega_{\mathrm{LO}}^2(0)}=\frac{\varepsilon_\infty}{\varepsilon_0} \tag{6}$$

even when an external pressure is applied to the crystal (which in any case is small). Using the expression we derived in Ref. 3 [Eq. (7)] for $\omega_{\mathrm{TO}}^2(0)$, we obtain

$$\frac{\partial\omega_{\mathrm{TO}}}{\partial P}=\frac{\omega_{\mathrm{TO}}}{3B}(2+3\alpha_p^2), \tag{7}$$

$$\frac{\partial\omega_{\mathrm{LO}}}{\partial P}=\frac{\omega_{\mathrm{TO}}}{2\sqrt{\varepsilon_0\varepsilon_\infty}}\left(\frac{\partial\varepsilon_0}{\partial P}-\frac{\varepsilon_0}{\varepsilon_\infty}\frac{\partial\varepsilon_\infty}{\partial P}\right)+\sqrt{\frac{\varepsilon_0}{\varepsilon_\infty}}\frac{\partial\omega_{\mathrm{TO}}}{\partial P}. \tag{8}$$

A series of calculations using these expressions gives the following values for 3C-SiC (in units of 10^{14} rad·s^{-1}·Mbar^{-1}): $\partial\omega_{\mathrm{TO}}/\partial P=0.77$, $\partial\omega_{\mathrm{LO}}/\partial P=0.74$. For the pressure dependence of the splitting between longitudinal and transverse optical frequencies $\Delta=\omega_{\mathrm{LO}}-\omega_{\mathrm{TO}}$ we obtain a very small negative value (which is contradicted by experiment in Ref. 12).[1)] Analysis shows that this difference is primarily due to the theory underestimating the ratio $\varepsilon_0/\varepsilon_\infty$ compared with experiment (see Table I). Therefore, we will use a different approach. We take the experimental values $B=2.46$ Mbar (from Ref. 3 and 6) and $\omega_{\mathrm{TO}}=1.43\times10^{14}$ rad·s^{-1}, $\omega_{\mathrm{LO}}=1.56\times10^{14}$ rad·s^{-1} (from Ref. 13) and the dielectric constant from Table I. The parameters η and ϑ are calculate as before, using the Harrison model. We thus we obtain $\partial\omega_{\mathrm{TO}}/\partial P=0.43\times10^{14}$ rad·s^{-1}·Mbar^{-1},

TABLE I. Dielectric characteristics of wide-gap semiconductors: initial parameters, calculation results and experimental data.

	d, Å	α_p	α_c	ε_0		ε_∞		$\partial\varepsilon_0/\partial P$, Mbar^{-1}	$\partial\varepsilon_\infty/\partial P$, Mbar^{-1}	$\partial e_T/\partial P$, Mbar^{-1}
				theory	experiment	theory	experiment			
SiC	1.88	0.26	0.97	6.36	9.7	5.83	6.5	−2.02	−1.45	−0.27
BN	1.57	0.34	0.94	5.83	—	5.02	4.5	−0.87	−0.48	−0.29
AlN	1.89	0.59	0.81	10.12	—	5.72	4.8	−6.51	0.14	−1.00
GaN	1.94	0.60	0.80	11.05	12.2	5.03	5.8	−6.9	0.26	−1.15

$\partial\omega_{\rm LO}/\partial P = 0.56\times 10^{14}$ rad·s^{-1}·Mbar^{-1}, which gives a value of 0.13×10^{14} rad·s^{-1}·Mbar^{-1} for $\partial\Delta/\partial P$. The calculations in Ref. 9 lead to nearly the same result. Analogous estimates of $\partial\varepsilon_0/\partial P$ and $\partial\varepsilon_\infty/\partial P$ give -1.65 and -1.19 Mbar^{-1} respectively, in fairly good agreement with the results given in Table I.

Unfortunately, we do not know of any experimental values of the elastic moduli and frequencies for the wide-gap nitrides. However, values of ε_0 and ε_∞ are known for gallium nitride. Using the value $B=0.93$ Mbar for the bulk compressibility obtained within the Keating–Harrison model,[14] we find the values -8.27 and $+0.28$ Mbar^{-1} for $\partial\varepsilon_0/\partial P$ and $\partial\varepsilon_\infty/\partial P$, respectively, in satisfactory agreement with the theoretical calculations. For the frequencies we obtain (in units of 10^{14} rad·s^{-1}·Mbar^{-1}): $\partial\omega_{\rm TO}/\partial P = 1.23$ and $\partial\omega_{\rm LO}/\partial P = 1.25$. For the splitting (in energy units) we have $\partial\Delta/\partial P \simeq 14$ cm^{-1}·Mbar^{-1}, which is approximately five times smaller than for 3C-SiC. This is logical because the value of the LO–TO splitting in the series of III–V and II–VI compounds decreases in general with increasing P.[12]

In deriving the expressions for the pressure dependence of $\Delta=\omega_{\rm LO}-\omega_{\rm TO}$ we used Eq. (6). However, the authors of Ref. 9 based their results on the relation

$$\omega_{\rm LO}^2-\omega_{\rm TO}^2=\frac{4\pi e_T^2 e^2}{M\Omega_0\varepsilon_\infty}, \tag{9}$$

which defines the Born transverse charge e_T (Ref. 4) (or Z^B in the notation of Ref. 9; M is twice the reduced mass, and Ω_0 is the volume occupied by one atom. For 3C-SiC the quantity e_T determined from Harrison's model[4] has the form

$$e_T = 4\alpha_p + \frac{8}{3}\alpha_p\alpha_c^2. \tag{10}$$

It is easy to show that

$$\frac{\partial e_T}{\partial P} = -\frac{8}{3B}\alpha_p\alpha_c^2\left(1+\frac{2}{3}\alpha_c^2-\frac{4}{3}\alpha_p^2\right). \tag{11}$$

The results of these calculations are given in Table I. The derivative $\partial e_T/\partial P$ is a negative quantity. According to the calculations of Ref. 9, the quantity $\partial Z^B/\partial P$ for SiC is close to our value (~ 0.5 Mbar^{-1}), but has the opposite sign. Not knowing any details from Ref. 9 makes it difficult for us to understanding the reason for this difference.

From the negative sign of the derivative $\partial e_T/\partial P$, it was concluded in Ref. 12 that Harrison's theory cannot be applied to silicon carbide. However, in their analysis of Eq. (9), from which they also derived the ''experimental'' dependence of e_T on P, the authors of this paper assumed that the high-frequency dielectric permittivity of 3C-SiC depends on pressure in exactly the same way as silicon and diamond. However, our work and calculations show[15] that this is not correct. Thus, we cannot rigorously associate the increase in the LO–TO splitting with an increase of the charge e_T. A situation is possible where e_T decreases with increasing P but ε_∞ decreases more rapidly. According to our data, this is exactly what happens.

In conclusion we note that the pressure dependence (5) of the Phillip's ionicity f_i has the form

$$\frac{\partial f_i}{\partial P} = -\frac{2}{B}\alpha_c^3\alpha_p^2. \tag{12}$$

With increasing pressure, the lattice constant decreases, the bond charge distribution becomes more symmetric, and the ionicity of the compound decreases. There is not enough evidence to expect the opposite case for IV–IV compounds, as the authors of Ref. 12 do.

This work was carried out with the partial support of Arizona University.

[1)] However, we must be careful in comparing with the data of Ref. 12, because the value of the bulk modulus that these authors used in their analysis of the experimental data is an average over data for silicon and diamond, equal to 3.22 Mbar,[3,6] rather than the true bulk modulus $B=2.46$ Mbar. This introduces an error in the frequencies and in their derivatives with respect to pressure.

[1] *Silicon Carbide and Related Materials*, in *Proceedings of the 5th Conference*, edited by M. G. Spencer *et al.* (Inst. Phys. Conf. Ser. **137**, Bristol and Philadelphia, 1993).
[2] S. Yu. Davydov and S. K. Tikhonov, Fiz. Tverd. Tela (St. Petersburg) **37**, 3044 (1995) [Phys. Solid State **37**, 1677 (1996)].
[3] S. Yu. Davydov and S. K. Tikhonov, Fiz. Tekh. Poluprovodn. **30**, 834 (1996) [Semiconductors **30**, 447 (1996)].
[4] W. A. Harrison, *Electronic Structure and Properties of Solids* [Mir, Moscow, 1983)], Vol. 1.
[5] L. D. Landau and E. M. Lifshitz, *Theory of Elasticity*, 3rd English ed. (Pergamon Press, Oxford, 1986; Nauka, Moscow, 1987).
[6] S. Yu. Davydov and S. K. Tikhonov, Fiz. Tekh. Poluprovodn. **30**, 968 (1996) [Semiconductors **30**, 514 (1996)].
[7] W. A. Harrison, Phys. Rev. B **24**, 5835 (1981).
[8] W. A. Harrison, Phys. Rev. B **27**, 3592 (1983).
[9] K. Karch, A. Zywietz, F. Bechstedt, P. Pavone, and D. Strauch, in *International Conference on Silicon Carbide and Related Materials–1995 (ICSCRM-95)*, Technical Digest (Kyoto, Japan, 1995) p. 87.
[10] J. C. Phillips, Rev. Mod. Phys. **42**, 317 (1970).
[11] C. Kittel, *Introduction to Solid-State Physics*, 5th ed. (Wiley, New York, 1976; Nauka, Moscow, 1978).
[12] D. Olego, M. Cardona, and P. Vogl, Phys. Rev. B **25**, 3978 (1982).

[13] W. J. Choyke, J. L. Jarnell, G. Dolling, and R. A. Cowley, Phys. Rev. **158**, 805 (1967).
[14] S. Yu. Davydov and S. K. Tikhonov, Fiz. Tekh. Poluprovodn. **30**, 1300 (1996) [Semiconductors **30**, 683 (1996)].
[15] H. Okumura, K. Ohta, K. Ando, W. W. Rühle, T. Nagamoto, and S. Yoshida, in *International Conference on Silicon and Related Materials–1995 (ICSCRM-95)*, Technical Digest (Kyoto, Japan, 1995), p. 419.

Translated by Frank J. Crowne

Optical properties of silicon-doped (100) GaAs layers grown by molecular-beam epitaxy

V. G. Mokerov, Yu. V. Fedorov, A. V. Guk, G. B. Galiev, V. A. Strakhov, and N. G. Yaremenko

Institute of Radio Engineering and Electronics, Russian Academy of Sciences, 113907 Moscow, Russia
(Submitted February 9, 1998; accepted for publication March 17, 1998)
Fiz. Tekh. Poluprovodn. **32**, 1060–1063 (September 1998)

The photoluminescence spectra of (100) GaAs layers, both undoped and doped with silicon, is investigated at $T=77$ K. It is found that along with the *B*-band, which corresponds to interband radiative recombination, the spectra of doped layers also exhibit a so-called Si-band located near $h\nu \simeq 1.4$ eV. In multilayer δ-doped structures, an additional band appears in the region $h\nu \simeq 1.47-1.48$ eV, which is called here the δ-band. The dependence of the energy positions, intensities, and shapes of these photoluminescence bands on the doping dose N_{Si}, laser excitation power, and temperature are investigated. It is shown that the Si-band is caused by optical transitions between the conduction band and a deep acceptor level (~ 100 meV) connected with Si atoms on As sites. It is also established that the dependences of the shape and intensity of the δ-band on temperature and photoluminescence excitation power are identical to the corresponding dependences for the *B*-band. The behavior of the δ-band in the photoluminescence spectra is viewed as evidence of quantum-well effects in the δ-doped structures. [S1063-7826(98)00909-0]

The amphoteric behavior of silicon as a doping impurity in gallium arsenide has attracted the unflagging interest of investigators of this material. It has been shown (see, e.g., Refs. 1–8) that the electrical activity of the incorporated silicon and the conductivity type depend strongly on the methods and regimes of growth of the epitaxial layers. Evidence for this conclusion is especially striking in molecular-beam epitaxy (MBE), where the mechanism that locates Si atoms at a given site of the GaAs crystal lattice is determined by the multiplicity of free chemical bonds and by kinetic phenomena at the growth surface.[2–8] It has been shown[2–5,7] that in MBE growth on (100) and (111) *B* planes, Si atoms behave essentially like donors, while on (111) *A* planes, depending on the growth conditions, they can behave either like acceptors or like donors.

One way to determine the nature of the electronic states connected with Si atoms in GaAs is by investigating photoluminescence (PL) spectra.[2–9] However, the optical properties of this material cannot always be interpreted unambiguously according to literature models. This applies with particular force when acceptor levels associated with Si atoms participate in optical transitions.

Our goal was to study optical transitions in the photon energy range from 1.3 to 1.6 eV for layers of GaAs with (100) orientation, doped either uniformly or δ-doped with silicon, by investigating PL spectra at various temperatures and excitation powers from the laser source.

EXPERIMENTAL PART

The layers we studied were grown by MBE in an MBE-32P Riber machine. As a substrate we used semi-insulating GaAs films with (100) orientation. The epitaxial growth took place at a substrate temperature T_s in the range 570°–610 °C, with arsenic-to-gallium flux ratios $P_{\mathrm{As}}/P_{\mathrm{Ga}}=15-20$, which corresponds to optimal conditions for creating structurally perfect and stoichiometric GaAs layers. This has been confirmed by measurements of the electron mobility μ_e of modulation-doped $N-$AlGaAs/GaAs heterostructures. In these structures, μ_e reaches its maximum $T=77$ K value [$\mu_e=1.7\times 10^5$ cm^2/(V·s)] when the flux ratios lie in this range; when they deviate to one side or another, the mobility decreases due to the generation of defects in stoichiometry.

Following growth of an undoped buffer layer (0.8 μm), uniformly doped layers 0.7–1.0/μm thick with dopant concentrations $n=10^{17}$, 2×10^{17}, 7×10^{17}, and 1×10^{18} cm^{-3} were grown at $T_s=610$ °C. The δ-doped structures, which were grown at $T_s=570$ °C, consisted of: an undoped buffer layer of thickness 0.8 μm, three δ-layers with $N_{\mathrm{Si}}=6\times 10^{12}$ cm^{-2} separated by distances of 300 Å, an undoped layer of GaAs with thickness 700 Å and 50 Å doped layer ($N=1.2\times 10^{18}$ cm^{-3}). The half-width of the doping profile of a single δ-layer measured by secondary ion mass spectrometry on an IMS4F machine in the highest resolution regime did not exceed 80 Å in thickness.

Measurements of the PL spectrum were made in the temperature range from 77 to 240 K in the range of photon energies from 1.3 to 1.6 eV. In order to excite the PL we used a Ar^+ laser with a wavelength $\lambda=514.5$ nm and a maximum power of 850 W/cm^2. The concentration and mobility of the current carriers in these samples were determined by measuring the Hall coefficient.

Figures 1–3 show PL spectra for undoped and doped samples measured at $T=77$ K. From the figures it is clear that for an undoped sample only one PL band is observed, called here the *B*-band, with a maximum at $h\nu=1.508$ eV corresponding to interband optical transitions in intrinsic GaAs. Its small width $h\Delta\nu=5$ meV is evidence of the high

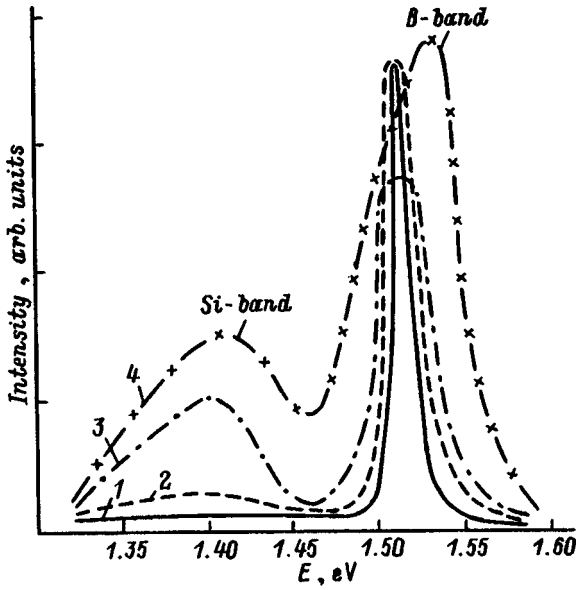

FIG. 1. PL spectra of undoped and doped (100) GaAs layers measured at a temperature $T=77$ K: *1*— undoped samples, *2, 3, 4*—uniformly doped samples with $n=2\times10^{16}$, 2×10^{17}, and 7×10^{17} cm^{-3}.

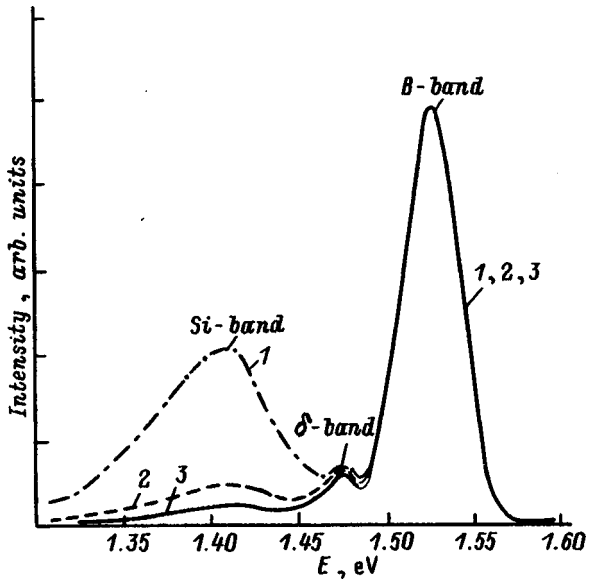

FIG. 3. PL spectra for a sample with three silicon δ-doped layers in (100) GaAs at $T=77$ K and at various excitation powers P, W/cm^2: *1* — 33, *2* — 340, *3* — 850 (the intensity of the *B*-band maximum is reduced to the same value for all the spectra).

quality of the layer as grown, and the absence of additional lines also indicates a low concentration of background impurities and defects in stoichiometry. Doping with silicon leads to an increase in the width of the *B*-band and a shift of its maximum towards higher energies.

In Si-doped layers, the *B*-band is accompanied by a PL band that for relatively low carrier concentrations ($n\simeq10^{17}$ cm^{-3}) is located near $h\nu\simeq1.4$ eV. Measurements of uniformly doped and δ-doped samples (see Figs. 1–3) show that this PL band appears only when the layers are doped with silicon, and is absent in undoped layers. Therefore, we call it here the Si-band. With increasing dopant dose, the Si-band also broadens, like the *B*-band, and its maximum shifts to larger $h\nu$. However, it is worth noting that under identical excitation conditions the PL intensity of the δ-band relative to the *B*-band always turns out to be smaller in δ-doped structures than it does in uniformly doped samples with the same average bulk concentration of silicon. In this case its low-energy edge is located at somewhat larger $h\nu$ in δ-doped structures than in uniformly doped layers.

Along with the *B*- and Si-bands, we observe an additional band in the PL spectra of δ-doped layers in the range $h\nu\simeq1.475-1.480$ eV (see Fig. 3), which we call here the δ-band. The intensity of this band increases with increasing dose of δ-dopant.

Figures 2 and 3 are plots of the PL spectra versus temperature and laser excitation power P for δ-doped structures. From Fig. 2 it is clear that the *B*-band becomes weaker with increasing temperature, and also broadens and shifts towards lower $h\nu$. As for the Si-band, it attenuates very rapidly with increasing temperature and virtually disappears at or above $T=150$ K. On the other hand, the behavior of the δ-band as the temperature varies is similar to that of the *B*-band.

From Fig. 3 it follows that increasing the laser excitation power P leads to growth in the intensity of all the PL bands; however, the rate of this growth is not the same for all of them. We observe that the rates are equal for the *B*-band and for the δ-band, and their spectral shapes and intensity ratios do not change with increasing P. On the other hand, the growth rate of the Si-band is at least an order of magnitude lower than for the other bands, which at high values of P leads to its weakening compared to the *B* and δ bands.

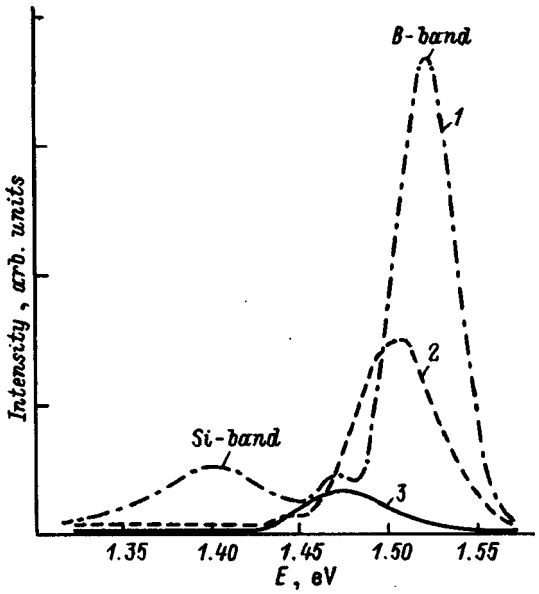

FIG. 2. PL spectra for a sample with three silicon δ-doped layers with $N_{Si}=6\times10^{12}$ cm^{-2} in (100) GaAs, measured at various temperatures T, K: *1* — 77, *2* — 150, *3* — 255.

DISCUSSION OF RESULTS

Let us begin with a discussion of the dependence of the PL spectra on concentration (or dose) of dopant N_{Si}. The increases we observed in the width of the *B*-band with in-

creasing N_{Si} and the shift of its maximum to higher energies $h\nu$ are caused by the donor-like behavior of a significant number of Si atoms and, as is well known, are manifestations of two effects:

— a decrease in the width of the band gap E_g due to merging of the band of donor states with the bottom of the conduction band, and

— an increase in the degree of occupation of the conduction band by electrons and, accordingly, an increase in the Fermi energy E_F.

Both these effects extend the spectral range for interband transitions towards small and large energies and, accordingly, broaden the *B*-band. The second effect, known as the Burstein-Moss effect, is responsible for the shift of the high-energy tail and the maximum of the *B*-band to larger $h\nu$.

As we already mentioned, analogous changes take place in the Si-band with increasing dopant dose N_{Si}. This provides direct proof that the initial states for optical transitions connected with the Si-band are also electrons in the conduction band rather than the donor level corresponding to an arsenic vacancy, as was assumed for the PL band near $h\nu = 1.37$ eV for GaAs layers with (111) *A*, (211) *A*, and (311) *A* orientations.[7,8] The final state for these optical transitions is probably an acceptor level located 100 meV above the top of the valence band. We assume that this deep level corresponds to acceptor behavior of some of the Si atoms, specifically those that occupy As sites in the GaAs lattice. We do not rule out the possibility that these Si atoms can also form certain complexes with defects in stoichiometry.

The temperature dependences of the PL spectrum, shown in Fig. 2 for the *B*-band, which match the regularities described in the literature for interband optical transitions quite well, are explained by the temperature-induced decrease in the width of the band gap E_g and an increase in the amount of nonradiative recombination due to electron-phonon interactions. On the other hand, the stronger attenuation of the Si-band and its disappearance at high temperatures can be logically explained by thermal ionization of holes from the acceptor level discussed here.

The considerable difference observed in the dependences of the PL intensity on laser excitation power for the *B*-band and the Si-band (Fig. 3) can be explained by the significant difference in the density of hole states that participate in these optical transitions. In the first case (the *B*-band), we are dealing with intrinsic optical transitions and, accordingly, with holes in the valence band, whose density exceeds by several orders of magnitude the concentration of holes in acceptor levels in the second case (the Si-band). Therefore, if the flux density of excitation photons is sufficiently large (comparable to or exceeding the concentration of Si atoms in acceptor states), the increase in the intensity of the Si- band should slow and then saturate, whereas the intensity of the *B* PL band should continue to increase.

The behavior of the δ-band, which is present in δ-doped structures, seems quite unusual when compared to the Si-band. Since this band is located above the Si-band in energy but below the *B*-band (i.e., for $h\nu < E_g$), it can be formally assigned to optical transitions with participation of one or several levels in the band gap that are shallower than the acceptor level of Si. However, in this case we would expect the band to attenuate even more strongly with temperature than the Si-band, and to see a more rapid saturation of the dependence of its intensity on PL excitation power. Instead, we find that the δ-band behaves exactly like the *B*-band with increasing temperature and PL excitation power. Hence, it should involve interband optical transitions, like the *B*-band. It is possible that the δ-band is due to the quantum-well effects in the narrow, *V*-shaped potential wells of δ-doped structures. In other words, it could be caused by radiative recombination of electrons in one of the two-dimensional quantum subbands of the *V*-shaped potential wells in the δ-layers with holes at maxima of the valence band between the δ-layers. It is possible that a number of other features of the intensity and shape of the Si-band in δ-doped structures that distinguish this band from its counterpart in uniformly doped layers are related to this effect.

CONCLUSIONS

Thus, our investigations of the PL structure of undoped and silicon-doped GaAs layers at $T = 77$ K show that, along with the *B*-band corresponding to interband radiative recombination, the spectra of the doped layers also contain a so-called Si-band which is located near $h\nu = 1.4$ eV for $N_{Si} \simeq 10^{17}$ cm^{-3}. Moreover, three-layer, δ-doped structures exhibit an additional band in the neighborhood of $h\nu \simeq 1.47-1.48$ eV, which we refer to here as the δ-band. By investigating the dependence of the PL spectrum on the dopant dose N_{Si}, the laser excitation power, and the temperature, we have established that the Si-band can be due to optical transitions between the conduction band and deep acceptor levels (~ 100 meV) connected with Si atoms on As sites. In contrast to the impurity-related Si-band, the dependence of the δ-band (which also appears at energies $h\nu < E_g$) on temperature and PL excitation power turns out to be identical to the corresponding dependences for the *B*-band. This prompts us to suggest that the δ-band, like the *B*-band, also may be due to interband optical transitions that are strongly modified due to the quantum-well effects in the multilayer δ-doped structures.

This work was carried out with the support of the Ministry of Science of the Russian Federation (the program ''Physics of Solid-State Nanostructures,'' Project 2-030/4).

[1] M. Kondo, C. Akayama, N. Okada, H. Sekiguchi, K. Domen, and T. Tanahashi, J. Appl. Phys. **76**, 914 (1994).
[2] S. S. Bose, B. Lee, and M. H. Stilman, J. Appl. Phys. **63**, 743 (1988).
[3] W. I. Wang, E. E. Mendez, T. S. Kuan, and L. Esaki, Appl. Phys. Lett. **47**, 826 (1985).
[4] A. Chin, P. Martin, P. Ho, J. Ballingall, Y. Yu, and J. Mazurowski, Appl. Phys. Lett. **59**, 1899 (1991).
[5] Y. Okano, H. Seto, H. Katakama, S. Sichine, I. Fujimoto, and J. Suzuki, Jpn. J. Appl. Phys. **28**, 151 (1989).
[6] S. Subbana, H. Kroemer, and J. Merz, J. Appl. Phys. **59**, 488 (1986).
[7] F. Piazza, L. Pavesi, M. Henini, and D. Johnston, Semicond. Sci. Technol. **7**, 1504 (1992).
[8] L. Pavesi, M. Henini, and D. Johnston, Appl. Phys. Lett. **66**, 2846 (1995).
[9] I. C. M. Henning, Y. A. R. R. Kessener, P. M. Koenraad, M. R. Leys, W. van de Vleuten, I. H. Wolter, and A. M. Frens, Semicond. Sci. Technol. **6**, 1079 (1991).

Translated by Frank J. Crowne

Mobility of charge carriers in double-layer PbTe/PbS structures

O. A. Aleksandrova, R. Ts. Bondokov, I. V. Saunin, and Yu. M. Tairov

St. Petersburg State Electrical Engineering University, 197376 St. Petersburg, Russia
(Submitted April 7, 1998; accepted for publication April 14, 1998)
Fiz. Tekh. Poluprovodn. **32**, 1064–1068 (September 1998)

The method of hot-wall epitaxy is used to grow epitaxial heterostructures of *p*-PbTe/*n*-PbS on BaF_2 substrates. Hall-effect measurements are analyzed in order to obtain the dependence of the effective carrier mobility on thickness and temperature in the ranges 0.1–2 μm and 100–300 K, respectively. It is found that this mobility depends on the thickness of the sample and on the individual thicknesses of its constituent layers. The effective mobility is calculated under the assumption that charge carriers are scattered by the surface of the structure and by dislocations that form at the heterojunction boundary. © *1998 American Institute of Physics.* [S1063-7826(98)01009-6]

INTRODUCTION

Lead-chalcogenide multilayer structures, both systems of superlattice type and systems with multiple quantum wells, have been studied intensely because they are promising device candidates for infrared engineering applications.[1,2] The electrical properties of these structures are primarily determined by the quality of the heterojunction boundaries. Until now, experimental results, e.g., Hall-effect measurements, have come from multilayer samples with buffer layers.[12] Measurements of this kind give information about parameters of the structure as a whole, but do not reveal the connection between properties of the heterojunction and the electrical characteristics, due both to the large number of layers and to the presence of the buffer layer itself. It is obvious that the larger the thickness of the latter, the larger the role it plays in determining the concentration and mobility of the charge carriers.

There are two easy ways to solve this problem: first, decrease the number of layers of the sample to a minimum (i.e., to two) and, second, stop using a buffer layer. Such two-layer structures with matched lattice parameters are widely used as wideband infrared radiation detectors.[3] In this paper we will discuss two-layer PbTe/PbS structures, with the goal of determining how the heterojunction acts as a scattering factor.

1. EXPERIMENTAL TECHNIQUES

We used the ''hot-wall'' method of thermal vacuum sputtering to deposit individual films of PbTe and PbS, along with *p*-PbTe/*n*n-PbS heterostructures, on freshly cleaved substrates of BaF_2.[4] The rate of growth of the layers was chosen from the range 1–2 μm/h, which is most typical for growing superlattices. The thicknesses of the PbTe and PbS layers were varied by varying the sputtering time. The temperature of the substrate was 520–570 K. This range was chosen so as to ensure epitaxial growth of the layers in the [111] direction while at the same time decreasing the probability of mutual diffusion of the chalcogens.[1] The carrier concentration in the as-grown films was fixed at a constant value by using a material batch whose composition corresponded to congruently evaporating material.[5]

The contacts for measuring the Hall EMF were made of indium. Measurements were made in constant electric and magnetic fields for two current and two magnetic field directions. The 0.5-mA current through the sample ran parallel to the heterojunction, while the magnetic field was applied perpendicular to the heterojunction and had a magnetic induction of 0.8 T. The temperature dependences were recorded in the range 100–300 K. Measurements were made both on samples with equal thicknesses of the PbTe and PbS layers but different total thicknesses, and on samples with different thickness ratios (different configurations) but the same total thickness of the structure. Carrier concentrations in all the samples were in the range $1—3\times10^{18}$ cm^{-3}.

2. RESULTS AND DISCUSSION

In order to improve the completeness and accuracy of our analysis of the two-layer structures, we first investigated the dependence of the carrier mobility on thickness and measurement temperature for individual films of PbTe and PbS. These ''touchstone samples'' were grown using the same fabrication regimes that were later used to grow heterostructures. The results obtained are shown in Fig. 1. In analyzing the data, which usually consisted of Hall-mobility measurements, we followed Mathiessens rule and subtracted out contributions to the mobility arising from scattering by thermal lattice vibrations and ionized impurities. Our analysis parallels that of Vaya *et al.*,[6] who also investigated films of *n*-type PbTe obtained by the ''hot-wall'' method. Taking into account the contribution of surface scattering, these authors derived the expression $\mu_r=\mu_d T^{p(d)}$, where $p=-(0.8+0.286d)$. The quantity μ_r is associated with scattering by grain boundaries, dislocations, and roughness of the substrate. For germanium films, Ramey *et al.*[7] included scattering by dislocations using the formulas of Dexter and Seitz,[8] and for the residual mobility they found an expression $1/\mu_r=A\log(b/d)$, where A and b are parameters that depend

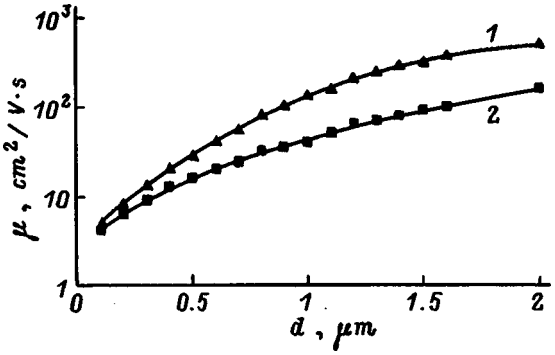

FIG. 1. Dependence of the Hall mobility of a charge carrier (μ) on film thickness (d) for the following materials: *1*— PbTe, *2*— PbS.

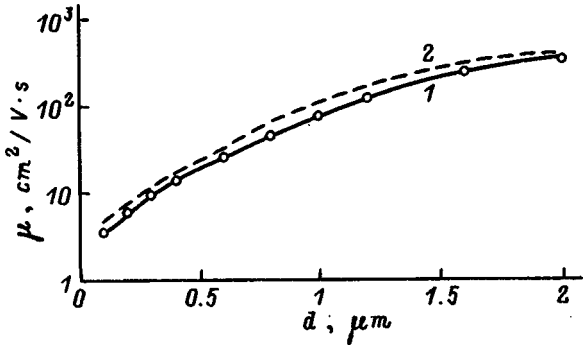

FIG. 2. Effective mobility of PbTe/PbS heterostructures versus thickness ($d_1=d_2$): *1*— experiment, *2*— calculations in which the heterostructures are represented as structures with layered nonuniformities [Eq. (3)].

on the growth conditions and structure of the film. If we approximate the curves in Fig. 1 by fourth-order polynomials

$$\mu=a_0x^4+a_1x^3+a_2x^2+a_3x+a_4,$$

where a_0-a_4 are dimensional coefficients, and x has the same dimensions as the thickness d (μm), then the following empirical expressions will be correct:

$$\mu_1=-90.7d^4+294.6d^3-127.1d^2+56.2d+0.3, \quad 0.1<d<2, \tag{1}$$

$$\mu_2=-0.7d^4+6.6d^3+18.9d^2+15.3d+2.5, \quad 0.1<d<2. \tag{2}$$

Here and in what follows labels 1 and 2 correspond to PbTe and PbS.

We can write the temperature dependence of the mobility in the form[9] $\mu=AT^{-p}$, where A is a constant that depends on the material parameters, and p is a coefficient that depends on the specific scattering mechanism. Values of p for various samples of PbTe and PbS are given in Table I. These values correlate with values of p obtained in Ref. 6.

In principle, thin films can also exhibit size effects that involve the average mean-free path of a charge carrier and the Debye screening length. However, the maximum values for both lengths calculated from the expressions given in Refs. 9 and 10 are 40 and 25 nm, respectively. Consequently, the appearance of dimensional effects in our data for lead telluride and lead sulfide in the temperature range 100–300 K, even for the thinnest samples (100 nm), is not very probable. It is known[11] that $p\cong2.5$ for sufficiently uniform films of lead chalcogenides, which usually is explained by invoking scattering by long-wave acoustic phonons and including the temperature dependence of the effective mass. For surface scattering we have $\mu\sim T^{-0.5}$ in PbTe. A number of papers[10] have reported scattering by dislocations, by the surface, and by grain boundaries for polycrystalline films. Thus, for films of lead telluride with thickness 1–2 μm grown on KCl substrates the mobility is observed to depend on temperature with an exponent $p=0.8$, which is associated with scattering by growth defects. Values of p with $1.5<p<2.0$ are associated with scattering by dislocations. The critical film thickness at which a network of dislocations forms, calculated using the method of Ref. 12, comes to 12 nm. Thus, we may assume that in films of PbTe and PbS with thicknesses $1\leqslant d_{1,2}\leqslant2$ μm the carrier mobility arises from scattering by misfit dislocations. For thicknesses less than 1 μm scattering by the surface and by growth defects will begin to affect the mobility of our samples, because there is no buffer layer.

TABLE I.

Sample	d, μm	d_1/d_2	p
PbTe	0.5	–	1.20
″	1.1	–	1.52
″	1.6	–	1.70
PbS	0.5	–	1.31
″	1.1	–	1.58
″	1.6	–	1.81
PbTe/PbS	0.5	1	0.50
″	1.0	1	1.68
″	1.6	1	2.34
″	1.6	0.45	1.25
″	1.6	2.2	1.92

Figure 2 (curve *1*) shows the experimental dependence of the effective mobility for *p*-PbTe/*n*-PbS heterostructures on the total layer thickness d ($d_1=d_2$). In general, multilayer heterostructures can be treated as samples with layer-like nonuniformities including changes in the carrier concentration $n(z)$ and mobility $\mu(z)$, and accordingly in the conductivity $\sigma(z)$, where z is the direction perpendicular to the plane of the layers. In particular, for two-layer structures the expression for the effective mobility of a charge carrier ($\mu^2B^2\ll1$) has the form[9]

$$\mu_{\text{eff}}=\mu_1(1+\beta)^{-1}+\mu_2(1+\beta^{-1})^{-1}, \tag{3}$$

where $\beta=\sigma_2d_2/\sigma_1d_1$. Curve *2*, shown by a dotted curve in Fig. 2, was obtained by substituting Eqs. (1) and (2) in Eq. (3). It is clear that values of the carrier mobility computed according to Eq. (3) are always larger than the experimental curves. We can thus assume that additional mechanisms for scattering of charge carriers are important for the layer thicknesses under discussion, which are not associated with scattering within the layers.

The experimental points plotted in Fig. 3 (curve *1*) reveal that the effective carrier mobility in PbTe/PbS structures

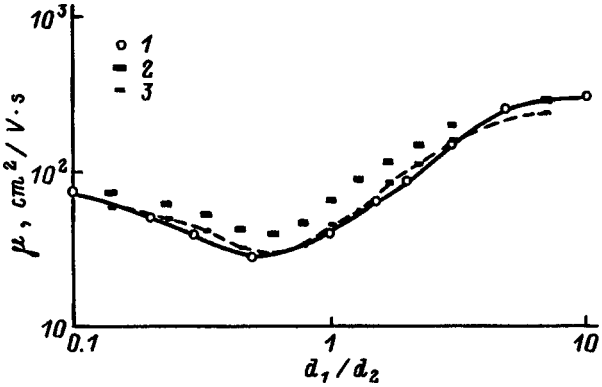

FIG. 3. Effective mobility of PbTe / PbS structures ($d=d_1+d_2=1.6$ μm) versus the ratio d_1/d_2: *1*— experiment, *2*— calculations in which the heterostructures are represented as structures with layered nonuniformities [Eq. (3)], *3*— calculations that include scattering by dislocations [Eq. (7)].

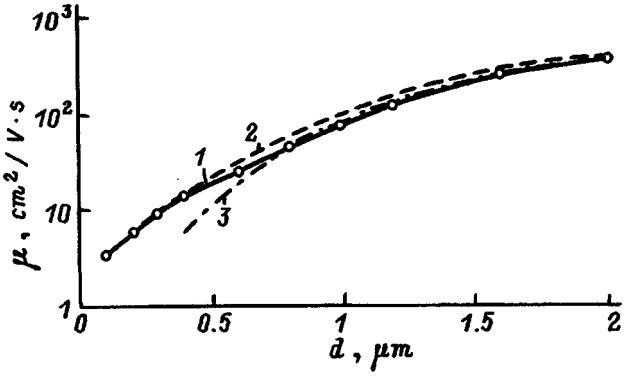

FIG. 4. Effective charge-carrier mobilities for PbTe/PbS structures ($d_1=d_2$): *1*— experiment, *2*— calculations for surface scattering [Eq. (4)], *3*— calculations for scattering by dislocations [Eq. (7)].

depends on the ratio of the thicknesses of the component heterostructure layers (d_1/d_2) even when their total width is held constant, $d=1.6$ μm. The observed minimum is explained by considering the rate at which the mobility of the PbTe layer decreases with decreasing ratio d_1/d_2 compared to its rate of increase in the PbS layer. In this figure, curve *2* shows the function $\mu_{\text{eff}}=f(d_1/d_2)$ calculated using Eq. (3). It is clear that, just as in the previous case, the experimental values of the effective mobility are smaller than the computed values. This result points to the appearance of additional mechanisms for the scattering of charge carriers in this case as well, whose nature must be clarified.

We investigated scattering in heterostructures in the same way as we did in binary films, i.e., by analyzing the temperature dependences of the effective carrier mobility in heterostructures of various thicknesses and configurations (i.e., d_1/d_2). The values of the coefficient p are listed in Table I. From this table it is clear that p is a stronger function of the total heterostructure thickness d than it is for individual PbTe and PbS films. Furthermore, the coefficient p is also found to depend on the ratio of layer thicknesses, d_1/d_2.

Basically, the presence of a boundary can give rise to two factors that contribute to the kinetic coefficients. First of all, a solid solution can arise at the boundary as a result of interdiffusion, which introduces disorder. However, as we noted above, our choice of growth temperatures and the data of Ref. 1 suggest that the creation of the metastable $PbS_{1-x}Te_x$ phase is not very likely. Secondly, it is possible for misfit dislocations to form by virtue of the mismatch between the lattice constants of lead telluride and lead sulfide. For these materials, the critical thickness for forming a network of dislocations determined experimentally is 2–3 nm.[1]

When $d_1=d_2$ it is also necessary to take into account scattering by the surface as a result of the decrease in the total thickness of the heterostructure. The carrier mobility in this case can be calculated by using the expression[6,10]

$$\mu_S=\frac{\mu_V}{1+l/d}, \tag{4}$$

where l is the mean-free path, d is the thickness of the structure, and μ_V is the mobility of a bulk film. Curve *2*, represented in Fig. 4 by the dashed curve, was obtained from Eq. (4). In this case the value of l is assumed to be 50 nm, and the bulk mobility is assumed to be μ_{eff}, which was calculated from Eq. (3) for $d=2$ μm. It is evident from the figure that agreement between experimental and calculated curves is good up to values of $d=0.5$ μm. This fact, together with the fact that $p=1.2$ for a heterostructure with a total thickness of 0.5 μm, actually points to an increasing role for surface scattering with decreasing thickness of the PbTe/PbS samples as a whole.

Misfit dislocations can be treated as scatterers and as charged inclusions that modify the potential.[9] The deformation potential associated with the lattice distortion arising from dislocations leads to a type of scattering.[8] However, further investigations show that we must also consider the effect of dislocations from the point of view of large-scale potential fluctuations. In other words, the electrostatic fields of dislocations are capable of decreasing the mobility to a larger extent than their deformation potentials.[13,14]

There are localized levels on the dislocation axis that can trap majority carriers and form inclusions of the opposite type of conductivity. For this reason, dislocations in an *n*-type crystal behave like negative line charges, and create a positive space charge around them. An electron moving toward a dislocation is repeled by it, which leads to scattering. In order to calculate this scattering we can consider each individual dislocation as a charged cylinder. The effective conductivity in this case is given by the expression[15] $\sigma_{\text{eff}}=\sigma_V(1-\delta)$, where σ_V is the bulk conductivity, and δ is the fraction of volume occupied by space-charge cylinders. The quantity σ_{eff} in an electronic semiconductor is determined by the effective concentration n_{eff} and mobility μ_{eff} of a charge carrier. In moderately nonuniform semiconductors $n_{\text{eff}}\simeq\overline{n}$, where $\overline{n}$ is the concentration averaged over the bulk.[9] Therefore, the general form of the effective mobility is[9,13]

$$\mu_{\text{eff}}=\mu_V(1-\delta). \tag{5}$$

The expression for the volume fraction occupied by space-charge cylinders in terms of their radius R and surface dislocation density N_s has the form[15] $\delta=\pi R^2 N_s$. If we as-

sume that networks of misfit dislocations are formed in both materials as a result of the growth of the PbTe/PbS heterostructure, and that the density of dislocations remains constant during subsequent increases in the thicknesses of both layers, then it is necessary to find the dependence $\delta = f(d)$ in explicit form in order to account for the thickness dependence of the volume fraction occupied by dislocations. The ratio of the volume occupied by the cylinders to the total volume is

$$\delta = \frac{N\pi R^2 a}{Sd},$$

where N is the number of cylinders, a is the characteristic sample size, S is the sample area, and d is its thickness. This expression can be rewritten as

$$\delta = N_l \frac{\pi R^2}{d},$$

where N_l is the line density of dislocations. Setting $N_l \simeq \sqrt{N_s}$, we finally have

$$\delta \cong \frac{\pi r^2}{d}\sqrt{N_s}. \tag{6}$$

Substituting Eq. (6) into Eq. (5), we obtain the dependence of the effective carrier mobility on sample thickness for scattering by dislocations

$$\mu_d = \mu_V\left(1 - \frac{\pi R^2}{d}\sqrt{N_s}\right). \tag{7}$$

The mobility calculated from Eq. (7) is shown in Fig. 4 by curve *3* (the dot-dashed curve). In these calculations we assumed that for $\delta = 0.01 \ll 1$ we have $\mu_d \to \mu_V$. In this case the mobility reaches its bulk value only for $d = 26$ μm. For the bulk mobility μ_V, just as in the case of surface scattering, we use the quantity $\mu_{\text{eff}}(d)$ calculated from Eq. (3). From the figure it is clear that Eq. (7) is in good agreement with the experimental data starting with $d \geqslant 0.7$ μm.

Equation (7) was also used to calculate μ_d for the case of fixed $d = 1.6$ μm and variable ratio d_1/d_2. Here the parameter d was chosen to be the true value of the thickness of the PbTe layer for the interval $0.5 \leqslant d_1/d_2 \leqslant 10$, and the same quantity for the PbS layer for the interval $0.1 \leqslant d_1/d_2 \leqslant 2$. In the range where these intervals overlapped we obtained the same value of the effective mobility $\mu_d(d_1/d_2)$ using either d_1 or d_2. The function constructed in this way is shown in Fig. 3 by curve *3*. The values of μ_d near $d_1/d_2 = 0.1$ and 10 are smaller than the experimental values. To explain this result, we argue that when the thickness of one of the layers that make up the heterostructure is small, scattering by the surface, which in this case has been deliberately ignored, becomes more effective. However, over a large range of values of d_1/d_2 we observe good agreement between the experimental data and calculations. Even better agreement is observed in the range $0.5 \leqslant d_1/d_2 \leqslant 2$, which is the most important for practical problems.

In summary, we have investigated the effective mobility of charge carriers in binary films and in two- layer PbTe/PbS heterostructures of various thicknesses and configurations in the temperature range 100–300 K. We have compared our experimental data with the results of calculations in which we represent the heterostructure samples as structures with layered nonuniformities. Good agreement between calculations and experiment is obtained when we assume that for total structure thicknesses $d = d_1 + d_2 \leqslant 0.5$ μm ($d_1 = d_2$) scattering is due to the surface, while for $d \geqslant 0.7$ μm a substantial role is played by scattering by dislocations. By considering samples with various configurations d_1/d_2 ($d = 1.6$ μm), we have shown that scattering of charge carriers by the heterojunction is due to the presence of misfit dislocations down to very small thicknesses of either of the PbTe or PbS layers.

[1] S. S. Borisova, I. F. Mikhaĭlov, L. S. Palatnik, A. Yu. Sipatov, A. I. Fedorenko, and L. P. Shpakovskaya, Kristallografiya **34**, 716 (1989) [Sov. Phys. Crystallogr. **34**, 426 (1989)].
[2] S. N. Davidenko, F. F. Sizov, and V. V. Teterkin, Ukr. Fiz. Zh. **38**, 938 (1993).
[3] T. A. Gavrikova and V. A. Zykov, Fiz. Tekh. Poluprovodn. **31**, 1342 (1997) [Semiconductors **31**, 1331 (1997)].
[4] S. L. Miloslavov, I. V. Saunin, and D. A. Yas'kov, Izv. Akad. Nauk SSSR, Neorg. Mater. **19**, 55 (1983).
[5] V. P. Zlomanov and A. V. Novoselova, *P-T-x State Diagrams of Metal-Chalcogen Systems* (Nauka, Moscow, 1987).
[6] P. R. Vaya, J. Majhi, B. S. V. Gopalam, and C. D. Dattarreyan, Phys. Status Solidi A **87**, 341 (1985).
[7] R. L. Ramey and W. D. McLennan, J. Appl. Phys. **38**, 3491 (1967).
[8] D. L. Dexter and F. Seitz, Phys. Rev. **86**, 964 (1952).
[9] E. V. Kuchis, *Galvanomagnetic Effects and Methods for Investigating Them* (Radio i Svyaz', Moscow, 1990).
[10] K. L. Chopra, *Thin Film Phenomena* (McGraw-Hill, New York, 1969; Mir, Moscow, 1972).
[11] Yu. I. Ravich, B. A. Efimova, and I. A. Smirnov, *Methods for Investigating Semiconductors Applied to the Lead Chalcogenides PbTe, PbSe, and PbS* (Nauka, Moscow, 1968).
[12] Yu. V. Kochetkov, V. N. Nikiforov, O. N. Vasil'eva, and A. M. Gas'kov, Bull. Moscow State Univ. Ser. 3, Physics, Astronomy **35**, 68 (1994).
[13] S. I. Pekar, Fiz. Tverd. Tela (Leningrad) **8**, 1115 (1966) [Sov. Phys. Solid State **8**, 890 (1966)].
[14] Yu. V. Kornyushin, L. S. Mima, and O. V. Tret'yak, Fiz. Tekh. Poluprovodn. **15**, 2159 (1981) [Sov. Phys. Semicond. **15**, 1254 (1981)].
[15] H. F. Matare, *Defect Electronics in Semiconductors* (Wiley, New York, 1971; Mir, Moscow, 1974).

Translated by Frank J. Crowne

SEMICONDUCTOR STRUCTURES, INTERFACES, AND SURFACES

Many-body effects and electron tunneling in metal-insulator-*p*-type semiconductor structures

G. M. Min'kov, A. V. Germanenko, and O. É. Rut

Institute of Physics and Applied Mathematics, Urals State University, 620083 Ekaterinburg, Russia
(Submitted October 13, 1997; accepted for publication December 5, 1997)
Fiz. Tekh. Poluprovodn. **32**, 1069-1072 (September 1998)

Investigation of the tunneling conductivity $\sigma_d(V)$ of structures made on a highly doped, narrow-gap *p*-type semiconductor HgCdTe reveals an abrupt increase in this quantity at voltages corresponding to the start of tunneling into the conduction band. It is shown that the observed functions $\sigma_d(V)$ cannot be described in the framework of a model based on single-particle tunneling. It is proposed that the abrupt increase in $\sigma_d(V)$ is attributable to tunneling into exciton states. © *1998 American Institute of Physics.* [S1063-7826(98)01109-0]

It is well known that single-particle tunneling into electronic states at the edges of allowed energy bands of the electrodes does not lead to sharp features in the voltage-current characteristics at the corresponding bias voltages.[1] Thus, e.g., for a metal-insulator-*p*-type semiconductor tunneling contact in which the semiconductor has a simple parabolic conduction band, the dependence of the differential conductivity $\sigma_d \equiv dj/dV$ on bias voltage (V) for $eV > E_g + E_F$ has the form

$$\sigma_d(V) \propto (eV - E_g - E_F)^{3/2},$$

where E_g is the width of the semiconductor band gap and E_F is the Fermi energy measured from the top of the valence band. The function $\sigma_d(V)$ will have this form if it is assumed that there is no surface band bending in the semiconductor, and that the tunneling transparency of the insulator does not depend on charge-carrier energy (E) or bias voltage in the ranges of E and V under discussion. In fact, these factors may profoundly change the functional dependence $\sigma_d(V)$, but they cannot change the smoothness with which the states of the conduction band are ''switched on'' in the process of tunneling.

The modification of tunneling by many-electron effects changes the function $\sigma_d(V)$. Beginning with the paper by Aronov and Altshuler,[2] many authors have shown that electron–electron interactions are one of the main reasons for the appearance of a ''zero-voltage anomaly'' in the voltage-current characteristics of tunneling contacts. However, the question of how the tunneling conductivity is affected by electron–electron interactions that mediate the tunneling of electrons into excitonic final states as well as conduction-band states of a *p*-type semiconductor has, to our knowledge, not been addressed, even though this phenomenon obviously should appear in tunneling experiments.

We investigated the dependence of the tunneling conductivity on bias voltage and magnetic field in *p*- $Hg_{1-x}Cd_xTe$–Al oxide structures in which the HgCdTe solid solution compositions were in the range $0.17 < x < 0.2$, which corresponds to $E_g = 20-80$ meV and a concentration of uncompensated acceptors $N_A - N_D = 1.5 \times 10^{18}\,\mathrm{cm}^{-3}$. The method used to prepare these tunneling contacts was described in Ref. 3.

Figure 1 shows the functions $\sigma_d(V)$ for one of the contacts. It is clear that there is a certain threshold value $V_{\mathrm{thr}} \approx 80$ mV at which an abrupt increase in σ_d is observed: i.e., a change in bias of only 5–7 mV causes σ_d to increases by more than an order of magnitude. In a quantizing magnetic field B oscillations in the tunneling conductivity (Fig. 1) are observed for bias voltages $V > V_{\mathrm{thr}}$. These oscillations are periodic with respect to inverse magnetic field $1/B$ at constant bias, with a period that is the same for either orientation $\mathbf{B} \perp \mathbf{n}$ or $\mathbf{B} \| \mathbf{n}$ (where $\mathbf{n}$ is normal to the plane of the tunneling contact). This fact, and also the fact that the positions of peaks of the oscillations in a magnetic field do not exhibit the angular dependence that is typical of the 2D state, implies that the observed oscillations are caused by tunneling into Landau levels derived from bulk semiconductor states. Thus, the positions of the oscillation peaks in coordinates V and B (Fig. 2) indicate the positions of Landau levels of bulk states, and their extrapolation to $B = 0$ makes it possible to directly determine the energy corresponding to the bottom of the conduction band. It is clear that within limits of measurement error the position of the step in the function $\sigma_d(V)$ coincides with the extrapolated point, and hence corresponds to the bias at which tunneling to the bottom of the conduction band begins.

In order to analyze the experimental results we calculated the function $\sigma_d(V)$ for single-particle tunneling into a semiconductor with a Kane dispersion relation. This is not difficult to do using the standard expression for the tunneling current

$$j \propto D \sum (\hat{v}\psi)^2,$$

where D is the tunneling transparency of the barrier, $(\hat{v}\psi)^2$ is

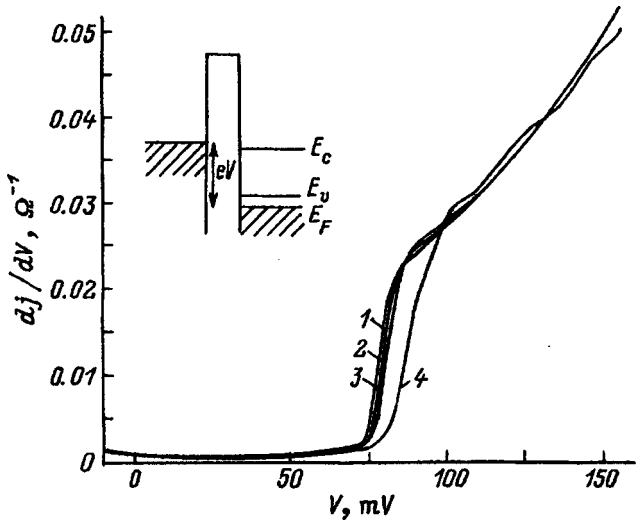

FIG. 1. Dependence of the differential resistance on bias voltage for one of the structures under study in a magnetic field $\mathbf{B}\|\mathbf{n}$; B, T: *1* — 0, *2* — 0.3, *3* — 0.6, *4* — 2.5. The inset shows the energy diagram for the tunneling contact.

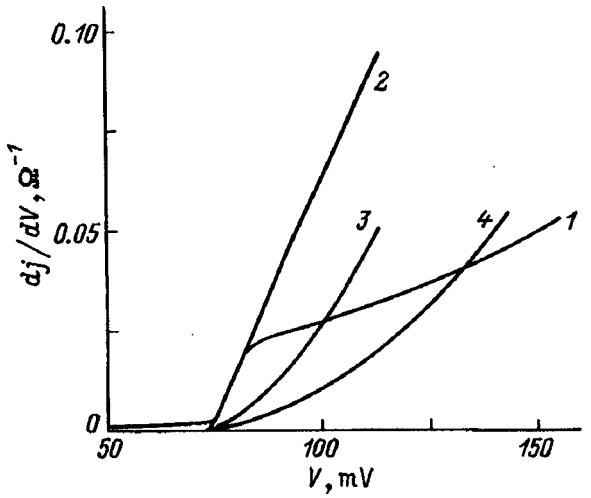

FIG. 3. Dependences of the tunneling conductivity on bias voltage V: *1*— experiment, *2–4*— calculations for the following values of surface potential φ_s, meV: *2*— −80, *3* — 0, *4* — 80.

the square of the velocity of semiconductor states at the semiconductor-insulator boundary, and the summation is taken over all the states of the semiconductor unoccupied by electrons. Thus, for this calculation we need to the know the dependence of $(\hat{v}\psi)^2$ on energy. This dependence is found for a model structure in which we assume that the insulator has a Kane energy spectrum with a large value of the band gap.[4] In this approximation the problem reduces to solving (numerically) a system of two differential equations[5] for flat bands and for various values of the surface potential. (In our case, as follows from a solution of the Poisson equation, the shape of the potential is parabolic.) Figure 3 shows calculated functions $\sigma_d(V)$ for several values of the surface potential (φ_s) that are not large enough to localize a 2D state.

It is clear that there is no abrupt increase in σ_d at biases corresponding to the bottom of the conduction band for any value of (φ_s). Furthermore, the experimentally observed function $\sigma_d(V)$ cannot be explained within the framework of single-particle tunneling into bulk semiconductor states for any changes of surface potential $\Delta\varphi_s$ brought on by changes in bias that obey the natural limitation $\Delta\varphi_s < V$. Thus, as shown in Fig. 4, agreement between the calculated and experimental functions $\sigma_d(V)$ requires that the change in the surface potential be at least 1.5 times larger than the value of the applied voltage.

We could assume that for $V \leqslant V_{\text{thr}}$ the structures under study support a surface potential sufficient for localization of 2D states with very small binding energy, and that the abrupt increase in σ_d for $V = V_{\text{thr}}$ is caused by tunneling into these states.[1] With increasing bias the surface potential decreases,

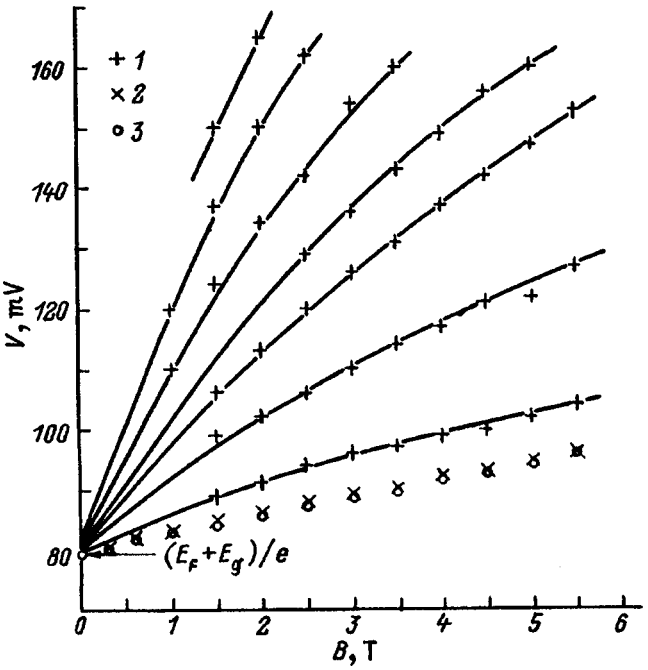

FIG. 2. Position of maxima in the tunneling conductivity *(1)* for $\mathbf{B}\|\mathbf{n}$ and position of the center of the step for $\mathbf{B}\perp\mathbf{n}$ *(2)* and $\mathbf{B}\|\mathbf{n}$ *(3)*.

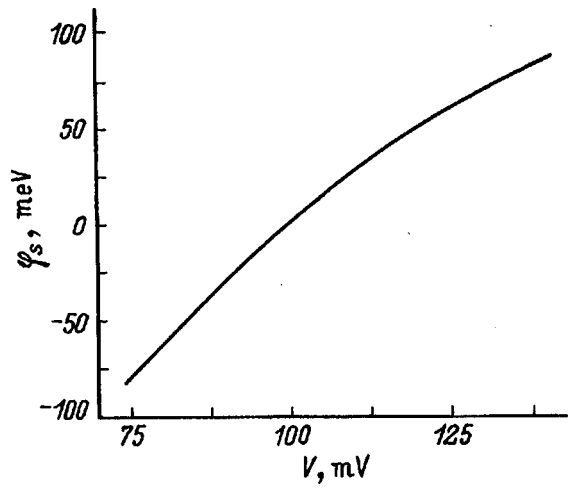

FIG. 4. Plot of of the surface potential φ_s versus the bias-voltage V required to obtain agreement between experimental and theoretical functions $\sigma_d(V)$ in the model of single-particle tunneling.

and for $V>V_{\rm thr}$ the localized 2D states disappear, so that for these biases the tunneling takes place into bulk states. This follows from the absence of angular dependence of the position of oscillation peaks in the tunneling conductivity. However, in this case our calculations show that shifts in the conductivity step with increasing magnetic field at large biases should be different for $\mathbf{B}\perp\mathbf{n}$ and $\mathbf{B}\|\mathbf{n}$. Even if we assume that the binding energy of the 2D states is only 1 or 2 eV, at $B=4$ T the difference in positions of the step for $\mathbf{B}\perp\mathbf{n}$ and $\mathbf{B}\|\mathbf{n}$ should come to 1.5–2 meV. (For larger binding energies this difference becomes still larger.) It is clear from the experimental results (Fig. 2) that within limits of measurement error (0.5 meV) the shifts in the step center are identical for $\mathbf{B}\perp\mathbf{n}$ and $\mathbf{B}\|\mathbf{n}$. Thus, possible mechanisms that could lead to the appearance of an abrupt step in the function $\sigma_d(V)$ for single-particle tunneling cannot explain the experimental data.

In our view, the abrupt step in the function $\sigma_d(V)$ for tunneling of electrons into a *p*-type semiconductor could be a consequence of electron–hole interactions. Actually, one of the reasons for the smooth change in $\sigma_d(V)$ at voltages corresponding to the bottom of the conduction band for single-particle tunneling is equality of the density of final states when $eV=E_g+E_F$. In contrast, when an electron tunnels into a *p*-type material, it can also end up in an ''exciton'' state, and the number of these states equals the concentration of free holes. Since the energy needed for tunneling into such states is close to E_g, this leads to an additional increase in $\sigma_d(V)$ at $eV=E_g+E_F$. Of course, in the structures under study the concentration of holes is so large that the radius of the excitonic state is greater than the screening length, so that excitons will not be stable and will decay after a time τ, which is determined by the screening time (τ_0) and the scattering time (τ_{SC}):

$$\tau\approx(1/\tau_0+1/\tau_{SC})^{-1}.$$

In this case the washing-out h/τ is on the order of 10 meV, i.e., larger than the ionization energy of the exciton, which in these materials is on the order of 0.1 meV. As an estimate we assume

$$\tau_{SC}\approx m_h\mu/e,$$

where m_h and μ are the effective mass and mobility of heavy holes, and $\tau_0\approx 1/\omega_p$, where ω_p is the plasma frequency. The value of the washing-out $h/\tau\approx 10$ is close to the width of the step observed experimentally.

It is perhaps more correct to consider the role of many-electron effects in tunneling into a strongly doped *p*-type semiconductor from another point of view. It is known that electron–electron interactions during tunneling of an electron into an *n*-type semiconductor leads to suppression of tunneling at small biases (the zero-bias anomaly). This takes place because an electron after tunneling must ''push apart'' the surrounding charge carriers. At small biases its excess energy (eV) is smaller than the energy required for this process, which also leads to suppression of tunneling at these biases.[6] In contrast, when an electron arrives in the conduction band of a *p*-type material after tunneling, it is attracted by the remaining charge carriers, which can lead to an increase in conductivity at energies corresponding to the bottom of the conduction band. Unfortunately, as far as we know, no papers have appeared in the literature that take into account the role of electron–electron interactions in the tunneling of electrons into a *p*-type semiconductor.

In principle, the experimental results can be qualitatively explained in another way. If electrons do not succeed in recombining with holes or leaving the region near the barrier after tunneling, the accumulation of charge in this region will lead to a change in potential and consequently to a slower increase in the conductivity for $eV>E_g+E_F$. Further studies of the current–voltage characteristics are necessary in order to unambiguously clarify the mechanism that explains this feature of tunneling into a *p*-type semiconductor.

The authors are grateful to V. A. Volkov for interest in this work and for useful discussions.

This work was supported in part by a grant from the Russian Fund for Fundamental Research No. 97-02-16168 and a grant from the program ''Physics of Solid-State Nanostructures.''

[1)] Because of the strong spin-orbit coupling, the bottom of the band of 2D states is shifted away from the point $k=0$ (Ref. 6), which should lead to an additional singularity (a maximum) in the density of final states near the bottom of the band and, consequently, to an abrupt singularity in σ_d at the corresponding bias.

[1] *Tunneling Phenomena in Solids* (Mir, Moscow, 1973).
[2] B. L. Altshuler and A. G. Aronov, Solid State Commun. **30**, 115 (1979).
[3] G. M. Min'kov, O. E. Rut, V. A. Larionova, and L. V. Germanenko, Zh. Éksp. Teor. Fiz. **105**, 719 (1994) [JETP **78**, 384 (1994)].
[4] P. Sobkowicz, Semicond. Sci. Technol. **5**, 183 (1990).
[5] A. V. Germanenko, G. M. Minkov, V. A. Larionova, O. E. Rut, C. R. Becker, and G. Landwehr, Phys. Rev. B **52**, 17254 (1995).
[6] L. S. Levitov and A. V. Shutov, Preprint: cond-mat/9501130, cond-mat/9607136.

Translated by Frank J. Crowne

Current transport in porous *p*-Si and Pd-porous Si structures

S. V. Slobodchikov, Kh. M. Salikhov, and E. V. Russu

A. I. Ioffe Physicotechnical Institute, Russian Academy of Sciences, 194021 St. Petersburg, Russia
(Submitted February 9, 1998; accepted for publication February 10, 1998)
Fiz. Tekh. Poluprovodn. **32**, 1073–1075 (September 1998)

Mechanisms are investigated for current transport in porous *p*-Si and Pd–*p-por*-Si structures in the temperature range 78–300 K. It is shown that at 78 K drift transport is decisive, with the participation of deep traps with a concentration $N_t \approx 1.3\times10^{13}$ cm^{-3}. At higher temperatures the diffusion mechanism takes over, with $I\sim\exp(-qV/nkT)$ and $n=10-20$. Relaxation processes for the reverse current and photocurrent (ascending branch) have a delayed character (up to $t\simeq100$ s) and are determined by the effect of traps at a depth $E_t=0.80$ eV. The temperature behavior of the photocurrent (without a bias) is connected with recombination at a level $E_r=0.12$ eV, and its value essentially depends on the contribution of the basal region of the diode structure. © *1998 American Institute of Physics.* [S1063-7826(98)01209-5]

In many publications in which porous silicon (*por*-Si) is investigated, most of the attention is focused on photo- and electroluminescence in the layers, and to a lesser degree on diode structures. Thus, the mechanism of current transport has not received much attention. For this reason, it is worth mentioning the few papers that either are completely devoted to this problem[1] or partially touch on it.[2] In our paper[3] we also discuss current transport in diode structures with a disordered p_0 layer.

In this article we report some new results of our studies of the electrical and photoelectric properties of porous *p*-type Si and Pd–*p-por*-Si diode structures, and consider special features of the current transport mechanism.

1. CURRENT-VOLTAGE CHARACTERISTICS AND CURRENT TRANSPORT MECHANISM

We used standard methods for obtaining layers of porous silicon using a solution of HF in a mixture of C_2H_5OH and crystals of *p*-Si with $\rho=1-10\ \Omega\cdot$cm. The time for electrochemical etching was varied in the range 10–50 minutes, and the current density in the range 20–300 mA/cm^2. In order to make Pd–*p-por*-Si diode structures we used samples with a thick layer ($w=50\ \mu$m) of porous silicon. The palladium was evaporated onto porous silicon in the form of circular contacts with area $S=3.14\times10^{-2}$ cm^2 at a pressure of 10^{-5} Torr. The thickness of these contacts was 400 Å in order of magnitude. Ohmic contacts were made by evaporating a thin layer of Al on the back side of the substrate.

Figure 1 shows the forward branches of the current-voltage characteristics (positive potential on *p-por*-Si) measured at temperatures 78, 100, and 300 K. Their characteristic features are as follows. At $T=100$ and 300 K the current-voltage characteristics could be described by the expression

$$I=I_0\exp\frac{qV}{nkT}, \tag{1}$$

where at $T=100$ K $n=20$ and at $T=300$ K $n=10$. At $T=78$ K and at relatively small injection levels it is found that $I\sim V^2$; with a further increase in voltage the current increases abruptly, and then once more follows a dependence close to V^2. Thus, in contrast to Ref. 1, we observed a temperature dependence for the current with a change in functional type $I=f(V)$. At $T=78$ K the shape of the current-voltage characteristic naturally forces us to postuate a current transport mechanism that is space-charge limited. At low injection levels we can assume

$$I=\frac{10^{-13}V^2\mu^*\varepsilon S}{w^3}, \tag{2}$$

where S is the area of the structure, $\varepsilon=3.3$ is the dielectric constant of porous silicon,[1] and w is the thickness of the porous silicon layer.

From Eq. (2) we derive an effective mobility $\mu^*=0.06$ cm^2/(V·s), i.e., an order of magnitude lower than in Ref. 3. The steep growth in the current is connected with occupation of trapped levels, while the subsequent nearly-quadratic dependence corresponds to the trapless region of the characteristics. Based on the critical voltage $V_1=17$ V corresponding to this transition, we can estimate, according to Ref. 4, the density of trapping levels

$$N_t=\frac{CV_1}{qwS}. \tag{3}$$

Here the capacitance $C=20$ pF and $N_t=1.3\times10^{13}$ cm^{-3}. Increasing the temperature leads to an increase in the concentration of equilibrium holes in the *p-por*-Si base region, and hence a decrease in the resistance of this region. On the other hand, if we accept a heterostructure version of the *p-por*-Si boundary, we should expect a temperature-induced decrease in the barrier at this boundary. The first effect leads to a redistribution of the applied voltage dropped across the contact regions as the latter increases, which increases the injection coefficient for holes I_p/I. The second effect can also produce this same result. Ultimately the diffusion component of the current will increase due to increases in the gradients dp/dx, dn/dx. If the current transport determined

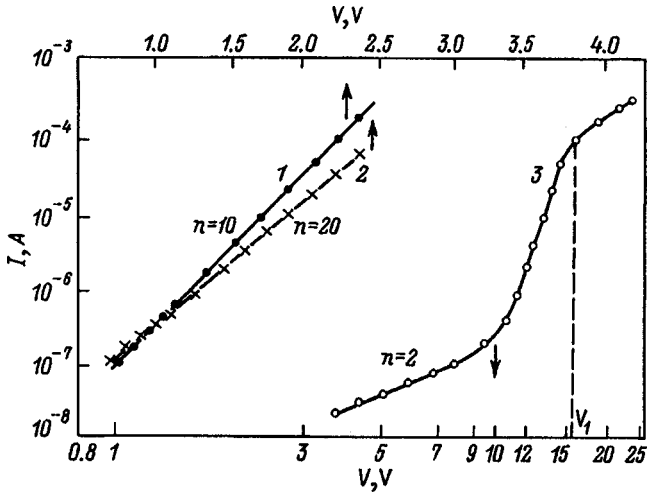

FIG. 1. Current-voltage characteristics of a Pd–*p-por*-Si structure; *T*, K: *1* — 300, *2* — 100, *3* — 78. The upper scale of the abscissa corresponds to curves *1* and *2*.

by expression (2) is entirely due to the drift mechanism, then increasing the temperature will lead to its gradual replacement by the diffusion mechanism.

In this case, according to Ref. 5, we should let

$$n=\cosh\frac{w}{L} \quad \text{for } w>L \tag{4}$$

in Eq. (1). Here L is the ambipolar diffusion length.

At room temperature the coefficient for hole injection I_p/I through the Pd–*por*-Si heterojunction into the porous silicon layer is large, and the injection coefficient for electrons is small, $I_n/I<1$. As we will show below, this implies that trapping of minority carriers takes place, and the capture cross section for electrons is quite different for the capture cross section for holes: $s_n \gg s_p$. Consequently, at $T=300$ K the current that flows in the structure is primarily due to holes. When the temperature is lowered to 100 K, the predominance of diffusive current transport is preserved, but the magnitude of the current becomes smaller for the same values of applied bias. This occurs because the number of active trapping centers for electrons increases due to the temperature-induced shift in the Fermi level. This difference is especially notable at higher biases when the recombination rate is increased due to electron pumping. In this case L in Eq. (4) decreases, causing n in (1) to increase.

The importance of deep traps is revealed when we investigate the relaxation of the reverse current and photocurrent at reverse biases. Figure 2 shows typical curves for the corresponding increase in current and photocurrent obtained from a step increase in the voltage ΔV. The steady-state value of the current is reached after several tens of seconds for various samples, sometime reaching values of 80–90 s. The delay is associated with the inertia of the current-injection process that changes the conductivity of a layer of *p*-Si. At the same time, a discontinuous change in voltage $\Delta V=V_2-V_1$ changes the current from a value $I_1\simeq\sigma_1 V_2/w$, which it reaches immediately after the jump in voltage (when the conductivity of the layer still has unmodulated value σ_1), to a value $I_2\simeq\sigma(I)V_2/w$ with the modulated value of the conductivity $\sigma=\sigma(I)$. The change in current $\Delta I\simeq(\sigma-\sigma_0)\Delta V/w$ takes place after a time Δt, whose duration is determined by peculiarities in the transport mechanism of dark (or illumination-induced) carriers injected into the porous *p*-layer. The new value I_2 is reached after a time considerably longer than the time for establishing the voltage, i.e., a ''delay'' of the current takes place. For a diffusive mechanism for current transport

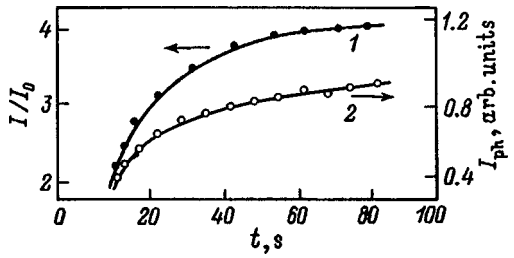

FIG. 2. Relaxation (growth) of the reverse current I/I_0 (curve *1*) and the photocurrent under reverse bias I_{ph} (curve *2*).

$$\Delta t\simeq\frac{w^2}{2D_n}. \tag{5}$$

For $\mu_n^*=6\times10^{-2}$ cm^2/(V·s) we have $\Delta t\simeq0.1$ s. However, this estimate disregards the presence of deep trapping levels. The motion of electrons injected under reverse bias can be viewed as a continuous process of capture and release by traps located at various depths in the band gap of Si and having different densities and capture cross section. We are unable to explain the increase in the reverse current and photocurrent using a model with a uniform distribution of traps in the band gap.[6] We assume that the discontinuous change of voltage and, accordingly, the increase in the injection of electrons changes the space charge which in turn affects $\psi(t)$, the trap distribution function. If we assume that the deepest traps have a time constant τ_1, then[7]

$$\psi(t)\sim\exp\left(-\frac{t}{\tau_1}\right). \tag{6}$$

Thus, the growth curve of the reverse current or photocurrent should change according to the relation

$$I=I_0\left[1-\exp\left(-\frac{t}{\tau_1}\right)\right]. \tag{7}$$

Good agreement is observed between experimental and calculated dependences based on Eq. (7) when $\tau_1=20$ s (Fig. 2). This time corresponds to a deep trap level, whose depth can be estimated from the time for thermal liberation of electrons

$$\tau=\tau_0\exp\frac{E_t}{kT}. \tag{8}$$

From Eq. (8) with $\tau_1=20$ s ($\tau_0\approx10^{-13}$ s) we find that the depth of the level is $E_t=0.80$ eV.

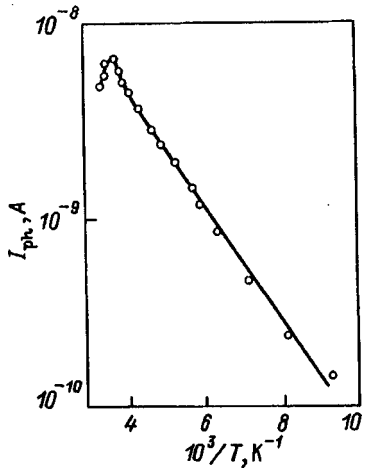

FIG. 3. Temperature dependence of the photocurrent of a diode structure without a bias.

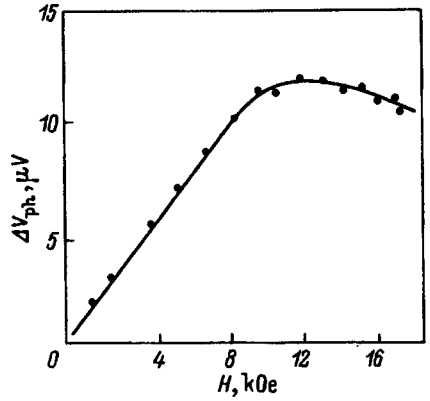

FIG. 4. Change in the photovoltage ΔV_{ph} in a magnetic field H for a sample with a Pd–*p-por*-Si diode structure.

2. PHOTOCURRENT AND PHOTOVOLTAGE

Figure 3 shows the temperature dependence of the short-circuit photocurrent ($V=0$) of the diode structures we studied in the temperature range 110–300 K. The exponential increase of I_{ph} with decreasing inverse temperature is replaced by a falloff which begins at room temperature. The photocurrent is determined by the separation of nonequilibrium carriers in the Schottky barrier of the Pd–*p-por*-Si structure. The change in photocurrent primarily reflects a corresponding change in lifetime of minority carriers (electrons) with temperature. In fact, it is well known that the total photocurrent of the structure is determined by two components

$$I_{ph}=I_d+I_b, \tag{9}$$

where I_d is the contribution from the space-charge region

$$I_d\sim[1-\exp(-\alpha w_1)], \tag{10}$$

and I_b is the contribution from the base region, i.e., the layer of porous *p*-Si

$$I_b\sim\frac{\alpha L_n}{(\alpha L_n+1)}\exp(-\alpha w_1). \tag{11}$$

In these relations, α is the absorption coefficient and w_1 is the thickness of the space-charge layer. Because of the small absorption coefficient α (the photocarriers are generated by monochromatic light with $\lambda=1.1$ μm) and the small thickness w_1, the primary contribution to the photocurrent comes from the base region, i.e., the component I_b from Eq. (11):

$$I_{ph}\sim L_n\sim\left(\frac{\mu_n^* kT}{q}\right)^{1/2}\exp\left(-\frac{E_r}{2kT}\right). \tag{12}$$

From the slope of the temperature dependence line, we find for the photocurrent that $E_r=0.12$ eV. We assume that the lifetime of the photocarriers is determined by this recombination level. The effect of a magnetic field on the photovoltage, shown in Fig. 4, is characteristic. In a magnetic field perpendicular to the diffusion current, the photovoltage increases with increasing field, reaches a maximum at $H=12$ kOe, and then begins to decrease. We should expect, however, a falloff in I_{ph} in the entire range of magnetic fields, although not a very sharp one because of the small effective mobility of the electrons:

$$D_n(H)=\frac{D_n(0)}{\sqrt{1+\left(\frac{\mu_n^* H}{c}\right)^2}}.$$

The observed experimental increase in photovoltage is probably due entirely to the increase in differential resistance of the Pd–⟨porous silicon⟩ barrier. Only at high fields does the falloff in short-circuit current I_{ph} begin to dominate, which predetermines the presence of a maximum and a falloff in the photovoltage.

[1] C. Peng, K. D. Hirschman, and P. M. Fauchet, J. Appl. Phys. **80**, 295 (1996).
[2] F. Namavar, H. P. Maruska, and N. M. Kalkhoran, Appl. Phys. Lett. **60**, 2514 (1992).
[3] S. V. Slobodchikov, Kh. M. Salikhov, E. V. Russu, M. M. Meredov, and A. I. Yazlyeva, Fiz. Tekh. Poluprovodn. **31**, 15 (1997) [Semiconductors **31**, 111 (1997)].
[4] A. Rose, Phys. Rev. **97**, 1538 (1955).
[5] É. I. Adirovich, P. M. Karageorgiĭ-Alkalaev, and A. Yu. Leĭderman, in *Double-Injection Currents in Semiconductors* (Nauka, Moscow, 1978), p. 73, 118–122.
[6] R. H. Bube, J. Appl. Phys. **34**, 3309 (1963).
[7] J. Wang, J. Appl. Phys. **75**, 332 (1984).

Translated by Frank J. Crowne

Determining surface recombination rates in epitaxial layers of n-$Cd_xHg_{1-x}Te$ from measurements of the planar magnetoresistance and relaxation times for nonequilibrium charge carriers

P. A. Borodovskiĭ, A. F. Buldygin, and V. S. Varavin

Institute of Semiconductor Physics, Russian Academy of Sciences (Siberian Department), 630090 Novosibirsk, Russia

(Submitted June 7, 1997; accepted for publication February 24, 1998)
Fiz. Tekh. Poluprovodn. **32**, 1076–1078 (September 1998)

The dependence of the planar magnetoresistance on magnetic field has been measured for epitaxial layers of n-Cd_xHg_{1-x} ($x=0.211$, 0.22) at 300 and 77 K. The 77 K measurements were made in electric fields below and above the threshold field for avalanche impact ionization. The measurement results for the planar magnetoresistance and relaxation time of nonequilibrium charge carriers are used to determine surface recombination rates. © *1998 American Institute of Physics.* [S1063-7826(98)01309-X]

In past studies of p-$Cd_xHg_{1-x}Te$/CdTe epitaxial-layer structures, measurements of the photomagnetic effect, photoconductvity, and Hall parameters (see, for example, Ref. 1) have been used to determine the surface recombination rate at the boundary between the epitaxial layer and the substrate or at the free surface of the epitaxial layer. In this report, we propose to use measurements of the planar magnetoresistance and relaxation time of nonequilibrium carriers to determine the rate of recombination at the boundary between the epitaxial layer and the substrate (or buffer layer), and at the free surface.

The theory of planar magnetoresistance of nonequilibrium charge carriers was discussed in Ref. 2 by G. E. Pikus. In Ref. 3, Lile investigated thin films of indium antinomide in strong electric fields, and used measurements of the planar magnetoresistance to infer the ratio of the surface recombination rates at the boundaries. The change in resistance of an epitaxial layer in a magnetic field B applied perpendicular to an electric field E in the plane of the layer (as in the case of the photomagnetic effect) for weak magnetic fields ($\mu B \ll 1$) is determined by the expression[2,3]

$$\frac{R(B)-R(0)}{R(0)}=\frac{\Delta R(B)}{R(0)}=-A_1EB+A_2B^2. \tag{1}$$

At sufficiently strong electric fields the linear term in Eq. (1) can be comparable in magnitude to the quadratic term, and consequently $\Delta R(B)\neq\Delta R(-B)$; i.e., a change in the direction of the magnetic field produced an asymmetry which indicates that the recombination rates at the epitaxial layer-substrate boundary and at the free surface are different.

The term that is linear in magnetic field can be isolated in the usual way:

$$\frac{\Delta R(-B)}{R(0)}-\frac{\Delta R(B)}{R(0)}=2A_1EB. \tag{2}$$

The theoretical expression for the coefficient A_1 when $\mu_m \gg \mu_p$ can be written in the form[3]

$$A_1EB\simeq\frac{1}{2}(\mu_nB)\frac{p\quad U\quad d}{n+p(kT/q)\;l}\left(\frac{L_D}{d}\right)^2\alpha_3, \tag{3}$$

where μ_n is the Hall mobility of the electrons, n and p are concentrations of electrons and holes, U is the voltage, l is the distance between the ohmic contacts of the sample, d is the thickness of the epitaxial layer, L_D is the ambipolar diffusion length, and T is the temperature. The dimensionless parameter α_3 is given by a rather cumbersome expression, but it can be shown[3] that for

$$d\ll L_D \quad \alpha_3\rightarrow\frac{d^2}{L_D^2}\left[\frac{S_2-S_1}{S_2+S_1}\right], \tag{4}$$

$$d\gg L_D \quad \alpha_3\rightarrow 2\left[\frac{S_2-S_1}{S_2+S_1}\right], \tag{5}$$

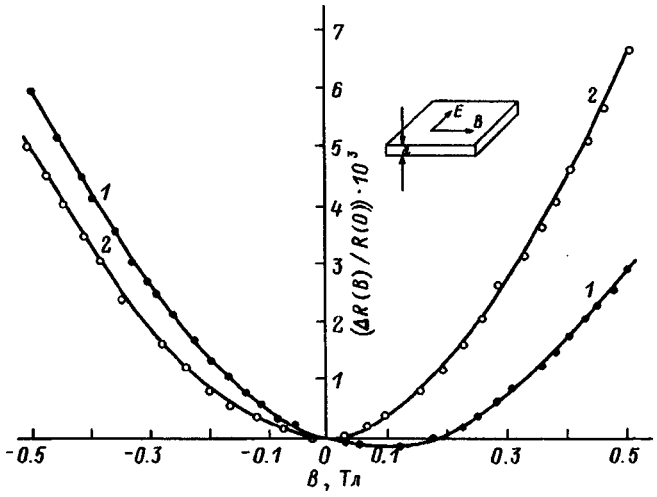

FIG. 1. Changes in the planar magnetoresistance in a magnetic field at $T=300$ K for samples 1 (curve *1*) and 2 (curve *2*). The sample parameters are listed in Table I.

TABLE I. Basic sample parameters.

Sample No.	x	d, μm	l, mm	$T=300$ K					
				μ_n, cm^2/(V·s)	μ_p, cm^2/(V·s)	τ_V, 10^{-8} s	τ_1, 10^{-8} s	S_1, cm/s	S_2, cm/s
1	0.22	7.5	2	7000	70	8	6.2	1500	2900
2	0.211	7.0	4	8000	80	4.2	3.5	2600	1000
3	0.211	6.0	3	7500	75	4.2	3	6300	2100

where S_1 and S_2 are surface recombination rates at the boundary between the epitaxial layer and a substrate (buffer layer) and at the free surface, respectively.

From Eq. (3) it follows that $EBA_1 \to 0$ for an epitaxial layer with ''n''-type conductivity at 77 K when $p/n \to 0$, whereas at room temperature ($n \approx p$) the linear term $EBA_1 \neq 0$ and the asymmetry in the function $\Delta R(B)$ should be observable as the magnetic field intensity varies. In a certain range of magnetic fields we may also observe negative magnetoresistance [$R(B) < R(0)$].

Once we determine the linear term A_1EB by measuring the planar magnetoresistance for known sample parameters we can determine the parameter α_3, and consequently the ratio of surface recombination velocities S_1/S_2.

We can determine absolute values of S_1 and S_2 by measuring the relaxation time of nonequilibrim charge carriers τ_1, which is related to the surface recombination by the standard relations[4]

$$1/\tau_1 = 1/\tau_V + D_p\lambda_1^2,$$
$$\tan \lambda_1 d = \frac{(S_1+S_2)D_p\lambda_1}{D_p^2\lambda_1^2 - S_1S_2}, \tag{6}$$

where τ_V is the bulk lifetime, D_p is the coefficient of minority carrier diffusion, and d is the epitaxial layer thickness.

For our experimental investigations we used tracy n-$Cd_xHg_{1-x}Te$/CdZnTe heterostructure samples grown by molecular beam epitaxy on semi-insulating GaAs substrates.[5] At room temperature we measured the magnetoresistance at constant current for voltages $U \simeq 1$ V applied to the sample. A microwave technique involving pulsed illumination of the sample by a semiconductor laser ($\lambda \simeq 0.92$ μm) was used to measure the relaxation time of nonequilibrium charge carriers τ_1.[4,6] In order to induce the condition $p \simeq n$ in samples cooled to liquid nitrogen temperatures, nonequilibrium charge carriers are generated in the bulk by applying voltage pulses ($\simeq 15$ ns) to the sample, which cause avalanche impact ionization. The microwave method used to measure τ_1, which is analogous to that described in Ref. 7, involves placing the sample at the center of the transverse cross section of a waveguide with dimensions 2×23 mm^2.

Figure 1 shows the dependences $\Delta R(B)/R(0)$ measured at room temperature for two samples prepared from epitaxial structures with CdTe contents $x_{CdTe} = 0.22$ and 0.211. The orientation of electric and magnetic fields shown in the inset implies that for positive directions of the magnetic field the carriers are concentrated at the epitaxial layer— ⟨buffer layer⟩ boundary, while for negative directions they are at the free surface. For the first sample (curve *1*) we have $S_1 < S_2$ and for the second we have $S_1 > S_2$. The values of S_1 and S_2 which we found, together with other parameters used in the calculations, are listed in Table I. It should be noted that room temperature the thickness of the film is comparable to the diffusion length [$d \simeq 1.3$–$1.6L_D$] and in the calculations we used the exact formulas from Ref. 3. The bulk lifetime τ_V is determined from calculations described in Refs. 4 and 6.

The measured magnetic field dependences for these samples when they are cooled to liquid-nitrogen temperatures are shown in Fig. 2. In a weak electric field the functions $\Delta R(B)/R(0)$ are symmetric (curves *1* and *2*), as follows from theory. After impact ionization in a strong electric field the curves exhibit substantial asymmetry and even a rather small negative magnetoresistance for sample 1 (curve *3*). In this case, a comparison of Figs. 1 and 2 reveals that at $T = 77$ K we have $S_1 > S_2$ for the first sample, while for the second sample (curve *4*) we have $S_1 < S_2$. Since at liquid-nitrogen temperatures we expect that $d \ll L_D$, we can use the simplified expression (4) to determine the value of the ratio S_1/S_2. The values of S_1 and S_2, together with other parameters, are listed in Table II. In a strong electric field the electron mobility decreases in proportion to $R(0)/R(E)$, where $R(E)$ is determined from the starting value of the current at the beginning of the pulse. The leading edge of the

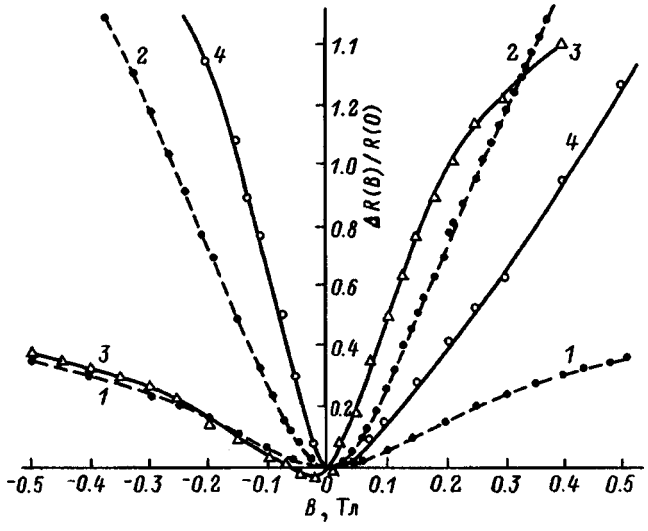

FIG. 2. Changes in the planar magnetoresistance in a magnetic field at $T = 77$ K for samples 1 and 2 in a weak electric field (curves *1* and *2* respectively) and in a strong electric field during avalanche impact ionization: 3—sample 1 ($U/l = 575$ V/cm, $n/n_0 = 2.8$), 4—sample 2 ($U/l = 365$ V/cm, $n/n_0 = 3.4$).

TABLE II. Sample parameters at $T=77$ K.

Sample No.	n_0, cm^{-3}	μ_n, $\mathrm{cm}^2/(\mathrm{V}\cdot\mathrm{s})$	μ_p, $\mathrm{cm}^2/(\mathrm{V}\cdot\mathrm{s})$	$\frac{U}{l}$, V/cm	$\frac{\mu_n(E)}{\mu_n(0)}$	$\frac{n}{n_0}$	τ_V, 10^{-6} s	τ_1, 10^{-6} s	S_1, cm/s	S_2, cm/s
1	7.5×10^{14}	4×10^4	400	575	0.5	2.8	5	0.9	420	280
2	3.2×10^{14}	1.16×10^5	800	365	0.67	3.4	3	2	51	64
3	3.2×10^{14}	7.4×10^4	800	440	0.48	2.9	3	1.25	131	146

voltage pulse is less than 1 ns in duration and avalanche impact ionization can be ignored. The resistance of the sample $R(0)$ is measured in a weak dc electric field ($U\simeq 1$ V). The level of carrier generation n/n_0 is determined from the ratio of currents at the end and the beginning of the pulse. Values of the bulk lifetime τ_V are established from a calculation as in Ref. 4, taking into account the concentration of electrons obtained from Hall measurements.

Sample 3, the results for which are listed in Tables I and II, was made from the same structure as sample 2. The difference between them was that the layer with increased CdTe content at the surface of the epitaxial layer was removed by etching. In this case, as is clear from Tables I and II, the relaxation time for nonequilibrium charge carriers τ_1 and the rate of surface recombination S_2 are greatly changed. Note also that the measured values of the surface recombination rate for $T=77$ K is much lower than at room temperature. Measurements of these quantities using the photomagnetic effect in Ref. 1 for an epitaxial layer with ''p''-type conductivity show conversely that when the sample is cooled surface recombination increases strongly.

As Pikus already pointed out in Ref. 2, even rather small differences between S_1 and S_2 can be detected by studying changes in the resistance of the magnetic field for sufficiently thin samples, and this method can be used to estimate the effect of various processing methods of the surface of the epitaxial layer on the surface recombination rate.

We wish to thank Yu. G. Sidorov for providing the epitaxial structures for making these measurements.

[1] G. Sarusi, A. Zemel, D. Eger, S. Ron, and Y. Shapira, J. Appl. Phys. **72**, 2312 (1992).
[2] G. E. Pikus, Zh. Tekh. Fiz. **26**, 22 (1956).
[3] D. L. Lile, J. Appl. Phys. **41**, 3480 (1970).
[4] P. A. Borodovskiĭ, A. F. Buldygin, and V. G. Remesnik, Fiz. Tekh. Poluprovodn. **28**, 2107 (1994) [Semiconductors **28**, 1159 (1994)].
[5] V. S. Varavin, S. A. Dvoretsky, V. I. Liberman, N. N. Mikhailov, and Yu. G. Sidorov, Thin Solid Films **267**, 121 (1995).
[6] P. A. Borodovskiĭ and A. F. Buldygin, Prib. Tekh. Eksp. **6**, 157 (1995).
[7] G. Nimtz, G. Bauer, R. Dornhays, and K. H. Muller, Phys. Rev. B **10**, 3302 (1974).

Translated by Frank J. Crowne

Physical model and results of numerical simulation of the degradation of a Si/SiO_2 structure as a result of annealing in vacuum

G. V. Gadiyak

Institute of Computer Technology, Russian Academy of Sciences (Siberian Department), 630090 Novosibirsk, Russia

J. H. Stathis

IBM Research Division, T. J. Watson Research Center, Yorktown Heights, New York 10598

(Submitted February 9, 1998; accepted for publication April 2, 1998)
Fiz. Tekh. Poluprovodn. **32**, 1079–1082 (September 1998)

A theoretical model is developed for the evolution of P_b-centers at a Si/SiO_2 boundary during annealing in vacuum. The model takes into account diffusion of atomic and molecular hydrogen and the reactions between the hydrogen and these centers at the boundary. The reaction constants are calculated in the diffusion approximation. The results of these calculations are found to agree with experiment in the temperature range 480°–800 °C and oxide thickness range 200–1024 Å for the (111) and (100) facets of silicon. © *1998 American Institute of Physics.* [S1063-7826(98)01409-4]

INTRODUCTION

The reaction of atomic hydrogen with defects at the boundary of a Si/SiO_2-structure is a matter of both scientific and technological interest. Contemporary silicon technology nearly always involves structures with a thermally grown oxide. The quality and functional properties of these structures depend primarily on the quality of the Si/SiO_2 interface. As devices continue to be miniaturized, the role of defects at this boundary increases. One method that is commonly used to decrease the influence of defects on the processes of carrier transport and degradation of these devices is to thermally process them in an atmosphere of hydrogen. Hydrogen atoms penetrate into the silicon dioxide and silicon, where they saturate the dangling bonds, thereby decreasing the density of defect states in the gap gap (including the density of surface states). Recent experimental and theoretical studies[1,2] have shown that in strong fields hot electrons can break off hydrogen atoms from the dangling bonds, thereby increasing the density of trapping centers. For this reason, there has been much interest recently in investigating the processes by which hydrogen interacts with defects and especially with defects at the Si/SiO_2 interface.[3–7] In those studies, the processes in which hydrogen participates are analyzed, and a scheme of chemical reactions between the defects and hydrogen is proposed. However, theoretical or computational investigations of these properties are yet to be carried out. In this paper we propose a scheme of chemical reactions and use them to derive a system of diffusion and rate equations which are solved numerically. The calculations are compared with the experimental data of Ref. 7.

PHYSICAL MODEL

Let us consider a structure consisting of a silicon substrate with a thermal oxide grown on it. The silicon substrate will have two possible facet orientations: (111) and (100). It is known that the Si/SiO_2 boundary contains so-called P_b-centers[8–10] which are related to dangling bonds in the silicon. For the (111) facet one state, referred to as P_b, is observed experimentally,[8,9] while on the (100) facet two states are observed, labeled P_{b0} and P_{b1}.[10] The number of states for the corresponding facet can be related to the coordination of an atom at the boundary and with the number of its dangling bonds. This analogy can be traced to quantum-chemistry calculations.[11] In these calculations, the saturation of dangling bonds of surface atoms by hydrogen leads to a decrease in the surface-state peak.[12] The densities of P_b-states were found to exhibit analogous regularities at the boundary in the experiments of, e.g., Refs. 7, 13, and 14.

Experimental studies (see Ref. 2) have shown that hydrogen is transported in the oxide in the neutral state, and can participate in reactions involving emission and passivation of P_b-centers. We can then write the following scheme of reactions on the (100) facet:

$$P_{b0}\mathrm{H} \rightleftharpoons^{k_2}_{k_1} P_{b0} + \mathrm{H}, \tag{1}$$

$$P_{b1}\mathrm{H} \rightleftharpoons^{k_4}_{k_3} P_{b1} + \mathrm{H}, \tag{2}$$

and on the (111) facet:

$$P_b\mathrm{H} \rightleftharpoons^{k_{12}}_{k_{11}} P_b + \mathrm{H}. \tag{3}$$

Here we assume that there are two independent P_b states at the (100) boundary, P_b-Pb0 and P_{b1}. The quantities k_1, k_2, k_3, k_4, k_{11}, and k_{12} are reaction constants for Eqs. (1)–(3). Furthermore, free atomic hydrogen can interact with the complex $P_b\mathrm{H}$ at the (111) boundary (a P_b-center saturated by hydrogen) or with hydrogen atoms at the P_{b0}- or P_{b1}-centers of the (100) facet. In this case we can write the following reaction for the (111) boundary:

$$P_bH+H \overset{k_{13}}{\Rightarrow} P_b+H_2, \tag{4}$$

and the (100) facet:

$$P_{b0}\mathrm{H}+\mathrm{H} \overset{k_5}{\Rightarrow} P_{b0}+H_2, \tag{5}$$

$$P_{b1}\mathrm{H}+\mathrm{H} \overset{k_6}{\Rightarrow} P_{b1}+H_2. \tag{6}$$

The system of chemical equations (1)–(6) can be written as a system of rate equations supplemented by the diffusion equation for the atomic and molecular hydrogen, as in Ref. 2:

$$\begin{aligned}\frac{\partial C_{\mathrm{H}}}{\partial t}=&\frac{\partial}{\partial x}\left(D_{\mathrm{H}}\frac{\partial C_{\mathrm{H}}}{\partial x}\right)-k_1C_{P_{b0}}C_{\mathrm{H}}+k_2C_{P_{b0}\mathrm{H}}\\&-k_3C_{\mathrm{H}}C_{P_{b1}}+k_4C_{P_{b1}\mathrm{H}}-k_5C_{P_{b0}\mathrm{H}}C_{\mathrm{H}}\\&-k_6C_{P_{b1}\mathrm{H}}C_{\mathrm{H}},\end{aligned} \tag{7}$$

$$\frac{\partial C_{P_{b0}\mathrm{H}}}{\partial t}=k_1C_{P_{b0}}C_{\mathrm{H}}-k_2C_{P_{b0}\mathrm{H}}-k_5C_{P_{b0}\mathrm{H}}C_{\mathrm{H}}, \tag{8}$$

$$\frac{\partial C_{P_{b0}}}{\partial t}=-k_1C_{P_{b0}}C_{\mathrm{H}}+k_2C_{P_{b0}H}+k_5C_{P_{b0}\mathrm{H}}C_{\mathrm{H}}, \tag{9}$$

$$\frac{\partial C_{P_{b1}\mathrm{H}}}{\partial t}=k_3C_{P_{b1}}C_{\mathrm{H}}-k_4C_{P_{b1}\mathrm{H}}-k_6C_{P_{b1}\mathrm{H}}C_{\mathrm{H}}, \tag{10}$$

$$\frac{\partial C_{P_{b1}}}{\partial t}=-k_3C_{P_{b1}}C_{\mathrm{H}}+k_4C_{P_{b1}H}+k_6C_{P_{b1}\mathrm{H}}C_{\mathrm{H}}, \tag{11}$$

$$\frac{\partial C_{\mathrm{H}_2}}{\partial t}=\frac{\partial}{\partial x}\left(D_{\mathrm{H}_2}\frac{\partial C_{\mathrm{H}_2}}{\partial x}\right)+k_5C_{P_{b0}\mathrm{H}}C_{\mathrm{H}}+k_6C_{P_{b0}\mathrm{H}}C_{\mathrm{H}}. \tag{12}$$

Here C_{H} and C_{H_2} are the concentrations of atomic and molecular hydrogen, $C_{P_{b0}}$ and $C_{P_{b1}}$ are the densities of states of P_{b0}- and P_{b1}-centers, and $C_{P_{b0}\mathrm{H}}$ and $C_{P_{b1}\mathrm{H}}$ are densities of states of these centers passivated by hydrogen, respectively. D_{H} and D_{H_2} are diffusion coefficients for atomic and molecular hydrogen. For the diffusion equations we use the following boundary conditions:

$$-D_{\mathrm{H}}\frac{\partial C_{\mathrm{H}}}{\partial x}(0,t)=k_{a1}C_{\mathrm{H},amb}-k_{a2}C_{\mathrm{H}}(0,t), \tag{13}$$

$$-D_{\mathrm{H}_2}\frac{\partial C_{\mathrm{H}_2}}{\partial x}(0,t)=k_{a3}C_{\mathrm{H}_2,amb}-k_{a4}C_{\mathrm{H}_2}(0,t), \tag{14}$$

where k_{a1}, k_{a3} and k_{a2}, k_{a4} are coefficients of adsorption and penetration of atomic and molecular hydrogen at the oxide surface, and $C_{\mathrm{H},amb}$ and $C_{\mathrm{H}_2,amb}$ are the concentrations of atomic and molecular hydrogen in the vacuum chamber. Deep in the silicon we can either specify the concentration of hydrogen or set the diffusion flux for atomic and molecular hydrogen equal to zero (a Neumann condition). At the Si/SiO_2 boundary we specify the condition of matching for diffusion fluxes of the components. In the diffusion equations (7) and (12), the coefficients D_{H} and D_{H_2} were different for the oxide and silicon and are specified by Arrhenius functions of temperature. The parameters for values of the pre-exponential factor and diffusion activation energy were taken from the literature.[15] The values for adsorption and penetration coefficients were taken from Ref. 2. In order to obtain the coefficients k_1, k_3, k_5, k_6, k_{11}, and k_{13} we used the diffusion approximation,[2,16] according to which they are calculated from the expression

$$k_i(T)=4\pi D_{\mathrm{H}}(T)r_0\xi_i, \tag{15}$$

where r_0 is the interaction radius for hydrogen with a P_b-center, usually equal to 10 Å, ξ_i is a fitting parameter, in our case equal to 1 in all the calculations, and i takes on the values 1, 3, 5, 6, 11, and 13 in accordance with the values of the reaction coefficients [Eqs. (1)–(6)]. For reaction coefficients k_2, k_4, and k_2 we used expressions of the form

$$k_j=f_j^{-1}\times\exp(-\delta E_{aj}/k_{\mathrm{B}}T), \tag{16}$$

where j takes on values 2, 4, and 12, (f_j^{-1}) is a frequency factor connected with vibration of the SiH bond, which in our case is of order $(10^{12}-10^{13})$ s^{-1}, and δE_{aj} is the energy needed to activate the emission of the hydrogen atom from a P_b-center on the (111) or (100) facets. The values of the parameters are listed in Table I.

TABLE I.

		E_a — activation energy, eV	$(f_a)^{-1}$ — frequency factor, s^{-1}
P_b^{111}	7	2.78	2×10^{13}
P_{b0}^{100}		2.86	2×10^{13}
P_{b1}^{100}		2.91	2×10^{13}
P_b^{111}	13	2.58	1.2×10^{12}
P_b^{111}	14	2.41	1×10^{11}

METHOD OF CALCULATION

We used an implicit scheme to solve the system of equations (7)–(12) numerically. The time derivatives were approximated by first-order differences, and the time step was allowed to increase from 10^{-9} s to 10^2 s with a growth rate $\delta t^n/\delta t^{n-1}=1.1$. In order to approximate the spatial derivatives we used a conservative scheme with second-order accuracy on a nonuniform grid. Various numbers of nodes were used in the calculations $N=10$, 200, 300. Comparison of these calculations showed that the results for a grid with a node number of 100 differed by less than 0.1% from results for grids with node numbers of 200 and 300. The nonlinear system of difference equations was solved by a successive scalar tridiagonal inversion using solutions from the previous iteration. The program was written in Fortran 77. The calculations were done on an IBM PC with a Pentium processor and a clock frequency of 150 MHz. The characteristic time for completing the computation with a grid number $N=200$ was 1 minute. The initial concentration of free hydrogen was set equal to zero. The experiments of Ref. 7 imply that the P_b-centers are initially saturated with hydrogen up to values of 3×10^{12} cm^{-2} for P_b^{111}, 3×10^{11} cm^{-2} for P_{b0}^{100}, and 6×10^{11} cm^{-2} for P_{b1}^{100}.

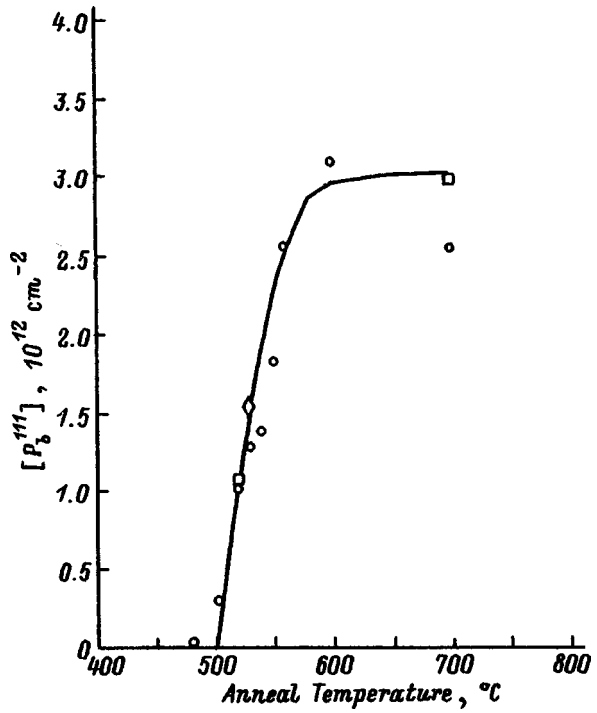

FIG. 1. Temperature dependence of the density of states of P_b-centers on the (111) surfaces of Si/SiO_2-structures with various oxide thicknesses annealed in vacuum. Solid curves—calculation; experiments of Ref. 7: circles— $L_0=254$ Å, diamonds— $L_0=254$ Å in an ROA atmosphere (see Ref. 7).

RESULTS OF CALCULATIONS AND DISCUSSION

In order to compare the results of calculations with experiment we tracked the evolution of the defect density P_b numerically for three oxide thicknesses— 204, 254, and 1024 Å — over a wide temperature range (480–800) °C for both surface orientations (111) and (100) in the course of a two hour vacuum anneal. These parameters correspond to annealings of structures in the experiments of Ref. 7. For calculating the reaction constants k_i in Eq. (15) we used values $r_0=10^{-7}$ cm and $\xi_i=1$, with values of the diffusion coefficients taken from the literature.[15] For calculating the reaction constants Eq. (16), the authors of Ref. 7 assumed values of the activation energy δE_{aj} and frequency factor f_j^{-1}, obtained by processing experimental curves. In this paper we used their data for the (111) and (100) facets. We compared the data of Ref. 7 with data presented in Refs. 13 and 14.

Figure 1 shows the density of P_b-centers for various thicknesses of a (111) oxide layer after a two-hour anneal in vacuum as a function of anneal temperature. Here we show the experimental data of Ref. 7. Good agreement is obtained between calculations and experiment when the parameters used are those given in the experiments of Ref. 7. This result indicates that the kinetics of releasing hydrogen from P_b-centers under these conditions is completely dominated by the binding energy of the hydrogen atom to a center and depends only slightly on the other parameters of the problem, such as the diffusion coefficient D_{H}, the adsorption coefficients (k_{a1},k_{a3}), and the penetration coefficients (k_{a2},k_{a4}) for hydrogen [Eq. (14)]. In other words, characteristic diffusion times for the process are much less than the relaxation time for hydrogen at P_b states for a two-hour anneal. Further evidence for this is the coincidence of the curves shown in Fig. 1 for various oxide thicknesses (254 and 1024 Å). In order to confirm the weak dependence of the annealing results on the diffusion coefficient, we ran calculations over a wide range of values of D_{H} (see Table II) and for various anneal temperatures. In order to make comparison easier, we list here the relative values of the density of states for P_{b0}- and P_{b1}-centers on the (100) facet. Results were normalized by the maximum value of the density of the corresponding state P_{b0} or P_{b1}. As is clear from the table, the latter begins to affect the value of the relative density of states P_b only for large decreases in the diffusion coefficient.

The results of varying the activation energy and frequency factor used in Refs. 7, 13, and 14 show that the density of states of P_b-centers is quite insensitive to their values. We note that the energy variations were from 2.41 to 2.78 eV, while the frequency factor was varied from 10^{11} s^{-1} to 2×10^{13} s^{-1} (see Table I). This wide scatter in values of these parameters attests to the need to pursue additional experimental data in order to choose them unambiguously. The value of the frequency factor $\sim10^{13}$ s^{-1} used in Ref. 7 is close in magnitude to the characteristic frequency of vibrations of the Si-H bond. Therefore, the parameters assumed in Ref. 7 for the frequency factor and energy for emission of a hydrogen atom from a P_b-center have more realistic physical justification, in our opinion, than the values used in Refs. 13 and 14. The computed and experimental values for the densities of states of P_{b0} and P_{b1} on the (100) facet also are found to be in good agreement. Both in the calculation and in experiment the value of the normalized density of states P_{b1} is always smaller in magnitude than the value of the density of states P_{b0}.

We also computed the density of states for the (100) facet in a model of dependent states P_{b0} and P_{b1}. If we assume that each atom of the (100) facet has two dangling

TABLE II.

Temperature T,°C	diffusion coefficients D_{H} (cm^2/s)	k_1, cm^3/s	k_3, cm^3/s	P_{b0}	P_{b1}
600	0.608×10^{-8}	0.7646×10^{-14}	0.7646×10^{-14}	0.903	0.814
600	0.608×10^{-12}	0.7646×10^{-18}	0.7646×10^{-18}	0.917	0.828
500	0.173×10^{-8}	0.2178×10^{-14}	0.2178×10^{-14}	0.058	0.040
500	0.173×10^{-12}	0.2178×10^{-18}	0.2178×10^{-18}	0.054	0.036

bonds connected with states P_{b0} and P_{b1}, then the occupation of these states by hydrogen atoms takes place in sequential fashion, starting with P_{b1} and only then state P_{b0}. This scheme of occupation of the state P_b by hydrogen changes the form of the reaction scheme. Instead of reactions (5) and (6) between hydrogen and centers occupied by hydrogen (P_{b0}H)- and (P_{b1}H), only reaction (5) is possible for hydrogen with a (P_{b0}H)-center. For the modified system of Eqs. (7)–(12) we ran calculations that showed worse agreement with experiment than those discussed above. Therefore, we can assume that the states P_{b0} and P_{b1} are probably connected with two different geometric configurations of the defect for a silicon atom at the Si/SiO_2 boundary.

In conclusion we note that this is the first paper to discuss a new model for describing the evolution of P_b-centers during vacuum annealing. We have chosen parameters whose values lie within physically justifiable intervals. We have achieved excellent agreement with experiment in a wide temperature range (500–800) °C and thickness range. This model can be easily generalized to calculations of the annealing of Si/SiO_2-structures with various types of doped substrates (p and n) and for describing annealing of new types of defects, which were observed, for example, in Refs. 6 and 17.

This work was carried out with the support of a grant from the Russian Fund for Fundamental Research No. 96- 01-00137.

[1] D. A. Buchanan, D. J. DiMaria, A. D. Marwick, and L. Dory, Appl. Phys. **76**, 3595 (1994).
[2] G. V. Gadiyak, Fiz. Tekh. Poluprovodn. **31**, 257 (1997) [Semiconductors **31**, 207 (1997)].
[3] K. L. Brower and S. M. Meyers, Appl. Phys. Lett. **57**, 162 (1990).
[4] D. L. Griscom, J. Electron. Mater. **21**, 763 (1992).
[5] J. H. Stathis and E. Cartier, Phys. Rev. Lett. **72**, 2745 (1994).
[6] E. Cartier and J. H. Stathis, Microelectron. Eng. **28**, 3 (1995).
[7] J. H. Stathis, J. Appl. Phys. **77**, 6205 (1995) [Erratum: J. Appl. Phys. **78**, 5215 (1995)].
[8] K. L. Brower, Appl. Phys. Lett. **43**, 1111 (1983).
[9] P. M. Lenahan and P. V. Dressendorfer, J. Appl. Phys. **55**, 3495 (1984).
[10] E. H. Poindexter, P. J. Caplan, B. E. Deal, and R. R. Razouk, J. Appl. Phys. **52**, 879 (1981).
[11] G. V. Gadiyak, Yu. N. Morokov, A. A. Karpushin, and M. Tomasek, Czech. J. Phys., Sect. B **35**, 54 (1985).
[12] G. V. Gadiyak, A. A. Karpushin, I. V. Korolenko, Yu. N. Morokov, I. Yu. Semenova, A. N. Sorokin, and M. Tomashek, Surfaces: Physics, Chemistry, Mechanics **9**, 72 (1986) [in Russian].
[13] K. L. Brower, Phys. Rev. B **42**, 3444 (1990).
[14] R. Khatri, P. Asoka-Kumar, B. Nielsen, L. O. Ruelling, and K. G. Lynn, Appl. Phys. Lett. **65**, 330 (1994).
[15] D. Fink, J. Krauser, D. Nagengast, T. Almeida Murphy, J. Exmeier, J. Palmetshofer, D. Brauning, and A. Weidinger, Appl. Phys. A: Mater. Sci. Process. **61**, 381 (1995).
[16] G. V. Gadiyak, G. A. Kachurin, I. I. Shatrov, and I. E. Tyschenko, Fiz. Tekh. Poluprovodn. **32**, 111 (1992) [Semiconductors **32**, 109 (1992)].
[17] E. Cartier and J. H. Stathis, Appl. Phys. Lett. **69**, 103 (1996).

Translated by Frank J. Crowne

LOW DIMENSIONAL SYSTEMS

The effect of a nonmonotonic potential profile on edge magnetic states

E. B. Gorokhov, D. A. Romanov, S. A. Studenikin, and V. A. Tkachenko

Institute of Semiconductor Physics, Russian Academy of Sciences (Siberian Department), 630090 Novosibirsk, Russia

O. A. Tkachenko

Novosibirsk State University, 630090 Novosibirsk, Russia

(Submitted May 5, 1997; accepted for publication May 20, 1997)
Fiz. Tekh. Poluprovodn. **32**, 1083–1088 (September 1998)

The dispersion law for electrons moving along a specularly reflecting boundary of a two-dimensional electron gas in the presence of a near-boundary potential well and a weak magnetic field is investigated theoretically. Numerical simulation is used to identify a number of features of the density of edge magnetic states that can be observed by magnetotransport and magnetooptics investigations. Ways to fabricate structures for studying these states are discussed. It is demonstrated that perfect-crystal interterrace boundaries can be created for a two-dimensional electron gas by introducing oblique slip planes into the heterostructure.
 [S1063-7826(98)01509-9]

I. INTRODUCTION

Edge magnetic states (EMS) have recently been successfully used in recent times to explain various experiments on quasi- two-dimensional (2D) electron gases in strong magnetic fields, in particular the integer-valued quantum Hall effect and Shubnikov-de Haas oscillations in semiconductor heterostructures.[1] In fact, EMS are the only current carrying states in the quantum-Hall-effect regime; therefore, they are responsible for all the phenomena of electron transport in quantizing magnetic fields.

During the earlier stages of investigating EMS, the edge of the region where an electron gas exists was treated simply as a geometrical boundary. This was followed by inclusion of the smooth electrostatic barrier of the depletion layer, and features of electronic screening in the quantum-Hall-effect regime were discussed extensively in Refs. 2, 3, and 4. Until, there have been no further discussions of more complex natures or shapes of the potential near the boundary. This is not surprising, since at low temperatures and strong magnetic fields the current-carrying quasi-1D quasiparticles are pressed tightly against the boundary and can avoid scattering by fluctuation-induced obstacles in the potential around them. In the one-electron picture, regardless of the behavior of the potential near the boundary, the current in the final analysis is determined by the number of Landau levels below the Fermi level far from the boundary, where the potential and electron gas are assumed to be uniform, the simplest regime from a theoretical point of view.

The situation changes radically in weaker magnetic fields, where scattering can no longer be ignored. In this case we can find the current along the boundary by solving the kinetic Boltzmann equation, in which we should use the dispersion relation for carriers in edge magnetic states. This dispersion relation, in turn, is determined by solving the Schrödinger equation with a specific profile for the near-boundary potential. The roadmap to solving this problem (taking into account collisions and the combined action of magnetic, electric, and high-frequency fields on an electron) as applied to EMS has not yet been fully identified. However, a number of useful conclusions from the point of view of experiment can be derived directly from analyzing the form of the dispersion relation, as we will show below by numerically simulating the edge current states.

Here a relevant analogy with magnetic surface levels for three-dimensional crystals is worth mentioning. Magnetic surface levels, which were first observed as peculiar resonance peaks in the rf impedance of metals at very weak magnetic fields,[5] were later identified from their contributions to a number of static effects in semiconductors.[6,7] As was shown, these latter effects can significantly affect the character of the surface potential.[8] Edge magnetic states in a two-dimensional electron gas have considerable advantages compared to the three-dimensional case with regard to further investigations (and possible applications) of these phenomena.

Contemporary methods for growing GaAs/AlGaAs structures make it possible to obtain mean-free pathS for an electron in the 2D gas greater than 10 μm. Methods available today for lithography allow us to create various shapes of the potential wells on scales smaller than the mean-free path of an electron. For example, by using a system of gate electrodes we can vary the depth and width of the potential well for a 2D electron gas in the lateral direction. This creates unique possibilities for controlling the dispersion relation of edge magnetic states by using a nonmonotonic profile for the edge potential. In other words, it is possible to ''prepare''

edge magnetic states beforehand with prespecified properties which should make themselves felt through static and high-frequency transport effects.

In this study we have primarily carried out a theoretical investigation of the dispersion relation of 2D electrons that ''hop'' along the boundary under the combined action of a weak magnetic field and a boundary electrostatic potential (created, e.g., by a strip-shaped gate electrode). We will also discuss some promising applications for EMS engineering.

THEORY

In order to avoid unnecessary complications, we will disregard spin and many-particle effects and concentrate on the orbital motion of a single electron. Let its motion be bounded by the region $y>0$ in the xy plane, so that the boundary of interest to us becomes the curve $y=0$. A uniform magnetic field H is directed along the z axis, and the vector potential is written using the Landau gauge $\mathbf{A}=(-Hy,0,0)$. For this choice the Hamiltonian of an electron has no explicit dependence on x. Therefore, we will look for a wave function in the form $\Psi(x,y)=\psi(y)\exp(ik_x x)$, where $\psi(y)$ satisfies the one-dimensional Schrödinger equation

$$-\frac{\hbar^2}{2m}\frac{\partial^2\psi}{\partial y^2}+\left[U(y)+\frac{m\omega_c^2}{2}(y+k_x l_B^2)^2\right]\psi=E_n(k_x)\psi, \tag{1}$$

where $\omega_c=eH/mc$ is the cyclotron frequency, $l_B=(c\hbar/|eH|)^{1/2}$ is the magnetic length, and $U(y)$ is the boundary potential. The dispersion relation of interest to us, i.e., the dependence of E_n on momentum $p_x=\hbar k_x$ in Eq. (1), is determined by the dependence on the position of the vertex of the magnetic parabola $y_0=-k_x l_B^2$ (which corresponds to the center of the classical electron orbit).

The bulk Landau levels are degenerate with respect to the position of the center of the orbit; therefore, E_n does not depend on k_x in any way. However, this dependence does appear when y_0 is comparable to the Larmor length $l_B\sqrt{n}$. This is because the range of motion of an electron is limited to only a portion of the magnetic parabola, a consequence of which is that the energy of a level with a given n increases with decreasing y_0. One result of this is the well-known picture of $E_n(k_x)$ curves for the usual EMS: these curves are equidistant and parallel to the abscissa for $y_0 \gg l_B\sqrt{n}$ and diverge like a fan as $y_0\to-\infty$.

The presence of a positive boundary potential $U(y)>0$ leaves this picture unmodified except for changing the rate of divergence of the curves for $y_0<0$. However, the situation changes qualitatively for $U(y)<0$. In this case the energy E_n obviously must lie below its bulk value for certain values of y_0, so that the dispersion curves become nonmonotonic. This phenomenon can be easily illustrated in the strong magnetic field limit, for which $l_B \ll w$, where w is the characteristic width of the boundary potential. In this case levels $E_n(y_0)$ follow the potential well adiabatically in the region $y>0$, so that this well is immediately transformed into the shape of the dispersion curves.

A more general case where a nonmonotonic potential profile affects the form of the dispersion curves was studied in Ref. 8 in the framework of the quasiclassical approximation. However, the most interesting situation (and probably the situation closest to experimental realization), when the magnetic length is comparable to the characteristic width of the boundary potential well, i.e., $l_B\sim w$, has not been analytically investigated. In this paper we obtain curves $E_n(y_0)$ for this situation numerically. In this case, for concreteness we use the characteristic parameters of a GaAs/GaAlAs heterostructure with a very thick spacer. The boundary potential is assumed to be created by a strip-like gate electrode.

A stipulation regarding the thickness of the spacer is of fundamental importance. The analogy with three- dimensional magnetic surface levels, whose observation requires perfect single-crystal surfaces,[5–7] indicates the importance of the specular reflection condition for electrons from the boundary. Therefore, in the case of EMS of a 2D electron gas a problem arises involving the fluctuation-induced potential at the boundary of the depletion region. The characteristic spatial scale l of these fluctuations corresponds to an average distance of order 10 nm between charged impurities in the δ-doped GaAlAs layer. It is known, for example, that scattering by this potential strongly decreases the mean-free path of electrons in quantum wires compared to a 2D gas.[4] This scattering can be avoided by placement of strip-like gates on structures with a very thick spacer. The boundary of the 2D gas will then be determined by a smooth rise in potential over a characteristic distance L of several hundred nanometers. This size determines the distance between the region of electron accumulation near the turning point and the region where the potential becomes strongly fluctuation-dominated. The condition $l \ll L$ allows us to assume that reflection of electrons from the boundary is specular and in calculating their dispersion relation we may use a one-dimensional potential well.

NUMERICAL RESULTS AND DISCUSSION

In order to find the dispersion relation $E_n(y_0)$ we numerically solved Eq. (1) for a certain realistic form of the boundary potential, using the ''QUANTUM'' program package described in Ref. 9. The boundary potential well $U(y)$ has the form illustrated in the inset in Fig. 1, with a width $w=500$ nm, which can be obtained by using contemporary lithographic methods.

Figure 1a shows the computed dispersion curves for EMS when the magnetic field intensity $H=0.3$ T, i.e., for the case where the cyclotron radius r_c and effective width of the potential w are the same order of magnitude ($r_c\simeq w$). It is clear that the character of the spectrum differs significantly from the picture discussed above. In particular, additional horizontal segments appear on the $E_n(y_0)$ curves, and the energy spacing ΔE between segments of neighboring levels considerably exceeds the value of the bulk quantum $\hbar\omega_c$. Near the Fermi level (2 to 4 meV for a typical GaAs/AlGaAs heterostructure) this distance turns out to be $\Delta E=1.4\hbar\omega_c$.

As is well known,[8] such horizontal segments in the dispersion law give rise to additional singularities in the electron density of states $\nu\sim(\partial E_n/\partial p_x)^{-1}$, which can lead to the appearance of additional peaks in the static conductivity

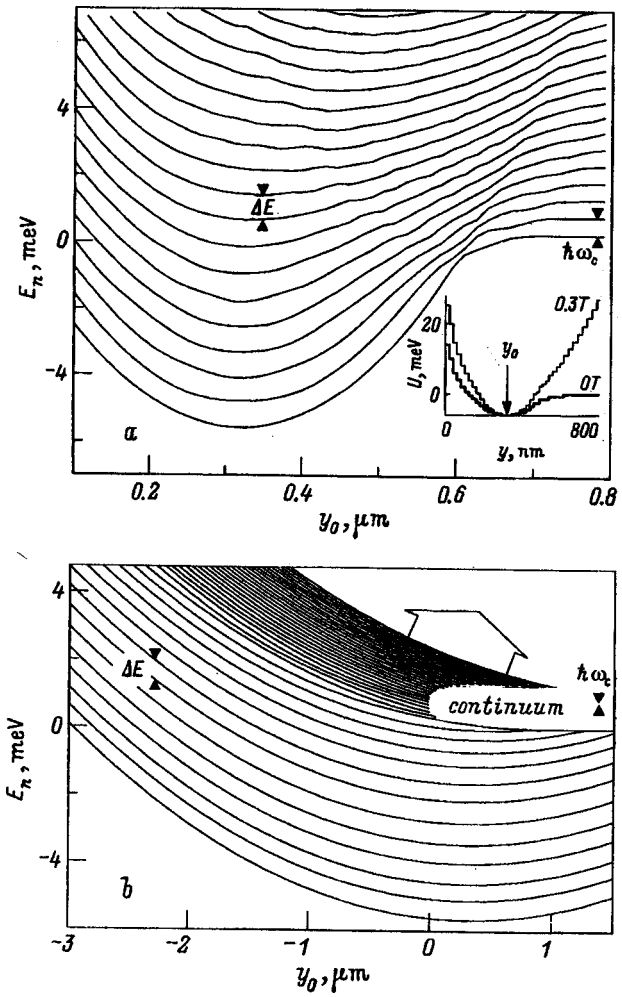

FIG. 1. Dispersion relation $E_n(y_0)$ of quasi-one-dimensional electrons in a weak magnetic field B as a function of the position of the center of the magnetic parabola (y_0) in the presence of an electrostatic potential well near the edge of the two-dimensional electron gas in a GaAs/AlGaAs structure with B, kG: a — 3, b — 0.2. The quantum number n increases by steps of unity starting from the lowest curve ($n=0$) to the uppermost, which corresponds to the following values of n: a — 18, b — 38. The white arrow in Fig. b represents the transition to a quasi-continuum spectrum. With increasing y_0, the curves asymptotically approach Landau levels $E_n=h\omega_c(n+1/2)$. In the calculations the gate-controlled electrostatic potential $U(y)$ and effective potential $U(y,y_0)$ are represented by piecewise-constant functions, as shown in the inset in Fig. a for one value of y_0.

when one of the horizontal segments passes through the Fermi level as the magnetic field varies. These new oscillations should appear against a background of the usual Shubnikov-de Haas oscillations; however, they will also exist in the high-temperature region (or at lower magnetic fields), where the latter are already washed out (this is an immediate result of the fact that ΔE is larger than the cyclotron quantum).

For weak magnetic fields ($r_c \gg w$) the situation differs greatly from the previous one. This case is illustrated in Fig. 1b. It is clear that in this case all the additional features of the density of states turn out to lie considerably below the energy region of interest near the Fermi level. In this region of interest the $E-y_0$ plane is clearly divided into two parts—a region of large interlevel spacings ($\Delta E \gg \hbar\omega_c$) and a region of small interlevel spacings ($\Delta E \simeq \hbar\omega_c$), in which the behavior of the dispersion curves is qualitatively different. In the second of these regions the dispersion curves are virtually indistinguishable from bulk Landau levels, while in a considerable portion of the first region they have nearly the same slope. The latter fact is connected with the smooth increase of the boundary potential shown in Fig. 1a, which leads to a strong singularity in the *reduced* density of states $\tilde{\nu} \sim [\partial(E_n - E_{n-1})/\partial p_x]^{-1}$. Therefore, this type of EMS should be easy to see in high-frequency experiments, for example in reflection spectra (of the type discussed in Ref. 10 or absorption due to interlevel transitions near the Fermi level (note that in contrast to the classical experiments,[5] the character of these transitions is controlled by the strip-like electrode).

In the range of system parameters under discussion, the predicted effects should be small, depending on whether the ratio of l_B to the width of the region occupied by the 2D electron gas is small or not. They nevertheless can be observed and studied experimentally because of their strong dependence on the boundary potential mentioned above, which suggests that modulation methods can be used successfully.

3. PROMISING WAYS TO ENGINEER EDGE MAGNETIC STATES

The specific example of EMS with a nonmonotonic dispersion relation discussed here involves structures with a wide spacer and a strip-like gate on the surface located roughly 500 nm from the edge of the 2D electron gas. However, analogous EMS can be studied without using strip-like metallic gates or thick spacers. In principle, it is enough to cut the 2D electron gas into two half-planes and apply a potential difference to them. In this case, a one-dimensional potential well will appear on one side of the cut whose parameters can be controlled by varying the potential on the other side. For example, in order to cut the 2D gas, we can etch out a line trench in the structure and thereby bring the depletion region close to the plane of the 2D gas along the corresponding line. However, in this case electrons in the edge potential well will be subjected to strong scattering in weak magnetic fields by the fluctuation-induced potential.

Another approach is to etch through the plane where the 2D electron gas is located, with subsequent regrowth of barrier material in the resulting line trench. In this case we succeed in avoiding the creation of a region of strong depletion (i.e., the appearance of a fluctuation-induced potential); however, the lateral boundaries of the 2D electron gas will be irregular, reflecting the complicated spatial profile of the edges of the trench.

The question of how strongly the expected roughness can affect the study of EMS in weak magnetic fields remains open. Therefore, in this paper we propose a new and original method for introducing perfect-crystal lateral barriers into the plane of the 2D electron gas. What we propose is to use slip planes that arise during plastic deformation of a sample. The principal features of such a slip plane are the following:

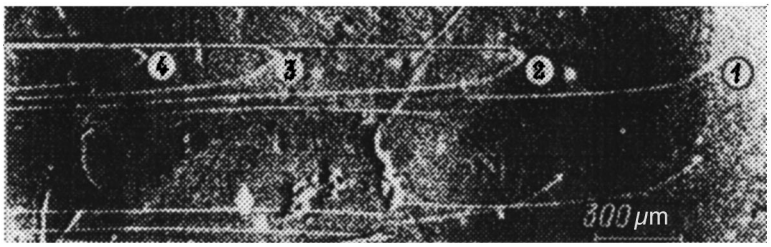

FIG. 2. *X*-ray topogram of a Ge sample coated with a glassy film of SiO_2, in which the development of mechanical stresses during annealing causes the generation of dislocations and their glide in crystal planes inclined to the surface. The horizontal line at the top is a step at the surface of (111) Ge. Numbers *1–4* denote heights in monolayers of the corresponding segments of the step and enumerate dislocation loops in the bulk of the Ge generated by a Frank-Reed source in one (111) slip plane.

1) the slip is caused by the creation (or exit at the surface) of a series of dislocations by a so-called Frank-Reed source, whose glide motion is restricted to some particular atomic plane of the family {111};

2) the magnitude of the slip (or height of the step) can be varied over an extremely wide range, and exactly corresponds to the number of gliding (or exiting at the surface) dislocations;

3) in regions free of dislocations there is no destruction of the crystal structure of the sample along the glide plane (i.e., after the slip the atomic half-planes once more join up with new half-planes without causing damage at the points of rupture). Thus this method can create an ideally smooth edge for the 2D gas, which is important for avoiding undesirable fluctuations in the boundary while studying EMS.

These features of slip planes were previously studied in detail using *x*-ray topograms and electron diffraction microscopy on single crystals of Ge (see Ref. 11). An example from this paper is reproduced in Fig. 2. In the upper part of the *x*-ray topogram a straight line is clearly visible—a sharp step on the (111) surface of the film. The step is formed by dislocations *1*, *2*, *3*, and *4* lying in a single atomic plane which is oblique to the sample plane (parallel to the plane of the photograph) so that we can observe the upper and lower segments of the dislocation loops in projections onto the crystal surface. It is clear that the upper segments of all dislocation loops generated by a single Frank-Reed source exit the surface of the sample with the formation of steps, while the height of a step increases by one interatomic distance (0.35 nm) with the creation of each new dislocation (the numbers 1, 2, 3, and 4 denote segments of the step, with heights in accordance with the number of monolayers). The layer segments of the dislocations pass into the depth of the crystal, located one on top of another in a single slip plane. In the lower part of the photograph we see two other dislocations, similar to the first slip bands, which are formed by the creation of single dislocation loops generated by other Frank-Reed sources, and the same type of planes inclined 54° to the sample surface.

We made a preliminary study of the possibility of introducing analogous slip planes into a GaAs/AlGaAs heterostructure with a 2D electron gas. Figures 2 and 3 show that it is possible to introduce perfect-crystal oblique slip in heterostructures for terracing of buried quantum wells. Slip bands can be created in a sample with a heterostructure that is clamped in a quartz cell by thermal expansion. The resulting slip does not interfere with photolithographic contouring of the sample surface, nor with the coating of the surface with gold contact areas. The corresponding abrupt steps at the surface of the structure (with heights of more than several tens of interatomic distances) are clearly visible in a Nomarski microscope in the form of long straight lines (Fig. 3). Segments of the bulk of the heterostructure on different sides of the slip plane are shifted relative to one another by the same number of interatomic distances as the sample surface. In this case a part of a GaAs half-plane of the buried quantum well matches up with the AlGaAs half-planes of the barrier. When the magnitude of this shift exceeds the width of the quantum well, the 2D electron gas is cut into two independent half-planes, each of which is bounded by an atomically sharp and structurally perfect rectangular lateral

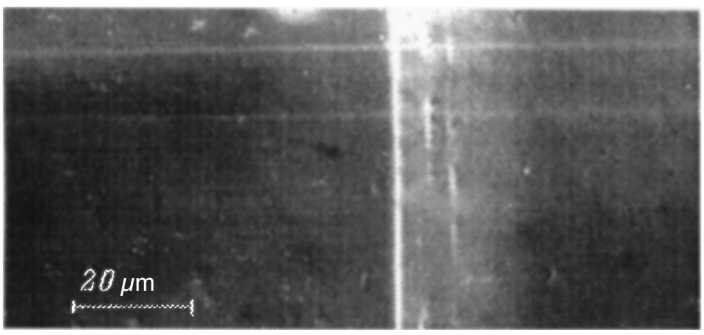

FIG. 3. An optical microphotograph of a segment of the surface of a GaAs/AlGaAs structure obtained by using a diffraction-contrast attachment to a Nomarski microscope. The horizontal line at the top is a step formed by slip bands in 111 planes. The vertical region at the center is a photolithographic relief with a mild slope that is generated before the creation of the slip band.

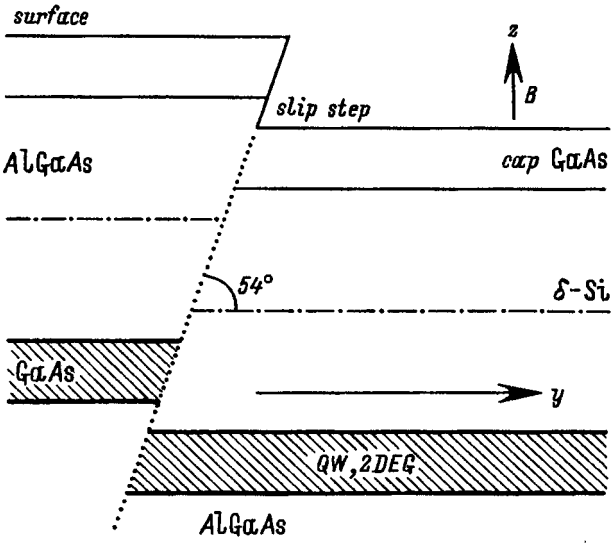

FIG. 4. Schematic diagram for terracing a buried quantum well. The dots represent the (111) slip plane.

barrier (Fig. 4). Confirmation of the latter assertion should be the subject an individual study.

In using such structures for the modulation of EMS described above, the boundary potential well at the edge of the half-plane of the electron gas can be created not only by a strip gate at a distant surface of the structure, but also by an external electric field (a voltage applied to neighboring terraces). In fact, lateral potential wells and barriers in the broken half-planes arise even at zero voltage, because at the junction the half-plane of the δ-doped donor layer in the AlGaAs turns out to be closer to the edge of the ''half-layer'' of a quantum well which lies on the other side of the slip plane. A solid upper metallic gate electrode (lower semiconducting electrode) can be used for additional control of the 2D electron gas concentration.

CONCLUSIONS

In this paper we have proposed and theoretically investigated a new type of edge magnetic state. These states possess an unusual dispersion relation which can be controlled by using an edge potential. The predicted features of these gates should lead to their experimental manifestation in the static kinetic characteristics, and also in the spectra of high-frequency and infrared absorption in weak magnetic fields. Further development of the method of modifying the EMS with the help of gate electrodes and terracing of buried quantum wells opens up the possibility of intentional creation of quasiparticles with predetermined and variable properties.

This work was supported in part by grants from the Russian Fund for Fundamental Research Nos. 96-02-19371*a* and 96-02-19187*a*, and also the Interdepartmental Scientific Research Program ''Physics of Solid-State Nanostructures'' (Grant No. 97-2025).

[1] R. J. Haung, Semicond. Sci. Technol. **8**, 131 (1993).
[2] D. B. Chklovskii, B. I. Shklovskii, and L. I. Glazman, Phys. Rev. B **46**, 4026 (1992).
[3] D. B. Chklovskii, K. A. Matveev, and B. I. Shklovskii, Phys. Rev. B **47**, 12605 (1993).
[4] K. Ismail, in *Nanostructures and Quantum Effects*, Springer Series in Material Science, edited by H. Sakaki and H. Noge (1994), Vol. 31. p. 61.
[5] M. S. Khaĭkin, Usp. Fiz. Nauk **96**, 409 (1968) [Sov. Phys. Usp. **11**, 785 (1970)].
[6] E. M. Skok, S. A. Studenkin, H. Hefele, and H. Pascher, JETP Lett. **37**, 554 (1983).
[7] V. T. Dolgopolov and S. S. Murzin, JETP Lett. **37**, 696 (1983).
[8] D. A. Romanov and L. D. Shvartsman, Solid State Commun. **53**, 677 (1985).
[9] V. A. Tkachenko, O. A. Tkachenko, G. L. Kotkin, and V. G. Tupitsin, Physica B **175**, 75 (1991).
[10] L. I. Magarilli, I. A. Panaev, and S. A. Studenikin, J. Phys.: Condens. Matter **7**, 1101 (1995).
[11] E. M. Trukhanov, E. B. Gorokhov, and S. I. Stenin, Phys. Status Solidi A **32**, 432 (1976).

Translated by Frank J. Crowne

Formation and passivation of defects in heterostructures with strained GaAs/InGaAs quantum wells as a result of treatment in a hydrogen plasma

I. A. Karpovich, A. V. Anshon, and D. O. Filatov

N. I. Lobachevskiĭ State University at Nizhniĭ Novgorod, 603600 Nizhniĭ Novgorod, Russia
(Submitted November 17, 1997; accepted for publication Jauuary 19, 1998)
Fiz. Tekh. Poluprovodn. **32**, 1089–1093 (September 1998)

The effect of processing heterostructures with GaAs/InGaAs quantum wells in the hydrogen plasma of an rf glow discharge on the photoluminescence spectrum and capacitive photovoltage of these structures is investigated. It is shown that strained quantum-well heterolayers hinder the diffusion of hydrogen and defects into the bulk, which causes the spatial distributions of recombination-active and passivated hydrogenic defect-like complexes in heterostructures, and the processes that create them, to differ appreciably from the same processes in uniform layers.
 [S1063-7826(98)01609-3]

The phenomenon of passivation of electrical and photoactive defects and impurities by atomic hydrogen, which has been studied comparatively well for uniform semiconductors (Si, GaAs, InP, etc.),[1–3] is not as well understood in nonuniform structures, especially in heterostructures with quantum wells. The action of hydrogen in these structures has its own peculiarities, associated with the effect of the heterojunction and elastic strain field on the processes of migration and formation of hydrogen-defect complexes, which usually lead to hydrogenated structures.

Hydrogenation of AlGaAs/GaAs heterostructures with weakly strained quantum wells leads to increased photoluminescence (PL) intensity in the quantum wells,[4,5] which is explained by passivation of nonradiative recombination centers at the heterojunction boundary by hydrogen. However, in GaAs/InGaAs heterostructures with strained quantum wells the passivation is much less pronounced, and even quenching of the PL in the quantum wells has been observed[4,6] with the appearance of a band of impurity PL.[4] The reasons why hydrogen affects these heterojunction quantum wells differently is not yet entirely clear. One reason may be related to the ability of strained heterolayers to interfere with defect and impurity diffusion.[7] In this case, we could encounter either a barrier or a quantum well in the material, depending on the sign of the strain created by defects and impurities in the quantum-well material.

In order to elucidate the role of this phenomenon in the process of migration and formation of hydrogen-defect complexes in heterostructure quantum wells, we have made a comparative study of the effect of hydrogenation on the PL spectrum and capacitive photovoltage of GaAs/InGaAs heterostructure quantum wells and uniform GaAs layers. The samples were hydrogenated by treating them in the hydrogen plasma of an rf glow discharge.

1. EXPERIMENTAL PROCEDURE

GaAs/InGaAs heterostructures and layers of GaAs were obtained by gas-phase epitaxy from metallorganic compounds at atmospheric pressure on a semi-insulating (001) GaAs substrate. Most of our experiments were carried out on heterostructure quantum wells with three $In_{0.27}Ga_{0.73}As$ quantum wells built into the skin layer, whose widths of 11, 4.8, and 1.9 nm decreased with distance from the surface. The thickness of the coating barrier layer of GaAs was 11 nm, the barrier layers near the wells were 34 nm, and the whole structure was 1 μm thick. The thickness of a control layer of GaAs, which was subjected to hydrogenation at the same time as the heterostructure quantum well, was 2.5 μm. The heterostructure quantum wells and the layer, which were intentionally undoped, had electron concentrations of $n_0 \approx 1 \times 10^{16}$ cm^{-3} and electron mobilities of 4.5×10^3 cm^2/(V·s).

An rf glow discharge was excited in a quartz tube filled with hydrogen with external ring electrodes held at a hydrogen pressure of 0.1 mm Torr with an rf voltage at 5 MHz. Samples were simultaneously placed in the dark discharge space that appears near the electrodes and in the glow discharge space in the central portion of the interelectrode gap. In the first case they are subjected to bombardment by protons with a maximum energy as large as several keV. For treatment in the glow discharge space, where the potential drop is negligible, this phenomenon can be disregarded.

Our methods of investigating the PL and capacitive photovoltage spectra were described in Refs. 8 and 9. The PL spectra were measured at 77 K, while the capacitive photovoltage spectra were measured at 300 K.

2. EXPERIMENTAL RESULTS AND DISCUSSION

2.1. Effect of hydrogenation on the photoluminescence spectra

Three quantum-well PL peaks and the peak corresponding to edge PL of the GaAs are visible in the PL spectrum of the heterojunction quantum wells (Fig. 1, curve *1*); the photon energy of the edge PL is $h\nu_m \approx 1.5$ eV. The marked decrease in the peak heights $I_{PL}(h\nu_m)$ with decreasing width of the quantum well is primarily due to the increased probability of thermal emission of nonequilibrium carriers from the narrower wells.[8]

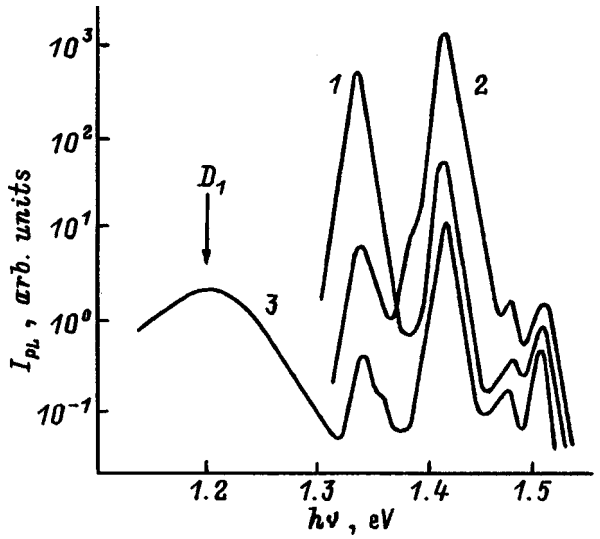

FIG. 1. Effect of processing of a heterostructure quantum well in a hydrogen plasma on its photoluminescence spectrum. *1*— before processing, *2*— processing in the glow discharge space (515 K, 1000 s), *3*— processing in the dark discharge space (300 K, 100 s).

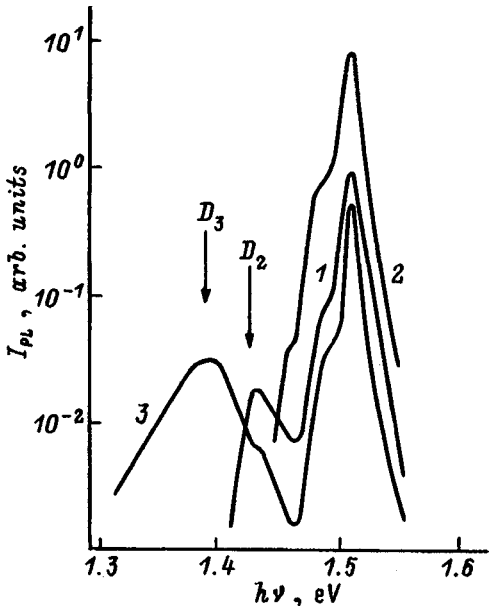

FIG. 2. Effect of processing of a uniform layer of GaAs in a hydrogenic plasma on its photoluminescence spectrum. *1*— before processing, *2*— processing in the glow discharge space (515 K, 1000 s), *3*— processing in the dark discharge space (300 K, 100 s).

After processing the heterostructure quantum wells in the dark discharge space for 100 sec at 300 K (in the course of this treatment the sample temperatures can increase by $\approx 100°$ for the longest processing time, which was $\sim 10^3$ s), the PL in the first quantum well was almost completely quenched, with relatively weak quenching in the other wells and in the GaAs (curve *3*). In this case a new broad impurity-related PL peak D_1 ($h\nu_m \approx 1.2$ eV) appeared. The appearance of similar PL peaks ($h\nu_m \approx 1.28$ eV) was reported in Ref. 4 after long periods of hydrogenation.

Such processing of the heterostructure quantum wells in the glow discharge space had virtually no effect on the PL spectrum. However, when the sample was heated to 515 K, processing in the glow discharge space also led to strong quenching of the PL in the first quantum well, but in this case the PL was enhanced in the other quantum wells and in the GaAs (curve *2*). For the optimal processing time (800 s) the PL intensity of the second quantum well increased by a factor of 30, in the third quantum well by a factor of 3, and in GaAs by a factor of 1.5. Thus, in heterostructure quantum wells made of GaAs/InGaAs effective hydrogen passivation of defects is also possible, but it occurs in quantum wells located behind the first quantum well.

In addition to a double edge PL peak caused by recombination of free excitons and excitons bound at carbon impurities, the PL spectrum of the GaAs layer (Fig. 2, curve *1*) also exhibited a weak impurity PL peak D_1 ($h\nu_m \approx 1.43$ eV) due to centers of unknown origin. After processing in the dark discharge space, the height of these peaks decreases somewhat, and immediately after processing the heterostructure quantum wells a new impurity PL peak D_3 appeared (curve *3*). However, this peak was located in a different place ($h\nu_m \approx 1.39$ eV) with a maximum intensity almost a factor of 2 smaller than the intensity of peak D_1 in the heterostructure quantum well; i.e., under the same processing conditions the radiative recombination centers generated in the heterostructure quantum wells are different from those generated in the uniform layer. It is interesting that in Ref. 4 a peak with $h\nu_m \approx 1.39$ eV was also observed in heterostructure quantum wells after hydrogenation of the structure at low doses and elevated temperature (550 K). In the uniform layer the enhancement of edge PL after processing in the glow discharge space (curves *1* and *2*) is much more pronounced than in the heterostructure quantum well. After such processing the peak D_2 disappears completely.

Figures 3 and 4 show the dependences of the PL intensity $I_{PL}(h\nu_m)$ in heterostructure quantum wells on the duration of processing in the glow discharge space and the dark discharge space, respectively. Note that in this experiment each sample was processed continuously for a specified time in order to eliminate the effect of interrupting the treatment process on the time dependence.

After processing in the glow discharge space at 300 K, a somewhat small initial dropoff is followed first by an increase in the PL intensity by a factor of 2 or 3 (Fig. 3, curves *1*, *4*, and *5*), and then a falloff which is most pronounced for the first quantum well (curve *1*). The roughly identical relative changes in I_{PL} for all the quantum wells most likely reflects the change in the surface recombination rate, which is equivalent to a change in the intensity of photoexcitation, and only after a time $t \sim 10^3$ s does the formation and accumulation of defects become significant in the neighborhood of the first quantum well (curve *1*).

At 515 K, this process clearly dominates even for short treatment times (curve *2*). In this case, the defect passivation begins to manifest itself more strongly in the neighborhood of the second quantum well with increasing processing time (curve *3*). For $t > 100$ s it becomes significant for the third quantum well (curve *6*). However, processing times $\geqslant 10^3$ s lead to catastrophic degradation of the structure, probably

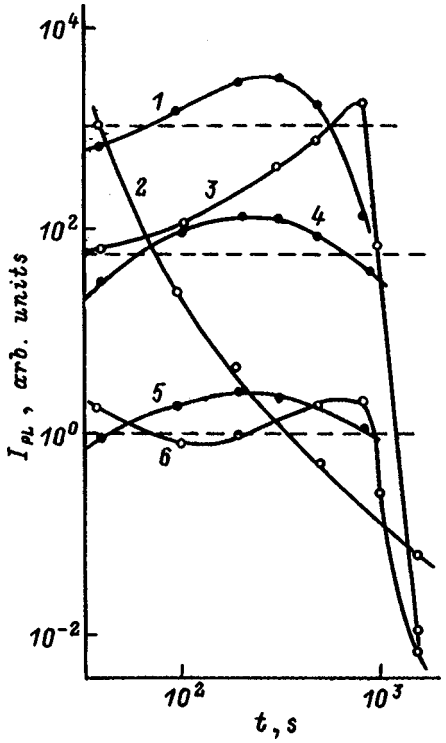

FIG. 3. Effect of processing time in the glow discharge space on the photoluminescence intensity from a heterostructure quantum well. Processing temperature, K: *1, 4, 5* — 300, *2, 3, 6* — 515. $h\nu = h\nu_m$, eV: *1, 2* — 1.335, *3, 4* — 1.42, *5, 6* — 1.47. The dashed lines indicate the PL intensities before processing.

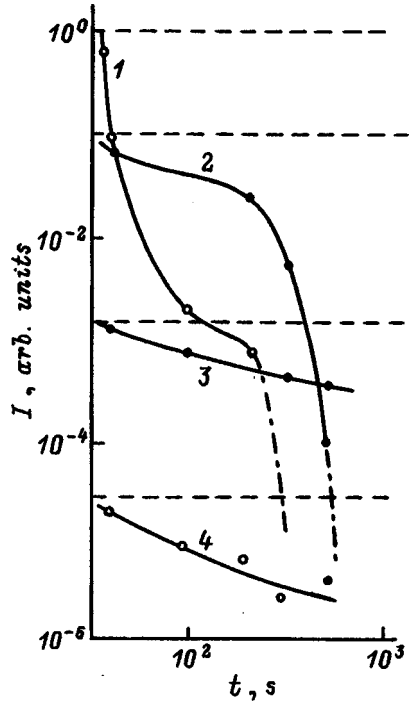

FIG. 4. Effect of processing time in the dark discharge space on the photoluminescence intensity from a heterostructure quantum well. $h\nu = h\nu_m$, eV: *1* — 1.335, *2* — 1.42, *3* — 1.47, *4* — 1.505.

caused by clustering of hydrogenic complexes.[10]

For processing in the dark discharge space (Fig. 4), the tendency for defects to form and accumulate first in the first quantum well (curve *1*), and for $t > 200$ s in the second quantum well as well (curve *2*), is superimposed on an overall monotonic decrease in the intensity of all the peaks (curves *2–4*) due probably to degradation of the surface. The passivating action of hydrogen under these conditions is not obviously apparent.

2.2. Effect of hydrogenation on the photosensitivity spectrum

The strong influence of strained heterostructures on the migration of hydrogen and formation of hydrogen-defect complexes in heterostructure quantum wells has also been confirmed by studies of the photosensitivity spectra $S_{\text{ph}}(h\nu)$. In investigating the process of defect formation, a convenient spectral characteristic is the normalized photosensitivity $S(h\nu) = S_{\text{ph}}(h\nu)/S_0$, where S_0 is the photosensitivity in the region of intrinsic absorption, because the values of S in the regions of absorption by the quantum well S_W and impurities S_D are virtually independent of the state of the surface (the band bending) and are determined primarily by optical absorption of quantum wells and impurities.[8]

The normalized photosensitivity spectra of the heterostructure quantum wells at 300 K (Fig. 5, curve *2*) exhibit a photosensitivity band from the quantum well in the range $1.23 < h\nu < 1.4$ eV, which has a certain structure. The edges of the photosensitivity bands for individual wells (marked by arrows) correspond to the PL peaks at 77 K with a temperature-induced shift of ≈ 80 meV. For the first quantum well $S_{W1}(1.27\,\text{eV}) \approx 6 \times 10^{-2}$.

Processing of the heterostructure quantum wells in the dark discharge space leads to the appearance of an impurity photosensitivity band for $h\nu > 1.0$ eV (curve *1*). Computer analysis of this band using the Lukovsky formula[11] for the

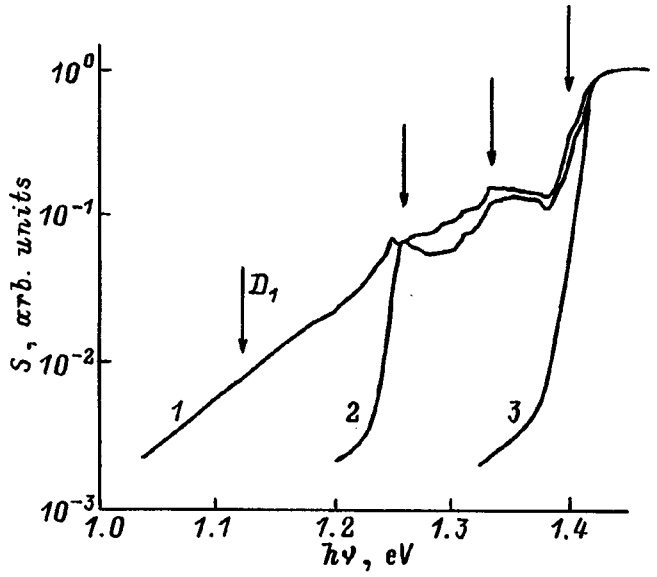

FIG. 5. Effect of processing a heterostructure quantum well and a uniform layer of GaAs in a hydrogen plasma on the capacitive photovoltage spectrum. *1*— a uniform layer before and after processing, *2*— a heterostructure quantum well before processing, *3*— a heterostructure quantum well after processing in the dark discharge space (300 K, 100 s).

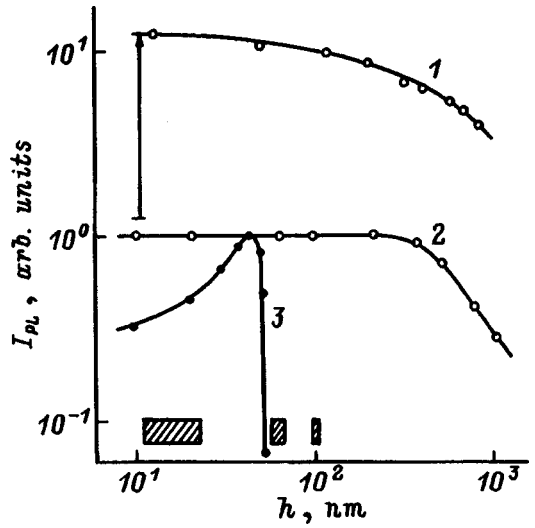

FIG. 6. Dependence of the photoluminescence intensity (77 K) on the thickness of the etched-away layer: *1*— uniform layer after processing in the glow discharge space ($h\nu_m = 1.505$ eV), *2*— uniform layer after processing in the dark discharge space ($h\nu_m = 1.39$ eV), *3*— heterostructure quantum well after processing in the dark discharge space ($h\nu_m = 1.2$ eV). The arrow indicates the magnitude of the PL enhancement effect after processing. The crosshatched rectangles show the position of the quantum wells.

spectral dependence of optical capture cross sections of an impurity center shows that it can be decomposed into three peaks associated with monoenergetic centers with similar values of the ionization energy $E_D = 0.98$, 1.10, and 1.17 eV and photosensitivities $S_D(1.27\,\text{eV}) = 1.2\times10^{-2}$, 1.6×10^{-2}, and 9×10^{-3}, respectively. The total impurity photosensitivity S_D is comparable to S_{W1}. We obviously can associate these centers (or the one at 1.1 eV) with the broad impurity PL band D_1.

Even when the PL from the first quantum well is completely quenched, the quantity S_{W1} remains nearly constant (curve *1*), and only the exciton photosensitivity peak disappears, which is apparent on curve *2*. Because of the overlap of photosensitivity bands $S_D(h\nu)$ and $S_W(h\nu)$, curve *1* is above curve *2*. The reduced sensitivity of S_W to defects is also characteristic of the capacitive photovoltage.[8]

Processing of heterostructure quantum wells in the glow discharge space, and also processing of the GaAs layer in either the glow discharge space or the dark discharge space (curve *3*) were not found to have any influence on the normalized photosensitivity spectra, although the absolute value of the photosensitivity changes during processing as a result of the change in the state of the surface.

2.3. Localization of hydrogen-defect complexes

By measuring the PL spectra on low-angle oblique planes obtained by chemical etching of the structures we can determine the depths at which passivating and recombination-active hydrogen-defect complexes form (D_1 and D_3).

In the GaAs layer the increased intensity of edge PL after processing in the glow discharge space (Fig. 6, curve *1*) and the increased intensity of peak D_3 induced by processing in the dark discharge space (curve *2*) are decreased by a factor of e at an etch depth $h \approx 10^3$ nm, which characterizes the effective free range for diffusion of hydrogen under these conditions. This depth is in agreement with diffusion profiles of deuterium (at similar processing temperatures) obtained by secondary ion mass spectrometry (SIMS) of deuterated single crystals of GaAs.[12] At this depth, hydrogen passivates background centers for nonradiative and radiative (D_2) recombination, which leads to a considerable enhancement of the edge PL of the layers after processing in the glow discharge space. It is likely that defects participate in the formation of D_3-centers, especially vacancies that are generated during proton bombardment of the surface and diffuse into the bulk together with hydrogen. In this case, the enhancement of recombination activity of the surface and bulk prevails over the passivating action of hydrogen.

The function $I_{PL}(h)$ has a different form for D_1-centers in the heterostructure quantum wells (curve *3*). As the surface layer is etched away, I_{PL} initially increases by almost a factor of 3 and then rapidly falls off as h approaches the depth at which the second quantum well is located. Thus, D_1- centers are localized in a thin surface layer of thickness less than 50 nm, and possibly in a still thinner layer near the second quantum well. The segment of increasing I_{PL} shown in Fig. 3 is caused by removal of a strongly damaged layer that forms near the surface, which creates a competing channel for rapid nonradiative recombination. Hydrogen and defects in the heterostructure quantum well are almost completely blocked by the first and second quantum wells. The relatively small and approximately equal amounts of quenching of the PL peaks for the second and third quantum wells, and also the GaAs (Fig. 1, curve *3*) can be explained by the increased recombination rate in the surface layer. Ther conditions of bounded diffusion give rise to high concentrations of primary defects and hydrogen, which initiate reactions in the heterostructure quantum wells that generate complexes different from those in the uniform layer. This situation leads, in particular, to the formation of the D_1-centers.

The ratio $S_D(1.27\,\text{eV})/S_{W1}(1.27\,\text{eV})$ can be used to estimate the surface concentration of luminescence centers $N_S(D_1)$.[13] If we identify the D_1-centers with one of the impurity photosensitivity centers (1.1 eV) and assume the optical capture cross section of the center to be $1\times10^{-16}\,\text{cm}^{-2}$ and the quantum-well absorption to be 7×10^{-3} (Ref. 14), then $N_S(D_1) \approx 2\times10^{13}\,\text{cm}^{-2}$. If all three centers of impurity photosensitivity are luminescence centers, then this value should be increased by a factor of 2.5. For more or less identical distributions of these centers in a defect region of width $\Delta z(D_1) = 50$ nm, the bulk concentration will be $N(D_1) \sim 10^{19}\,\text{cm}^{-3}$. This value is in complete agreement with data on the concentration of deuterium in the GaAs surface barrier layer of a deuterated GaAs/InGaAs heterostructure with a superlattice consisting of quantum wells.[6] However, in the region of the superlattice itself, the concentration of deuterium is decreased by almost a factor of 2, whereas our estimate applies more to the second than to the first barrier layer.

The concentration of D_3 centers in the uniform GaAs layer is considerably smaller. If the probabilities of radiative recombination at centers D_1 and D_3 are not too different,

then the fact that $\Delta z(D_3)=10^3$ nm gives $N(D_3) \leqslant 10^{16}$ cm^{-3}.

When heterostructure quantum wells are processed in the glow discharge space, the passivating action of hydrogen does not reach farther than the third quantum well, i.e., it is limited to a depth of $\approx$90 nm. We may conclude this from the sharp falloff in the effect of enhanced PL from the second to the third quantum well (Fig. 1, curve *2*). The weak enhancement of GaAs edge PL in the heterostructure quantum well may be entirely due to the decrease in total recombination rate in the surface region.

CONCLUSIONS

These studies show that strained quantum-well heterolayers of InGaAs embedded in the surface region of a GaAs layer can hinder the diffusion of hydrogen and defects generated at the surface from migrating into the bulk. This phenomenon turns out to have a decisive influence on the spatial distribution, type, and concentration of hydrogenic complexes that form. The formation of recombination-active complexes dominates in the immediate vicinity of the surface, but a significant passivation effect is obtained for these defects only in the region of the semiconductor behind the first quantum well, and only under the right processing conditions.

We wish to thank B. N. Zvonkov for providing the structures and I. G. Malkina for help in carrying out individual experiments.

This work was carried out with the financial support of Goskombuz RF (Grant 94-7.10-3005).

[1] M. Stavola, Acta Phys. Pol. A **82**, 585 (1992).
[2] R. Rahbi, B. Pajot, J. Chevallier, A. Marbeuf, R. C. Logan, and M. Gavand, J. Appl. Phys. **73**, 1723 (1992).
[3] E. M. Omeljanovsky, A. V. Pakhomov, and A. Y. Polyakov, Semicond. Sci. Technol. **4**, 947 (1989).
[4] Y.-L. Chang, I.-H. Tan, E. Hu, J. Merz, V. Emeliani, and A. Frova, J. Appl. Phys. **75**, 3040 (1994).
[5] Yu. A. Bumaĭ, B. S. Yavich, M. A. Sinitsyn, A. G. Ul'yashin, N. V. Shlopak, and V. F. Voronin, Fiz. Tekh. Poluprovodn. **28**, 276 (1994) [Semiconductors **28**, 166 (1994)].
[6] S. M. Lord, G. Roos, J. S. Harris, and N. M. Johnson, J. Appl. Phys. **73**, 740 (1992).
[7] Y. C. Chen, J. Singh, and P. K. Bhattacharya, J. Appl. Phys. **74**, 3800 (1993).
[8] I. A. Karpovich and D. O. Filatov, Fiz. Tekh. Poluprovodn. **30**, 1745 (1996) [Semiconductors **30**, 913 (1996)].
[9] I. A. Karpovich, V. Ya. Aleshkin, A. V. Anshon, N. V. Baĭdus', B. N. Zvonkov, and S. M. Plankina, Fiz. Tekh. Poluprovodn. **26**, 1886 (1992) [Semiconductors **26**, 1057 (1992)].
[10] Y.-L. Chang, M. Krishnamurthy, I.-H. Tan, T. Hu, J. Merz, P. M. Petroff, A. Frova, and V. Emiliani, J. Vac. Sci. Technol. B **11**, 170 (1993).
[11] G. Lukovsky, Solid State Commun. **3**, 299 (1965).
[12] R. Rahbi, B. Pajot, J. Chevallier, A. Marbeuf, R. C. Logan, and M. Gavand, J. Appl. Phys. **73**, 1723 (1993).
[13] I. A. Karpovich, A. V. Anshon, N. V. Baĭdus', L. M. Batukova, Yu. A. Danilov, B. N. Zvonkov, and S. M. Plankina, Fiz. Tekh. Poluprovodn. **28**, 104 (1994) [Semiconductors **28**, 63 (1994)].
[14] V. Ya. Aleshkin, A. V. Anshon, and I. A. Karpovich, Fiz. Tekh. Poluprovodn. **27**, 1344 (1993) [Semiconductors **27**, 742 (1993)].

Translated by Frank J. Crowne

Localized states near the band gap of GaAs caused by tetrahedral arsenic clusters

S. N. Grinyaev and V. A. Chaldyshev

Tomsk State University, 634050 Tomsk, Russia

(Submitted November 13, 1997; accepted for publication January 29, 1998)
Fiz. Tekh. Poluprovodn. **32**, 1094–1099 (September 1998)

The method of $4\times4\times4$ extended unit cells developed previously for calculating the electronic energy spectrum of gallium arsenide with defects is used to investigate the spectrum of gallium arsenide with simple arsenic clusters of tetrahedral symmetry containing 17 and 35 arsenic atoms. The waves functions and energies of localized states in the vicinity of the band gap are calculated, and electron density patterns are obtained. A comparative analysis is made of the energies and electron density of these states for various clusters. It is shown that localized states in the vicinity of the band gap can be interpreted as the result of splittings due to interactions of the host with the set of A_1 levels generated in the band gap by noninteracting As_{Ga} antisite defects that make up the cluster. The occupation of these states by electrons is discussed.
 [S1063-7826(98)01709-8]

INTRODUCTION

Cluster formations have long been used primarily for modelistic descriptions of the properties of crystals. Recently, however, these clusters have become more and more objects of interest in their own right, especially after success was achieved in the technology of obtaining clusters made up of various materials in their free state.[1–9] Such clusters can be used as elements for constructing new materials. Along with free clusters there is interest in various clusters in media, in particular, clusters that consist of intrinsic crystal defects. In this paper we will discuss clusters made up of arsenic atoms in gallium arsenide.

The properties of gallium arsenide containing excess arsenic are determined by the ability of arsenic to incorporate in the lattice. Since this capability is multifaceted and not well studied, it is interesting to start our discussion with the simplest clusters.

The simplest of these is a cluster made up of five arsenic atoms, consisting of an antisite defect As_{Ga} at the center and four arsenic atoms in the first layer. In its energy ground state this cluster is stable and has tetrahedral T_d symmetry.[10,11] Furthermore, if the entire second layer consists of As_{Ga} antisite defects, then all of these together with atoms of the third layer form a cluster of 29 arsenic atoms with symmetry T_d. The electronic structure of such a cluster was studied by us in Ref. 12.

In this paper we consider clusters of 17 and 35 arsenic atoms centered on one of the As atoms of gallium arsenide and having symmetry T_d. The first of these consists of the central atom, four As_{Ga} antisite defects in the first layer and 20 atoms of the second layer. Our second cluster includes another 12 As_{Ga} defects in the third layer and six arsenic atoms in the fourth layer in addition to these atoms. Although the ideal tetrahedral configuration is not characteristic of arsenic, the GaAs host is capable of preserving the cubic symmetry of the cluster, which is confirmed by experimental studies.

The electronic spectrum was computed using the method described in Ref. 13, with the help of the method of pseudopotentials using the model of extended unit cells.[14,15] The size of the unit cell was chosen to be $4\times4\times4$. As a basis we used symmetric Bloch functions for gallium arsenide. The defect potential was constructed in the form of differences of ion pseudopotentials of the substitutional atoms screened by a Thomas-Fermi function with exchange corrections.[12] In this case, arsenic atoms located within the cluster were screened by an electron gas with a density equal to $10e/\Omega_0$, where Ω_0 is the volume of a unit cell of ideal gallium arsenide, and e is the electron charge, whereas the external (boundary) atoms of the cluster were screened, like atoms of the GaAs host, by an electron gas with a density equal to $8e/\Omega_0$. Corrections due to spin-orbit interaction were disregarded in these calculations. In contrast with the authors of Ref. 12, we used 30 rather than 50 of the lowest bands of ideal GaAs to expand the defect crystal functions. This corresponds to including contributions from states of Bloch electrons down to energies of 45–50 eV (for the various representations) compared to ~60 eV from Ref. 12. Numerical estimates for a cluster of 29 atoms show that the qualitative structure of the electronic spectrum when only 30 bands are included coincides with that obtained in Ref. 12, and the change in the position of individual levels does not exceed 0.1–0.2 eV.

The results of our wave function calculations are shown (Figs. 1–3) as patterns of electron-charge density in the plane (111) that pass through the center of the cluster. In these figures the patterns of charge density in this plane are given within a rectangular extended unit cell. The charge density of electrons is given in units of e/Ω, where Ω is the volume of the extended unit cell. In these units, the minimum contour and step between contour lines equals three. The positions of atoms in the plane that pass through the center of the cluster are indicated by squares, while the po-

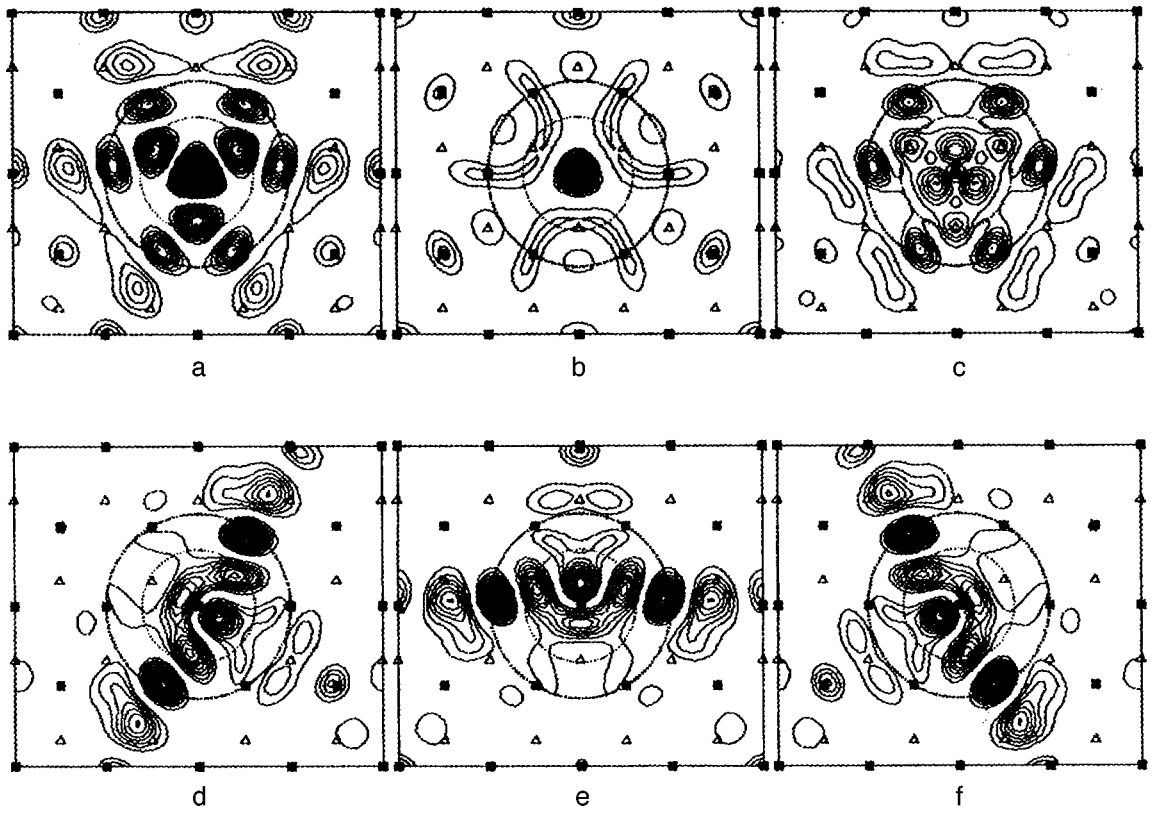

FIG. 1. Charge density in localized states with energies near the band gap for a cluster of 17 arsenic atoms. Patterns of density in the (111) plane are shown where this plane passes through the center of the cluster within an extended unit cell. The dark squares are positions of atoms in this plane and the light triangles are projections of the positions of atoms in the next parallel plane. The minimum contour corresponds to a charge density equal to 3 in units of e/Ω, and the step between contours is also equal to 3 in these units. The symmetry of the states and their energies relative to the top of the valence band are as follows: a — (A_1, $E=0.58$ eV), b — (A_1, $E=1.56$ eV), c — (T_2 averaged, $E=1.20$ eV), d — (T_{2x}, $E=1.20$ eV), e — (T_{2y}, $E=1.20$ eV), f — (T_{2z}, $E=1.20$ eV).

sition of atoms in the nearest parallel plane are denoted by triangles. The circles shown in the density patterns are intersections of the plane under discussion with coordination spheres constructed around the central arsenic atom.

CLUSTER OF 17 ARSENIC ATOMS

Calculations show that for a cluster of 17 arsenic atoms there are three localized levels in the vicinity of the band gap of the ideal crystal. Two states have symmetry A_1 and energy $E=0.58$ and 1.56 eV; the third state is threefold degenerate and has T_2 symmetry and an energy $E=1.20$ eV. Here and in what follows we will measure energies from the top of the valence band. The bottom of the conduction band corresponds to an energy $E_c=1.53$ eV. It is clear that only the lowest A_1 level and the T_2 level can lie in the band gap. The second A_1 level is located in an allowed band and hence is a ''resonance.'' Comparison of the number of states lying below the level E_c with the total number of valence electrons shows that states in the band gap are completely occupied, while state A_1 in the conduction band is empty.

Figure 1 shows patterns of charge density for electrons in these states. From these patterns it follows that the electron density is primarily localized at the geometric limits of the cluster, although there are appreciable ''tails'' outside the boundary.

Pattern a corresponds to state A_1 with energy $E=0.58$ eV. Comparison of this picture with the pattern of electron density of an As_{Ga} antisite defect (see Fig. 3 in Ref. 12) shows clearly that the charge density profile within the cluster is primarily determined by a superposition of charge densities of four identical As_{Ga} defects centered on Ga atoms of the first layer.

Pattern b corresponds to state A_1 with an energy $E=1.56$ eV lying in the conduction band. A sharp maximum is observed at the center of the cluster; most of the charge of the electron gas is concentrated in the vicinity of the first and second neighbors.

Patterns c, d, e, and f show charge densities belonging to the threefold degenerate level T_2 with energy $E=1.20$ eV. Pattern c shows a representation of the T_2 charge density averaged with respect to components x, y, z. In patterns d, e, and f we see partial densities with respect to these components, respectively. The charge density patterns for the components transform into one another under rotation by $\pm 120°$.

The electronic charge density belonging to level T_2 is primarily determined, as in case a, by a combination of wave functions of As_{Ga} antisite defects. Actually, the hypothetical fourfold degenerate level $E_{AD}=1.10$ eV formed by four localized A_1 states of noninteracting As_{Ga} antisite defects of

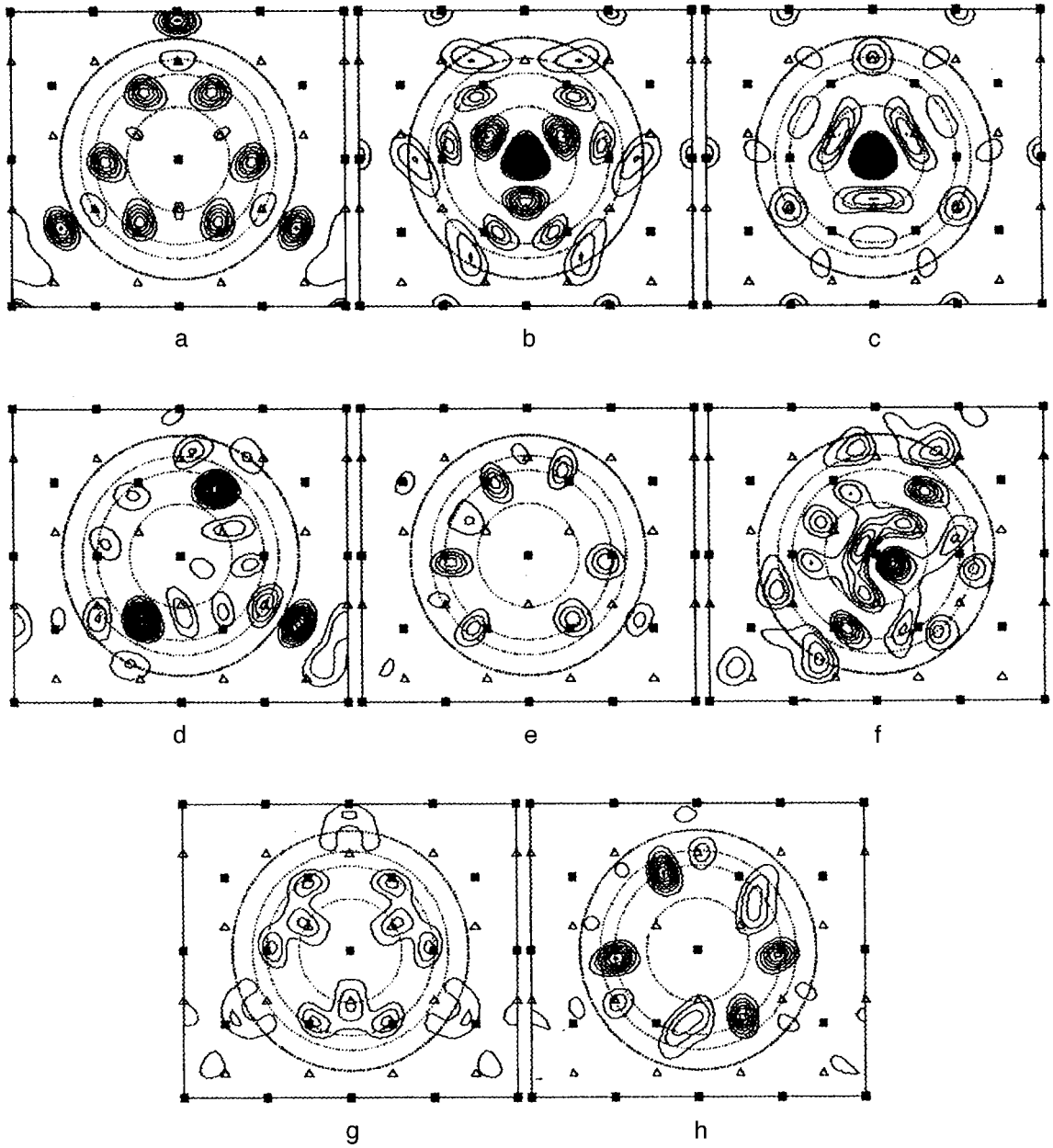

FIG. 2. Charge density in localized states with energies near the band gap for a cluster of 35 arsenic atoms. Density patters are shown in the plane (111) passing through the center of the cluster within an extended unit cell. The dark squares are positions of atoms in this plane, the light triangles projections of the positions of atoms in the next parallel plane. The minimum contour corresponds to a charge density equal to 3 in units of e/Ω, and the step between the contours is also equal to 3 in these units. The symmetries of the states and their energies relative to the top of the valence band are as follows: a — (A_1, $E=-0.15$ eV), b — (A_1, $E=0.74$ eV), c — (A_1, $E=1.40$ eV), d — (T_2, $E=0.45$ eV), e — (T_2, $E=0.95$ eV), f — (T_2, $E=1.50$ eV), g — (E, $E=1.33$ eV), h — (T_1, $E=1.70$ eV).

the first layer is split under the action of the interaction with all of the neighbors as follows:

$$4AD=A_1+T_2,$$

since the cluster has symmetry T_d. Here A_1 corresponds to the energy $E=0.58$ eV and T_2 corresponds to energy $E=1.20$ eV. The original levels with energy $E=1.56$ eV are possibly related to resonance levels of an isolated antisite defect.

The positions of these levels relative to the band-gap edges are shown in Fig. 4a. Note that a 17-atom cluster in gallium arsenide can act as a multicharge donor, since in the ground state the levels T_2 and A_1, which lie in the band gap, are completely occupied, while level A_1 located above the top of the conduction band is empty.

CLUSTER OF 35 ARSENIC ATOMS

For this cluster the following states appear in the vicinity of the band gap of gallium arsenide: three levels of type A_1 with energies $E=-0.15$, 0.74, and 1.40 eV; ; three triply degenerate levels of type T_2 with energies $E=0.45$, 0.95, and 1.50 eV; one doubly degenerate level of type E with energy $E=1.33$ eV; and one triply degenerate level of type

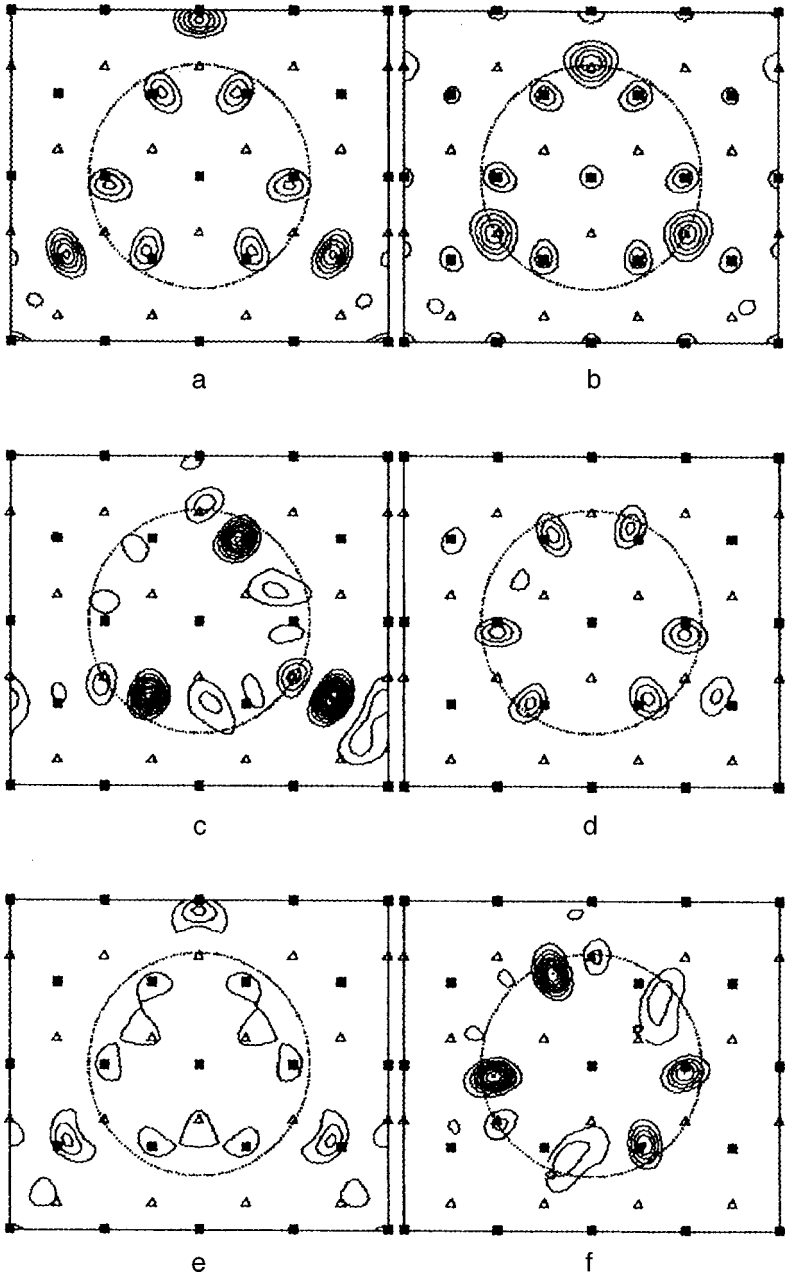

FIG. 3. Charge density in localized states with energies near the band gap for clusters of 31 arsenic atoms. Density patterns are shown in the (111) plane passing through the center of the cluster within an extended unit cell. The dark squares are positions of atoms in this plane, the light triangles projections of the positions of atoms in the nearest parallel plane. The minimum contour corresponds to a charge density equal to 3 in units of e/Ω, and the step between contours also equals 3 in these units. The symmetries of the states and their energies relative to the top of the valence band are as follows: a — (A_1, $E=0.10$ eV), b — (A_1, $E=1.46$ eV), c — (T_2, $E=0.79$ eV), d — (T_2, $E=1.94$ eV), e — (E, $E=1.57$ eV), f — (T_1, $E=1.84$ eV).

T_1 with energy $E=1.70$ eV. The first level of the A_1-type levels with energy $E=-0.15$ eV lies below the valence band edge, while the triply degenerate level T_1 is located in the conduction band.

As in the previous section, and in Ref. 12, we compare energy levels located near the band gap with levels obtained by splitting a 16-fold level formed by As_{Ga} antisite defects in the first and third layer:

$$16AD = 2A_1 + E + T_1 + 3T_2.$$

The positions of these levels are shown in Fig. 4b. It is clear that one of the levels with symmetry A_1 ($E=1.40$ eV) does not enter into this level set, and has a different origin.

In order to analyze the nature of these states we consider the patterns of electron density for a 35-atom cluster (Fig. 2). Patterns a, b, and c correspond to states with symmetry A_1, d, e, f to symmetry T_2, listed in order of increasing energy.

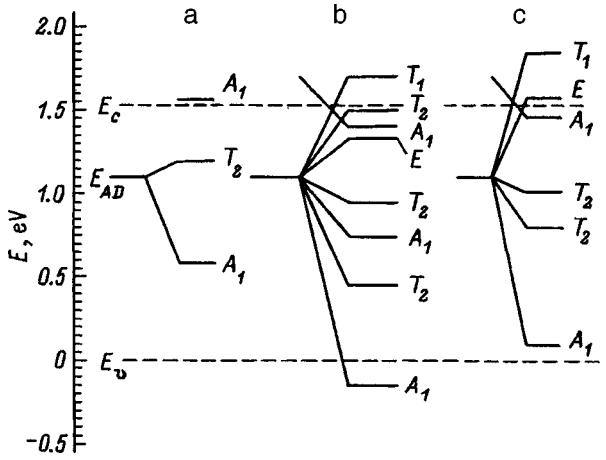

FIG. 4. Scheme of localized states near the band gap: a — 17-atom cluster, b — 35-atom cluster, c — cluster of 31 arsenic atoms formed by replacing Ga atoms of the third layer with As. The origins of these states from isolated antisite defects are shown.

Patterns g and h correspond to the representations E and T_1. For the three-dimensional representations we show density patterns for the first component only. The remaining components can be obtained by rotations through 120°. The two-dimensional representation E gives identical patterns for density in the plane (111) for both components.

For comparison we calculated a cluster of 31 arsenic atoms formed by replacing Ga atoms with As only in the third layer. The levels obtained for the neighborhood of the band gap are shown in Fig. 4c, while the electron density patterns corresponding to it are shown in Fig. 3. In comparison with scheme b, these levels are shifted upward somewhat, and there are no A_1 states between the lowest T_2 levels and the T_2 state near the bottom of the conduction band. In other respects, the order of appearance of the levels is preserved. The splitting of levels of noninteracting antisite defects of the third layer is given by the relation

$$12AD = A_1 + E + T_1 + 2T_2.$$

It thus follows that the second level A_1 with energy $E = 1.46$ eV does not enter into this expansion and has another origin.

By considering the electron-density patterns for clusters of 17 and 35 atoms (Figs. 1a and 1d; Figs. 2b and 2f) we see that states of the 35-atom cluster that are absent from scheme c originate with defects of the first layer and are slightly shifted due to interaction with defects of the third layer. The remaining states of the cluster of 35 arsenic atoms come from antisite defects of the third layer. This is easily seen by comparing patterns a, d, e, g, h in Fig. 2 with patterns a, c, d, e, h in Fig. 3. The higher levels of type A_1 in the first and second layer contribute to the A_1 state with energy $E = 140$ eV, which comes from the conduction band (see Figs. 1b, 3a, and 2c).

In the ground state all the levels lying in the band gap are occupied, while level T_1, which is located in the conduction band, is 2/3 occupied. Because of the transfer of electrons from this level to the conduction band, this level is ionized and ''metallization'' of the gallium arsenide takes place.

This work was carried out within the framework of the program ''Fullerenes and Atomic Clusters'' and with the support of the Russian Fund for Fundamental Research.

[1] G. Benedek, T. P. Martin, and C. Pacchioni, *Elemental and Molecular Clusters* (Heidelberg, Springer, 1988).
[2] P. Jena, S. N. Khana, and B. K. Rao, *Physics and Chemistry of Finite Systems: Clusters to Crystals* (Dordrecht, Kluwer, 1992).
[3] H. Haberland, *Clusters of Atoms and Molecules* (Berlin, Springer, 1994).
[4] G. Onida, L. Rening, R. W. Godby, R. DelSole, and W. Andreoni, Phys. Rev. Lett. **75**, 818 (1995).
[5] N. Binggeli and J. R. Chelikowsky, Phys. Rev. Lett. **75**, 493 (1995).
[6] A. K. Ray and B. K. Rao, J. Phys.: Condens. Matter **9**, 2859 (1997).
[7] L. I. Kurkina and O. V. Farberovich, Fiz. Tverd. Tela (St. Petersburg) **38**, 1416 (1996) [Phys. Solid State **38**, 783 (1996)].
[8] J. C. Grossman and L. Mitas, Phys. Rev. B **52**, 16735 (1995).
[9] S. N. Khana and P. Jena, Phys. Rev. B **51**, 13705 (1995).
[10] D. J. Chadi and K. J. Chang, Phys. Rev. Lett. **60**, 2187 (1988).
[11] J. Dabrowsky and M. Scheffler, Phys. Rev. B **40**, 1039 (1989).
[12] S. N. Grinyaev and V. A. Chaldyshev, Fiz. Tekh. Poluprovodn. **30**, 2195 (1996) [Semiconductors **30**, 1144 (1996)].
[13] S. N. Grinyaev and V. A. Chaldyshev, Izv. vuzov. Fizika **39**, No. 8, 13 (1996).
[14] R. A. Evarestov, *Quantum-Chemistry Methods in Solid-State Theory* (Leningrad State Univ. Publ., Leningrad, 1982).
[15] R. A. Evarestov and V. P. Smirnov, J. Phys.: Condens. Matter **9**, 3023 (1997).

Translated by Frank J. Crowne

Weak-field magnetoresistance of two-dimensional electrons in $In_{0.53}Ga_{0.47}As/InP$ heterostructures in the persistent photoconductivity regime

D. D. Bykanov, A. M. Kreshchuk, S. V. Novikov, T. A. Polyanskaya, and I. G. Savel'ev

A. I. Ioffe Physicotechnical Institute, Russian Academy of Sciences, 194021 St. Petersburg, Russia
(Submitted February 5, 1998; accepted for publication February 10, 1998)
Fiz. Tekh. Poluprovodn. **32**, 1100–1107 (September 1998)

The weak-field magnetoresistance of the two-dimensional electron gas (2DEG) in a modulation-doped $In_{0.53}Ga_{0.47}As/InP$ heterostructure is studied as the state of the system is converted to a state with persistent photoconductivity by illuminating the sample with interband light. The concentration dependences of the parameters that characterize the phase (H_φ) and spin (H_s coherence are investigated, both in the low-concentration regime where only the first quantum-well subband is occupied by carriers, and in the regime where the second subband is occupied. A qualitative description of all the features observed in experiment is obtained by taking into account the redistribution of charge in the persistent photoconductivity state and the importance of processes that take place in the second quantum-well subband even when its occupation is small. © *1998 American Institute of Physics.* [S1063-7826(98)01809-2]

1. INTRODUCTION

In our previous paper[1] we investigated the effect of spin-orbit splitting of quantum-well subbands on the weak localization of two-dimensional electrons located in $In_{0.53}Ga_{0.47}As/InP$ heterostructures. We showed that this splitting, which is attributable to the absence of symmetry of the quantum well at the heterojunction, plays an important role. In the same paper, we reported the initial results of our study of heterostructures in the persistent photoconductivity state in which the second quantum-well subband is occupied. We noted that spin-orbit scattering becomes less important when carriers appear in the second subband. This is inferred from the increase in the characteristic parameter H_φ (with dimensions of magnetic field) which is inversely proportional to the phase relaxation time of the wave function of the electrons τ_φ, and also the decrease of the parameter H_s, which characterizes the spin-orbit scattering rate τ_s^{-1}. In their theoretical analysis of the magnetoresistance associated with the suppression of weak localization of two-dimensional electrons in two subbands under conditions of fast intersubband scattering, Iwabuchi *et al.*[2] took into account only the change in the diffusion coefficient connected with the change in the density of states. In this case, both parameters H_φ and H_s should increase discontinuously when carriers appear in the second subband. However, intersubband transitions can also lead to slipping of the phase and electron spin. This effect can also increase the characteristic magnetic fields by decreasing the effective values of τ_φ and τ_s. Thus, the decrease in H_s when the second subband became occupied, which we observed in Ref. 1, remains unexplained and requires additional discussion.

In this paper we present results of a detailed study of how the sign-changing magnetoresistance of two-dimensional electrons in $In_{0.53}Ga_{0.47}As/InP$ heterostructures changes as the state of the structure is changed by the persistent conductivity effect, prior to occupation of the second quantum-well subband.

2. SAMPLES AND EXPERIMENTAL METHOD

Modulation-doped $In_{0.53}Ga_{0.47}As/InP$ heterostructures with 2D electron gases were grown by liquid-phase epitaxy on substrates of semi-insulating InP(100). These structures consisted of the following layers, listed outward from the InP surface: a *p*-type InP buffer with concentration $p<10^{15}$ cm^{-3} and thickness $d=1$ μm; a layer of InP that acted as a source of electrons with a donor concentration in the range 10^{16} cm^{-3} to 2×10^{17} cm^{-3}; and a top layer of $In_{0.53}Ga_{0.47}As$ containing the 2D electron gas (with $p\simeq10^{15}$ cm^{-3} and $d=0.3$ μm).[3] As the structure reaches thermal equilibrium, electrons from the donors in the InP layer are transferred to the narrow-gap InGaAs layer, forming a 2D electron gas in the potential well of the heterojunction. The state of the heterostructure is changed by illumination with light from a GaAs light-emitting diode placed in the sample holder immediately adjacent to the sample. In this case, electron-hole pairs are generated in the space charge layer of the InGaAs and are separated by the built-in electric field so that electrons fall into the quantum well at the heterojunction, while the holes neutralize the space charge in the InGaAs. As a result, the 2DEG concentration increases until the built-in charge in the InGaAs layer is fully compensated. This new state of the sample, which remains unchanged for a long time at low temperatures, is referred to as the persistent photoconductivity state. If this state is indeed generated by the mechanism described above, then the maximum change in the 2DEG concentration is determined by the residual concentration of impurities in the narrow-gap layer, in our case the $In_{0.53}Ga_{0.47}As$ layer. In order to obtain a 2DEG with a high mobility, this layer is made as pure as possible. As a result, the change in concentration of the 2DEG due to persistent photoconductivity is very slight. It was shown in Ref.

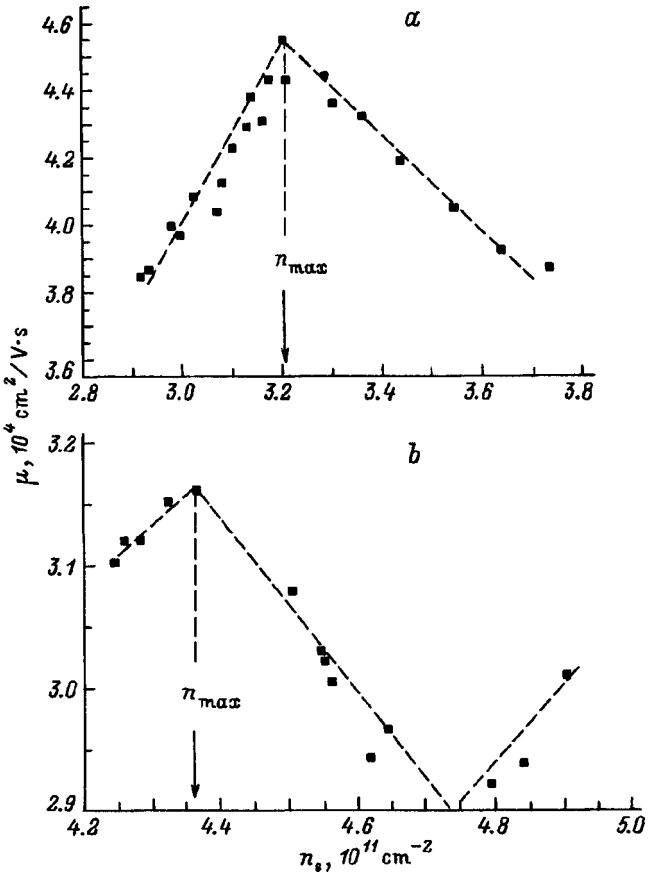

FIG. 1. Mobility of 2D electrons on InP/$In_{0.53}Ga_{0.47}As$ heterostructures at $T=1.85$ K plotted versus concentration n_s. Initial electron concentration n_s^0, 10^{11} cm^{-2}: *a* — 2.9, *b* — 4.25. Functions were obtained by feeding a train of light pulses to the sample and making galvanometric measurements in the persistent photoconductivity regime. The maxima for these functions correspond to the appearance of carriers in the second quantum-well subband.

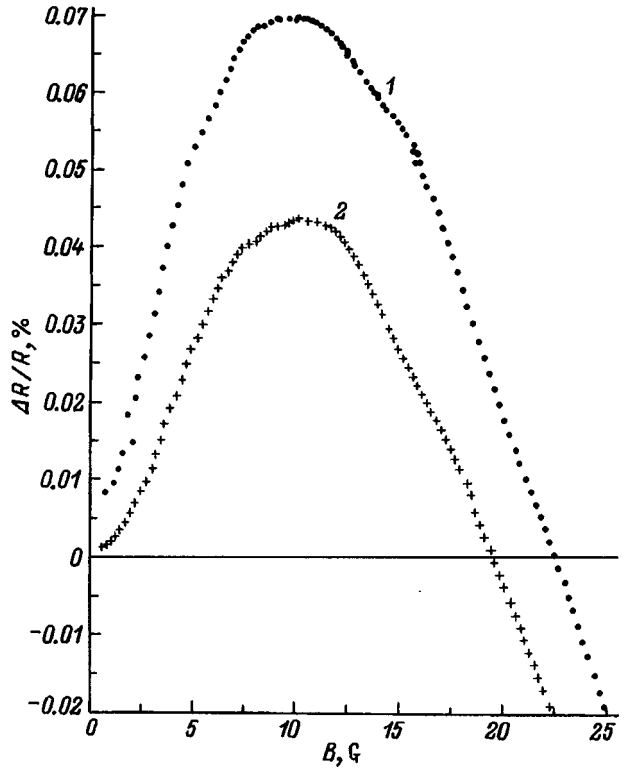

FIG. 2. Plots of the magnetoresistance $\Delta R/R$ versus magnetic field B in the region where the second quantum-well subband starts to be occupied ($T=1.85$ K) for two states of the sample with electron concentrations n_s: *1* — $0.98n_{max}$, *2* — $1.02n_{max}$.

4 that when the top layer of the structure is InGaAs with a thickness less than 1 μm, it is necessary to take into account charging not only of the residual impurities in the layer but also states at the InGaAs surface. This makes it possible to use persistent photoconductivity to generate large changes in the 2DEG concentration even in samples with low impurity concentrations in the narrow-band layer. For this reason, the samples we chose to investigate had a top-layer thickness of 0.3 μm. In these structures, one quantum-well subband was occupied in the initial state and two subbands were occupied in the saturated persistent photoconductivity regime. The change in 2DEG parameters under the action of successive light pulses can be seen in Fig. 1, which shows the dependence of the low-temperature ($T=1.85$ K) mobility μ on the Hall carrier concentration n_s for the two samples we studied.

It is well known (see, e.g., Ref. 5) that the mobility in a 2DEG decreases at the start of occupation of the second quantum-well subband. This is connected with the appearance of a new channel for momentum relaxation via intersubband scattering. In the ideal case, we should observe a discontinuous drop in the mobility. However, in real structures this transition is washed out by thermal and collisional broadening, and also by large- scale fluctuations in the 2DEG concentration.[6] Thus, the maximum in the function $\mu(n_s)$ observed in experiments is evidence that, despite the different initial concentration of the 2DEG, the second quantum-well subband is occupied in both samples. The position of this maximum allows us to determine the carrier concentration n_{max} at which occupation of the second quantum-well subband begins.

The preparation of the sample and method of measuring the magnetoresistance were described in Ref. 1. We refined the accuracy of the present experimental measurements over those reported in Ref. 1 by automating them. As a result of identifying a larger number of experimental points, we were able to observe changes in the experimental dependences for small changes in the state of the sample. This flexibility is very important for addressing the central problem of this paper–investigating weak localization effects in the presence of spin-orbit scattering under conditions where the Fermi level is located near the bottom of the second quantum-well subband. Figure 2 shows two curves for the dependence of the magnetoresistance

$$\frac{\Delta R}{R}=\frac{[R(B)-R(0)]}{R(B)}$$

on magnetic field B for two states of the sample with con-

centrations close to $n_{\max}$. It is clear that a 5% change in concentration leads to an appreciable change in the function $\Delta R/R = f(B)$.

3. EXPERIMENTAL RESULTS AND ANALYSIS

The experimental dependence of the magnetoresistance on magnetic field (Fig. 2) clearly demonstrates that the latter changes sign, both for $ns < n_{\max}$, when the electrons are concentrated in only one quantum-well subband, and for $n_s > n_{\max}$, when the carriers begin to occupy the second subband. It is well known that changes in either the temperature or the magnetic field lead to quantum corrections to the 2DEG conductivity that are proportional to the constant $G_0 = e^2/2\pi^2\hbar$. For this reason, the experimental dependences of the magnetoresistance are converted to magnetoconductivity dependences, based on the expression

$$\frac{\Delta\sigma(B)}{G_0} = \frac{-(\Delta R/R)}{G_0 R(0)},$$

which is correct in weak magnetic fields such that $\mu B \ll 1$. The dependence of the sign-changing magnetoconductivity on magnetic field has a singular point (like the dependence of the magnetoresistance), i.e., an extremum. We will use the parameters of this extremum, namely the value of magnetic field B_m at which it is observed and the absolute value of the magnetoconductivity $G_m \equiv |\Delta\sigma(B_m)/G_0|$ at the extremum, as quantities that characterize the experimental behavior of the magnetoconductivity. Figures 3b and 3c show the experimental dependence of these quantities on carrier concentration n_s. The various points on this plot correspond to various states of a single sample obtained by successively illuminating the latter with light pulses from a GaAs light-emitting diode. The vertical dashed line in this figure corresponds to the concentration $n_{\max}$, i.e., the density that maximizes the function $\mu(n_s)$. It is clear that both quantities B_m and G_m decrease with increasing concentration. However, the sharp drop in the absolute value of the magnetoconductivity G_m occurs at exactly the point where carriers first appear in the second subband, i.e., for $n_s \geqslant n_{\max}$, whereas the decrease in the magnitude of the magnetic field B_m begins when $n_s < n_{\max}$, i.e., before there are any electrons in the second subband. In the region $n_s > n_{\max}$ we observe a local maximum in the quantity B_m.

In order to understand the physical meaning of these features, let us pause to discuss the theory of magnetoconductivity associated with the suppression of weak localization in the presence of spin-orbit scattering. The interference between coherent electron states (weak localization) is determined not only by the phase of the wave function of an electron, but also by its spin polarization. The latter is taken into account by considering the triplet and singlet contributions to the interference term.[7,8] For the case of strong spin-orbit interaction ($\tau_s \ll \tau_\varphi$) the singlet term plays the primary role. As a result of a reversal of sign, the temperature-induced correction to the conductivity and magnetoresistance in a weak magnetic field becomes positive (the so-called ''antilocalization'' effect). As the magnetic field increases, the singlet contribution to the interference is suppressed,

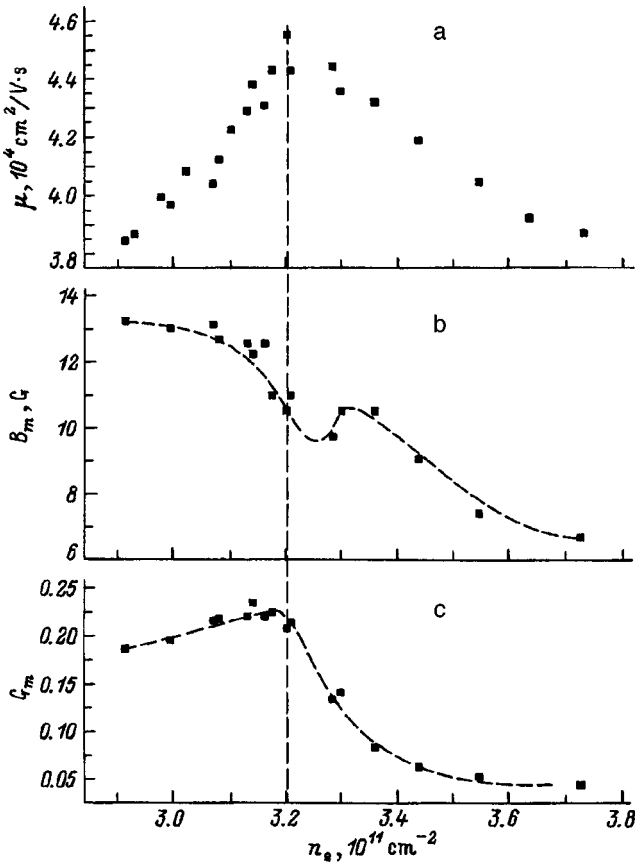

FIG. 3. Concentration dependences of the mobility (a), along with parameters that characterize the antilocalization minimum in the magnetic field dependence of the magnetoconductivity: b — magnetic field B_m, c — modulus of the normalized magnetoconductivity G_m.

while the triplet contribution becomes more important and the magnetoresistance becomes negative. This sign-changing feature of the magnetoresistance is evidence of a rather strong spin-orbit coupling in the electron gas, and can be used to study its nature.

In III–V compounds, the most effective mechanism for relaxation of a spin by carriers is the Dyakonov–Perel' mechanism, involving the combined action of any momentum relaxation mechanism with the splitting of the band of delocalized states. In this case, two terms appear in the expression for the quantum magnetoconductivity:

$$\frac{\Delta\sigma}{G_0} = \Phi_1(B) + \Phi_3(B), \tag{1}$$

which correspond to the suppression of coherence of the singlet (Φ_1) and triplet (Φ_3) states. The terms in Eq. (1) have different signs, and thus lead to a sign-changing magnetoresistance. A characteristic parameter of the singlet term is the time for phase slip τ_φ of the electron wave function and the corresponding value of the characteristic magnetic field

$$H_\varphi \equiv \frac{\hbar c}{4eD\tau_\varphi}, \tag{2}$$

where $D = \sigma/e^2\nu$ is the diffusion coefficient, σ is the conductivity, and ν is the density of states. The expression for $\Phi_1(B)$ in the 2D case usually is written in the form

$$\Phi_1(B) = -\frac{1}{2} f_2\left(\frac{B}{H_\varphi}\right), \tag{3}$$

$$f_2(x) = \Psi\left(\frac{1}{2} + \frac{1}{x}\right) + \ln x,$$

where $\Psi(x)$ is the digamma function.

The triplet term $\Phi_3(B)$ is related to suppression of the phase and the spin coherences by the magnetic field, and depends on τ_φ and on the characteristics of the spin-orbit relaxation. At this time it is known[10] that the functional form of the expression $\Phi_3(B)$ is determined by the dependence of the spin splitting $\Omega(k)$ on wave vector k and by the corresponding mechanisms for spin relaxation. If only one spin relaxation mechanism dominates, then the following expression, postulated in the first papers on quantum corrections,[8] is correct:

$$\Phi_3(B) = \frac{3}{2} f_2\left(\frac{H}{H_\varphi + H_s}\right), \tag{4}$$

where the quantity

$$H_s \equiv \frac{\hbar c}{4eD\tau_s} \tag{5}$$

is determined by the time for spin relaxation due to the spin-orbit interaction (i.e., τ_s).

When the slip in spin coherence is determined by several different spin-orbit interaction mechanisms, it becomes necessary to include interference of these processes. The upshot of this is that we must use a more complex expression for the triplet term than (4) to correctly determine the characteristic spin relaxation time, with several parameters that characterize the spin splitting.[10] In this case, the form of the dependence of the magnetoresistance on magnetic field is qualitatively unchanged. In this paper it was not our intention to investigate the problem of spin relaxation mechanisms in great detail. Therefore, in analyzing the experimental dependences we used Eq. (4) to describe the triplet terms and Eq. (1) for $\Delta\sigma(B)$. In this case, analysis of Eq. (1) shows that the value of the magnetoconductivity G_m at the extremum is unambiguously determined by the single parameter $b = H_s/H_\varphi$. Therefore, starting from the data shown in Fig. 3c and using the experimental values of G_m we can determine the value of the ratio of characteristic magnetic fields b. Moreover, we can find the values of the magnetic fields that characterize the slips in phase (H_φ) and spin (H_s) coherence from the magnitude of the magnetic field corresponding to the extremum B_m (Fig. 3b). The concentration dependences of the characteristic magnetic fields obtained in this way are show in Fig. 4. The vertical straight line in this figure represents the concentration $n_{\max}$.

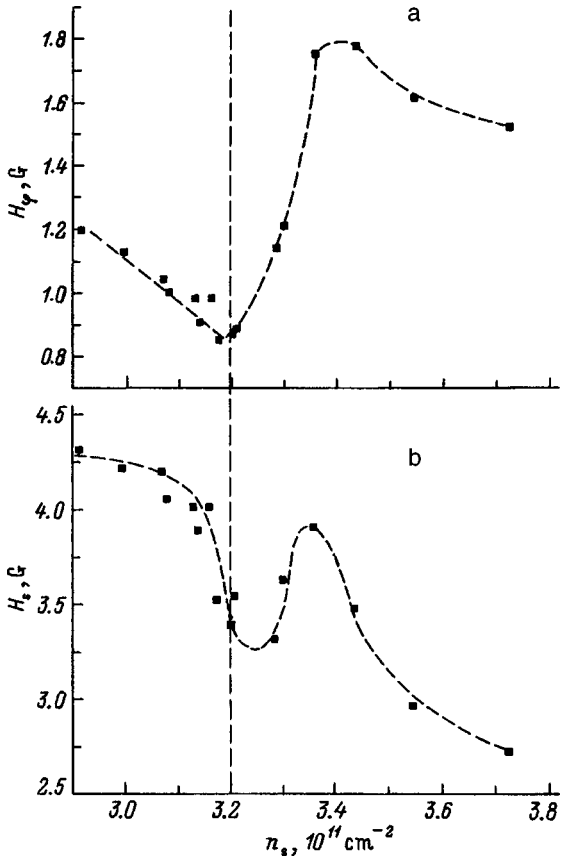

FIG. 4. Dependence of the phase coherence parameter H_φ (a) and spin coherence parameter H_s (b) on the electron concentration. The dashed line corresponds to the concentration $n_{\max}$ at which the carriers begin to occupy the second quantum-well subband.

4. ANALYSIS OF THE CONCENTRATION DEPENDENCES OF THE CHARACTERISTIC MAGNETIC FIELDS

4.1. Phase coherence parameter

Consider the concentration dependence of the magnetic field H_φ, which characterizes the rate of phase relaxation of the electron wave function due to inelastic collisions, shown in Fig. 4a. For small n_s electrons are present only in the lowest subband; therefore, the quantity H_φ is determined by the diffusion length for electrons in the first subband within a time τ_φ. In other words, $H_\varphi = H_{\varphi 1}$. In Ref. 1 it was shown that the phase of an electron in the first subband of these structures relaxes via electron-electron collisions with small momentum transfers.[11] In this case, to first approximation we have $\tau_\varphi \sim \sigma_0$ and $H_\varphi \sim (D\tau_\varphi)^{-1} \sim \sigma_0^{-2}$ (where σ_0 is the conductivity at $B=0$). As the carrier concentration increases in the channel (i.e., as σ_0 increases) a falloff in the magnitude of H_φ is observed. When both quantum- well subbands are occupied, the quantity H_φ we have found is the effective parameter that determines the properties of electrons in both the first and second subbands, as well as intersubband transitions. When the intersubband relaxation is fast, with a time $\tau_{12} \ll \tau_\varphi$, the diffusion and the inverse relaxation time should be averaged with weight coefficients equal to the densities of states in the subbands. In this case, for the 2DEG we obtain

$$H_\varphi \cong \frac{1}{\sigma}(\sigma_1 H_{\varphi 1} + \sigma_2 H_{\varphi 2}), \tag{6}$$

where $\sigma = \sigma_1 + \sigma_2$ is the conductivity of a system consisting of two subbands, and the labels correspond to the subband labels. If the carrier concentration in the second subband is much smaller than that in the first, i.e., $\sigma_1 \gg \sigma_2$, then

$$H_\varphi \cong H_{\varphi_1}\left(1+\frac{\sigma_2}{\sigma}\frac{H_{\varphi 2}}{H_{\varphi 1}}\right)\approx H_{\varphi 1}\left(1+\frac{\sigma}{\sigma_2}\right). \tag{6a}$$

Here we assume that the phase of the wave function for electrons in both subbands relaxes electron-electron interactions with small momentum transfers,[9] and that $H_{\varphi 2}/H_{\varphi 1} \approx (\sigma_1/\sigma_2)^2$. Analysis of Eq. (6a) shows that for $n_s > n_{\max}$ we should see a discontinuous jump in the magnitude of H_φ associated with the significant contribution of phase relaxation from electrons in the second subband to the effective phase relaxation rate. If the occupation of the second subband is further increased, we should observe a decrease in H_φ associated with violation of the condition $\sigma_1 \gg \sigma_2$, and in the limit of strong occupation of the second subband, when $\sigma_1 \approx \sigma_2$, the condition $H_\varphi \approx H_{\varphi 1}$ should hold. It is easy to see that the analysis given here qualitatively describes the experimental function $H_\varphi(n_s)$ shown in Fig. 4a over the entire range of 2DEG concentrations.

Thus, the abrupt jump in the magnitude of H_φ, which characterizes the slip in phase coherence when carriers appear in the second quantum-well subband, is related not to a jump in the density of states, as Iwabuchi *et al.*[2] have asserted, but rather to the fast rate of phase relaxation $1/\tau_\varphi$ of the wave function for electrons in the second quantum-well subband when the occupation of the latter is small.

4.2. SPIN COHERENCE PARAMETER

Consider the variation of the spin coherence parameter H_s with 2DEG concentration shown in Fig. 4b in the persistent photoconductivity regime. From these data it is clear that there is a general tendency for H_s to decrease with increasing n_s in the persistent photoconductivity regime. This tendency, which is already apparent even when $n_s < n_{\max}$, which correspond to occupation of only the first quantum-well subband so that $H_s = H_{s1}$, is determined only by the diffusion coefficient D and the spin relaxation time τ_s for electrons in the first quantum-well subband.

In our previous paper,[1] we investigated in detail the processes of spin-orbit relaxation for a series of $InP/In_{0.53}Ga_{0.47}As$ heterostructures with different carrier concentrations and only one quantum-well subband occupied. In this case, we showed that the rather rapid spin relaxation of electrons in these structures is connected with the existence of a spin splitting of the electronic subbands due to the lowered symmetry that accompanies this structure.[7] The symmetry is lowered, first of all, by the absence of an inversion center in the crystal lattices of the III–V compounds (the Dresselhaus mechanism[12]) and, secondly, by the asymmetric (triangular) shape of the quantum well at the heterojunction connected with the presence of the built-in electric field F (the Rashba mechanism[13]). In Ref. 1 we used a new theory[10] that independently takes into account the contributions of various spin relaxation mechanisms in order to analyze the 2DEG magnetoresistance in these structures. We found that the spin coherence parameters increase rapidly with increasing n_s, and a comparative analysis of the experimental concentration dependences and the theoretical dependences in these structures supports the Rashba mechanism.[13] In this case, the magnitude of the spin splitting of the bands is proportional to the wave vector k of an electron and the built-in electric field F, whereas for the characteristic spin-orbit scattering rate we can write the expression

$$\frac{1}{\tau_s} = \alpha^2 \tau k_F^2 F^2, \tag{7}$$

where the coefficient α is a constant that characterizes the energy spectrum of the semiconductor in which the 2DEG is localized, τ is the momentum relaxation time, and k_F is the wave vector of an electron at the Fermi level. In the case where only one quantum-well subband is occupied we have

$$k_F = \sqrt{2\pi n_s}, \quad D = \frac{\pi\hbar^2}{m^2} n_s \tau$$

and the spin coherence parameter connected with the Rashba mechanism is determined only by the magnitude of the built-in field:

$$H_s = \frac{m^2 c}{2e}\alpha^2 F^2. \tag{8}$$

The field F at the heterojunction is determined by the charge distribution in the structure and to first approximation depends linearly on the 2DEG concentration. This explains the dependence we found in Refs. 1 and 14 of the spin coherence parameter H_s on the 2DEG concentration, specifically, the rapid increase of H_s with increasing n_s for samples with concentrations n_s in the range $(2-5.5)\times 10^{11}$ cm^{-2}, for which only the first quantum-well subband is filled. The fall-off of H_s with increasing n_s shown in Fig. 4b for $n_s < n_{\max}$ at first glance contradicts both the theoretical expression (8) and the experimental results obtained in Ref. 14. However, it is necessary to note that the electric field at the heterojunction is determined not only by the charge of the 2D electrons, but also by the entire distribution of charges in the system. When the distribution of charge in the system is arbitrary, it is not possible to find an analytic expression for the average electric field. This problem was solved numerically by Ando[15] for the case where the narrow-band semiconductor layer contained both a 2DEG and a residual impurity distribution with a "squared-off" concentration, $N_0 \ll n_s$. The analytic results obtained in Refs. 16–18 for approximating the calculated curves can be represented in the form

$$F = \frac{4\pi e}{\chi}(f n_s + N_0), \tag{9}$$

where f is in turn a coefficient determined by the shape of the wave function of the 2D electrons, and χ is the dielectric permittivity.

Persistent photoconductivity in these structures is associated with the separation of carriers by the built-in electric field, the trapping of holes by residual ionized acceptors in the layer of narrow-gap InGaAs material, and also by surface states in the case of a thin top layer.[4] This implies that if illumination of the system by interband light leads to an increase in n_s by an amount Δn, then at the same time the

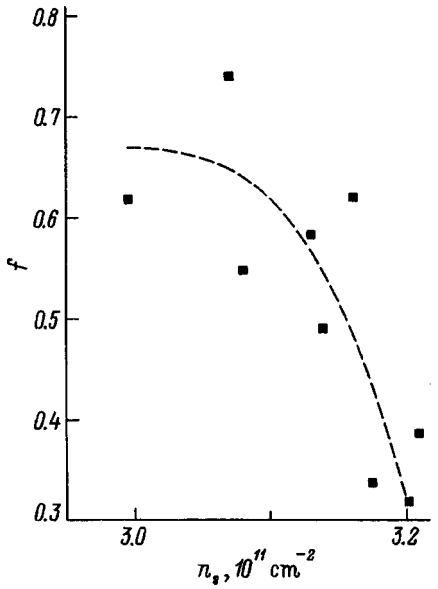

FIG. 5. Concentration dependence of the parameter f in the expression (9) for the electric field F in the heterostructure, obtained from the function $H_\varphi(n_s)$ in the region where only the first quantum-well subband is occupied (see Fig. 4a).

concentration N_0 must decrease by the same amount. As a result, for the average field in the persistent photoconductivity state we can write the expression

$$F=F^0+\frac{4\pi e}{\chi}\Delta n(f-1). \tag{10}$$

Here and in what follows, ''0'' labels parameters of the system's initial state. It is clear that the change in the field F and, accordingly, the parameter H_s, with increasing electron concentration in the persistent photoconductivity regime is determined by the coefficient f: H_s increases when $f>1$ and decreases when $f<1$. Substituting Eq. (10) into Eq. (8) and comparing the change in ΔH_s for corresponding changes in the 2DEG concentration Δn_s, we find the magnitude of the parameter f

$$f=\frac{2\dfrac{\Delta n}{n_s^0}+\dfrac{N_0^0}{n_s^0}\dfrac{\Delta H_s}{H_s^0}}{2\dfrac{\Delta n}{n_s^0}+\dfrac{\Delta H_s}{H_s^0}}, \tag{11}$$

where $\Delta n=n_s-n_s^0$, and $\Delta H_s=H_s-H_s^0$. Figure 5 shows the concentration dependence of the parameter f determined from the experimental function $H_s(n_s)$ using Eq. (11) for $n_s<n_{\max}$. The value of the concentration of residual impurities in the initial state is determined from the maximum change in 2DEG concentration in the saturation regime of the persistent photoconductivity: $N_0^0=8\times10^{10}$ cm^{-2}. Such a large value of N_0^0 is determined by the charging of states at the surface of the thin $In_{0.53}Ga_{0.47}As$ layer which contains the 2DEG and which is the capping layer of the structure. From the data shown in Fig. 5 it is clear that the experimental function H_s corresponds to a value $f=0.6\pm0.1$ at concentrations close to the initial one, and decreases to a value $f\cong0.35$ as $n_s\to n_{\max}$. The parameter f was introduced in Refs. 15–17 in order to achieve the best agreement with numerical calculations, and was close to 0.5. This value is in fairly good agreement with the experimental results we have obtained for states of our structures close to their initial states. At present, there are no theoretical predictions of how this parameter should change during the redistribution of charge that accompanies the persistent photoconductivity.

Since $\Delta F=4\pi e\Delta n(f-1)/\chi$ [see Eq. (10)] and since $f<1$, the value of the built-in field F [Eq. (9)] in the persistent photoconductivity regime decreases in our case and, accordingly, the magnitude of H_s [Eq. (8)] decreases as well, which removes the contradiction mentioned above for the function $H_s(n_s)$ when $n_s<n_{\max}$, as represented by the data from Ref. 1 plotted in Figs. 3b and 3c. Thus, the falloff in H_s which we observed previously as the sample entered the persistent photoconductivity regime[1] is connected not with filling of the second subband, as we asserted in that paper, but rather with the redistribution of charge in the system that takes place in the persistent photoconductivity regime and leads to a decrease in the built-in field in the quantum well, despite the increase in the 2DEG concentration.

Let us now consider the function $H_s(n_s)$ at concentrations that exceed $n_{\max}$, i.e., when the first carriers appear in the second quantum-well subband. From the data shown in Fig. 4b it is clear that the magnitude of H_s exhibits a local maximum when occupation of the second subband begins, against the background of general tendency for it to decrease. Here, just as in the previous case with H_φ, the value of H_s determined experimentally is an effective parameter which is determined, in general, by the times τ_{si}, the diffusion coefficients D_i in the first $(i=1)$ and second $(i=2)$ subbands, and by the intersubband electron transitions. In the case of fast intersubband relaxation we can write

$$\tau_s^{-1}=\frac{\tau_{s1}^{-1}g_1+\tau_{s2}^{-1}g_2}{g_1+g_2}, \quad D=\frac{D_1g_1+D_2g_2}{g_1+g_2},$$

where g_1 and g_2 are densities of states in the first and second subbands, respectively. The lower numerical labels, as before, correspond to the quantum-well subband labels. As a result, we obtain

$$H_s=\frac{\sigma_1H_{s1}+\sigma_2H_{s2}}{\sigma}. \tag{12}$$

When the primary spin relaxation mechanism in both subbands is the Rashba mechanism, the quantities H_{s1} and H_{s2} do not depend on the electron wave vector, and are determined only by the value of the built-in electric field F. This implies that the parameters H_{si}, which characterize the spin relaxation rate in the first and second subbands, are close in magnitude, regardless of the level of occupation of the second subband. Thus, setting $H_{s1}\cong H_{s2}$ and $\sigma\cong\sigma_1\gg\sigma_2$, for small occupations of the second subband, we can rewrite Eq. (12) in the form

$$H_s\approx H_{s1}\left(1+\frac{\sigma_2}{\sigma}\right). \tag{13}$$

The analysis given above indicates that the electric field F, and hence H_{s1}, will decrease with increasing concentration in the persistent photoconductivity regime. Thus, there are two competing factors: with increasing concentration, the quantity H_{s1} decreases, while the conductivity of the second subband increases. This also leads to the maximum in the function $H_s(n_s)$ observed in experiment at a concentration that slightly exceeds the value of $n_{\max}$ (for $n_s = 3.35 \times 10^{11}$ cm^{-2} in Fig. 4b). Thus, when the second quantum-well subband is occupied, a local maximum is observed in the quantity H_s, which arises from the fact that, due to overcoming of the Rashba mechanism for the spin relaxation we have $H_{s2} \approx H_{s1}$, i.e., the same order of magnitude for any carrier concentration in the second subband. The contribution of the second subband increases as its conductivity increases.

CONCLUSION

We have investigated the weak-field magnetoresistance of the 2D electron gas in modulation doped $In_{0.53}Ga_{0.47}As/InP$ heterostructures as the state of the system is changed by illuminating the sample with interband light and converting it into a state with persistent photoconductivity.

Analysis of corresponding changes in the magnitude and position of the extremum (the so-called antilocalization maximum) in the dependence of the magnetoconductivity on magnetic field allows us to determine parameters for all states of the sample that characterize the destruction of the phase coherence (H_φ) and spin coherences (H_s). The functions $H_\varphi(n_s)$ and $H_s(n_s)$ obtained in this way were analyzed in the low-concentration regime, where the carriers are located in the first quantum well subband only, and in the regime of weak occupation of the second subband. We have obtained the following basic results:

—The abrupt jump in the magnitude of H_φ (which characterizes the phase coherence) when carriers appear in the second quantum-well subband is associated with a high rate of phase relaxation of the wave function of electrons in the second subband when the occupation of the latter is small, and not with the jump in the density of states, as was previously assumed.[17]

—The falloff in H_s we observed previously[1] after the sample enters the persistent photoconductivity regime is associated with the redistribution of charge in the system which takes place in the persistent photoconductivity regime and which leads to a decrease in the built-in field in the quantum well, despite the increase in 2DEG concentration, and not with the occupation of the second subband, as we proposed in Ref. 1;

—When the second quantum-well subband is occupied, a local maximum is observed in the quantity H_s. This is related to the fact that the quantities $H_{s2} \approx H_{s1}$ for any concentration of carriers in the second subband (due to overcoming of the Rashba mechanism in the processes of spin-orbit interaction), while the contribution of the second subband increases with increasing conductivity of the latter.

The mechanisms we have described allow us to qualitatively understand all the features observed experimentally. However, a quantitative description of these features will be possible only through refinement of the dependence of the magnitude of the built-in electric field on the charge distribution in the selectively doped heterostructures and the redistribution of this charge in the persistent photoconductivity regime, and also refinement of the theoretical expressions that describe weak localization of electrons in the two quantum-well subbands for various ratios of the characteristic times of the system, including the intersubband scattering time.

This work was financially supported by funds from INTAS-RFFI (Grant No. 95-IN/RU-533) and the Russian Fund for Fundamental Research (Grant No. 98-02-18396).

[1] A. M. Kreshchuk, S. V. Novikov, T. A. Polyanskaya, and I. G. Savel'ev, Fiz. Tekh. Poluprovodn. **31**, 459 (1997) [Semiconductors **31**, 391 (1997)].
[2] Sh. Iwabuchi and Y. Nagaoka, J. Phys. Soc. Jpn. **58**, 1325 (1989).
[3] L. V. Golubev, A. M. Kreshchuk, S. V. Novikov, T. A. Polyanskaya, I. G. Savel'ev, and I. I. Saĭdashev, Fiz. Tekh. Poluprovodn. **22**, 1948 (1988) [Sov. Phys. Semicond. **22**, 1234 (1988)].
[4] A. M. Kreshschuk, S. V. Novikov, and I. G. Savel'ev, Fiz. Tekh. Poluprovodn. **26**, 1375 (1992) [Sov. Phys. Semicond. **26**, 771 (1992)].
[5] S. Mori and T. Ando, Phys. Rev. B **19**, 6433 (1979).
[6] A. M. Kreshchuk, S. V. Novikov, T. A. Polyanskaya, I. G. Savel'ev, and A. Ya. Shik, J. Cryst. Growth **146**, 153 (1995).
[7] K. B. Efetov, Zh. Éksp. Teor. Fiz. **78**, 2017 (1980) [Sov. Phys. JETP **51**, 1015 (1980)]; S. Hikami, A. I. Larkin, and Y. Nagaoka, Prog. Theor. Phys. **63**, 707 (1980).
[8] B. L. Al'tshuler, A. G. Aronov, A. I. Larkin, and D. E. Khmel'nitskiĭ, Zh. Éksp. Teor. Fiz. **81**, 788 (1981) [Sov. Phys. JETP **54**, 850 (1981)].
[9] M. I. D'yakonov and V. I. Perel', Zh. Éksp. Teor. Fiz. **60**, 1954 (1971) [Sov. Phys. JETP **33**, 1053 (1971)].
[10] F. G. Pikus and G. E. Pikus, Phys. Rev. B **51**, 16928 (1995).
[11] B. L. Altshuler, A. G. Aronov, and D. E. Khmelnitskiĭ, J. Phys. C **15**, 7367 (1982).
[12] G. Dresselhaus, Phys. Rev. **100**, 580 (1955).
[13] Yu. L. Bychkov and E. I. Rashba, J. Phys. C **17**, 6093 (1984).
[14] A. M. Kreshchuk, S. V. Novikov, T. A. Polyanskaya, and I. G. Savel'ev, Semicond. Sci. Technol. **13**, 384 (1998).
[15] T. Ando, J. Phys. Soc. Jpn. **51**, 3842 (1982).
[16] F. Stern and S. D. Sarma, Phys. Rev. B **30**, 840 (1984).
[17] J. Yoshida, IEEE Trans. Electron Devices **33**, 154 (1986).
[18] G. M. Gusev, Z. D. Kvon, I. G. Neizvestnyi, and V. N. Ovsuk, Solid State Commun. **46**, 169 (1983).

Translated by F. Crowne

Energy spectrum of a nonideal quantum well in an electric field

O. L. Lazarenkova and A. N. Pikhtin*)

St. Petersburg State Electrotechnical University, 197376 St. Petersburg, Russia
(Submitted February 9, 1998; accepted for publication February 10, 1998)
Fiz. Tekh. Poluprovodn. **32**, 1108–1113 (September 1998)

The effect of an electric field on the energy spectrum of a quantum well with macroscopic fluctuations is studied. The Stark shift of the quasibound states in a quantum well and three field-dependent broadening mechanisms (field-induced homogeneous broadening and broadening due to well width and depth fluctuations) are calculated in a wide range of electric fields. As an example, the effect of an electric field on the energy spectrum of electrons in a 12-nm-wide $GaAs/Al_{0.3}Ga_{0.7}As$ quantum well with 5% width and depth fluctuations is determined. © *1998 American Institute of Physics.* [S1063-7826(98)01909-7]

An electric field has a considerable influence on not only charge transport processes but also the position and width of resonances (quantum-well levels) in a quantum well. This must be taken into account when calculating the characteristics of modern nano- and optoelectronics devices, and in a number of cases it can produce qualitatively new results.

Epitaxial layers in real heterostructures can exhibit thickness fluctuations δL_z and fluctuations of the composition of the solid solution, which all lead to fluctuations of the quantum well width and depth. As usual, we assume that one of the characteristic dimensions of the structure is much smaller than the other two ($L_z \ll L_x$, L_y). This makes it possible to ignore the quantization of electron motion in the x,y plane and to study the problem of a one-dimensional quantum well, each bound state of which is associated with two-dimensional subbands which correspond to the kinetic energy of a carrier in the plane of the well. The effects due to microscopic composition fluctuations in the solid solution should be the same as those observed in three-dimensional systems.[1,2] In the present paper we solve the one-dimensional problem, assuming that the fluctuations in the x,y plane are macroscopic and that they are to be treated additively.

1. SPECTRUM OF AN IDEAL HETEROSTRUCTURE WITH A PIECEWISE-CONSTANT POTENTIAL IN AN ELECTRIC FIELD

The Schrödinger equation for a quantum well in an electric field **F** perpendicular to the plane of the well is

$$\left[-\frac{\hbar^2}{2m^*}\frac{\partial^2}{\partial z^2}+V(z)-qFz\right]\psi(E,z)=E\psi(E,z), \tag{1}$$

where m^* and q are, respectively, the particle mass and charge, $V(z)$ is a piecewise-contant potential, and $\psi(E,z)$ is the particle wave function, which is generally a continuous function of the coordinates and the energy.

For $F=0$ the solution of the equation is a discrete set of eigenenergies and eigenfunctions corresponding to the bound states. Mathematically, such states correspond to poles of the resolvent of the Hamiltonian. When $F\neq 0$, all eigenvalues of the Hamiltonian are embedded in the continuous spectrum, and this distinguishes them fundamentally from the $F=0$ stationary states. The poles of the resolvent move off the real axis into the complex plane. Lorentzian resonance peaks, called Breit–Wigner resonances,[3]

$$L_n(E)=|I_n(E)|^2=C_n \Big/ \left\{1+\left(\frac{E-E_n}{\Gamma_n/2}\right)^2\right\}, \tag{2}$$

are observed in the electronic spectrum. The width Γ_n of the observed line is determined by the imaginary part, while the energy E_n of a resonance is determined by the real part of the corresponding eigenvalue. The existence of such pronounced resonances indicates the existence of quasibound states (quantum-well levels) with finite lifetime, even in the presence of an electric field. In Eq. (2) n is the number of the quasibound state and C_n is a normalization constant.

As the electric field is increased, the poles move farther away from the real axis, and the width of the resonance lines increases as a result. Perturbations of the energy spectrum near quasibound states are much larger than the changes occurring elsewhere in the spectrum. This makes it possible to replace the real spectrum by a sum of functions of the form (2).

The completeness and normalization of the wave functions of the continuous spectrum are expressed as follows:

$$\int_{-\infty}^{+\infty}\psi^*(E,z)\psi(E,z')\,dE=\delta(z-z') \tag{3}$$

and

$$\int_{-\infty}^{+\infty}\psi^*(E,z)\psi(E',z)\,dz=\delta(E-E'). \tag{4}$$

The assumption adopted makes it possible to obtain after substituting into Eqs. (3) and (4) the particle wave function in the form

$$\chi(E,z)=\sum_{n=1}^{\infty} I_n(E)\chi_n(z), \tag{5}$$

the expressions

$$\sum_{n=1}^{\infty}\sum_{m=1}^{\infty}\chi_n^*(z)\chi_m(z')\int_{-\infty}^{+\infty}I_n^*(E)I_m(E)dE=\delta(z-z') \quad (6)$$

and

$$\sum_{n=1}^{\infty}\sum_{m=1}^{\infty}I_n^*(E)I_m(E')\int_{-\infty}^{+\infty}\chi_n^*(z)\chi_m(z)dz=\delta(E-E'), \quad (7)$$

respectively. Here χ_n is a solution of the Schrödinger equation (1), which corresponds to the resonance energy $E=E_n$ and which decreases at $-\infty$.

As the field decreases, Γ_n approaches zero and I_n becomes a delta function. We then obtain from Eq. (6) the conditions

$$\sum_{n=1}^{\infty}\chi_n^*(z)\chi_n(z')=\delta(z-z') \quad (8)$$

and

$$\int_{-\infty}^{+\infty}I_n^*(E)I_m(E)dE=\delta_{nm}.$$

The latter condition implies

$$\int_{-\infty}^{+\infty}|I_n(z)|^2dz=1. \quad (9)$$

The normalization condition (9) gives $C_n=2/\pi\Gamma_n$.

Taking a similar limit in Eq. (7), the normalization of the infinite sum to a delta function becomes the well-known normalization for the *n*th bound state:

$$\int |\chi_n(z)|^2dz=1. \quad (10)$$

As the field is increased, the width of the level increases and the level can no longer be modeled by a delta function, but the values of the integrals (9) and (10) remain the same. In the approximation of weakly interacting levels these normalization conditions can therefore be used for quasibound states in a quantum well in an external electric field. The condition (8) ensures that the basis employed in the expansion (5) is complete. The error of the approximation is determined by the ratio of the width of the resonance peaks and the spacing between them.

Since the integral of $|\chi_n(z)|^2$ to $+\infty$ diverges, the normalization condition (10) requires regularization. Let $\chi_n=0$ outside a certain interval. As this interval increases, the value of the normalization constant of the wave function stabilizes, so that it is sufficient to take several well widths for the integration limits. For levels located closer to the continuum this interval must be increased. On the other hand, the saturation interval increases because the amplitude of the function outside a well increases. This corresponds to an increase in the probability of tunneling through a triangular barrier. However, this process is already taken into account through the field-induced broadening of the quasibound states in Eq. (2). The interval of the normalization integration of the wave function must therefore be limited by the first node outside the well.

To make the computational results universal, it is convenient to employ relative units. We shall measure the coordinate in terms of z/L_z, where L_z is the width of the well, and we shall measure ε in terms of the first quantum-well level of a particle of mass m^* in an infinite well of width L_z:

$$E_1^{\infty}=\frac{\pi^2\hbar^2}{2m^*L_z^2}.$$

We take as the origin the center of the well bottom. In such units the $(n+1)$-st state appears in a well of depth $V/E_1^{\infty}=\tilde{\nu}=n^2$. It is convenient to measure the electric field F which determines the slope of the potential in terms of

$$f=qFL_z/[V-E_n(0)],$$

since the distance from the level to the well edge determines the position and width of the level. In this system of units the analysis can be limited to fields $f\leqslant f_0=2$, where f_0 corresponds to the slope of the potential such that the the *n*th level would lie above a triangular barrier if the position of the level did not change as the field increased. The quantity f_0 can serve as an estimate of the ionization field.

The positions and widths of the levels calculated as a function of the electric field for different effective well depths are shown in Figs. 1 and 2, respectively.

We see from Fig. 1 that for any *n* and dimensionless well depth $(n-1)^2<\tilde{\nu}<n^2$ the field-dependence of the position of a quantum-well level qualitatively resembles a Stark shift of the $1s$ line of atomic hydrogen. In weak fields, even levels with $n\geqslant 2$ shift downwards in energy, while perturbation theory in the infinite-well approximation predicts a quadratic shift to higher energies.[4] The appearance of new higher-lying states has the effect that in a weak field, when $\tilde{\nu}\geqslant(n+1)^2$, the level shift can be described in the infinite-well approximation using the level positions calculated for an infinite well in a zero field (dashed lines in the figure). Fields for which the following condition is satisfied:[4,5]

$$\frac{qFL_z}{E_1^{\infty}}\leqslant 1, \quad (11)$$

or in our units

$$f\frac{E_1^{\infty}}{V-E_n(0)} \quad (12)$$

are assumed to be weak. For the first level we compared our calculations not only with the infinite-well approximation but also with the quadratic Stark shift in weak fields, which was calculated by the variational method proposed in Ref. 5 . The corresponding curves are presented in Fig. 1 (dot-dashed lines).

The effect of an electric field on the level width Γ is trivial (Fig. 2). As the *n*th level approaches the continuum, the interaction of the levels becomes stronger and Γ increases. This process is affected by the presence of quasibound states between the *n*th level and the continuum. As a result, for well depths $\tilde{\nu}\sim n^2$, where the *n*th state becomes the top state in the quantum well, the slope of the dependence which we are considering changes sharply.

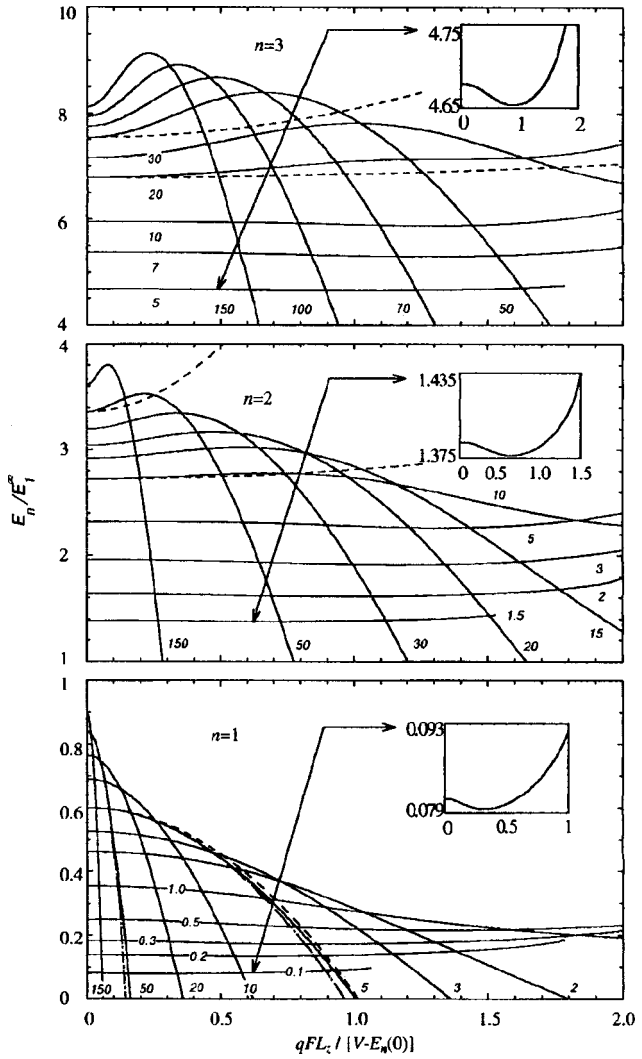

FIG. 1. Positions of the first three quantum-well levels $n=1$, 2, and 3 in an ideal quantum well plotted as a function of the electric field. The values of the dimensionless well-depth parameter are indicated. Dashed line — perturbation theory in the infinite-well approximation; dot-dashed line — quadratic Stark shift, calculated by a variational method in the weak-field limit. The energy is measured from the center of the well bottom.

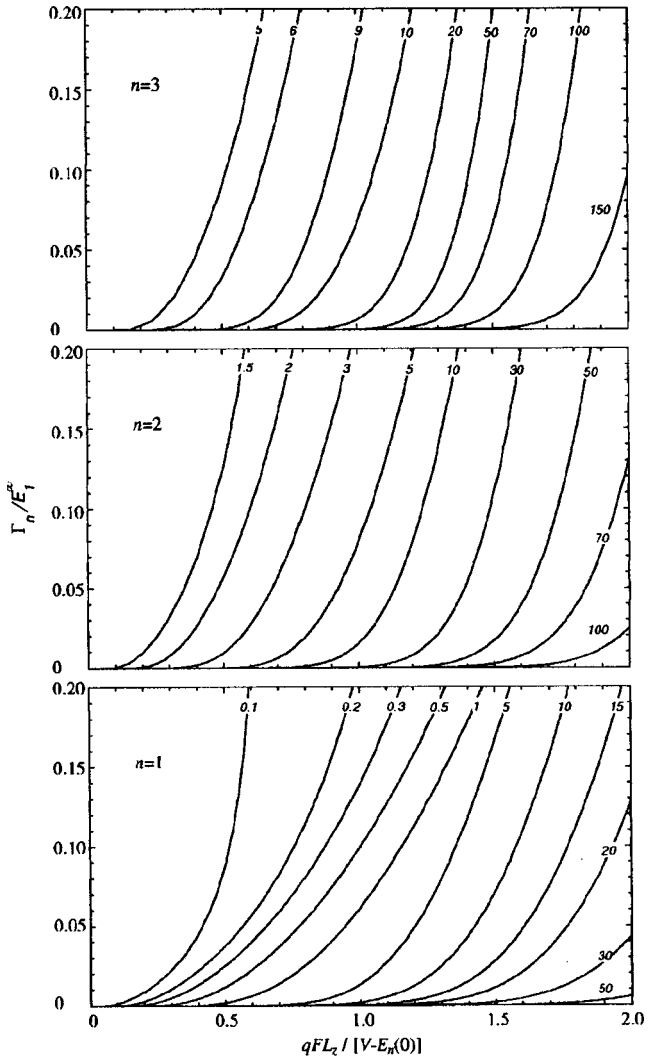

FIG. 2. Field-induced broadening of the quantum-well levels $n=1$, 2, and 3 versus the electric field. The values of the dimensionless well depth parameter are indicated.

2. INFLUENCE OF WIDTH FLUCTUATIONS OF A QUANTUM WELL

The fluctuations δL_z of the thickness of a heterolayer in the x,y plane produce nonuniform broadening of the spectrum in a manner so that, even in the absence of a field, instead of an infinitely narrow level of a one-dimensional ideal quantum well we obtain a resonance whose shape is described by a Gaussian contour. The corresponding nonuniform broadening $(\Gamma_{\delta L_z})_n$ is proportional to the absolute value of the well-width derivative of the position of the quantum-well level

$$(\Gamma_{\delta L_z})_n = \left|\frac{\partial E_n}{\partial L_z}\right| \kappa_{\delta L_z} \delta L_z . \tag{13}$$

The coefficient $\kappa_{\delta L_z}$ depends on the parameters of the fluctuations (for example, on the characteristic dimensions (L_x, L_y) of the islands that form the surface roughness) and is of the order of 1.

In dimensionless units

$$\frac{\partial E_n}{\partial L_z} = \frac{\partial[\varepsilon_n(\tilde{v})E_1^\infty]}{\partial L_z} = \frac{2E_1^\infty}{L_z}\left(\frac{\partial \varepsilon_n}{\partial \tilde{v}}\tilde{v} - \varepsilon_n\right). \tag{14}$$

The field-dependence of the well-width derivative of the position of the energy levels is complicated (Fig. 3) and far from trivial. On the one hand, as the well width is increased, the dimensionless well depth $\tilde{\nu}$ increases, which in the real scale can be accompanied by both a rising of the levels located close to the continuum and by a lowering of deeper levels. This mechanism wholly determines the derivative in a zero field. The derivative changes from small positive values for wells with depth $\tilde{\nu} \sim (n-1)^2$ to $-n^2$ for wells of infinite depth. On the other hand, a triangular barrier, through which carriers tunnel, forms in an electric field. For the same field $F \neq 0$ and fixed energy, the tunneling probability increases with increasing width of the well. As a result, the higher-lying levels sink. As the field is increased, the slope of the potential increases and the upper states gradually merge with

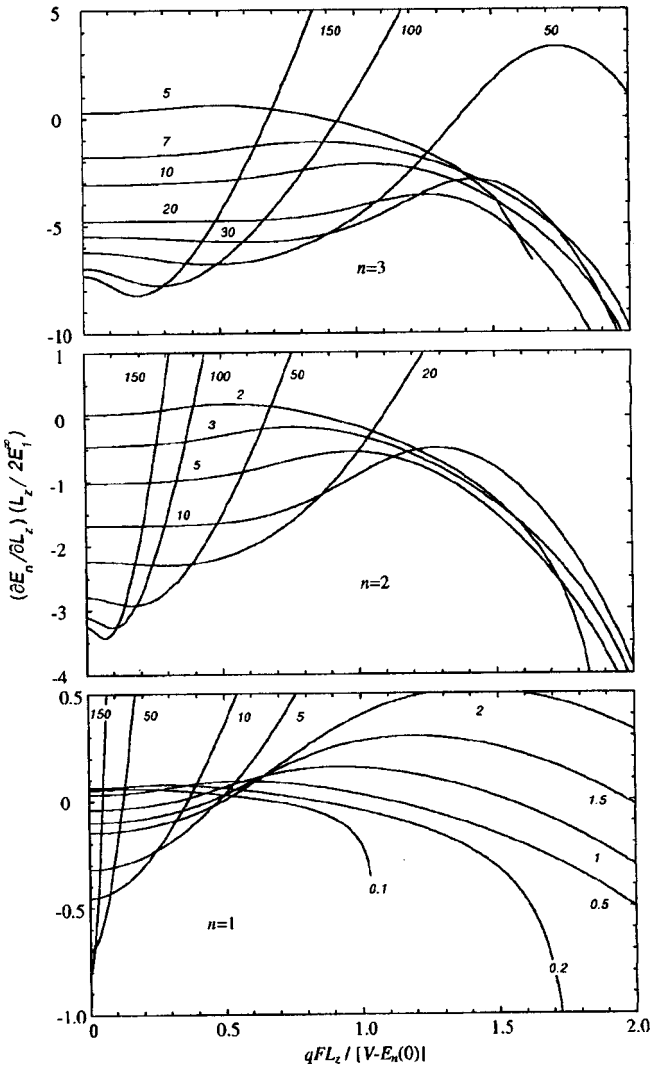

FIG. 3. Quantum well width derivative of the position of a quantum-well level $n=1$, 2, and 3 as a function of the electric field. The values of the dimensionless well depth parameter are indicated.

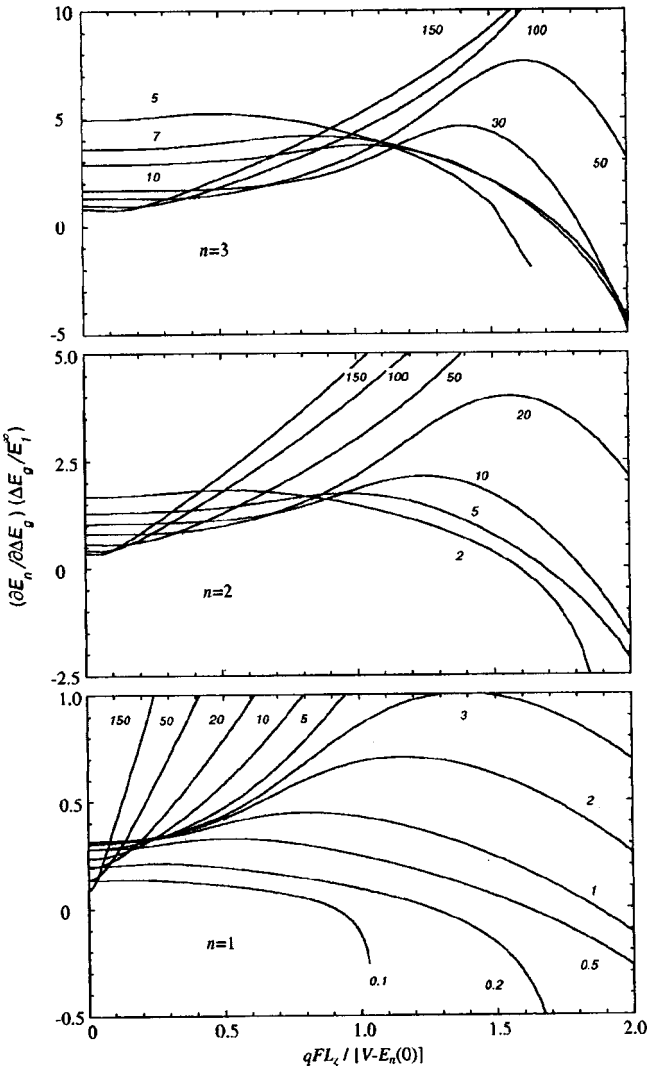

FIG. 4. Band gap offset derivative of the position of a quantum-well level $n=1$, 2, and 3 as a function of the electric field. The values of the dimensionless well depth parameter are indicated.

the continuum, and in the process the influence of the second mechanism on the nth level increases. Since the dimensionless well width is proportional to $(L_z)^2$, the well width derivative of the position of the energy levels for $n \geqslant 2$ decreases somewhat in weak fields (11). It then increases, and it can pass through zero and increase further. We note that the existence of extrema in the field dependences of $(\partial E_n/\partial L_z)$ could correspond to a maximum and minimum of broadening, depending on whether or not the derivative changes sign. As the field increases further, the negative value of the derivative increases; i.e., the corresponding broadening increases right up to merging with the continuum.

3. INFLUENCE OF POTENTIAL (QUANTUM-WELL DEPTH) FLUCTUATIONS

We shall now examine in a similar manner the effect of fluctuations of the potential on the spectrum. It is often assumed that such fluctuations can be ignored if the quantum-well material is a binary compound, for example, GaAs or InP, and not a solid solution. This is not entirely true. If the barriers are prepared from a solid solution, then fluctuations of the composition of the solution will also result in fluctuations of the quantum-well width. It is useful to take as the fluctuating parameter the offset ΔE_g of the band gap of the barrier and well materials, assuming the depth of the well $V(z)$ to be proportional to it. Then, by analogy with Eq. (13),

$$(\Gamma_{\delta \Delta E_g})_n = \left| \frac{\partial E_n}{\partial \Delta E_g} \right| \kappa_{\delta \Delta E_g} \delta \Delta E_g, \tag{15}$$

where

$$\frac{\partial E_n}{\partial \Delta E_g} = \frac{\partial (\varepsilon_n E_1^\infty)}{\partial [\tilde{v}(\Delta E_g/V) E_1^\infty]} = \frac{V}{\Delta E_g} \frac{\partial \varepsilon_n}{\partial \tilde{v}} = \frac{E_1^\infty}{\Delta E_g} \frac{\partial \varepsilon_n}{\partial \tilde{v}} \tilde{v}. \tag{16}$$

In a zero field the band gap offset derivative is positive (Fig. 4). This reflects the fact that as the well depth increases, the levels rise, approaching their values in an infinite well (Fig. 1). For constant well width, this is more pronounced for levels with larger values of n, which corresponds to a larger value of the derivative. It is interesting that for levels with

$n \geqslant 2$ and $F=0$ the derivative decreases as $\tilde{\nu}$ increases, in accordance with the decrease in the sensitivity of the levels to depth fluctuations. For the bottom level, the derivative at first increases, reaches its greatest value at $\tilde{\nu}=1$, where the higher-lying levels first appear, and then decreases, approaching zero for an infinite well. The band gap offset derivative of the position of an energy level has three characteristic sections as a function of the field. On the initial section it is essentially constant. As the field increases, the interaction with the continuum increases. As a result, all levels sink all the more, the more strongly the upper levels press against it (Fig. 1). The well-width derivative increases (Fig. 4). As the field increases further, the upper levels gradually merge with the continuum, decreasing the pressure on the lower levels. The process is accompanied by an inflection in the field-dependence of the level positions (Fig. 1). The inflection point corresponds to the maximum of the derivative under consideration (Fig. 4), which corresponds to maximum broadening.

4. SPECTRUM OF A NONIDEAL GAAS/(AL, GA)AS QUANTUM WELL

As an illustration of the possibilities of the proposed method, we shall trace the effect of an electric field on the electron energy spectrum in a $GaAs/Al_{0.3}Ga_{0.7}As$ quantum well with the following parameters: $V=224.5$ meV, $L_z=12$ nm, and $m^*=0.08m_0$. These parameters correspond to $E_1^{\infty}=33.1$ meV and $\tilde{\nu}=6.78$.

The spectral line can be described in a general form by the convolution of a Gaussian contour $G(E)$ of width $\Gamma^{inh}=\sqrt{\Gamma^2_{\delta\Delta E_g}+\Gamma^2_{\delta L_z}}$ and the function (2), which takes into account the uniform broadening Γ^{hom} due to carrier tunneling through the triangular barrier formed in an electric field:

$$g_n(E)=L_n(E)G_n(E)$$
$$=\int_{-\infty}^{+\infty} L_n(E',\Gamma_n^{hom})G_n(E-E',\Gamma_n^{inh})dE'.$$

We note that in experiments measuring specific effects it is also necessary to take into account the field-independent uniform line broadening due to interactions with phonons.

Figure 5 shows the computed spectra Σg_n, which take into account the above-considered broadening mechanisms in the presence of macroscopic fluctuations of the composition $\delta\Delta E_g/\Delta E_g=5\%$ and thickness nonuniformity $\delta L_z/L_z=5\%$ of the quantum-well layer. For definiteness, the temperature broadening was assumed to be constant in the calculations: $\Gamma_T=1.47$ meV. The energy spectrum of the quantum well was found to be much more sensitive to layer thickness fluctuations than to composition fluctuations of the solid solution. The effect of the latter mechanism is generally noticeable only in weak fields, because the band gap offset derivative (Fig. 4) starts to decrease approximately when the field-induced broadening increases considerably (Fig. 2). As a result, the spectrum changes relatively monotonically. The effect of band gap fluctuations increases with increasing height of the levels and with increasing field. Well width fluctuations affect the spectrum completely differently. In the first place, in a zero field, for the same relative magnitudes of the fluctuations, broadening due to the thickness nonuniformity of the heterolayer is much larger than the broadening due to the composition nonuniformity of the solid solution. In the second place, broadening minima due to the corresponding behavior of $\partial E_n/\partial L_z$ (Fig. 3) appear in the field range where tunneling through the triangular barrier is weak.

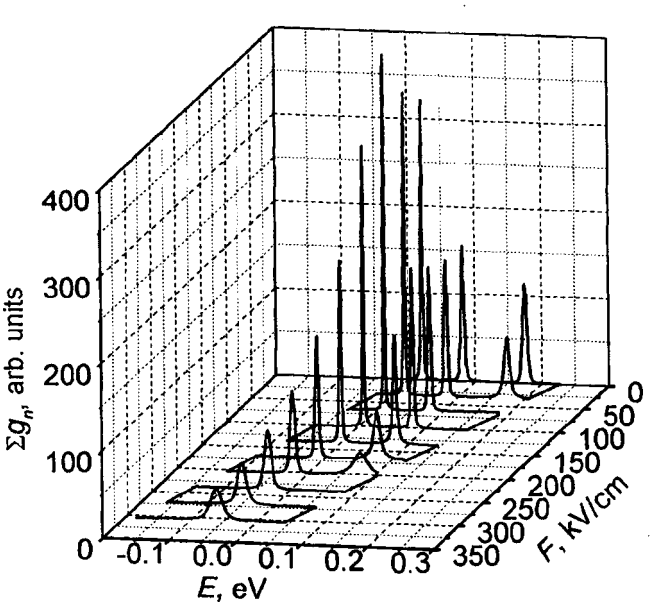

FIG. 5. Effect of an electric field on the electron energy spectrum in a nonideal $GaAs/Al_{0.3}Ga_{0.7}As$ quantum well with allowance for the field-induced broadening, broadening due to macroscopic composition fluctuations $\delta\Delta E_g/\Delta E_g=5\%$, and nonuniformity of the layer thickness $\delta L_z/L_z=5\%$ with $L_z=12$ nm.

In closing, we note that the families of dimensionless curves presented in Figs. 1–4 can be used to construct the spectra of single quantum wells with arbitrary parameters and to analyze specific experimental data. The differences found in the effect of thickness and quantum well depth fluctuations on the energy spectrum of the well in an electric field, on the one hand, could be used to determine the reasons for the nonuniform broadening of the observed spectra and, on the other, to estimate the effect of the internal (local) electric field in real structures.

*)Fax: (812) 234-3164; e-mail: pikhtin@fvleff.etu.spb.ru

[1] A. N. Pikhtin, Fiz. Tekh. Poluprovodn. **11**, 425 (1977) [Sov. Phys. Semicond. **11**, 245 (1977)].
[2] S. D. Baranovskiĭ and A. L. Éfros, Fiz. Tekh. Poluprovodn. **12**, 2233 (1978) [Sov. Phys. Semicond. **12**, 1328 (1978)].
[3] M. C. Reed and B. Simon, in *Methods of Modern Mathematical Physics*, Academic Press, N. Y., 1872 [Mir, Moscow, 1982, Vol. 4, Chap. 12, p. 66].
[4] E. L. Ivchenko and G. E. Pikus, in *Superlattices and Other Heterostructures. Symmetry and Optical Phenomena*, edited by M. Cardona (Springer Verlag Berlin, 1995, 1997) Chap. 3, p. 96.
[5] G. Bastard, E. E. Mendez, L. L. Chang, and L. Esaki, Phys. Rev. B **28**, 3241 (1983).

Translated by M. E. Alferieff

Effect of the quantum-dot surface density in the active region on injection-laser characteristics

A. R. Kovsh,*) A. E. Zhukov, A. Yu. Egorov, V. M. Ustinov, Yu. M. Shernyakov, M. V. Maksimov, A. F. Tsatsul'nikov, B. V. Volovik, A. V. Lunev, N. N. Ledentsov, P. S. Kop'ev, and Zh. I. Alferov

A. F. Ioffe Physicotechnical Institute, Russian Academy of Sciences, 194021 St. Petersburg, Russia

D. Bimberg

Institut für Festkörperphysik, Technische Universität Berlin, D-10623 Berlin, Germany
(Submitted March 23, 1998; accepted for publication March 23, 1998)
Fiz. Tekh. Poluprovodn. **32**, 1114–1118 (September 1998)

A new method of increasing the surface density of self-organized semiconductor quantum dots formed by molecular-beam epitaxy is proposed. A comparative analysis of the characteristics of injection lasers based on quantum-dot arrays with different surface density is made. It is shown that the use of quantum-dot arrays of higher density makes it possible to decrease substantially the threshold current density in the region of large losses and to increase the maximum gain and the maximum output radiation power. © *1998 American Institute of Physics.* [S1063-7826(98)02009-2]

In semiconductor physics, there has recently been steady interest in low-dimensional systems — so-called quantum wires and quantum dots (QDs). It has been shown theoretically that as a result of three-dimensional carrier quantization, by using QDs in the active region of injection heterolasers it should be possible to decrease substantially the threshold value of the current density and its temperature sensitivity[1] and to increase the specific and differential gain.[2] Great progress has now been made in the development of heterolasers based on QDs which are formed as a result of the influence of the spontaneous transformation of an elastically strained layer on an array of three-dimensional islands.[3,4] Specifically, record-low threshold current densities J_{th} of 63 and 18 A/cm^2 at room temperature and cryogenic temperatures, respectively, have been reported for a laser with an active region based on (In, Ga)As QDs in an (Al, Ga)As matrix[5] as well as 12 A/cm^2 at 77 K in a system of InAs QDs deposited in an InGaAs matrix lattice-matched with an InP substrate.[6] However, these low values of J_{th} have been obtained thus far only in samples with four cleaved faces, and an appreciable increase of the threshold current density has been observed in samples with a stripe cavity.[7]

It has been shown that in QD-based lasers superlinear growth of J_{th} with increasing radiation-output losses α_{out} is observed apparently as a result of gain saturation due to the finite number of states in the QD array.[8] Therefore, the QD surface density N_{QD} is one of the key factors determining J_{th} in QD lasers. Higher values of the density N_{QD} of a QD array used as the active region would make it possible to decrease the influence of gain saturation by increasing the maximum achievable gain. Thus, this would result in lower values of J_{th} in stripe lasers.

The method of multiple deposition of several rows of dots has been proposed for increasing the QD density.[9,10] However, the number of repeatedly deposited rows cannot be arbitrarily large and is limited by the plastic relaxation of the stress as well as by lateral association of neighboring QDs.[11] In the present paper we report a new method for increasing the density of a QD array in the growth plane. It is shown that this method of producing a QD array in the active region of a laser diode substantially improves the diode characteristics.

Transmission electron microscopy (TEM) showed that the surface density of (In, Al)As QDs in an AlGaAs matrix is $(1-2)\times10^{11}$ cm^{-2} (Ref. 12), which is two to four times higher than the value 5×10^{10} cm^{-2} observed for (In, Ga)As QDs formed under the same conditions and with the same effective thicknesses of the deposited In-containing layer.[13] This effect can be explained by the lower rate of migration of adsorbed Al atoms along the surface of a growing crystal. However, (In, Al)As QDs have much too large a band gap and their application as the recombination region of a laser is hindered by the strong thermal emission of carriers from QDs into energetically close matrix states. It would be desirable to combine a high density of (In, Ga)As QDs and a high localization energy of (In, Ga)As QDs in the composition of the active region. It has been shown that when several QD rows separated by spacer layers with thickness of the order of the island height are deposited, the subsequent rows of QDs form precisely above the tops of the islands in the preceding row.[14] Such vertical coupling of the QDs is due to the influence of the nonuniform stress distribution on the surface potential of In and Ga atoms.[15] It is logical to assume that vertical coupling will also occur if (In, Al)As dots are used in the first row or the first few rows and then several layers of (In, Ga)As QDs are deposited. As a result, the (In, Ga)As

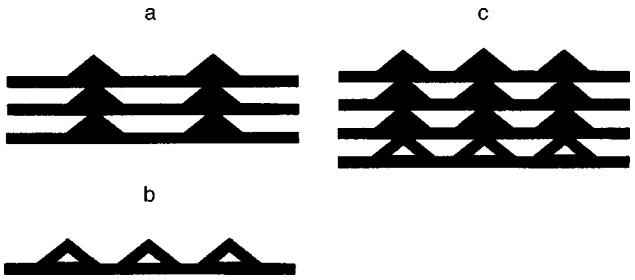

FIG. 1. Schematic representation of arrays of quantum dots in an AlGaAs matrix. a — Vertically coupled (In, Ga)As quantum dots; b — (In, Al)As quantum dots; c — composite vertically coupled (In, Al)As/(In Ga)As quantum dots.

QD array has a high surface density N_{QD}, which is fixed by the (In, Al)As QDs (Fig. 1).

The experimental structures were grown by molecular-beam epitaxy (MBE) in a Riber 32P system with a solid-state As_4 source. The active region was located at the center of a 200-nm-thick $Al_{0.15}Ga_{0.85}As$ layer, which is separated from the surface and the substrate by short-period AlAs/GaAs superlattices. The active region of one structure consists of an array of vertically coupled (In, Ga)As QDs (VCQDs), separated by 5-nm-thick AlGaAs spacers. The second structure contains a single QD array formed by deposition of an (In, Al)As layer. Finally, the active region of the last structure contains a QD array formed by depositing an (In, Al)As layer followed by triple deposition of (In, Ga)As layers with 5-nm-thick spacers. The transition from layerwise growth to island growth was observed directly during growth upon the appearance of a RHEED pattern. All three structures were grown in a standard (MBE) regime of enrichment with the group-V element. The substrate temperature was equal to 480 °C during deposition of the active region and a 100-nm thick AlGaAs cover layer and 600 °C for the rest of the structure. The photoluminescence investigations were performed with excitation by an Ar^+ laser with pump power density 100 W/cm^2.

Figure 2 shows the photoluminescence (PL) spectra of the structures described above. This figure clearly shows that ''predeposition'' of (In, Al)As QDs results in a short-wavelength shift of the maximum of the PL spectrum. It was shown earlier that the position of the maximum of the PL line depends strongly on the island size, which is determined by the effective thickness of the deposited (In, Ga)As.[16] The short-wavelength shift of the PL maximum indicates a decrease in QD sizes, which, assuming the amount of deposited material is the same, should result in a higher surface density of (In, Ga)As islands. We see from this figure that, as noted earlier, the (In, Al)As QDs themselves have a higher interband transition energy than (In, Ga)As QDs. Therefore, only the latter will determine the optical transition energy when composite (In, Al)As/(In, Ga)As VCQDs are placed in the active region of an injection heterolaser. The lasing wavelength therefore is close to the optical transition energy of

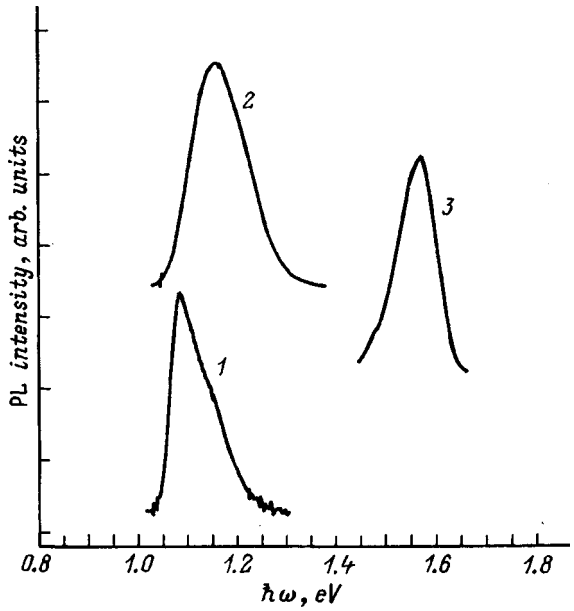

FIG. 2. Photoluminescence (PL) spectra of structures containing quantum dots in an $Al_{0.15}Ga_{0.85}As$ matrix. The pump power density is 100 W/cm^2. *1* — Vertically coupled (In, Ga)As quantum dots obtained by triple deposition of (In, Ga)As; *2* — vertically coupled (In, Al)As/(In, Ga)As quantum dots obtained by deposition of (In, Al)As and subsequent triple deposition of (In, Ga)As; 3 — (In, Al)As quantum dots.

(In, Ga)As QDs, while the surface density of the VCQD array is determined by the density of (In, Al)As QDs.

The laser structure (in what follows, LAS1) with an active region based on the above-described composite (In, Al)As/(In, Ga)As VCQD array in an $Al_{0.15}Ga_{0.85}As$ matrix was grown in the standard double-heterostructure geometry with separate confinement of the electronic and light waves. The substrate temperature during growth of the emitter layers and $Al_xGa_{1-x}As$ ($x=0.15-0.6$) waveguides was equal to 700 °C. The laser diodes, shown schematically in Fig. 3, were fabricated both in a ''fine mesa''-type stripe construction and in a geometry with four cleaved faces. Contacts to the laser diodes were formed by depositing and fusing-in (at 450 °C) metallic AuTe/Ni/Au and AuZn/Ni/Au layers to a n^+-GaAs substrate and to a p^+-GaAs contact layer, respectively. The mesa structure was passivated chemically and protected with a 0.2-μm-thick Al_2O_3 layer by magnetron deposition. The electroluminescence was investigated using pulsed (pulse repetition frequency 5 kHz, pulse duration 200 ns) and continuous pumping. The lasing wavelength for all laser diodes investigated was close to 0.85 μm, which was also the wavelength at the maximum of the PL peak of the LAS1 structure, recorded after the top contact layer was removed by chemical etching. This attests to the fact that lasing occurs through the ground state of the QDs.

Figure 4 shows the threshold current density plotted as a function of the reciprocal $1/L$ of the cavity length at room temperature for a given laser. In addition, the same dependence for a laser structure (in what follows, the structure LAS2) consisting of 10 rows of (In, Ga)As VCQDs in an AlGaAs matrix, which are formed without predeposition of (In, Al)As QDs, is shown for comparison.[17] For low exit

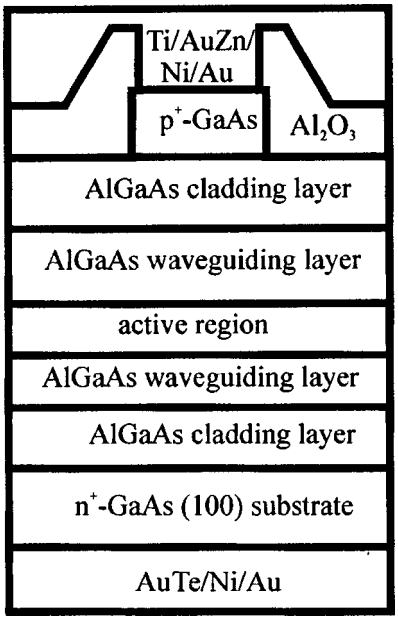

FIG. 3. Schematic representation of the test laser which is based on an array of composite (In, Al)As/(In, Ga)As quantum dots in a AlGaAs matrix.

losses, which corresponds to the case of large cavity lengths, the threshold current densities of both structures are virtually identical, while for an infinite cavity length (geometry with four cleaved faces) the threshold current density of the LAS2 structure is lower. However, as the cavity length decreases, the threshold current density of the LAS2 structure increases much more rapidly than in the case of the LAS1 structure. To determine the reasons for this behavior we shall determine the dependence of the optical gain on the pump current. This dependence can be constructed by using the data in Fig.

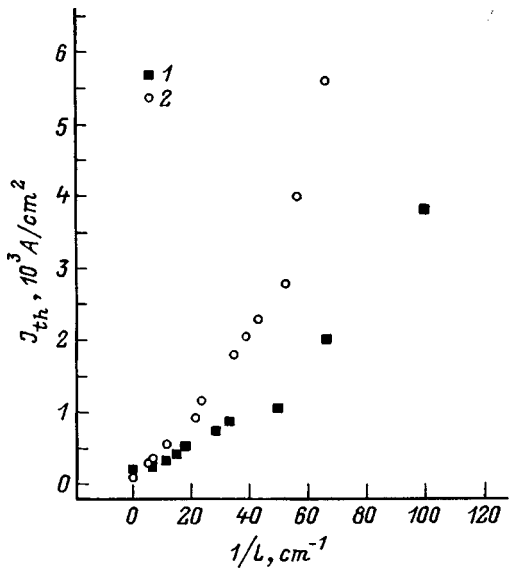

FIG. 4. Threshold current density J_{th} at 300 K versus the reciprocal $1/L$ of the length of a stripe cavity for LAS1 and LAS2 structures containing, respectively, arrays of composite (In, Al)As/(In, Ga)As QDs (1) and InGaAs QDs (2) in an $Al_{0.15}Ga_{0.85}As$ matrix. The stripe width is 100 μm. The data for $1/L=0$ correspond to samples with four cleaved faces.

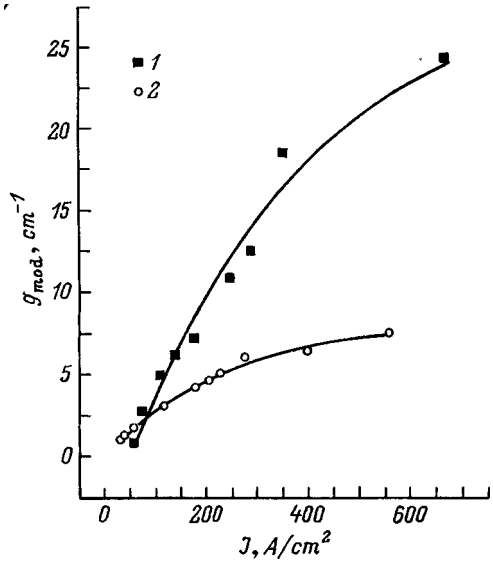

FIG. 5. Mode gain g_{mod} versus pump current density J for LAS1 (1) and LAS2 (2) structures, referred to one layer of quantum dots.

3 and taking into account the fact that at the lasing threshold the mode gain g_{mod} equals the total losses

$$g_{\mathrm{mod}}=\alpha_{\mathrm{in}}+\alpha_{\mathrm{out}}=\alpha_{\mathrm{in}}+\frac{1}{L}\ln\left(\frac{1}{R}\right), \tag{1}$$

and also by using the cavity length dependence of the external quantum yield η_{dif}. By analyzing the dependence $1/\eta_{\mathrm{dif}}=f(L)$ it is possible to determine the internal quantum efficiency η_{in} and internal losses α_{in}. These quantities are $\eta_{\mathrm{in}}\sim 60\%$ and $\alpha_{\mathrm{in}}\sim 5\ \mathrm{cm}^{-1}$ for LAS2 and $\eta_{\mathrm{in}}\sim 70\%$ and $\sigma_{\mathrm{in}}\sim 2.5\ \mathrm{cm}^{-1}$ for LAS1.

The desired pump current dependence of the mode gain of QDs, normalized to the number of (In, Ga)As QD layers, which equals 3 or 10 for the LAS1 and LAS2 cases, respectively, is shown in Fig. 5. We see from this figure that a higher pump current density is required in order to achieve low gain in the LAS1 structure. This is attributable to the higher transmission current than in the LAS2 structure as a result of the higher density of QDs in which a population inversion must be produced. The transmission currents J_{tr} corresponding to zero gain were determined by extrapolating the experimental curves $g(J)$, equal to 45 and 7 A/cm^2 in LAS1 and LAS2 structures, respectively.

As the pump current increases, the gain in the LAS2 structure saturates rapidly, while in the LAS1 structure it continues to grow and becomes much higher than in LAS2. This behavior is due to the increase in the maximum gain achieved on QDs, which is proportional to the density of the array of dots. Therefore, the most important effect in the low-gain region is due to the transmission current, and increasing N_{QD} results in higher values of the threshold current density. Gain saturation is more important in the high-gain region, and the threshold current density in this region decreases as N_{QD} increases. It should be noted that similar behavior is also observed for the theoretically computed

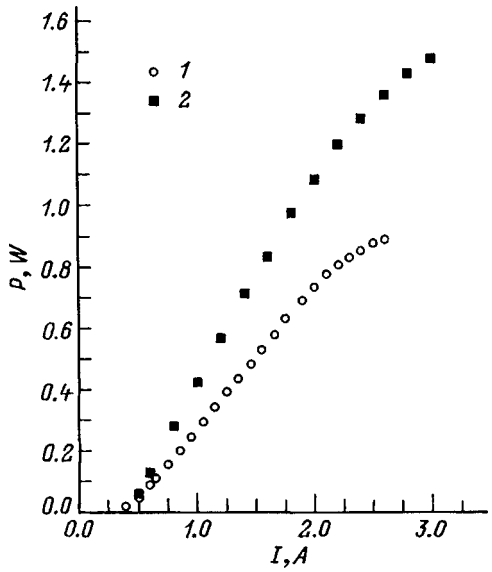

FIG. 6. Power versus current characteristics of LAS1 (1) and LAS2 (2) structures in a continuous-wave regime with heat-transfer temperature of 15 °C. The stripe length is 1000 μm and the stripe width is 100 μm.

pump current density dependences of the gain for a QD array with different surface densities.[18]

Higher values of the maximum gain would also make it possible to increase the maximum power of the laser radiation. Figure 6 shows the output power P at both mirrors versus the pump current I for the structures studied. The maximum power was equal to 0.9 W for the LAS1 structure, while for the LAS2 structure with an increased QD surface density the value achieved is 1.5 times higher and equals 1.5 W. We also note that increasing the QD density of states by increasing N_{QD} decreases the population of the matrix states at the same pump level, which in turn makes it possible to decrease the parasitic currents and overheating of the structure caused by recombination through higher-lying states. This is important for achieving high output radiation power.

In summary, in the present paper we showed that it is possible to increase the surface density of QDs. We found that the use of higher-density VCQD arrays, formed by ''predeposition'' of (In, Al)As QDs, as the active region in an injection laser increases the maximum gain and the maximum radiation power up to 1.5 W in the continuous regime. Further progress in using Al-containing QDs as centers of stimulated formation of (In, Ga)As QDs can be made by determining the optimal number of (In, Al)As QDs rows, the percentage Al content, and the thickness of spacer layers and by optimizing the growth conditions for composite (In, Al)As/(In, Ga)As QD arrays.

This work was supported by the Russian Fund for Fundamental Research (Grant 96-02-17824) and the Project INTAS-96-0467.

*E-mail: kovsh@beam.ioffe.rssi.ru

[1] Y. Arakawa and H. Sakaki, Appl. Phys. Lett. **40**, 939 (1982).
[2] M. Asada, Y. Miyamoto, and Y. Suematsu, J. Quant. Electron., **QE-22**, 1915 (1986).
[3] L. Goldstein, F. Glas, J. Y. Marzin, M. N. Charasse, G. Le Roux, Appl. Phys. Lett. **47**, 1099 (1985).
[4] P. M. Petroff and S. P. DenBaars, Superlattices Microstruct. **15**, 15 (1994).
[5] V. M. Ustinov, A. Yu. Egorov, A. R. Kovsh, A. E. Zhukov, M. V. Maksimov, A. F. Tsatsul'nikov, N. Yu. Gordeev, S. V. Zaitsev, Yu. M. Shernyakov, N. A. Bert, P. S. Kop'ev, Zh. I. Alferov, N. N. Ledentsov, J. Bohrer, D. Bimberg, A. O. Kosogov, P. Werner, and U. Gosele, J. Cryst. Growth **175/176**, 689 (1997).
[6] V. M. Ustinov, A. E. Zhukov, A. Yu. Egorov, A. R. Kovsh, S. V. Zaitsev, N. Yu. Gordeev, V. I. Kopchatov, N. N. Ledentsov, A. F. Tsatsul'nikov, V. Volovik, P. S. Kop'ev, Zh. I. Alferov, S. S. Ruvimov, Z. Liliental-Weber, and D. Bimberg, Electron. Lett. (1998) (in press).
[7] S. V. Zaitsev, N. Yu. Gordeev, Yu. M. Shernyakov, V. M. Ustinov, A. E. Zhukov, A. Yu. Egorov, M. V. Maximov, P. S. Kop'ev, Zh. I. Alferov, N. N. Ledentsov, N. Kirstaedter, and D. Bimberg, Superlattices Microstruct. **21**, 559 (1997).
[8] O. G. Schmidt, N. Kirstaedter, N. N. Ledentsov, M. H. Mao, D. Bimberg, V. M. Ustinov, A. Yu. Egorov, A. E. Zhukov, M. V. Maximov, P. S. Kop'ev, and Zh. I. Alferov, Electron. Lett. **32**, 1302 (1996).
[9] V. M. Ustinov, A. Yu. Egorov, A. E. Zhukov, N. N. Ledentsov, M. V. Maksimov, A. F. Tsatsul'nikov, N. A. Bert, A. O. Kosogov, P. S. Kop'ev, D. Bimberg, and Zh. I. Alferov, in *Proceedings of the Mater. Research Society*, 1995 Fall Meeting, Boston, MA, 1995, EE 3.6.
[10] Q. Xie, A. Madhukar, P. Chen, and N. Kobayashi, Phys. Rev. Lett. **75**, 2542 (1995).
[11] A. F. Tsatsul'nikov, A. Yu. Egorov, A. E. Zhukov, A. R. Kovsh, V. M. Ustinov, N. N. Ledentsov, M. V. Maksimov, B. V. Volovik, A. A. Suvorova, N. A. Bert, and P. S. Kop'ev, Fiz. Tekh. Poluprovodn. **31**, 851 (1997) [Semiconductors **31**, 722 (1997)].
[12] A. F. Tsatsul'nikov, A. Yu. Egorov, A. E. Zhukov, A. R. Kovsh, V. M. Ustinov, N. N. Ledentsov, M. V. Maksimov, A. V. Sakharov, A. A. Suvorova, P. S. Kop'ev, Zh. I. Alferov, and D. Bimberg, Fiz. Tekh. Poluprovodn. **31**, 110 (1997) [Semiconductors **31**, 88 (1997)].
[13] S. S. Ruvimov, P. Werner, K. Scheerschmidt, U. Gosele, J. Heydenreich, U. Richter, N. N. Ledentsov, M. Grundmann, D. Bimberg, V. M. Ustinov, A. Yu. Egorov, P. S. Kop'ev, and Zh. I. Alferov, Phys. Rev. B **51**, 14 766 (1995).
[14] A. Yu. Egorov, A. E. Zhukov, P. S. Kop'ev, N. N. Ledentsov, M. V. Maksimov, V. M. Ustinov, A. F. Tsatsul'nikov, N. A. Bert, A. O. Kosogov, D. Bimberg, and Zh. I. Alferov, Fiz. Tekh. Poluprovodn. **30**, 1682 (1996) [Semiconductors **30**, 879 (1996)].
[15] N. N. Ledentsov, V. A. Shchukin, M. Grundmann, N. Kirstaedter, J. Bohrer, O. Schmidt, D. Bimberg, V. M. Ustinov, A. Yu. Egorov, A. E. Zhukov, P. S. Kop'ev, S. V. Zaitsev, Zh. I. Alferov, A. I. Borovkov, A. O. Kosogov, S. S. Ruvimov, P. Werner, U. Gosele, and J. Heydenreich, Phys. Rev. B **54**, 8743 (1996).
[16] A. Yu. Egorov, A. E. Zhukov, P. S. Kop'ev, N. N. Ledentsov, M. V. Maksimov, V. M. Ustinov, A. F. Tsatsul'nikov, Zh. I. Alferov, D. L. Fedorov, and D. Bimberg, Fiz. Tekh. Poluprovodn. **30**, 1345 (1996) [Semiconductors **30**, 707 (1996)].
[17] A. E. Zhukov, V. M. Ustinov, A. Yu. Egorov, A. R. Kovsh, A. F. Tsatsul'nikov, M. V. Maximov, N. N. Ledentsov, S. V. Zaitsev, N. Yu. Gordeev, Yu. M. Shernyakov, P. S. Kop'ev, and Zh. I. Alferov, J. Electron. Mater. **27**, 106 (1998).
[18] L. V. Asryan and R. A. Suris, in *Proceedings of the International Symposium ''Nanostructures: Physics and Technology,''* St. Petersburg, 1996, p. 354.

Translated by M. E. Alferieff